

TR 2988 S

TR 2988 S

# **STELLINGEN**

behorende bij het proefschrift:

**SEDIMENTATION IN RESERVOIRS**

van

**C.J. Sloff**

april 1997

## STELLINGEN

1. In een twee-dimensionale horizontale morfologische berekening is het onjuist in een bijna-kritische of superkritische stromingssituatie de waterbeweging en morfologie te ontkoppelen.
2. Voor praktische toepassingen waardevolle één-dimensionale morfologische berekeningen met behulp van een numeriek schema van het Lax-Wendroff type zijn alleen mogelijk wanneer gebruik wordt gemaakt van een kunstmatige viscositeit, bij voorkeur een type met "*Total Variation Diminishing*" eigenschappen.
3. De waterstanden ter plaatse van een watersprong, berekend met een één-dimensionaal numeriek *shock-capturing* model worden door Rahman en Chaudry (1993) ten onrechte vergeleken met metingen.  
M. Rahman and M.H. Chaudry (1995) Simulation of hydraulic jump with grid adaptation. J. Hydraulic Research, IAHR, Vol.33, No.4, p.555.
4. De ontbrekende fundamentele schakel in het kwantificeren van dichtheidsstromen van sediment is een voldoende geverifieerd wiskundig model voor de sediment-water interactie.
5. Het spoelen van fijn sediment door middel van dichtheidsstromen kan als een zeer efficiënte hydraulische methode worden beschouwd om de *trap-efficiency* van een stuwmeer te reduceren.
6. In tegenstelling tot de gangbare veronderstelling worden negatieve economische, sociale, morfologische en milieu effecten niet alleen veroorzaakt door de stuwdam, maar vooral door het bijbehorende stuwmeer.
7. Als gevolg van de trendmatige groei van het aantal kleine stuwmeren, is een aanzienlijk grotere investering vereist in onderzoek naar reservoir sedimentatie.
8. Het falen van de satellieten in een baan om de planeet Mars kan door rivier-morfologen als een teleurstelling worden ervaren.  
Baker, V.R. (1982) The channels of Mars, Univ. of Texas Press, Austina, Texas, USA.
9. Met de huidige techniek kunnen wiskundige modellen kernproeven niet geheel vervangen. Daarom zal de vraag naar aanvullende empirische informatie leiden tot hervatting van kernproeven.
10. Naast de kwaliteit bepaalt helaas vooral de presentatie de waardering voor de op een congres gepresenteerde wetenschapsresultaten.

11. De voortdurende speurtocht naar de oorsprong van het heelal wordt gevoed door het "eindig" denken van de mens.
12. Voor de westerse wereld wordt de armoede in ontwikkelingslanden duidelijker naarmate deze landen verwestelijken.
13. Een sterke bevordering van de economische ontwikkeling van Kaapverdië zal zich voordoen wanneer de monopoliepositie van de nationale luchtvaartmaatschappij wordt doorbroken.
14. In het aanbieden van videorecorders met drie knappe (weergave-)koppen aan de consument wordt door de industrie voorbij gegaan aan de noodzaak voor een vierde knappe kop voor de bediening van het apparaat.



TR 2928

# SEDIMENTATION IN RESERVOIRS

To my father

Cover design: Renske Schoonen-Sloff

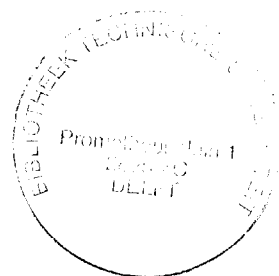
This thesis is also published in the series '*Communications on Hydraulic and Geotechnical Engineering*' of the Faculty of Civil Engineering, Delft University of Technology, report nr. 97-1

# Sedimentation in reservoirs

## PROEFSCHRIFT

ter verkrijging van de graad van doctor  
aan de Technische Universiteit Delft  
op gezag van de Rector Magnificus Prof.dr.ir. J. Blaauwendraad,  
in het openbaar te verdedigen ten overstaan van een commissie,  
door het College van Dekanen aangewezen,  
op dinsdag 15 april 1997 te 13.30 uur

Cornelis Johannes SLOFF  
civiel ingenieur  
geboren te Heerjansdam



Dit proefschrift is goedgekeurd door de promotor:  
Prof.dr.ir. M. de Vries

Samenstelling promotiecommissie:

Rector Magnificus	voorzitter
Prof.dr.ir. M. de Vries	em. hgl. Technische Universiteit Delft, promotor
Prof.dr.s.ir. J.K. Vrijling	Technische Universiteit
Prof.dr.ir. C. van den Akker	Technische Universiteit Delft
Prof.dr.ir. H.J. de Vriend	Universiteit Twente en Technische Universiteit Delft
Prof.dr. J.H.J. Terwindt	Universiteit Utrecht
Dr.ir. C. Kranenburg	Technische Universiteit Delft
Dr.ir. J.S. Ribberink	Universiteit Twente

Dit proefschrift is tot stand gekomen in samenwerking met het Waterloopkundig  
Laboratorium, Delft.

**ISBN 90-9010530-1**

Copyright © by C.J. Sloff, 1997



## **Abstract**

Due to sedimentation processes, reservoirs designed to store, use and regulate river runoff are losing their capacity, and are therefore seriously threatened in their performance. To master the reservoir-sedimentation issues the endeavour to a good prediction of the processes, and to a better understanding of the reservoir behaviour is essential. From these processes a more profound study is made of turbidity currents in reservoirs. These suspension underflows are able to carry fine sediments towards the dam where they can be sluiced out, reducing the deposition rate. In this thesis the properties and development of such turbidity currents are studied by means of a two-dimensional depth-averaged (2-DH) two-layer mathematical model. The model is developed as a blend of conventional approaches and state-of-the-art techniques. To analyze the structure of solutions of the 2-DH model and an equivalent one-dimensional (1-D) model the method of characteristics is used. Further, after studying density-current fronts and internal jumps, some 1-D and 2-DH analytical solutions are used to gain insight in the mechanics of the propagating turbidity current, and to verify numerical solutions. For the 1-D approach a numerical finite-difference technique (based on MacCormack's scheme) is adopted, which is also applicable to simulate the fronts and jumps in the propagating density current. Some of the used numerical procedures were found to be also very useful in computing morphological processes in an open channel flow. For testing and verification the numerical model is applied to some laboratory experiments and field observations.

## **Samenvatting**

### **Sedimentatie in stuwmeren**

Stuwmeren ontworpen om rivierafvoeren te bergen, te benutten, en te reguleren, verliezen hun capaciteit door aanzandingsprocessen. Hun functie wordt daardoor ernstig bedreigd. Om deze reservoir-sedimentatie problematiek te bestrijden is het essentieel te streven naar een goede voorspelling van de processen en naar meer inzicht in de werking van stuwmeren. Uit deze processen is een meer diepgaande studie verricht naar suspensie dichtheidsstromen in reservoirs. Dit type dichtheidsstromen is in staat fijn sediment naar de dam te voeren, waarna het kan worden geloosd zodat de hoeveelheid aanzanding wordt gereduceerd. In dit proefschrift zijn de eigenschappen en de ontwikkeling van zulke dichtheidsstromen van gesuspendeerd sediment bestudeerd met behulp van een wiskundig tweedimensionaal dieptegemiddeld (2-DH) twee-lagen model. Het model is gebaseerd

op een combinatie van traditionele en nieuwe technieken. De "karakteristieke methode" is gebruikt om de structuur van de oplossingen van dit 2-DH model en een overeenkomstig één-dimensionaal (1-D) model te analyseren. Na het bestuderen van interne fronten en sprongen zijn vervolgens enkele 1-D en 2-DH analytische oplossingen bestudeerd om inzicht te krijgen in de mechanica van het voortplantende suspensiefront, en voor verificatie van numerieke oplossingen. Voor de 1-D aanpak is een numerieke eindige-differentie methode (op basis van het MacCormack schema) gekozen, die ook toepasbaar is voor het simuleren van de interne fronten en sprongen in de ontwikkelende dichtheidsstroom. Een deel van de numerieke methoden bleek ook bruikbaar te zijn voor het berekenen van morfologische processen in open waterlopen. Voor toetsing en verificatie is het numerieke model toegepast voor enkele laboratorium experimenten en veldwaarnemingen.

# Table of contents

Abstract	iii
Samenvatting (Abstract in Dutch)	iii
<b>Chapter 1 Introduction</b>	
1.1 General	1
1.2 Storage reservoirs and reservoir-sedimentation issues	3
1.3 Methods to preserve reservoir capacity	8
1.4 Modelling techniques	11
<b>Chapter 2 Mathematical model</b>	
2.1 Introduction	15
2.2 Basic equations for a 2-DH two-layer model	
2.2.1 General model	17
2.2.2 2-DH Boussinesq model	20
2.2.3 Decoupling of baroclinic and barotropic flow	22
2.3 Galappatti's model for a 2-DH turbidity current	25
2.4 Flow structure and sediment transport	
2.4.1 General structure and basic equations	35
2.4.2 Lower sub-layer of a turbidity current	39
2.4.3 Upper sub-layer of a turbidity current	40
2.4.4 Depth-integrated velocity and roughness scale	41
2.4.5 Concentration profile and suspended-sediment transport	43
2.5 Closure relations for the two-layer model	48
<b>Chapter 3 Characteristic analysis</b>	
3.1 Introduction	55
3.2 Characteristic conditions	56
3.3 Analysis of characteristics for the 1-D 2-layer flow	60
3.4 Analysis of characteristics for the 2-DH 2-layer flow	
3.4.1 Introduction	64
3.4.2 Internal subcritical flow	65
3.4.3 Internal supercritical flow	67
3.5 Number of boundary conditions	69
3.6 Discussion	71

## **Chapter 4 Gravity-current fronts**

4.1	Introduction	75
4.2	Gravity-current fronts in laboratory and in the field	76
4.3	Theoretical considerations on shock relations for front propagation in a one-dimensional 2-layer flow	81
4.4	Shock relations for front propagation in a one-dimensional 2-layer flow	86
4.5	Conceptual model for 2-DH front propagation	94

## **Chapter 5 Analytical similarity solutions**

5.1	Introduction	99
5.2	1-D self-similar solutions	
5.2.1	Introduction and derivation	100
5.2.2	Self-similar solutions for lock-exchange flows	104
5.2.3	Self-similar solutions for sluicing operations	110
5.2.4	Discussion	111
5.3	Axi-symmetric 2-DH radial flows	
5.3.1	Construction of 2-DH self-similar solutions	113
5.3.2	Analysis of 2-DH self-similar currents	117

## **Chapter 6 Numerical model**

6.1	Introduction	129
6.2	Overview of numerical methods for discontinuous flows	
6.2.1	Introduction	131
6.2.2	Space-centred schemes	135
6.2.3	Upwind schemes	136
6.2.4	High-resolution schemes: FCT and TVD algorithms	138
6.2.5	Choice of the numerical solution method	141
6.3	MacCormack scheme	142
6.4	1-D model discretization using MacCormack's scheme	
6.4.1	Baroclinic flow	145
6.4.2	Barotropic flow	149
6.5	Conventional artificial viscosity approach	151
6.6	TVD artificial viscosity approach	158
6.7	Boundary conditions	
6.7.1	Type of boundary conditions and well posedness	165
6.7.2	Discretization of boundary conditions	169
6.8	Initial conditions	175
6.9	Stability and accuracy	179

6.10	Shock tracking	189
6.11	Conclusions	193
<b>Chapter 7 Test cases</b>		
7.1	Introduction	197
7.2	Laboratory experiments of turbidity currents in Minnesota	197
7.3	Laboratory experiments of turbidity currents in Delft	204
7.4	Experiments of turbidity-current fronts in Lausanne	207
7.5	Laboratory experiments of lock-exchange flows	209
7.6	Morphological computation of a bed front in a channel	213
7.7	Turbidity current in glacier-fed Peyto Lake, Alberta, Canada	215
7.8	Conclusions	220
<b>Chapter 8 Conclusions</b>		223
<b>References</b>		229
<b>Main symbols</b>		243
<b>Acknowledgements</b>		247
<b>Appendix A Conceptual model for front propagation in a 2-DH 2-layer model</b>		251
<b>Appendix B Total variation diminishing (TVD) artificial viscosity</b>		
B.1	Roe's linearization of the non-linear system	259
B.2	Flux limiters	267
B.3	Entropy fix	269
<b>Curriculum vitae (in Dutch)</b>		271



# Chapter 1

## Introduction

### 1.1 General

Reservoirs designed to store river runoff are seriously threatened in their performance by sedimentation processes, which is a natural consequence of interrupting the river course. The quiescent pool behind the dam generates favourable conditions for particle settling, such that important storage capacity is lost. Replacement of this lost storage and construction of new reservoirs to satisfy the increasing demand becomes more difficult due to constraints imposed by environmental, social, political and environmental concerns. Therefore a growing research effort is made to minimize the trap efficiency of reservoirs and to maximize the long-term storage volume. Engineers are challenged by the difficult questions emerging. How to incorporate reservoir problems in feasibility studies (cost-benefit analyses) including environmental and technical effects, limitations on benefit and possible measures? Or what is the impact of sedimentation on the reservoir performance, and what is the impact of the reservoir on stream-system morphology? Obviously a good prediction of the processes, and the endeavour to better understanding of the reservoir behaviour is essential to master the reservoir-sedimentation issues.

This thesis addresses the problem of reservoir sedimentation from a hydraulic engineering point of view. This means that the study focuses primarily on the flow and sediment-transport processes in a reservoir, with only few extensions to other themes. In the following sections it is shown that the many geophysical processes which are involved in deposition and distribution of the sediments are complex and often poorly understood. Therefore any reliable quantification of detailed sedimentation processes can exist only if we are able to simulate all the mechanisms using appropriate models. Anticipating on the reduction of the deposition rate a choice is made for a more profound investigation of turbidity currents, i.e., density currents caused by sediment suspensions. Turbidity currents occur when the river inflow contains sufficient suspended particles to plunge below the clear and quiescent reservoir water, after which it continues as a dense underflow capable of transporting the sediments over long distances. If the current can reach the dam it can be effectively used to sluice fine sediments through the

reservoir if it is released through bottom outlets in the dam.

To gain more insight in the behaviour and physics of turbidity currents in reservoirs a mathematical model is presented in chapter 2. The nature of these currents allows for a two-layer stratified-flow model which is presented in a 2-DH (depth-integrated) form and consists of balance equations for momentum and for mass of sediment and fluid of a turbulent underflow in a ambient fluid of finite depth. To quantify the flow and sediment structure of these currents, required for closure of the depth-integrated model, an additional semi-empirical model is developed based on laboratory and field data. Furthermore some relations for physically important mechanisms as friction and interfacial mixing are proposed and evaluated. The analogy between turbidity currents and other types of density currents (e.g., saline currents) is here an important postulate.

In chapter 3 the mathematical model, consisting of a number of partial differential equations, is further examined using the method of characteristics. It is shown how disturbances develop in the solution as physically relevant wave fronts, inherent to the hyperbolic character of the basic equations. On basis of these results important criteria, limitations and simplifications of the model are detected which are valuable for other types of 2-D models as well. As the characteristics are a fundamental part of the solution they play an important role in the analytical and numerical approaches in the following chapters.

It is not a universal fact that gravity currents developing in reservoirs are smooth. Usually they are characterized by various discontinuities such as internal hydraulic jumps and naturally the advancing front or head of the current. The computation of the front is relevant to approximate when or whether it reaches the dam where it can be vented. In the model these phenomena can be represented with partially empirical shock-relations which act as internal boundary conditions. In chapter 4 it is shown that alternatively, by rewriting the 1-D basic equations, the front (and other shocks) can be captured properly as discontinuous solutions or shock waves of the mathematical model. Theoretical considerations on these shock relations are given for 1-D as well as for 2-D fronts. In chapter 5 the complete discontinuous solution for the two layer model (in a somewhat simplified form) is studied analytically for self-similar density currents. Both for 1-D plane and 2-D radial developing underflows these exact solutions are analyzed and explained. Self-similar solutions are especially meaningful for verification of the numerical method presented in chapter 6.

Although important insight can be obtained from this analytical approach for the simplified model, a numerical approach is required to solve the complete non-linear and non-homogeneous model. The methodology to compute 1-D discontinuous turbidity currents is the topic of chapter 6. A numerical shock-capturing scheme is chosen after a review of available schemes from Computational Fluid Dynamics.



Furthermore special attention is paid to artificial viscosity techniques, boundary-value treatment and certain numerical tricks to optimize accuracy and stability of the computations. Some test cases for the 1-D numerical model are presented in chapter 7 to validate the two-layer approach.

## 1.2 Storage reservoirs and reservoir-sedimentation issues

For thousands of years dams have ensured an important supply of water for domestic usage, irrigation, energy generation and other purposes (e.g., Sloff, 1991). Reservoirs behind the dams store the unstable flood waters of the river runoff increasing and conserving the manageable and stable amount of fresh water. Furthermore they create head for hydro-electric power generation (often referred to as white coal, and presently responsible for about 20% of the worlds primary electric energy production) which is often a primary motivation to their design. Over the last hundred years the number of dams has increased from 1000 to over 36000, of which 85 % was built in the last 40 years (Veltrop, 1991). About 80 % of these dams are between 15 and 30 m high, about 15 % between 30 and 60 m, and about 5 % exceeds the 60 m (up till 300 m). The total amount of water which can be stored in these reservoirs is about 5500 km<sup>3</sup> of which one-third is dead storage and cannot be used. A large growth of reservoir volume and the number of dams is expected for the coming decades, related to the fast economic development, growth of the world population and the expanding irrigated agriculture (Osborne, 1995, Veltrop, 1991). On the other hand a growing resistance of environmental, social, cultural, political and economical nature imposes important constraints on the construction of new dams. The awareness of the serious impacts of reservoirs also imposes responsibilities to engineers, although they will not be able to sufficiently satisfy all (often conflicting) interests.

A serious threat to available storage is imposed by reservoir sedimentation. The annual loss of storage in reservoirs is roughly 1% corresponding to a about 50 km<sup>3</sup> world wide (Mahmood, 1987). Some reservoirs have a much higher storage loss, e.g., the Sanmenxia Reservoir in China loses about 1.7% yearly, the Sefid-Rud reservoir in Iran about 2%, and the Welbedacht reservoir in South Africa loses about 5% of its capacity. In the meantime significant transformations can occur in the stream basin due to the redistribution of sediments and discharges. Sloff (1991) reviewed these phenomena by means of a survey of the scattered literature in order to find the remaining gaps in the applied theory. Theoretical approaches are here desired to estimate the sedimentation threat and even to reconsider the design. In the past highly empirical models were used for this purpose, but often resulted (sometimes deliberately) in an underestimation of the actual sedimentation rate.

This can be ascribed to failing theory as well as to a lack of data. For instance sedimentation rates of the Sefid-Rud reservoir in north-west Iran can be estimated with a 60 years old highly empirical approach (Tolouie et al., 1993) to be about  $35 \cdot 10^6 \text{ m}^3/\text{a}$ . However, after construction (in 1962) the measured rate was about  $45 \cdot 10^6 \text{ m}^3/\text{a}$  causing a storage loss of over 30% in 1980. The original predicted useful reservoir life of one century based on old data, was found to be actually about 30 years (Pazwash, 1982). Not until 1980 flushing operations were started which were able to regain about 7% of the lost capacity.

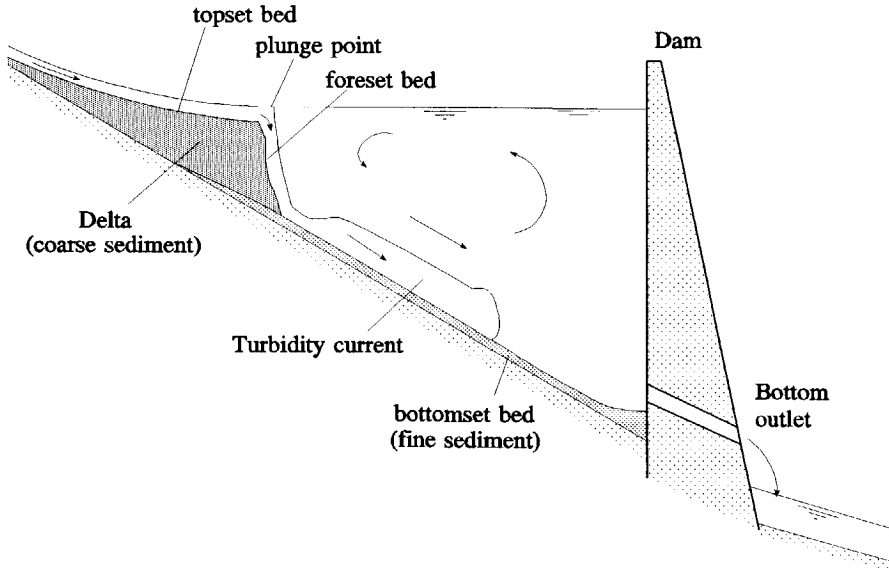


Figure 1.1 Schematic presentation of principle sedimentation processes in river-fed storage reservoirs.

Figure 1.1 shows the principle processes involved with sedimentation in a storage reservoir as treated in Sloff (1991). The distribution principles of these sediments in the reservoir and the associated river reach can be subdivided into four groups which will be summarized in the following. Note that the grain-size distribution of river sediments is an essential feature in these processes.

*Coarse sediments and deltaic deposits*

Mainly the coarse sediment fractions are deposited in the head of the reservoir by backwater effects during high discharges, forming a delta. Successively the most upstream part is called the tail reach (transition from river to delta), the middle part is called topset bed (with a practically constant slope, about 1/2 to 2/3 times the original bed slope), and the lower part is called foreset bed (with a slope about 6 1/2

to 100 times the topset slope). In this profile the delta proceeds into the reservoir while the foreset slope can be considered as a front which appears as an area of instability and slumping. A simple 1-D computational example for an advancing delta is given in figure 1.2. It is computed using the model presented in this thesis (Chapter 6) using uniform sediment, a constant width, and a constant inflow. A similar result was reported by Hotchkiss and Parker (1991).

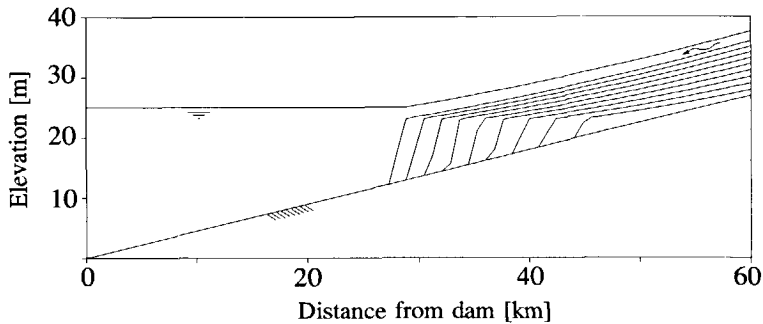


Figure 1.2 Example of a delta development due to backwater effects in a 1-D reservoir with uniform sediment and fixed lake level.

When the delta toe reaches the dam the slumping of the delta face can block the entrance to the bottom outlets. Deltaic deposits may result in unattractive swamps (in combination with fine sediments), and extend the backwater and sedimentation effect further upstream (see also figure 1.2). The latter effect will cause for instance an increased flooding risk, silting up of harbours in the upper reach, and problems for navigation by shoaling and by less clearance below bridges. Furthermore an adaptation of the river regime may occur where for instance a braided channel becomes a single meandering stream, such that important branches for navigation can disappear (Vanoni, 1977).

Some interesting features can be observed in reservoir deltas. During pool drawdowns a channel is created in the deposits by retrogressive erosion. Its slope approaches that of the original river bed. Furthermore a clear sorting effect is seen where the topset slope continues into the foreset slope (Fan & Morris, 1992a, Schoklitsch, 1935). At this point an abrupt change develops from gravel to sand, which is also common in natural streams and has often been associated with pronounced bimodality in the bed material (Poalo et al., 1992).

The complex morphological development of the delta is highly dependent on the stochastic riverine inflow parameters, sediment properties, the shape of the valley, and the operation of the reservoir. Since input data are usually insufficient, and since the actual physics cannot be modelled accurately (mainly empirically) it is still difficult to obtain reliable predictions on the delta development.

### *Fine sediments in homogeneous flow*

A large part of the fine sediments transported in suspension or as washload are transported beyond the delta after which they settle out to form the bottomset bed. They are more evenly spread than coarse sediment, but their distribution is highly dependent on reservoir circulation and stratification, for instance generated by river inflow and wind shear, or precluded by an ice cover. Also for this type of deposition the quantification methods still yield rough predictions.

In case of cohesive sediments, consolidation and the pattern of shrinkage cracks formed during filling and emptying of the reservoir may result in a impermeable blanket which is strong and dense enough to resist erosion (this feature can also be found on the delta, but to a lesser extent). The effectiveness of desiltation methods is reduced by these phenomena.

### *Turbidity currents*

Another important transport mode for fine sediments, i.e., silt and clay, is the turbidity current. It is formed when the turbid river inflow plunges below the clear reservoir water and continues as a density underflow. Also other processes can generate them, such as underwater slides (slumping of delta front) or coastal erosion. Turbidity currents are driven by an excess gravity force (negative buoyancy) due to the presence of sediment-laden water in a clear ambient fluid. These low velocity currents are capable of transporting large quantities of sediment over long distances. Not all reservoir researchers were convinced of their importance, as they have often been considered as rare events. On the other hand, the abundance of evidence in literature, indicates that turbidity currents become more and more accepted as potential measure to reduce sedimentation although their contribution is less than deltaic deposit processes (usually they create large mud deposits, turbites, in front of the dam). Examples of field studies in lakes and reservoirs are for instance Chikita (1989, 1992), Chikita et al. (1991), Fan (1986, 1991), Gould (1960), Lambert and Giovanoli (1988), Nizery and Bonnin (1953), Normark and Dickenson (1976), Smith et al. (1964), and Weirich (1984). Some well-known field studies from oceans and seas are for instance Hay et al. (1982), Heezen and Ewing (1952), Inman et al. (1976), Prior et al. (1987), and Shepard et al. (1977).

In many reservoirs the formation of a turbidity current is a well known spectacle with the lake-shore residents, since the plunge point is clearly marked on the reservoir surface by a dividing line of clear and turbid water covered with driftwood and debris. It can be seen in large Chinese reservoirs, but also in Europe and other places, for instance where the river Rhine enters the Bodensee (Schoklitsch, 1935). The plunge point is usually located near the transition of topset

and foreset beds on the delta (Fan & Morris, 1992a, Chikita, 1991), and constitutes a complex and rapid 3-D flow variation with noticeable fluid mixing. Downstream of this point the current follows the river channel or spreads over the bottom as a dense layer advanced by a front. Meanwhile a reverse flow or circulation is formed in the reservoir which meets the river flow at the plunge point. It provides the pressure necessary to arrest the plunge point. More details on the typical structure of the turbidity current and its front are treated later in this thesis.

### *Downstream river sediments*

Since sediments are trapped and discharges are regulated by the reservoir the downstream reaches are exposed to significant morphological changes (Sloff, 1991). A decrease in sediment supply causes degradation and bank erosion as the riverbed slope decreases over long distances (Bruk, 1985). An example of erosion downstream and sedimentation upstream is given in figure 1.3, resulting from

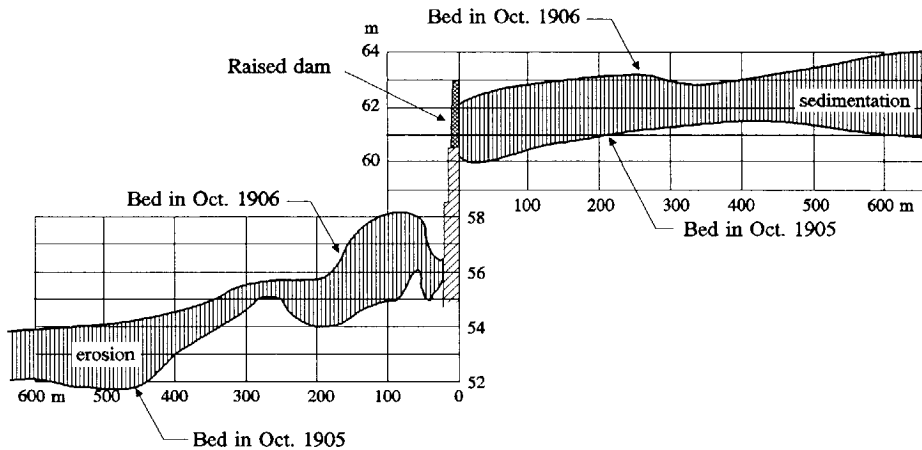


Figure 1.3 Measured bed variations due to heightening of a dam in the Yuba river (below Parks Bar bridge) after Schoklitsch (1935).

heightening a dam in the Yuba river in the USA (Schoklitsch, 1935). Erosion of the river bed may have various negative consequences, for instance the drying up of irrigation-water intakes, failure of bridge piers, lowering of groundwater table, and retreat of the river delta. On the other hand the riverbed and water depth stabilizes, for instance by changing from regime from a braided to single-channel river, which is favourable for navigation (Zhang & Qian, 1985). Note that especially coarse sediments are trapped, hence changing the grain-size distribution in the river. Degradation effects are counteracted by the effect of the modified discharge regime. Reduction of flood peaks, with erosive ability, is characterised

by a net aggradation of the downstream reach. Whether degradation or aggradation dominates is highly uncertain, but anyway, in both cases the river will change noticeably.

The processes and impacts described here comprise the most important reservoir-sedimentation issues. Other processes, such as sedimentation by tributaries and rare events like landslides and mud flows are not further discussed here. To minimize their sedimentation threat to storage reservoirs it is necessary to understand the mechanisms and to invent appropriate counter measures. Furthermore the continued construction of new reservoirs and the conservation of existing reservoirs necessitates careful planning and operation, particularly when realizing that not the dam provokes the impacts, but that reservoirs do. In the following section the most popular methods for mitigation of reservoir-sedimentation problems are discussed.

### **1.3 Methods to preserve reservoir capacity**

Without any mitigating measures the viability of many reservoirs is questionable, as the impacts and losses are not balanced by the profits. The most important motive to use strategies for controlling reservoir sedimentation still is the preservation of reservoir storage (especially if appropriate sites for replacement are unavailable), but impacts up- and downstream of the reservoir gain more consideration now. The commonly applied measures can be subdivided in three groups (Brown, 1943, Fan, 1985, Fan & Morris, 1992b, and Sloff, 1991):

- Methods to reduce the inflow of sediment into the reservoir, e.g., by means of erosion control in the catchment, or by means of bypassing of sediment-laden flows. Fighting the problem at its cause through reduction of sediment yield from the basin can be very effective. Nevertheless, it can also become very expensive, and it will become effective in the long run only.
- Methods using the hydraulics of the flow to reduce accumulation of sediments, or to induce erosion of accumulated material (sluicing and flushing). Therefore operation of the reservoir has to be adapted. In many reservoirs this is the most attractive way to reduce sedimentation.
- Methods based on hydraulic dredging and mechanical excavation. This is an often used efficient alternative but a very costly one. Disposal of the sediment usually imposes severe constraints. A most promising technique seems the use of available head difference, i.e. syphon-dredging systems, to evacuate sediments (Scheuerlein, 1987).

Hydraulic methods (second group) are the most interesting techniques for hydraulic engineers with interest in morphological processes. Sluicing techniques are defined

as routing sediments through, and releasing them from the reservoir while keeping them in suspension. Flushing techniques are defined as erosion of deposits by increased flow velocities. Both these approaches require substantial and long drawdown of water levels, involving great losses, and they require large bottom sluices. Their application is restricted to small and middle-sized reservoirs (Ackers & Thompson, 1987). A third technique which is not attended with these drawbacks is venting of density currents, which are able to transport sediments single-handedly to the dam. When the front of the current reaches the dam the bottom outlets can be opened to vent the turbid underflow.

Flushing and sluicing are old techniques which have proven their value for many reservoirs. During sluicing operations the reservoir is partially emptied for creating sufficient shear to sustain suspension. Under optimal conditions it is possible to arrest further sedimentation, as even small amounts of newly deposited sediments can be eroded. Since the highest sediment concentrations are found in the rising limb of the flood hydrograph at the beginning of the wet season (Fan & Morris, 1992b, Ackers & Thompson, 1987), it is most effective to sluice these flows through the nearly empty reservoir and to start the refilling with the less turbid water following the peak. Two early successful examples of this type of sluicing are the Old Aswan dam on the Nile river in Egypt (Mahmood, 1987) and the Bhatgarh dam in India (Brown, 1943). As an extension of sluicing operations, recovering part of the lost storage is only possible by flushing operations in which the reservoir surface is fully drawn down. During these operations a channel is formed in the deposits primarily by means of retrogressive erosion, while flood-plain deposits are hardly affected (their build-up can only be delayed). After some period the initially unstable channel reaches some kind of equilibrium state after which flushing is completed. Clearly such techniques, which produce riverine conditions, are most effective in small or gorge-type reservoirs.

Effective flushing operations were reported for instance by Tolouie et al. (1993) where about 7% of the original capacity of the Sefid-Rud reservoir in Iran could be regained. They proposed a further improvement by pumping water into the consolidated flood-plain deposits to encourage their erosion through the piping mechanism. Also Schoklitsch (1935) presents some examples of flushing, but underlines the negative environmental impacts to the downstream reach due to the sudden release of sediment-laden flow (see also Sloff, 1991). With this warning in 1935 Schoklitsch was apparently far ahead of his time. Other successful flushing operations, mainly in China are discussed by Fan (1985) and Fan & Morris (1992b). These experiences show that flushing should be performed periodically, and complete drawdown is essential (otherwise only a small flushing cone is obtained, Scheuerlein, 1987). Still various improvements and variations of the technique are possible, such as using highly unsteady flows or moving sediments from active storage to dead storage.

Flushing and sluicing operations are best be considered during the design of the dam and the operating rules, although flexibility is necessary as future variations in the imposed conditions are uncertain. For successful flushing it is necessary that bottom outlets (usually tunnel-type) do not become clogged. Di Silvio (1990) showed that the initial and final phases of the operation are most critical for the occurrence of permanent clogging. To avoid this, the cross section of tunnel and gates must be sufficiently large and the operation of the gate must be well thought-out. Di Silvio showed that masses of sediment ('dunes') from the collapsing banks of the flushing channel may lead to temporary clogging, but usually they are washed away after the reservoir level rises.

If turbidity currents are occurring or likely to occur on a regular basis it is attractive to sluice them out, especially for large reservoirs where water-level drawdown yields unacceptable water losses. The formation of a turbid underflow and its ability to reach the dam requires a concentrated inflow of fine sediments, a sufficient depth and bed slope, and a smooth bottom. The last smooth-bed criteria compels some pre-conditioning of the reservoir, for instance the removal of trees, sills, and other obstacles. Favourable for propagation is the presence of a channel which is either the original river channel or a flushing channel.

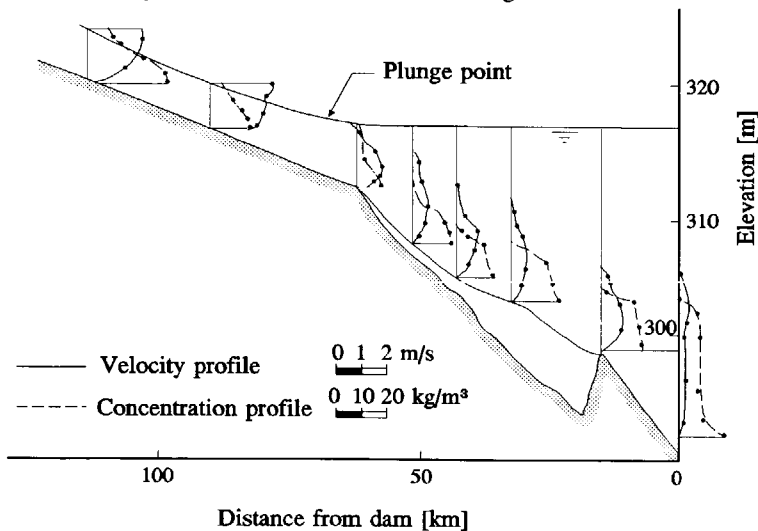


Figure 1.4 Measured turbidity current in Sanmenxia reservoir (China) during 16-18 August 1961 (after Bruk, 1985).

A very effective example of density-current venting is reported by Duquenois (1956) where 45% of the incoming sediment load was released from the Iril Emda reservoir in Algeria. Other examples, especially from China, indicate ratios of silt discharges to silt inflow ranging from 18 to 36% (Fan, 1985, Fan & Morris, 1992b). In figure 1.4 an example is given of a density current vented from the



Sanmenxia reservoir in China. A typical detail in this figure is the submerged dam about 15 km upstream of the dam site (caused by a bank failure). It appeared that the mud was piled up in front of the submerged dam, before it could flow over and reach the dam. Sometimes it is suggested to wait with sluicing until a muddy pool (fluid mud) is formed behind the dam, which is vented afterwards before it consolidates.

At present (1996) the knowledge about turbidity currents in reservoirs is limited and sluicing techniques are highly empirical. Since it is much less investigated than other processes and techniques, we have chosen to make a more profound study of the physics and modelling techniques for these currents. In the following section a short introduction is given to general modelling techniques to assess reservoir-sedimentation processes. After that, in the following chapters, the results of our model study for turbid underflows is treated.

## **1.4 Modelling techniques**

For sake of fighting the reservoir-sedimentation problems a need exists for quantification of the processes. Prediction of capacity losses, impacts on the stream, and distribution of sediments, as well as the efficiency of mitigating measures require modelling techniques which can be used to determine operating rules and feasibility demands of the project. In the previous sections it is shown that various complex and coupled mechanisms determine the issues. Furthermore we are dealing with large uncertainties in measured and forecasted data. For instance the sediment yield, which is the source of all sedimentation problems can usually not be predicted accurately and with sufficient detail. Early modelling attempts have often proved to be unreliable, which forced engineers to put a significant effort in inventing more sophisticated approaches.

The most expensive but most appealing type of models are the scale models in a hydraulic laboratory. Unfortunately complete similarity between the prototype and model cannot be achieved due to the variance in scale effects when studying different processes at once (De Vries, 1993). Although for certain 3-D processes (e.g. delta formation, design of outlets) scale models are more trustworthy than available mathematical models, they are not widely used. Instead a growing interest is paid to computational modelling.

Based on experiences from many existing reservoirs a number of empirical techniques have been devised which have become very popular among engineers. The most simple group of empirical methods are developed some decades ago to

predict the trap efficiency of reservoirs (the ratio of incoming sediment load that is used to give a quick approximation of storage loss, but are certainly not suitable for design purposes. Brune's (1953) and Churchill's (1948) graphical methods are often recommended (Graf, 1984). There are more complex empirical relations which also account for the distribution of the sediments, notably the deltaic deposits. Some methods are referred to by Graf (1984) and Sloff (1991) but still they are highly inaccurate.

When the empirical models became more complex due to inclusion of physics the engineers and scientists began to switch to mathematical modelling of hydrodynamic and morphological processes. Presently this type of modelling is most common and popular to study reservoir sedimentation. Most of these models are still 1-D, especially when predicting long-term morphological behaviour. On the other hand 2-D and 3-D models are used more often to study hydrodynamic processes in the reservoir such as thermal stratification. When switching from 1-D to higher dimensions some of the remaining empiricism (for closure) can be eliminated, but other difficulties of physical and mathematical nature appear.

A state of the art review of applied methodology given by Sloff (1991), for mathematical modelling of sedimentation in reservoirs, revealed the main gaps in the present knowledge. This study resulted in various recommendations for further research and engineering applications. The different processes, described in the previous section, still require different approaches and different simplifications. For instance to model delta formation it is at least necessary, even essential, to consider the unsteady inflow hydrograph, reservoir operation (lake level and flushing), and sorting effects of sediment. On the other hand, the high uncertainties in available data and sediment yield still do not fully justify the effort to implement more detailed features, such as the formation of distributary channels, wave action and other fully 3-D actions. In reviewing literature the most promising results can be obtained (economically) using the most advanced 1-D or 2-D morphological models, preferably in combination with statistical analyses and notably with reliable methods for predicting sediment yield. A similar argumentation applies for the methodology to model other processes which are relevant for reservoir sedimentation, particularly if one realizes that these models are primarily used to support decisions for reservoir design and operation.

The literature study presented in Sloff (1991) and the considerations above led to a choice to develop a model for turbidity currents in reservoirs. Initially also the challenging and relevant topics of delta formation and drawdown flushing mechanics were selected, but successfulness of modelling these phenomena (e.g., channel erosion) is doubtful since their basic mechanisms are not well understood and described. The goal of this research is to develop a model to study the development of turbidity currents in reservoirs, and to assess their physics. The results are primarily derived for research purposes and discussed in the following

chapters. It was found that the most important limitation of this approach is the lack of good field data, which is a problem inherent to the phenomenon.



## Chapter 2

### Mathematical model

#### 2.1 Introduction

Hydrodynamic and morphological processes in reservoirs are very complex and irregular, and many phenomena are poorly understood and described. This makes it impossible to give an exact and complete quantification of sedimentation with the present state of technology, especially when appreciating the defects of the available data. To make a contribution to the understanding of at least one of these phenomena, we have decided initially that this study focuses on modelling reservoirs where turbidity currents are to be expected. In the following a choice is made for the type of model starting from an evaluation of the present state of mathematical modelling techniques. Then, in section 2.2, the full basic equations for water and sediment of the chosen model from Sloff (1994a) are presented, together with the basic assumptions and relevant simplifications. To assess the problem of correctly representing the convective-diffusive behaviour of suspended sediment the commendable approach of Galappatti (1983) and Galappatti and Vreugdenhil (1985) is applied for the underflow, which is treated in section 2.3. Additionally, closure relations are required for flow structure and sediment transport, which is of course an inevitable consequence of schematization and integration. The partially empirical, partially theoretical study of these relations is discussed in section 2.4, while some special considerations are given on interfacial mixing and boundary friction in section 2.5.

Most models for turbid underflows are in some way analogous to models for conservative saline and thermal density currents for which a lot of references exists. By contrast to the latter the sediment in a turbidity current is in general a non-conservative contaminant. Sediments can be entrained and deposited at the bed, thus changing the total amount of sediments in suspension. For a swift turbidity flow on a steep slope the net pick-up of sediments increases its negative buoyancy through which it accelerates and picks-up more sediments. Although this is a credible phenomenon, most turbidity currents in reservoirs are of a net depositing nature with relatively low velocities and low densities. Contrary to self-accelerating turbidity currents are those which lose their transport energy and eventually die out by settling of particles. Clearly the dynamic interactions between sediment

exchange, sediment suspension, mean flow and turbulence are very delicate, hence turbidity-current modelling is much more difficult than modelling of open-channel flow or conservative density currents. To quantify the underflow it is important to realize that it is originating and determined by the integral behaviour of the fluid and sediment mixture. A different behaviour than individual particles is due to their aggregation and the resulting mutual interactions between the particles. In many matters this is a common feature. For instance a single water molecule does not exhibit a boiling point, as this is an effect of collectivity of the molecules.

Early models such as that of Hinze (1960) and Keunen (1951, 1952) are based on a rather crude simplification of the integral flow assuming uniform layer depth with steady-state characteristics. The resulting model is a Chézy-type equation also called a 'slab' model due to the absence of space-differentials. Also the model of Plapp and Mitchell (1960) was formulated for a steady-state, but their approach included space differentials. Unfortunately these models are failing to correctly describe the sediment-flow interaction and the overall unsteadiness of the flow. More advanced mathematical models are required to achieve this.

One of the most relevant advances in turbidity-current modelling techniques is due to Bagnold (1962) with the formulation of the energy-based auto-suspension principle, which assesses the question why (fully turbulent) turbidity currents are able to maintain themselves. Irrespective the exact physical mechanisms he considered the energetics of the current (extending Knapp's concept, 1938), and developed a simple model based on the power provided by gravity, counteracted by power needed to maintain suspension and power expended against bottom friction (empirically). To correct some over-simplifications and deficiencies, improvements or alternatives to Bagnold's model were suggested by various researchers (e.g., Pantin, 1979, Pallesen, 1983). For instance Pantin corrected the auto-suspension criterium by coupling the power for supporting suspension to the power to maintain turbulence by bed friction, and by including the power expended on the bed load. Pantin and later Parker et al. (1986) used the corrected Bagnold approach for closure of sediment transport in their layer models. These applications showed that the energy approach seems especially useful for modelling highly erosive self-accelerating underflows, where sediment entrainment is coupled to available turbulent kinetic energy rather than to bed-shear stresses. However, the superiority of this approach to other models cannot be proved for low-velocity depositing turbidity currents. There is no direct evidence (at most circumstantial) that sediment-flow interaction in nature obeys these energy considerations, particularly when considering that many other often neglected factors (unsteadiness, interfacial mixing, ambient flow, bed forms, etc.) also contribute to the energy balance in a very complex way.

Whereas 1-D layer models are still the most commonly used (e.g., Akiyama & Stefan, 1985, 1988, Hay, 1987, Graf, 1983b) there are some extensions to 2-DV

approaches (transversally averaged). Stacey and Bowen (1988a) presented a 2-DV model based on the mixing length theory. Some of their results on turbulence characteristics are used for our model as well in section 2.4. More sophisticated and promising is the 2-DV model of Brørs and Eidsvik (1989) and Eidsvik and Brørs (1989) which uses dynamic turbulence modelling. Also for these models the delicate flow-sediment interaction and the lack of data delays the progress, and still impede a justified extension to 3-D. Similarity in modelling turbid flow in sedimentation basins for sewer systems can be used as a reference for further research (e.g., Devantier and Larock, 1987).

Considering this overview of existing models it can be observed that there is still need for improvement. Most layer models are still limited to 1-D and one layer (turbidity current entering a infinitely deep ambient fluid), or they do not account for shocks. Although their simplicity compared to a fully 2-DV or 3-D model is obvious, the price to be paid for simplicity is the requirement of empirical closure relations to describe physical processes which are still rather obscure. On the other hand, the much more advanced turbulence models for 2-DV and 3-D approaches are only in a very early stage of development (with respect to sediment-fluid interaction) and at the time (in 1991) their superiority over layer models could not be proved. For reservoir sedimentation we have finally chosen, in agreement with observed stratification, to develop a two-layer model with a clear quiescent upper layer and a turbulent dense lower layer which is free to exchange sediment with the bed. The derivation of this model and the required closure relations is treated in Sloff (1994a). In the following sections a summary is given of this study.

## **2.2 Basic equations for a 2-DH two-layer model**

### **2.2.1 General model**

To schematize the complex 3-D dynamics of a turbidity current into a reservoir an unsteady two-layer model can be used, which is derived by depth-integration of the 3-D hydrodynamic equations for water-sediment mixtures. In Sloff (1994a) a complete derivation of this model is treated following the approach presented by Sloff (1993a) for 1-D sediment-laden flows in unstratified channels. For generality and to capture spreading effects of the underflow it was kept 2-D in plan by only applying depth-averaging. Furthermore the effects of large concentrations were retained in the equations, provided that the flow remains turbulent, and only afterwards they were neglected by adopting the Boussinesq approximation (defined later in this section). Equations of mass and momentum for fluid and sediment were determined by means of depth-integration of Reynolds equations for four

contiguous sub-layers as defined in figure 2.1: a bottom layer consisting of uniform sediment and pores filled with stagnant water, a bed-load layer close to the bed in which sediment is transported as bed load, a suspended-load layer extending up to the density interface in which sediment is transported as suspension, and a clear-water upper layer. The final two-layer model is formulated by combining the equations of the three lower layers to one turbid underflow layer.

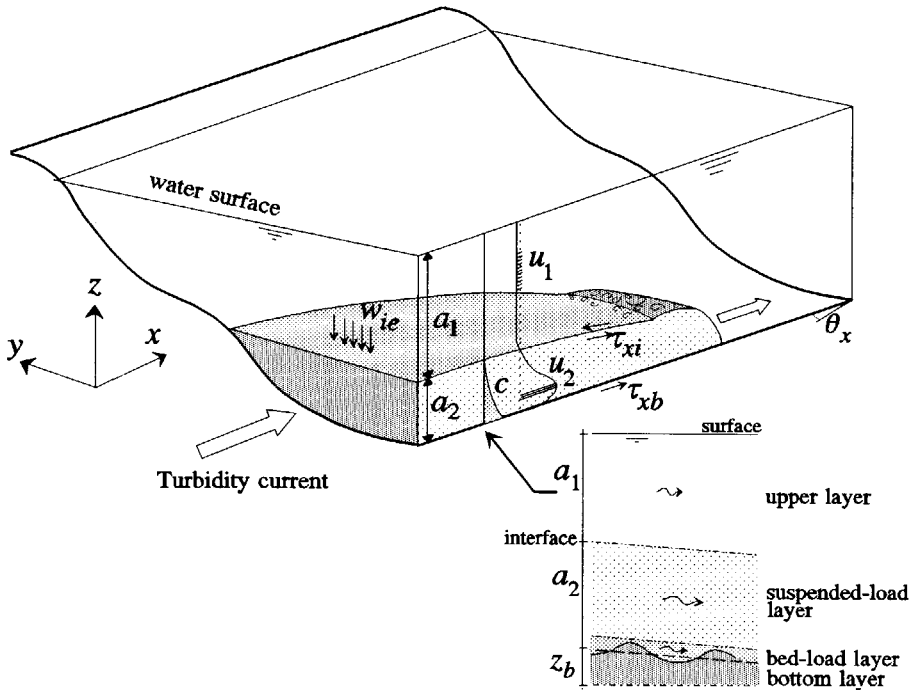


Figure 2.1 Definition sketch.

Some of the most important assumptions in these derivations are (Sloff, 1994a):

- The density difference between the layers is small ( $< 5\%$ ), but sufficient for stability of the stratification.
- The underflow is fully turbulent ( $Re_D = u_2 a_2 / \nu > 3000$ ), and turbulence breakdown (e.g., at large concentrations due to sediment pick-up) is not considered. Viscous shear stresses are fully neglected, while horizontal gradients in turbulent shear-stresses are neglected compared to those in vertical directions (no horizontal diffusion). The Reynolds equations of the flow are derived using the eddy-viscosity concept (e.g., van Rijn, 1987).
- Pressure is assumed to be hydrostatic.
- The equations are derived along a tilted coordinate system along the average reservoir bottom slope. Hence the gravity-acceleration vector is decomposed to allow for steep slopes in the following way:



$$\vec{g} = (g_x, g_y, g_z) \quad (2.1)$$

- Bed-load concentrations do not contribute to the motion of the underflow layer, as their effect on density is negligible compared to suspended load.
- Similarity of velocity and concentration profiles applies for all directions at every location. The dimensionless shape functions for these profiles are treated in section 2.4. For shape factors, originating after multiplications of profiles (e.g., in convection terms), the 'slab'-approximation is used, which states that these factors are taken equal to unity (Ellison and Turner, 1959).
- At the density interface interfacial mixing and interfacial shear-stress is imposed, at the bottom a bed shear-stress. These concepts are further discussed in section 2.4.
- Temporal and spatial variations in the density are small such that an asymptotic approach can be used to define the depth-integrated suspended-sediment concentration from the convection-diffusion equation. This method proposed by Galappatti (Galappatti, 1983, Galappatti and Vreugdenhil, 1985) and extended to 2-DH models by Wang (1989) accounts for the spatial and temporal adaptation of suspension profiles to the changing flow conditions.
- Buoyancy effects of interstitial fluid (fluid between particles) of the underflow are neglected. For instance to model features of warm-water turbidity currents entering a cold ambient, or fresh-water riverine turbidity currents entering a coastal environment (e.g., see Hürzeler et al., 1996).

The resulting system of basic Eulerian equations in general form are presented in Sloff (1994a, 1994b). It consists of eight partial differential equations which are non-linear in their dependent variables, but quasi-linear in their derivatives. Furthermore it is in agreement with Vreugdenhil's (1979) model for conservative saline currents, which in turn corresponds to the original often cited model of Schijf and Schönfeld (1953) if reduced to 1-D. If concentrations and density differences are neglected the model governs unsteady shallow-water flow on a mobile bed, which clearly illustrates the generality of the model. In chapter 3 some insight in the mathematical behaviour of this fully coupled system is given by studying characteristic propagation phenomena.

The primary closure for the proposed model consists of relations for velocity and sediment profiles, boundary shear stresses (notably bed-shear), entrainment velocities (interfacial mixing), bed-load transport and sediment fall-velocity. These closure relations are treated in section 2.4. In the following sub-sections simplified versions are presented which are the final basis for the computational model.

## 2.2.2 2-DH Boussinesq model

It is quite ambitious to solve and analyze the complete system of equations, since some simplifications are allowed which make the model much easier to work with. One of the most commonly applied simplifications in stratified flow modelling for practical situations is the use of the Boussinesq approximation. It states that density differences only affect body forces, hence it affects the 3-D Reynolds equations by taking the density of the fluid-sediment mixture  $\rho_m$  equal to the fluid density  $\rho_f$  everywhere except when multiplied with gravity  $g$  (notably in pressure gradients). Note that formally this simplification is not justified for underflows with higher density differences than about 5%. For instance, starting from the analogy to open-channel flows, the results of Sloff (1993a, 1993b) show that high sediment concentrations noticeably affect wave speeds, flow instability, and morphology. These effects cannot accurately be resolved if Boussinesq's approximation is applied. The resulting equations for the reservoir are listed below (Sloff, 1994a).

Momentum equations (equations of motion) upper layer:

$$\frac{\partial q_{1x}}{\partial t} + \frac{\partial}{\partial x} \left( \frac{q_{1x}^2}{a_1} \right) + \frac{\partial}{\partial y} \left( \frac{q_{1x}q_{1y}}{a_1} \right) + g_z a_1 \frac{\partial h_s}{\partial x} + \frac{\tau_{xi}}{\rho_f} - g_x a_1 = 0 \quad (2.2)$$

$$\frac{\partial q_{1y}}{\partial t} + \frac{\partial}{\partial x} \left( \frac{q_{1x}q_{1y}}{a_1} \right) + \frac{\partial}{\partial y} \left( \frac{q_{1y}^2}{a_1} \right) + g_z a_1 \frac{\partial h_s}{\partial y} + \frac{\tau_{yi}}{\rho_f} - g_y a_1 = 0 \quad (2.3)$$

Mass balance equation (continuity equation) upper layer:

$$\frac{\partial a_1}{\partial t} + \frac{\partial q_{1x}}{\partial x} + \frac{\partial q_{1y}}{\partial y} - w_{ie} = 0 \quad (2.4)$$

Momentum equations (equations of motion) lower layer:

$$\begin{aligned} & \frac{\partial q_{2x}}{\partial t} + \frac{\partial}{\partial x} \left( \frac{q_{2x}^2}{a_2} \right) + \frac{\partial}{\partial y} \left( \frac{q_{2x}q_{2y}}{a_2} \right) + \frac{1}{2} g_z \sigma' \frac{\partial C_s a_2^2}{\partial x} + \\ & + g_z a_2 \frac{\partial h_s}{\partial x} + g_z a_2 \sigma' C_s \frac{\partial z_b}{\partial x} + \frac{(\tau_{xb} - \tau_{xi})}{\rho_f} - g_x a_2 = 0 \end{aligned} \quad (2.5)$$

$$\begin{aligned} \frac{\partial q_{2y}}{\partial t} + \frac{\partial}{\partial x} \left( \frac{q_{2x} q_{2y}}{a_2} \right) + \frac{\partial}{\partial y} \left( \frac{q_{2y}^2}{a_2} \right) + \frac{1}{2} g_z \sigma' \frac{\partial C_s a_2^2}{\partial y} + \\ + g_z a_2 \frac{\partial h_s}{\partial y} + g_z a_2 \sigma' C_s \frac{\partial z_b}{\partial y} + \frac{(\tau_{yb} - \tau_{yi})}{\rho_f} - g_y a_2 = 0 \end{aligned} \quad (2.6)$$

Mass balance equation of mixture (continuity equation) lower layer:

$$\frac{\partial a_2}{\partial t} + \frac{\partial q_{2x}}{\partial x} + \frac{\partial q_{2y}}{\partial y} + w_{ie} = 0 \quad (2.7)$$

Sediment balance equation:

$$(1 - \epsilon_p) \frac{\partial z_b}{\partial t} + \frac{\partial (s_{bx} + s_{sx})}{\partial x} + \frac{\partial (s_{by} + s_{sy})}{\partial y} + \frac{\partial a_2 C_s}{\partial t} = 0 \quad (2.8)$$

Modified Galappatti's equation for suspended-sediment:

$$\frac{\partial C_s}{\partial t} + \left( \frac{L'_a u_2}{T'_a} \right) \frac{\partial C_s}{\partial x} + \left( \frac{L'_a v_2}{T'_a} \right) \frac{\partial C_s}{\partial y} = \left( \frac{w_s}{a_2 T'_a} \right) (C_{se} - C_s) \quad (2.9)$$

The definition of Galappatti's equation (2.9) and associated coefficients is given in section 2.3. In case of a fixed-bed model for density currents with small concentrations of conservative matter (e.g., salt) equation (2.8) can be discarded, and the following formulation must be used to quantify the dilution effect by entrainment:

$$\frac{\partial C_s}{\partial t} + u_2 \frac{\partial C_s}{\partial x} + v_2 \frac{\partial C_s}{\partial y} = \left( \frac{w_{ie}}{a_2} \right) C_s \quad (2.10)$$

Due to assumptions concerning the turbulence structure and entrainment in section 2.3 equation (2.9) does not converge to equation (2.10) when fall velocities disappear. This implies that the proposed model is not capable to correctly represent the mixing effect according to equation (2.10). In section 2.3 we corrected this by decoupling this effect from the suspension relaxation effect (without entrainment) such that it can be superimposed on the equation as a source term.

The following variables were defined (see also figure 2.1):

- $a_1, a_2$  = depth of upper layer and lower layer respectively
- $C_s$  = averaged volumetric suspended-sediment concentration
- $h_s$  = water-surface level =  $z_b + a_2 + a_1$

$q_{1x}, q_{1y}$	= discharge per unit width in $x, y$ -direction in upper layer
$q_{2x}, q_{2y}$	= discharge per unit width in $x, y$ -direction in lower layer
$s_{bx}, s_{by}$	= bed-load transport in $x, y$ -direction (per unit of width)
$s_{sx}, s_{sy}$	= suspended-load transport in $x, y$ -direction (per unit of width)
$w_{ie}$	= entrainment velocity at the interface (negative by definition)
$w_s$	= fall velocity of sediment particles (relative to $z$ -axis)
$z_b$	= bed level
$\theta_x, \theta_y$	= average bed slope in $x, y$ -direction
$\epsilon_p$	= porosity of the bed material
$\rho_f$	= density of water (upper layer)
$\rho_s$	= density of lower layer = $\rho_f(\sigma' C_s + 1)$
$\rho_s$	= density of sediment particles
$\sigma'$	= relative sediment density = $(\rho_s - \rho_f)/\rho_f$
$\tau_{xi}, \tau_{yi}$	= shear stress at density interface in $x, y$ -direction
$\tau_{xb}, \tau_{yb}$	= bed shear-stress in $x, y$ -direction

### 2.2.3 Decoupling of baroclinic and barotropic flow

In the presented form the system can be solved numerically with appropriate initial and boundary conditions. However, the significant (computational) effort to achieve this can be reduced significantly (of the order of ten times as little) by decoupling baroclinic and barotropic parts. It is shown in chapter 3 how the method of characteristics of the full system, presented in Sloff (1992, 1994b), revealed a clear distinction in magnitude and interaction of wave fronts associated to internal waves and external waves (e.g., at the surface). According to these results it is justified for small density differences to simplify the system by decoupling the internal flow phenomena, i.e. baroclinic part, from the external flow phenomena, i.e. barotropic part. External flow is only weakly influenced by density differences and baroclinic features, which can for instance be illustrated by the insignificance of the water-surface depression above an intruding gravity-current front. From a computational point of view this decoupling is particularly attractive since the stability requirements on the time step (section 6.9) can be relaxed significantly by eliminating the large barotropic celerities.

Starting from the previously presented non-linear Boussinesq model a full decoupling is not allowed, but a 'weak-interaction' form must be derived as is proposed by Vreugdenhil (1979). This interaction between external and internal flow can be obtained by defining the following dependent variables:

$$a_1 + a_2 = a \quad (2.11)$$

$$q_{1x} + q_{2x} = q_x \quad (2.12)$$

$$q_{1y} + q_{2y} = q_y \quad (2.13)$$

The equations for barotropic or external flow are found by adding the basic (Boussinesq) equations of both layers (Sloff, 1994a). Their final form is obtained after simplification of convection terms by assuming small density differences and imposing the stability (or hyperbolicity) requirement for two-layer flow (eq. 3.16). The baroclinic part of the flow is now affected by the barotropic part by relations (2.11) to (2.13). By eliminating the gradient of water-surface (a barotropic feature) through combination of the momentum equations, the baroclinic part of the model is defined. It is now possible to define different forms of momentum equations by various combinations of equations of mass and motion. Although this seems a trivial operation, their weak solutions in discontinuous flows can be seriously different (see chapter 4), due to non-linear manipulation of derivatives.

2DH decoupled model for the barotropic flow (Sloff, 1994a)

The following 2-DH basic equations for the barotropic (external) flow in the reservoir are derived by adding equations (2.2) and (2.5), equations (2.3) and (2.6), and equations (2.4) and (2.7):

$$\frac{\partial q_x}{\partial t} + \frac{\partial}{\partial x} \left( \frac{q_x^2}{a} \right) + \frac{\partial}{\partial y} \left( \frac{q_x q_y}{a} \right) + g_z a \frac{\partial h_s}{\partial x} - \frac{\tau_{xb}}{\rho_f} - g_x a = 0 \quad (2.14)$$

$$\frac{\partial q_y}{\partial t} + \frac{\partial}{\partial x} \left( \frac{q_x q_y}{a} \right) + \frac{\partial}{\partial y} \left( \frac{q_y^2}{a} \right) + g_z a \frac{\partial h_s}{\partial y} - \frac{\tau_{yb}}{\rho_f} - g_y a = 0 \quad (2.15)$$

$$\frac{\partial a}{\partial t} + \frac{\partial q_x}{\partial x} + \frac{\partial q_y}{\partial y} = 0 \quad (2.16)$$

Clearly these relations are the classical shallow-water equations which do not need further explanation. Any interaction with internal waves and other internal phenomena is eliminated by neglecting terms with  $(u_1 - u_2)$  and  $(v_1 - v_2)$  in the convection relations.

2DH decoupled model for the baroclinic flow (Sloff, 1994a)

The first alternative set of momentum equations which is directly derived from the

original Boussinesq model is written in terms of  $q$  and  $a$  and is therefore called the *QA system*.

$$\begin{aligned} \frac{\partial q_{2x}}{\partial t} - \frac{a_2}{a_1} \frac{\partial q_{1x}}{\partial t} + \frac{\partial}{\partial x} \left( \frac{q_{2x}^2}{a_2} \right) - \frac{a_2}{a_1} \frac{\partial}{\partial x} \left( \frac{q_{1x}^2}{a_1} \right) + \frac{\partial}{\partial y} \left( \frac{q_{2x} q_{2y}}{a_2} \right) - \frac{a_2}{a_1} \frac{\partial}{\partial y} \left( \frac{q_{1x} q_{1y}}{a_1} \right) + \\ + \frac{1}{2} g_z \sigma' \frac{\partial C_s a_2^2}{\partial x} + g_z a_2 \sigma' C_s \frac{\partial z_b}{\partial x} + \frac{\tau_{xb}}{\rho_f} - \left( 1 + \frac{a_2}{a_1} \right) \frac{\tau_{xi}}{\rho_f} = 0 \end{aligned} \quad (2.17)$$

$$\begin{aligned} \frac{\partial q_{2y}}{\partial t} - \frac{a_2}{a_1} \frac{\partial q_{1y}}{\partial t} + \frac{\partial}{\partial x} \left( \frac{q_{2x} q_{2y}}{a_2} \right) - \frac{a_2}{a_1} \frac{\partial}{\partial x} \left( \frac{q_{1x} q_{1y}}{a_1} \right) + \frac{\partial}{\partial y} \left( \frac{q_{2y}^2}{a_2} \right) - \frac{a_2}{a_1} \frac{\partial}{\partial y} \left( \frac{q_{1y}^2}{a_1} \right) + \\ + \frac{1}{2} g_z \sigma' \frac{\partial C_s a_2^2}{\partial y} + g_z a_2 \sigma' C_s \frac{\partial z_b}{\partial y} + \frac{\tau_{yb}}{\rho_f} - \left( 1 + \frac{a_2}{a_1} \right) \frac{\tau_{yi}}{\rho_f} = 0 \end{aligned} \quad (2.18)$$

This set of momentum equations is obtained by combination of the original Boussinesq equations (2.5)-(a<sub>2</sub>/a<sub>1</sub>)·(2.2) and equations (2.6)-(a<sub>2</sub>/a<sub>1</sub>)·(2.3). Hence water-surface gradients and gravity-acceleration terms are eliminated.

The second alternative set can be obtained in a analogous way, but now  $q$  is decomposed by taking  $q_{ix} = u_i a_i$  and  $q_{iy} = v_i a_i$ , and subsequently the time derivatives of  $a_i$  in the original momentum equations are eliminated by using the associated continuity equations (e.g., see Tan Weiyan, 1992, p.38-40). Since variables are now  $u$  and  $a$  (and others) the model is called *UA system*.

$$\begin{aligned} \frac{\partial (u_2 - u_1)}{\partial t} + \frac{1}{2} \frac{\partial}{\partial x} (u_2^2 - u_1^2) + v_2 \frac{\partial u_2}{\partial y} - v_1 \frac{\partial u_1}{\partial y} + \frac{1}{2} g_z \sigma' a_2 \frac{\partial C_s}{\partial x} + \\ + g_z \sigma' C_s \frac{\partial (a_2 + z_b)}{\partial x} + \frac{\tau_{xb}}{\rho_f a_2} - \left( \frac{1}{a_2} - \frac{1}{a_1} \right) \frac{\tau_{xi}}{\rho_f} - \left( \frac{u_2}{a_2} + \frac{u_1}{a_1} \right) w_{ie} = 0 \end{aligned} \quad (2.19)$$

$$\begin{aligned} \frac{\partial (v_2 - v_1)}{\partial t} + u_2 \frac{\partial v_2}{\partial x} - u_1 \frac{\partial v_1}{\partial x} + \frac{1}{2} \frac{\partial}{\partial y} (v_2^2 - v_1^2) + \frac{1}{2} g_z \sigma' a_2 \frac{\partial C_s}{\partial y} + \\ + g_z \sigma' C_s \frac{\partial (a_2 + z_b)}{\partial y} + \frac{\tau_{yb}}{\rho_f a_2} - \left( \frac{1}{a_2} - \frac{1}{a_1} \right) \frac{\tau_{yi}}{\rho_f} - \left( \frac{v_2}{a_2} + \frac{v_1}{a_1} \right) w_{ie} = 0 \end{aligned} \quad (2.20)$$

For both sets of momentum equations the continuity equation of the lower layer, equation (2.7), must be added to complete the baroclinic model. Also equations for sediment (2.8) and concentration (2.9), (2.10) remain unaltered. The *QA system* greatly coincides with Vreugdenhil's (1979) model, and for both models the

characteristic celerities are accurate. Furthermore it can be shown that the expected error in computing with the decoupled model is of the order of the density difference (i.e.,  $\sigma' \cdot C_s$ ) which is reasonable if compared to the errors introduced for example by the closure relations for sediment transport. Obviously the interaction between the external and internal flow weakens if the density difference decreases, and even allows for a quasi-steady approach were barotropic flow is computed as a steady flow profile (as proposed in sub-section 6.4.2 on basis of propagation properties).

In most of the presented models in literature the general Boussinesq model is simplified to a one-layer model by assuming an infinite 'reservoir' depth. Through this assumption the water-surface gradient in the Boussinesq equations can be discarded from the beginning, hence it is a rigid-lid approach. Also upper-layer balance equations are not longer necessary. However, Sloff (1994a) showed with a simple theoretical consideration that only in a really infinite deep reservoir (e.g., for submarine canyons) this rigid-lid assumption is justified. Later in this thesis this postulate is further demonstrated for intruding gravity currents in a shallow ambient fluid, emphasizing the importance of using a two-layer model to compute turbidity currents in reservoirs.

### **2.3 Galappatti's model for a 2-DH turbidity current**

We assume that the transport of suspended sediment in the (turbulent) turbidity current can be described with the convection-diffusion model which follows from conservation of mass for a unit volume (Sloff, 1994a, van Rijn, 1987). If, in combination with appropriate diffusion coefficients, flow velocities and boundary conditions, this partial differential equation is solved it is possible to describe the complete concentration field of the 3-D flow. This full solution still requires a significant computational effort, and notably due to the uncertainty in the near-bed sediment exchange and the sediment-flow interactions this solution cannot realize a high level of accuracy. Particularly these last processes, of high uncertainty, are of vital importance to the (vertically and horizontally) adjustment of concentration profiles in a turbid underflow which determine the average density of the current at each point. It is worthwhile to study new approaches, such as Galappatti's approach, which can be used in our 2-DH model and which deal with these uncertainties.

In a straight-on depth-integration of the convection-diffusion equation for the underflow the adjustment of profiles and average concentrations is replaced by a sediment-entrainment function, which is different than the original bed-boundary

condition (Wang, 1989). Such a term is usually an empirical or semi-empirical which requires calibration, and therefore reduces the predictive power of these depth-integrated models. Obviously, another more robust approach is needed to overcome this problem. Galappatti (Galappatti, 1983, Galappatti and Vreugdenhil, 1985) proposed an asymptotic solution to the 1-D convection-diffusion model which can be used if the deviation of shape of the concentration profile from the shape of the equilibrium profile is small. The depth-integrated form of the equation is found by substituting an asymptotic solution of the depth-integrated concentration into it, and by using a concentration or gradient type bed-boundary condition. The depth-averaged concentration  $C_s$  is then theoretically determined instead of empirically, since the convection-diffusion equation is actually solved (although approximately, only for lower order terms). Consequently the resulting equation for the depth-averaged suspended-sediment concentration, which we call Galappatti's equation, does not involve any empirical entrainment function, and is therefore much more robust. Wang (1989) extended the originally 1-D Galappatti's equation to two-dimensions, and in this section a further extension of this theory is summarized for 2-D turbidity currents as derived in Sloff (1994a). The applicability and validity of the original approach was studied by Wang (1992).

Consider the 3-D convection-diffusion equation for suspended sediment (with reasonably low concentrations) which is obtained by applying the Reynolds procedure and the eddy-viscosity concept, and subtracting the continuity equation for the mixture (of fluid and sediment).

$$\begin{aligned} \frac{\partial c_s}{\partial t} + u \frac{\partial c_s}{\partial x} + v \frac{\partial c_s}{\partial y} + w \frac{\partial c_s}{\partial z} - \frac{\partial}{\partial x} \left( \epsilon_{sx} \frac{\partial c_s}{\partial x} \right) - \frac{\partial}{\partial y} \left( \epsilon_{sy} \frac{\partial c_s}{\partial y} \right) = \\ = w_s (1 - c_s)^\alpha \frac{\partial c_s}{\partial z} + \frac{\partial}{\partial z} \left( \epsilon_{sz} \frac{\partial c_s}{\partial z} \right) \end{aligned} \quad (2.21)$$

where  $\alpha$  is taken equal to zero for low-concentration turbid flows. The sediment-flow interaction is determined by the sediment mixing coefficients  $\epsilon_{sx}$ ,  $\epsilon_{sy}$  and the particle fall velocity  $w_s$ . After normalizing the equation it can be rewritten in terms of differential operators

$$L[c_s(\hat{\eta})] = D[c_s(\hat{\eta})] \quad (2.22)$$

with transformed coordinates

$$\tau = \frac{w_s}{a_2}(t - t_0) ; \quad \xi = \frac{w_s}{u_2 a_2}(x - x_0) ; \quad \bar{\zeta} = \frac{w_s}{v_2 a_2}(y - y_0) ; \quad \hat{\eta} = \frac{z - z_b}{a_2}$$

and with normalized velocity profiles

$$\begin{aligned} \psi_u(\hat{\eta}) &= u(\hat{\eta})/u_2 = \text{normalized main flow-velocity profile in } x\text{-direction} \\ \psi_v(\hat{\eta}) &= v(\hat{\eta})/v_2 = \text{normalized main flow-velocity profile in } y\text{-direction} \end{aligned}$$



These profiles are formulated theoretically in section 2.4 for turbid underflows.

At the interface no exchange of sediment is assumed which results in the following boundary condition:

$$\left[ \varepsilon_{sz} \frac{\partial c_s}{\partial z} + w_s c_s - w_{ie} c_s \right]_{z_i} = \left[ \varepsilon'_{sz} \frac{\partial c_s}{\partial \hat{\eta}} + c_s - c_s w'_e \right]_{\hat{\eta}=1} = 0 \quad (2.23)$$

Where  $w'_e = w_{ie}/w_s =$  normalized fluid entrainment coefficient  
 $\varepsilon'_{sz} = \varepsilon_{sz}/(w_s a_2) =$  normalized diffusion coefficient

In the further analysis we considered  $w'_e$  very small, but yet it may become significant since  $w_s$  is usually very low in silt and clay suspensions. Later in this section more attention is paid to this problem.

At reference level  $z_a$  (i.e.,  $\hat{\eta} = \hat{\eta}_a$ ) two types of bed-boundary conditions are proposed:

\* concentration type / Dirichlet type:  $c_s(\hat{\eta} = \hat{\eta}_a) = c_a \quad (2.24)$

\* gradient type / Von Neumann type:  $[\partial c_s / \partial \hat{\eta}]_{\hat{\eta} = \hat{\eta}_a} = [\partial c_e / \partial \hat{\eta}]_{\hat{\eta} = \hat{\eta}_a} \quad (2.25)$

where  $c_e(\hat{\eta}) = C_{se} \cdot \bar{a}_0(\hat{\eta})$  is the equilibrium concentration,  $\bar{a}_0(\hat{\eta})$  is the equilibrium concentration-profile function, and  $c_a = c_e(\hat{\eta}_a)$  is the equilibrium bed concentration. The gradient type condition assumes that at level  $z_a$  the upward diffusive flux is only determined by local conditions. Note that the equilibrium condition is easily obtained by means of integration if all gradients in (2.21) to  $t, x, y$  are zero:

$$c_e + \varepsilon'_{sz} \frac{\partial c_e}{\partial \hat{\eta}} = 0 \quad \Leftrightarrow \quad c_e(\hat{\eta}) = c_a \exp \left[ - \int_{\hat{\eta}_a}^{\hat{\eta}} (\varepsilon'_{sz})^{-1} d\hat{\eta} \right] \quad (2.26)$$

The required relation which expresses  $\varepsilon'_{sz}$  as function of the depth, is treated more completely in sub-section 2.4.5. Also the resulting equilibrium concentration profile is derived in that sub-section.

Now the theory of Galappatti states that the (approximate) solution of the convection-diffusion equation can be presented as an asymptotic expansion

$$c_s = \sum_{j=0}^n c_j \quad (2.27)$$

where  $c_j$  is one order of magnitude smaller than  $c_{j-1}$ . Galappatti assumed that terms on the left side of (2.21) are an order of magnitude smaller than on the right hand side, such that after substitution of this asymptotic solution into (2.22), terms of the

same order of magnitude can be collected as follows:

$$D[c_j] = \begin{cases} 0 & \text{for } j=0 \\ L[c_{j-1}] & \text{for } j>0 \end{cases} \quad (2.28)$$

Formally also the boundary conditions should be treated in this manner (see Wang, 1989, 1992), and a bed-boundary condition should be used for each term  $c_j$ . However, Galappatti made the important assumption that only the zeroth-order term contributes to the (yet unknown-) depth-averaged concentration so that the bed-boundary condition only has to be used once (for  $c_0$ ):

$$\int_{\hat{\eta}_a}^1 c_j d\hat{\eta} = \begin{cases} C_s & \text{for } j=0 \\ 0 & \text{for } j>0 \end{cases} \quad (2.29)$$

Alternatively Wang (1989) proposed a more general approach by introducing a set of test functions which we also applied here, such that

$$\int_{\hat{\eta}_a}^1 c_j(\hat{\eta}) \psi_u(\hat{\eta}) d\hat{\eta} = \begin{cases} C_s & \text{for } j=0 \\ 0 & \text{for } j>0 \end{cases} \quad (2.30)$$

In this way the concentration-type bed-boundary condition (2.24) becomes

$$\sum_{j=0}^n c_j(\hat{\eta} = \hat{\eta}_a) = c_a \quad (2.31)$$

A similar formulation can be used for the gradient-type condition (2.25).

The exact solution to each of the collected terms is defined by applying an inverse operation on them (or particularly on shape functions for velocity and concentration). The inverse operator applied to a function  $g(\hat{\eta})$  can be written for the presented two-layer model (Sloff, 1994a) as:

$$D^{-1}[g(\hat{\eta})] = f(\hat{\eta}) = (\bar{a}_0(\hat{\eta}) - \bar{a}_0(1)w'_e) \int_{\hat{\eta}}^1 \left( \frac{g(\hat{\eta})}{\bar{a}_0(\hat{\eta}) - \bar{a}_0(1)w'_e} \right) d\hat{\eta} + \int_{\hat{\eta}}^1 g(\hat{\eta}) d\hat{\eta} + \varphi_0 \bar{a}_0(\hat{\eta}) \quad (2.32)$$

where constant  $\varphi_0$  follows from

$$\int_{\hat{\eta}_a}^1 f(\hat{\eta}) \, d\hat{\eta} = 0 \quad (2.33)$$

If the term  $\bar{a}_0(1)w_e' = 0$  (zero mixing or zero concentration at the interface), then this inverse operator is equal to that of Galappatti.

For unsteady 2-DH problems no more than the first-order solution can be applied in practice (Wang, 1989, 1992):  $c_s = c_0 + c_1$ . Furthermore we neglect horizontal diffusion and assume similarity of concentration and velocity in all horizontal directions (no helical flow). Then the resulting Galappatti equation in terms of a dimensionless adaptation time and length can be expressed as derived by Sloff (1994a):

$$C_{se} - C_s = T_a' \frac{a_s}{w_s} \frac{\partial C_s}{\partial t} + L_a' \frac{u_2 a_s}{w_s} \frac{\partial C_s}{\partial x} + L_a' \frac{v_2 a_s}{w_s} \frac{\partial C_s}{\partial y} \quad (2.34)$$

where

$$L_a' = \frac{\gamma_2}{\gamma_0} - \frac{\alpha_2}{\alpha_0} = \text{dimensionless adaptation length if a concentration-type bed-boundary is used}$$

$$L_a' = \frac{\gamma_2 + \alpha_0}{\gamma_0} - \frac{\alpha_2}{\alpha_0} = \text{dimensionless adaptation length if a gradient-type bed-boundary is used}$$

$$T_a' = \frac{\gamma_1}{\gamma_0} - \frac{\alpha_1}{\alpha_0} = \text{dimensionless adaptation time if a concentration-type bed-boundary is used}$$

$$T_a' = \frac{(\gamma_1 + 1)}{\gamma_0} - \frac{\alpha_1}{\alpha_0} = \text{dimensionless adaptation time if a gradient-type bed-boundary is used}$$

The coefficients in these adaptation scales are defined as

$$\gamma_j = \bar{a}_j(0) \quad ; \quad \alpha_j = \int_{\hat{\eta}_a}^1 \psi_u(\hat{\eta}) \bar{a}_j(\hat{\eta}) \, d\hat{\eta}$$

$$\bar{a}_1(\eta) = D^{-1}[\bar{a}_0(\eta)] \quad ; \quad \bar{a}_2(\eta) = D^{-1}[\psi_u(\eta) \bar{a}_0(\eta)]$$

Since  $\tilde{a}_0(\hat{\eta})$  represents the equilibrium concentration profile, and  $\psi_u(\hat{\eta})$  the velocity profile, the use of Galappatti's model is only possible if mathematical relations (shape functions) can be defined for these profiles. For complicated flow and sediment profiles, as can be found in turbidity currents, the solution to the inverse operator requires numerical integration of shape functions. In Sloff (1994a) polynomial regression coefficients for turbid underflows have been determined from such numerical computations for a large number of possible shape functions under various conditions. Further, the derivation of the semi-empirical relations for these shape functions are discussed in section 2.4. Galappatti has carried out a similar exercise for open channel flows, in which he showed that by using simple profile functions, the adaptation time depends on the ratio  $w_s/u_*$ , the boundary level  $\hat{\eta}_a$ , and the roughness scale  $\hat{\eta}_0$  (or Chézy value). This dependence also exists for turbidity currents, although here also a dependence exist on the densimetric Froude numbers of the underflow by a parameter  $\hat{\eta}_m$  which is the dimensionless level of the velocity maximum in the turbidity current ( $\hat{\eta}_m=0.15$  if internally supercritical,  $\hat{\eta}_m=0.40$  if internally subcritical as is shown in section 2.4). For the profiles of section 2.4 some examples are given to illustrate the dependence of  $T_a'$  and  $L_a'$  on the parameters.

In figures 2.2 to 2.7 numerically computed adaptation scales are plotted as a function of the ratio  $w_s/u_*$  where  $u_*$  is the shear velocity in direction of the velocity vector as defined in section 2.4. For comparison two different roughness scales are used which are quite realistic in laboratory and field. These results were found to correspond qualitatively to those of Galappatti for open-channel flow, proving the analogy between the applications. It can be seen that  $L_a'$  and  $T_a'$  values for internally subcritical currents ( $\hat{\eta}_m=0.4$ ) are lower than those for supercritical currents ( $\hat{\eta}_m=0.15$ ) due to lower turbulence intensity (lower diffusion coefficients), such that redistribution of the sediments in the vertical by turbulent diffusion is retarded. A similar behaviour is also present for lower roughness scales ( $\hat{\eta}_0$ ) since bed-roughness generates the turbulence in this model.

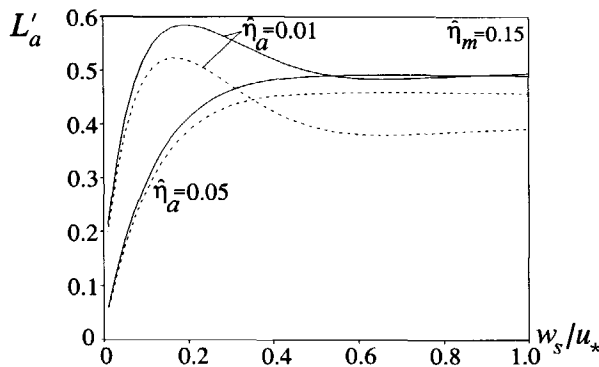


Figure 2.2 Adaptation lengths for  $\eta_m=0.15$  and concentration type b.c.  
 Legend: drawn lines:  $\eta_0 = 0.0067$ , dashed lines:  $\eta_0 = 0.000116$ .

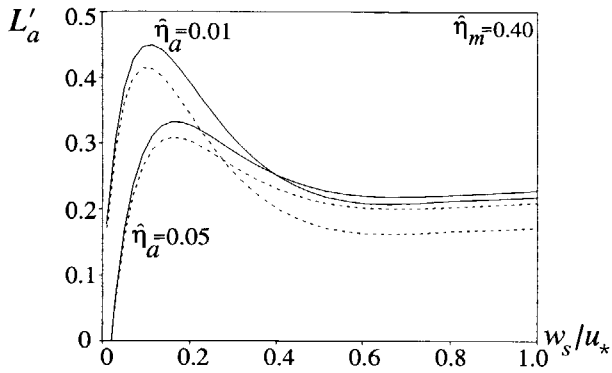


Figure 2.3 Adaptation lengths;  $\eta_m=0.40$ , concentration type b.c.(legend fig.2.2).

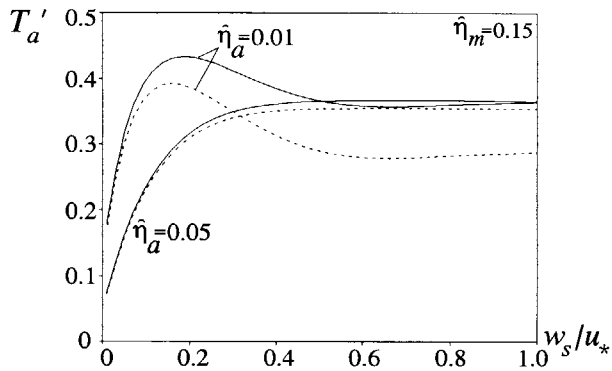


Figure 2.4 Adaptation times:  $\eta_m=0.15$ , concentration-type b.c. (legend fig.2.2).

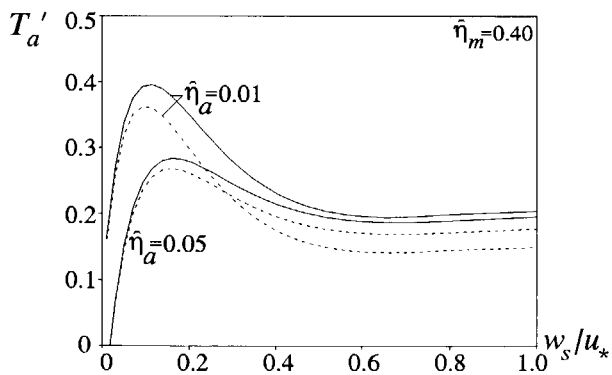


Figure 2.5 Adaptation times:  $\eta_m=0.40$ , concentration-type b.c. (legend fig.2.2).

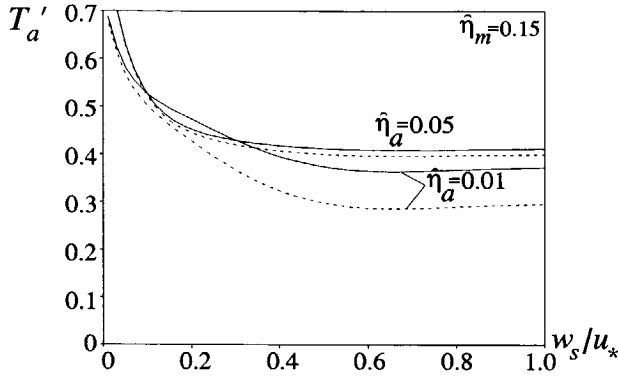


Figure 2.6 Adaptation times:  $\eta_m=0.15$  and *gradient-type* b.c. (legend fig.2.2).

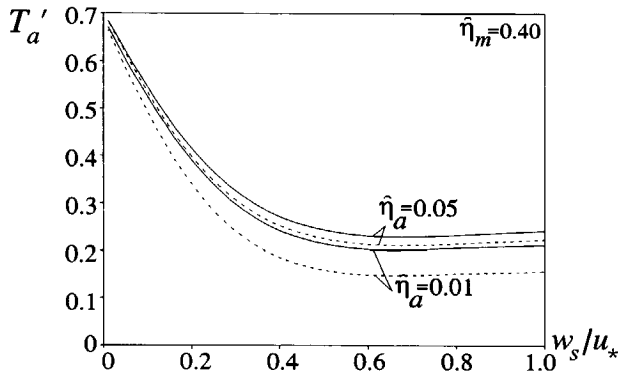


Figure 2.7 Adaptation times:  $\eta_m=0.40$  and *gradient-type* b.c. (legend fig.2.2).

The dependence on the reference level  $\hat{\eta}_a$  enters the coefficients by the equilibrium-concentration profile (i.e., by  $\tilde{a}_0$ ) given by equation (2.26). Its effect becomes pronounced at low  $w_s/u_*$  values since for low  $\hat{\eta}_a$  the contribution of the lower (most turbulent) part of the underflow is greater than for large  $\hat{\eta}_a$ .

A quite important difference in  $T'_a$  can be observed between the model derived by using a gradient bed-boundary (condition 2.24), and that derived by using a concentration bed boundary (condition 2.25). In particular for low values of  $w_s/u_*$  the adaptation time computed with the gradient-type bed-boundary is much larger. It should be noted that  $L'_a$  for the gradient-type b.c. are not completely given by Sloff (1994a) but this is not essential as it was found that for most cases it can be assumed that (for both types of boundaries, see also sub-section 2.4.5):

$$L'_a = T'_a \quad (2.35)$$

It is expected that in a depositing turbidity current the gradient-type boundary condition yields better results, also when viewing the validation presented by Wang and Ribberink (1986). Obviously for increasing turbulence rates (increasing  $u_*$ , decreasing  $w_s/u_*$ ) the value of  $T'_a$  should increase in a depositing current since settling is opposed by the turbulence. In an eroding current this is not trivial since the increased turbulence eases the upward redistribution of entrained sediments.

To justify the use of Galappatti's model certain rules have to be obeyed. The validity of the model was studied by Wang and Ribberink (1986) who showed that it can only be applied for gradually varied flow (i.e., time scale of flow  $T \gg a_2/u_*$ ; length scale  $L \gg u_2 a_2/u_*$ ). It can further be shown that  $w_s/u_*$  should be small (e.g., less than 0.4) for accuracy of the first-order solution. Quantitatively these conclusions were verified by Wang (1989, 1992). He showed mathematically that the first-order asymptotic solution will be accurate enough to replace an exact model if a certain convergence radius  $R_\alpha$  is not exceeded. Basically, through the sediment-diffusion coefficient, this radius depends on  $w_s/u_*$  (higher convergence at lower  $w_s/u_*$ ). Consequently it restricts the validity of the model to situations in which the shape of the concentration profile does not deviate too much from the shape of the equilibrium concentration profile (hence it only improves the equilibrium transport model).

In many cases the first-order solution still appeared to give good predictions outside the convergence domain as well (Wang, 1989). Wang showed additionally with a simple morphological model that exactness of the results strongly depends on the normalized wave number  $k \tau_2/w_s$  ( $k = \pi/L$ ) and a relative frequency  $(a_2/w_s)(2\pi/T)$ . The model performs well if these numbers do not significantly exceed the convergence radius  $R_\alpha$ . For the longest waves (smallest  $k$ ) the agreement is best, while for the shortest admissible waves with length  $2 \cdot \Delta x$  ( $k = \pi/\Delta x$ ,  $\Delta x =$  numerical space step) the agreement is poor dependent on whether they fall within the convergence radius. On the other hand the shortest waves are physically not relevant and will be damped out quickly. To illustrate these rules we consider the turbidity current of Bonnacaze et al. (1993) of 100 g sediment with  $D_{50} = 23 \mu\text{m}$  released in a 0.3 m deep flume by removing a lock. Some preliminary calculations showed that at  $x = 4$  m from the head of the flume, 80 s after release the following results can be found:

$$- \quad \frac{w_s}{u_*} \approx 0.22 \quad \text{gives} \quad R_\alpha \approx 5$$

$$\left(\frac{a_2}{w_s}\right)\left(\frac{2\pi}{T}\right) = \frac{336}{T} < R_\alpha (=5) \quad \text{if } T > 67 \text{ s}$$

$$\frac{q_2}{w_s} \frac{\pi}{L} \leq k \frac{q_2}{w_s} \leq \frac{q_2}{w_s} \frac{\pi}{\Delta x} = \frac{3.632}{\Delta x} < R_\alpha$$

Due to the low celerity of the underflow the time-scale of the flow amply exceeds  $T_{min}$  of about 70 s. On the other hand the limitation of the relative wave number results in a  $\Delta x_{min}$  of 0.75 m which is indeed much smaller than the physical  $L$ , but much higher than desired for the numerical solution with sharp shock waves. Although it seems contradictory to use Galappatti's model in situations with shock waves (where  $L < L_{min}$ ,  $T < T_{min}$ ), it was found afterwards that the presented limitations are not fatal and can be circumvented quite easily in a numerical model (see section 6.10). Bonnezaze et al. (1993) used a model slightly similar to Galappatti's model to compute the concentration in their lock-exchange experiments.

In the derivation of the adaptation coefficients the exchange term  $\tilde{a}_0(1)w_e'$  is neglected based on the often applied assumption of negligible mixing and on the low concentration near the interface. In reality the turbid underflow does not only erode and deposits sediments at the bed, but to a similar extent it also 'erodes' clear water from the upper layer. The importance of this effect just appeared during computations by comparing dilution effects in nearly conservative turbidity currents and conservative saline density currents. Essentially the entrainment velocity at the interface has a similar, but counter-productive effect on the average concentration as the settling out of sediments. Again the concentration profile is modified and needs a certain adaptation time/length to readjust. Therefore it seems worthwhile to correct Galappatti's model for this purpose in future studies. However, we are not convinced that it is sufficient to recalculate the adaptation coefficients proposed in this chapter without neglecting  $w_e'$ .

In this study we assumed (crudely) that the adaptation (diffusive) effects of this entrainment phenomena are negligible compared to settling, and that dilution can be superimposed on Galappatti's equation as a source term as follows

$$\frac{\partial C_s}{\partial t} + \left(\frac{L'_a u_2}{T'_a}\right) \frac{\partial C_s}{\partial x} + \left(\frac{L'_a v_2}{T'_a}\right) \frac{\partial C_s}{\partial y} = \left(\frac{w_s}{a_2 T'_a}\right) (C_{se} - C_s) + \left(\frac{w_{ie}}{a_2}\right) C_s \quad (2.36)$$

In this way the model allows for dilution in the traditional way, even if  $w_s$  approaches zero (conservative density current expressed by equation 2.10). When applying a direct depth-integration on the convection-diffusion equation one obtains



indeed this new source term next to an empirical sediment-entrainment term. It is therefore fully consistent with the chosen approach. The values of  $C_s$  computed with equation (2.36) can be used to compute the suspended-sediment transport rate as (in  $x$ -direction)

$$\int_{z_a}^{z_i} u c_s dz = a_2 u_2 \int_{\eta_a}^1 \psi_u(\eta) c_s(\eta) d\eta = a_2 u_2 C_s \quad (2.37)$$

This convective part of the transport (neglecting horizontal diffusion) is similar in  $y$ -direction.

In the following section the vertical structure of the turbid underflow (turbulence) is modelled in a semi-empirical approach. The results of this model were used by Sloff (1994a) to determine the adaptation coefficients in Galappatti's model as presented in this section.

## 2.4 Flow structure and sediment transport

### 2.4.1 General structure and basic equations

The delicate and complex interaction between flow and density in the turbidity current is particularly dependent on the turbulence structure and the exchange of water and sediment at the bed and interface. In the derivation of the model some important assumptions have been made on this structure which require a practical quantification. In this section a semi-empirical model is presented (derived in Sloff, 1994a) which is based on observed velocity and concentration profiles and the analogy with conservative density currents and with open-channel flow. The results of this study were used to define adaptation scales in Galappatti's model (previous section) and to formulate a sediment-transport equation for turbidity currents.

The turbulence related flow structure and the sediment-concentration distribution in a turbidity current are coupled in a complex way, which makes it quite difficult to quantify these effects directly within a layer model without serious simplifications. Even in complete turbulence models (e.g., Eidsvik and Brørs, 1989, Stacey and Bowen, 1988a), accounting for the spatial and temporal development of these currents, it is still not possible to represent the exact processes in the vertical.

In general turbidity currents in reservoirs are of a turbulent boundary-layer type, although also laminar types exist with very high concentrations (fluid-mud layers).

The two-layer system in the reservoir is schematized according to figure 2.8. The lower layer is defined as the suspended-sediment transport layer and actually consists of two sub-layers: a dense turbulent sub-layer covered by a turbulent mixing layer (interfacial sub-layer) with a strong density gradient. Usually the underflow depth  $a_2$  is greatly taken by this interfacial shear layer. The transition between the sub-layers is located approximately at the level of the pronounced velocity maximum. These definitions are common in literature in describing turbidity currents (e.g., Parker et al, 1987).

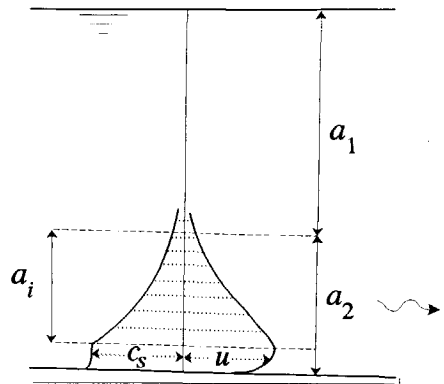


Figure 2.8 Schematic diagram.

From reported measurements in laboratory and field can be concluded that it is possible to define a standard velocity and concentration profile for 'equilibrium' turbidity currents.

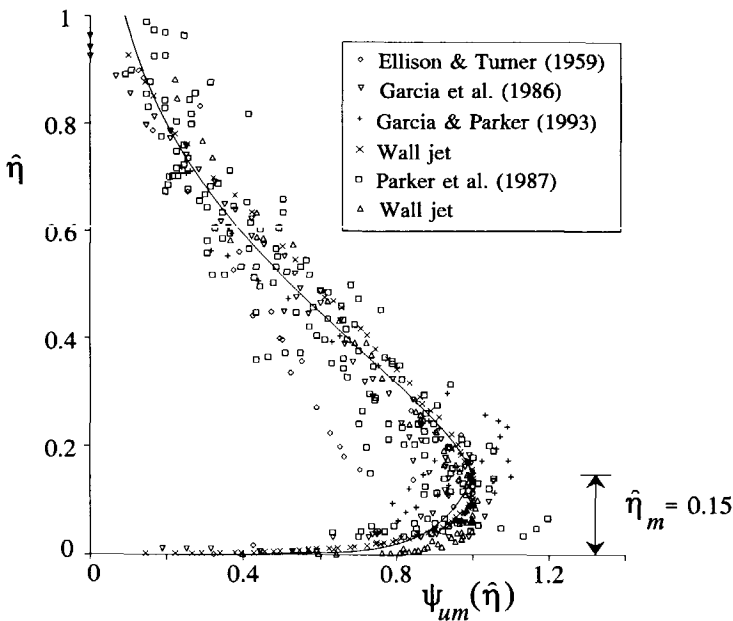


Figure 2.9 Velocity profiles of internally supercritical density currents.

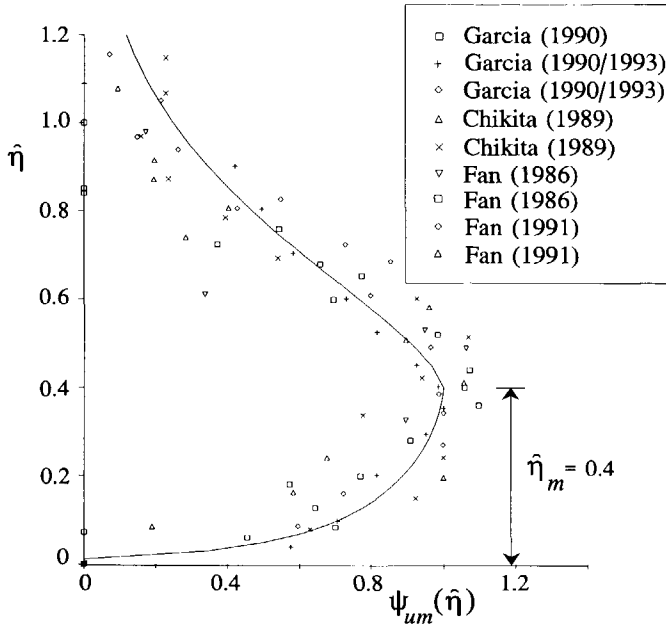


Figure 2.10 Velocity profiles of internally subcritical density currents.

In figure 2.9 and 2.10 measured dimensionless velocity profiles are plotted from internally supercritical density currents and internally subcritical density currents respectively. The vertical coordinate  $\hat{\eta}$  represents the dimensionless depth  $(z-z_b)/a_2$ , and the horizontal coordinate represents the dimensionless velocity function  $\psi_{um}$  defined as  $\psi_{um} = u(z)/u_{max}$  where  $u_{max}$  is the maximum flow velocity in the turbidity current. Data of turbidity currents in a laboratory flume from Garcia (1985, 1990, 1993), Garcia et al. (1986), Garcia and Parker (1993), and Parker et al. (1987) are plotted. Additionally data is plotted from turbidity currents in the field presented by Chikita (1989) and Fan (1986, 1991), and data from saline currents presented by Ellison and Turner (1959) and Garcia (1990). For resemblance some measurements of turbulent wall jets in a wind tunnel are added to show the similarity in shape between density current and wall jet velocities. The figures show a tendency of similarity between different profiles measured at different conditions and different locations. The drawn lines in the figures are the best fits to the data. Note that scatter in these figures is partially caused by inaccuracy of the measurement devices and by differences in instability and stratification of the currents. For example Stacey and Bowen (1988a) concluded that the measurements of Ellison and Turner (1959) are at an experimental scale which is being affected by molecular processes. Furthermore the discrepancies in defining interface levels in literature is another important source of variance.

From these similarity collapses (figs. 2.9 and 2.10) it has been concluded that the velocity maximum is located at about 15% of the underflow depth for internally supercritical turbidity currents and at 40 % for internal subcritical currents ( $\hat{\eta}_m$ ). Below this velocity maximum the turbidity current has an approximately logarithmic profile, and is dominated by boundary-generated turbulence (e.g., Ashida & Egashira, 1975). Therefore the elaboration of the mixing length theory for open channel flow is adopted for this sub-layer. In the sub-layer above the velocity maximum a regression equation is defined for the velocity profile based on laboratory experiments reported in literature. From both profiles the distribution of the fluid-diffusion coefficient has been derived from the mixing length theory accounting for turbulence damping effects by density gradients. The profiles derived in this way are assumed to be representative for all directions ( $x,y$ ) provided that secondary (helical) currents are negligible.

In its basic form we assume that the flow structure of the turbidity current is governed by the 3-D Reynolds equations, simplified by applying Boussinesq's approximation (sub-section 2.2.2) and neglecting viscous shear stress. If  $S_{xz}$  and  $S_{yz}$  are the local turbulent shear stresses in  $x,y$ -direction respectively, then the 'Reynolds-stress Boussinesq' approximation (different to the Boussinesq approximation above) and Prandtl's mixing-length concept yield (Sloff, 1994a):

$$-S_{xz} \approx \rho_f \varepsilon_{fx} \frac{\partial u}{\partial z} \approx \rho_f l_m^2 \cdot F(Ri) \cdot \left| \frac{\partial u}{\partial z} \right| \frac{\partial u}{\partial z} \quad (2.38)$$

in which  $F(Ri)$  is a damping function which expresses the effect of stratification on turbulence by means of a gradient Richardson number  $Ri$  as is shown hereafter,  $\varepsilon_{fx}$  is the fluid diffusion coefficient and  $l_m$  is the mixing length for momentum (i.e., the quantity suppressed by  $Ri$ ). This formulation is only valid for the small concentrations on which our two-layer approach is based (here errors were found to be less than 1% if compared to a more complete formulation). The gradient Richardson number is a well known measure for stabilizing effect of stratification on turbulence in a shear flow:

$$Ri = - \left( \frac{g_z}{\rho} \right) \frac{(\partial \rho / \partial z)}{(\partial u / \partial z)^2 + (\partial v / \partial z)^2} \quad (2.39)$$

The stability threshold for which the flow is unstable (turbulent) is usually taken as  $Ri < 0.25$  (e.g., Miles, 1990, and references reported in there). In practical situations, for instance due to boundary mixing, the flow is turbulent for  $Ri < 0.4$  to  $0.6$  (Garcia, 1993). Larger density gradients or smaller velocity gradients make the flow more stable. The instability of the initial interface in a developing turbidity current results in Kelvin-Helmholtz instabilities which generates the interfacial sub-layer by means of mixing processes (entrainment and turbulence). Although one

can expect that eventually the interfacial mixing layer stabilizes, it is shown that due to bed-generated turbulence (outside this layer) this process of layer expansion persists (Piat & Hopfinger, 1981). In a two-layer model these effects are usually expressed empirically by means of entrainment relations (section 2.5).

### 2.4.2 Lower sub-layer of a turbidity current

For the derivation of the (logarithmic) flow structure in the lower sub-layer of the turbidity current the analogy with open-channel flow is used. Prandtl's mixing concept, leading to the law of the wall, is applied here without accounting for stratification effects ( $F(Ri)=0$ ). In harmony with Stacey and Bowen's (1988a) observed damping effect near the velocity maximum and the observed exponential increase of concentration towards the bed, we assumed a parabolic shear stress profile  $S_{xz}$  with a zero value at  $\hat{\eta}_m$ , and we assumed a linear mixing length profile. Here  $\hat{\eta}_m$  is the dimensionless level of the velocity maximum (i.e.,  $\hat{\eta}_m=0.15$  for super, and  $\hat{\eta}_m=0.4$  for subcritical currents). Integration yields for the velocity profile in the lower sub-layer:

$$\frac{u(\hat{\eta})}{u_{*x}} = \frac{1}{\kappa} \left[ \ln \left( \sqrt{\frac{\hat{\eta}_0}{\hat{\eta}}} \cdot \frac{1 - \sqrt{1 - (\hat{\eta}/\hat{\eta}_m)^2}}{1 - \sqrt{1 - (\hat{\eta}_0/\hat{\eta}_m)^2}} \right) + \sqrt{1 - (\hat{\eta}/\hat{\eta}_m)^2} - \sqrt{1 - (\hat{\eta}_0/\hat{\eta}_m)^2} \right] \quad (2.40)$$

- where  $u_{*x}$  is the shear velocity in  $x$ -direction =  $\tau_{bx}/(\tau_b \rho_f)^{1/2}$
- $\kappa$  is the von Karman constant ( $\approx 0.4$ ).
- $\hat{\eta}$  is the dimensionless elevation =  $(z - z_b)/a_2$
- $\hat{\eta}_m$  is the elevation at which  $u(z)$  is maximal
- $\hat{\eta}_0$  is the roughness scale: the elevation at which  $u(z)=0$
- $\tau_{bx}$  is the  $x$ -component of the bed-shear stress.

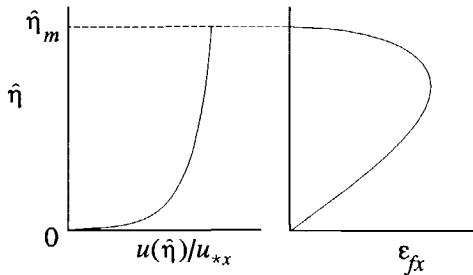


Figure 2.11 Velocity and diffusion coefficient below velocity maximum.

The corresponding fluid diffusion coefficient is defined as

$$\varepsilon_{fx} = l_m^2 \left| \frac{\partial u}{\partial z} \right| = u_{*x} \kappa a_2 \hat{\eta} \sqrt{1 - (\hat{\eta}/\hat{\eta}_m)^2} \quad (2.41)$$

The diffusion coefficient varies from zero at the bed to zero at the velocity maximum. The maximum value of  $\varepsilon_{fx}$  is located at level  $\hat{\eta} = \sqrt{2}/2 \cdot \hat{\eta}_m$ . A plot of equations (2.40) and (2.41) is given in figure 2.11. Assuming similarity of profiles in all directions these formulations also hold for the velocity profiles in  $y$ -direction.

### 2.4.3 Upper sub-layer of a turbidity current

Due to the significance of stratification effects in the upper sub-layer the derivation of an analytical formulation is much more complex. To find such an expression we determined empirical relations for the dimensionless velocity and concentration profiles reported in literature. The resulting stress, Richardson number and diffusion coefficient profiles (using again the mixing length theory) have been compared to the profiles presented by Stacey and Bowen (1988a).

A fit of the velocity data presented in figures 2.9 and 2.10 yields the following relation:

$$u(\hat{\eta}) = u_m \cdot \exp(-3 \cdot \{\hat{\eta} - \hat{\eta}_m\}^{3/2}) \quad \text{if} \quad \hat{\eta}_m \leq \hat{\eta} \leq 1 \quad (2.42)$$

where  $u_m$  = maximum velocity (at  $\hat{\eta} = \hat{\eta}_m$ ). A fit of concentration data from Garcia (1985), and Parker et al (1987) yields:

$$c(\hat{\eta}) = c_m \cdot \exp\left(-2 \cdot \frac{\hat{\eta} - \hat{\eta}_m}{1 - \hat{\eta}_m}\right) \quad \text{if} \quad \hat{\eta}_m \leq \hat{\eta} \leq 1 \quad (2.43)$$

where  $c_m$  = maximum concentration at level  $\hat{\eta}_m$ . Again these formulas are also assumed to hold both in  $x$ - and in  $y$ -direction. These profiles are not applicable to laminar stratified flows. The general form of the damping function  $F(Ri)$  may be expressed as

$$F(Ri) = (1 + \gamma' Ri)^{-n_f} \quad (2.44)$$

where  $\gamma'$  and  $n_f$  are calibration constants. In the following we used Stacey and Bowen's (1988a) calibrated coefficients  $\gamma' = 6.5$  (or 3.5) and  $n_f = 4$ . Additionally the turbulent length scale or mixing length is given by the relations (Stacey and Bowen, 1988a):

$$l_m = \kappa \cdot a_2 (\hat{\eta} + \hat{\eta}_0) \quad \text{if} \quad 0 < \kappa \hat{\eta} < 0.2 \quad (2.45)$$

$$l_m = \kappa \cdot a_2(0.5 + \hat{\eta}_0) \quad \text{if} \quad \kappa \hat{\eta} > 0.2 \quad (2.46)$$

By substitution of the relations above into equation (2.38) we can express gradient Richardson number, shear-stress and diffusion coefficient profiles which were found to be greatly corresponding to Stacey and Bowen's results (Sloff, 1994a). In figure 2.12 we plotted these relevant parameters qualitative.

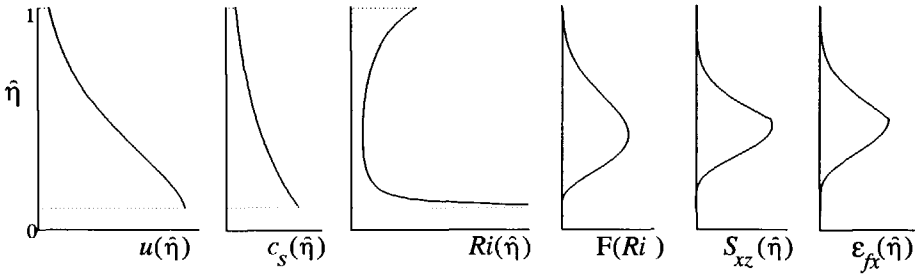


Figure 2.12 Relevant flow parameters plotted for equilibrium flow above the velocity maximum.

These figures show how  $Ri$  is minimal at level  $\hat{\eta}_{zm} \approx \hat{\eta}_m + 0.4 \cdot (1 - \hat{\eta}_m)$  which implies that the flow there is locally most unstable. At the interface the turbulent shear stress equals  $\tau_{vi}'$  (the interfacial shear stress and a pseudo shear stress induced by entrainment of stagnant water from the upper layer). From figure 2.12 it follows that this value is often very small compared to the bed-shear stress and may be neglected (with respect to momentum transfer) for stable turbidity currents. This assumption does not agree with other approaches (e.g., Abraham et al. 1979, saline current) where the location of the interface is in the middle of the mixing layer (e.g.,  $\hat{\eta} \approx 0.7$  for a subcritical density current). There the shear stresses are of the same order of magnitude as the bed-shear stress. It is clear that the definition of the upper boundary of the dense underflow is representative for the magnitude of this interfacial shear stress (see also section 2.5).

#### 2.4.4 Depth-integrated velocity and roughness scale

Combination of the presented analytical and semi-empirical formulations constitute the profile function for velocity in an underflow which are for instance used in the derivation of Galappatti's model. For our two-layer model depth-integration of the relations (2.40) and (2.42) yields for the average velocity in  $x$ -direction the following relation (Sloff, 1994a)

$$u_2 = \frac{u_{*x}}{\kappa} \left\{ \hat{\eta}_m \left[ -1.4867 \cdot \ln \left( \frac{\hat{\eta}_0}{\hat{\eta}_m} \right) - 1.4632 \right] + I_u \cdot f(\hat{\eta}_0, \hat{\eta}_m) \right\} \quad (2.47)$$

where  $I_u$  and  $f_u$  are functions expressed by

$$I_u = \int_{\hat{\eta}_m}^1 \exp[-3(\hat{\eta} - \hat{\eta}_m)^{3/2}] d\hat{\eta} \approx -0.35 \hat{\eta}_m^3 - 0.014 \hat{\eta}_m^2 - 0.069 \hat{\eta}_m + 0.425 \quad (2.48)$$

$$f(\hat{\eta}_0, \hat{\eta}_m) = \ln \left[ \frac{\sqrt{\hat{\eta}_0/\hat{\eta}_m}}{1 - \sqrt{1 - (\hat{\eta}_0/\hat{\eta}_m)^2}} \right] - \sqrt{1 - (\hat{\eta}_0/\hat{\eta}_m)^2} \quad (2.49)$$

Equation (2.47) gives a relation for the depth-averaged flow velocity  $u_2$  as a function of the bed-roughness length  $\hat{\eta}_0$  and relative depth of maximum velocity. When the roughness is expressed in terms of a  $C_D$  or Chézy values then the following relation expresses the relation between the roughness scale and these roughness parameters (in a 1-D flow  $v_2$  disappears):

$$C_D = \frac{u_*^2}{u_2^2 + v_2^2} \quad ; \quad C = \sqrt{\frac{g}{C_D}} \quad ; \quad u_* = \left( \frac{\tau_b}{\rho_f} \right)^2 \quad (2.50)$$

where  $u_*$  is the shear velocity. For internally super and subcritical density currents we plotted this relationship (while using eq. 2.47) in figure 2.13.

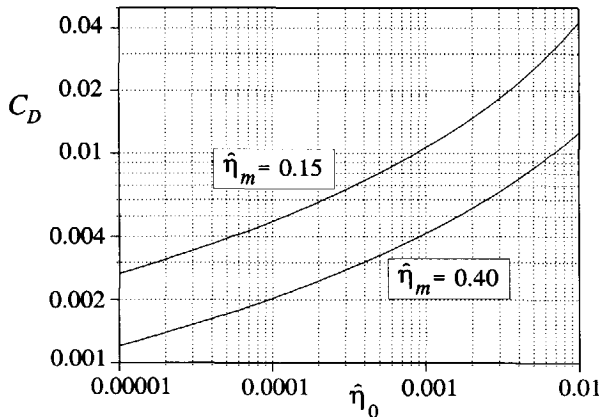


Figure 2.13 Relation between bed-friction coefficient  $C_D$  and roughness length scale  $\hat{\eta}_0$  for  $\hat{\eta}_m=0.15$  (supercrit.) and  $\hat{\eta}_m=0.4$  (subcrit.) respectively.



The sensitivity of this result to the various parameters is studied by Sloff (1994a). In general it can be concluded that the model accuracy remains within the limitations of accuracy of values of  $\hat{\eta}_0$  and  $\hat{\eta}_m$ .

Again it should be underlined that the equations presented have to be used with care. They are primarily based on experimental velocity and concentration profiles which can only approximate the erratic behaviour of a turbidity current. In reality many more factors can affect the actual velocity profile. For instance due to entrainment of water from above and sediment from below pressure gradients may occur which modify the velocity profile, but are not explicitly included in our approach. The velocity reduction induced by water entrainment can be incorporated by an entrainment term in the 2-layer model which acts as interfacial shear, without accounting for a redistribution of the velocity profile. Note that also the choice of the depth  $a_2$  (and consequently level  $\hat{\eta}_m$ ) is a point of uncertainty for which no agreement exists in literature.

Since we neglected secondary currents we assume that the presented velocity profiles also hold for the velocities in y-direction.

#### 2.4.5 Concentration profile and suspended-sediment transport

The concentration profile is deducible from the turbulence profile through the diffusion coefficient in the convection-diffusion equation. This is the link between sediment and flow interaction, and is relevant for the definition of Galappatti's coefficients which is treated in section 2.3. By assuming an equilibrium situation in which the underflow is steady and uniform this equation and its solution reduce to relation (2.26) in section 2.3. Although in Sloff (1994a) also a modified form for large concentration is analyzed, based on Richardson and Zaki's (1954) correction of fall velocity, we have restricted the final results to the present low-concentration situation. If the normalized sediment-diffusion coefficient  $\varepsilon_{sz}' = \varepsilon_{sz}/(w_s a_2)$  for all values of  $\hat{\eta} = (z - z_b)/a_2$ , and the equilibrium reference concentration  $c_a$  are known the concentration profile can be formulated. Therefore we assumed that  $\varepsilon_{sz} = \psi' \cdot \varepsilon_{fx}$  where  $\psi' = \beta \cdot \phi$  in which  $\beta$  is a factor describing the difference in the diffusion of a discrete sediment particle and the diffusion of a fluid particle, and  $\phi$  expresses the damping of the fluid turbulence by the sediment particles (van Rijn, 1984b). Here the  $\phi$  factor reduces Karman's constant. Especially for the sub-layer below the velocity maximum where the highest concentrations are found we can now define a profile function in a similar way as is conventional in open channel flow. In the upper sub-layer we already assumed the concentration profile to be expressed by equation (2.43), so that we only have to link it to the lower sub-layer profile (value  $c_m$  at  $\hat{\eta} = \hat{\eta}_m$ ).

A drawback of the proposed fluid diffusion-coefficient profile is the zero diffusion near the velocity maximum  $\hat{\eta}_m$  as can be seen in figures 2.11 and 2.12. Hence an internal boundary against diffusive mixing exists causing an unrealistic discontinuity in the concentration profile.

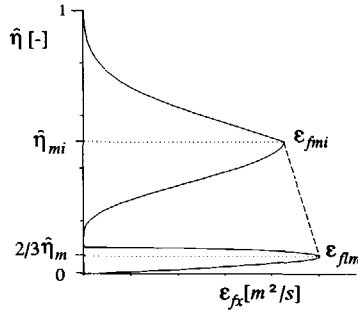


Figure 2.14 Linear bridge connecting the homogeneous parts of the diffusion coefficients according to mixing length theory.

To overcome this problem Launder and Spalding (1972) proposed to use a linear bridge connecting the maxima  $\epsilon_{fmi}$  and  $\epsilon_{flm}$  in the sub-layer above and below the velocity maximum respectively as shown in figure 2.14. For the derivation of the concentration profile now three sub-layers must be considered.

The further integration of this model and the resulting (equilibrium) concentration profiles are presented in Sloff (1994a). The result is used in Galappatti's model to define the adaptation scales (section 2.3). A relevant parameter, analogous to open-channel flow, is a suspension parameter  $Z$  defined as

$$Z = \frac{w_c}{\psi \kappa u_*} = \frac{w_c}{\beta \phi \cdot \kappa u_*} \quad (2.51)$$

where  $u_*$  is the shear velocity in the direction of the shear stress. Firstly it is assumed constant over the depth with  $\phi=1$  to allow for analytical integration of equation (2.26), and  $\beta$  is defined as (van Rijn, 1984b)

$$\beta = 1 + 2 \cdot [w_s / u_*]^2 \quad (2.52)$$

Furthermore the value of  $\epsilon_{fmi}$  is based on a local value of  $Ri = 0.4$  in the damping function  $F(Ri)$  (approximately corresponding to the stability limit). After verification of this assumption we found that the resulting concentrations are rather insensitive to this value, as well as for  $n_f \approx 4$  in  $F(Ri)$ .

Instead of taking the damping function  $\phi$  equal to unity it is more appropriate to relate it to the local concentration as proposed by van Rijn (1984b) and illustrated in figure 2.15. For relatively large concentrations which can be found close to the

bed (in the lowest sub-layer) the concentration profile can only be obtained numerically due to the dependence of  $\varepsilon_{sz}$  on the concentration. The same problem was encountered by van Rijn (1984b) in open channel flow and he proposed to a simplified method in which he defined a modified suspension number  $Z'$  through which the first order concentration profile (equation 4.36) can be corrected for additional effects:

$$Z' = Z + \varphi = \frac{w_s}{\beta \kappa u_*'} + \varphi \quad (2.53)$$

where  $Z$  was defined by equation (2.51) with  $\phi=1$ , and where  $\varphi$  is the overall correction factor representing all additional effects. The value of  $\varphi$  is determined by means of trial and error for the lowest part of the turbidity current ( $\hat{\eta} \leq \hat{\eta}_m \sqrt{2/2}$ ). Multiple fifth-order concentration profiles have been computed numerically and for various sets of hydraulic parameters ( $w_s/u_*'$ ,  $c_a/c_0$ ,  $\hat{\eta}_a$ ,  $\hat{\eta}_m$ ) where  $c_0 \approx 0.65$ . Then the  $\varphi$ -values have been determined that yield analytical zeroth-order concentration profiles (with  $\phi=1$ ) coinciding with those numerically computed with  $\phi \neq 1$ . Especially the equality of value  $c_s(\hat{\eta}_m \sqrt{2/2})$  in the numerical and analytical approach is used to find appropriate values of  $\varphi$ , since errors in this value significantly affect the rest of the profile. By means of the method of least squares a regression equation is found in Sloff (1994a) from about 800,000 different  $\varphi$ -values which expresses  $\varphi$  as a function of the hydraulic parameters with inaccuracy of about 5% (where  $0.01 \leq w_s/u_*' \leq 1$ ,  $\hat{\eta}_a \geq 0.01$ ). This high accuracy resulted in a large regression equation, but it is worth the computational effort. Only for small values of  $\hat{\eta}_a$  the sensitivity to small variations in  $Z'$  increases. Van Rijn (1984b) proposes a minimum reference level of  $\hat{\eta}_{a,min} = 0.01$  at which the concentration profile can be predicted with an error less than a factor 2 if the error in  $Z'$  is less than 20%. We do not want to violate the basic theoretical model too much, and consider the increase of accuracy by using a more complex regression equation more relevant than the decrease of computation time.

In figure 2.16 is shown how the concentration profile expressed by the equations presented by Sloff (1994a), varies with the value of  $Z$  for sub- and supercritical turbidity currents. Besides for deriving adaptation scales for Galappatti's model (section 2.3) these results can also be used to define a relation for the equilibrium concentration  $C_{se}$  by depth-integration of the concentration-profile functions over the underflow depth. Using some approximations (to make the equation more manageable) the resulting equations become for internally sub- and supercritical

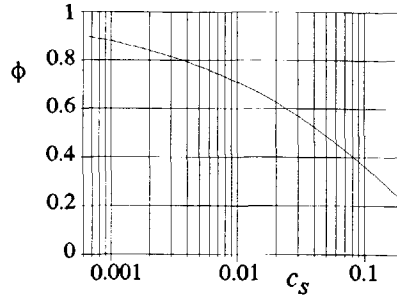


Figure 2.15 Damping factor  $\phi$ .

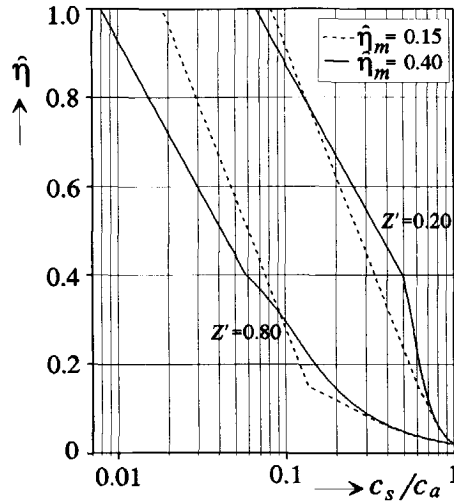


Figure 2.16 Concentration profiles for  $Z=0.2$  and  $Z=0.8$  and two flow types ( $\hat{\eta}_m$ ).

currents:

For  $\hat{\eta}_m = 0.15$ :

$$C_{se} = c_a \cdot \left[ \frac{0.121}{\hat{\eta}_a} \left( 3 - \sqrt{9 - 400 \hat{\eta}_a^2} \right) \right]^{Z'} \left\{ 0.15 Y_a \left[ -\frac{2}{3} (Z')^2 Y_a^2 + (Z') Y_a - 1 \right] + \exp(-0.67(Z')) \cdot [3.74 \cdot 10^{-3} (Z')^2 + 15.0 \cdot 10^{-3} (Z') + 0.4114] \right\} \quad (2.54)$$

where  $Y_a = (\hat{\eta}_a / 0.15) - (\sqrt{2}/2)$

For  $\hat{\eta}_m = 0.4$ :

$$C_{se} = c_a \cdot \left[ \frac{0.483}{\hat{\eta}_a} \left( 2 - \sqrt{4 - 25 \hat{\eta}_a^2} \right) \right]^{Z'} \left\{ 0.4 Y_a \left[ -\frac{2}{3} (Z')^2 Y_a^2 + (Z') Y_a - 1 \right] + \exp(-0.749(Z')) \cdot [16.88 \cdot 10^{-3} (Z')^2 + 45.0 \cdot 10^{-3} (Z') + 0.3766] \right\} \quad (2.55)$$

where  $Y_a = (\hat{\eta}_a / 0.4) - (\sqrt{2}/2)$

A comparison of successfully computed and measured concentration and velocity profiles for verification of the theory is given in figure 2.17. The first three plots are profiles from experiments Run 9, Run 17 (both internally supercritical), and Depo3 (internally subcritical) measured by Garcia (1985, 1990) in a laboratory flume. The fourth plot is an internally supercritical profile from flume experiment

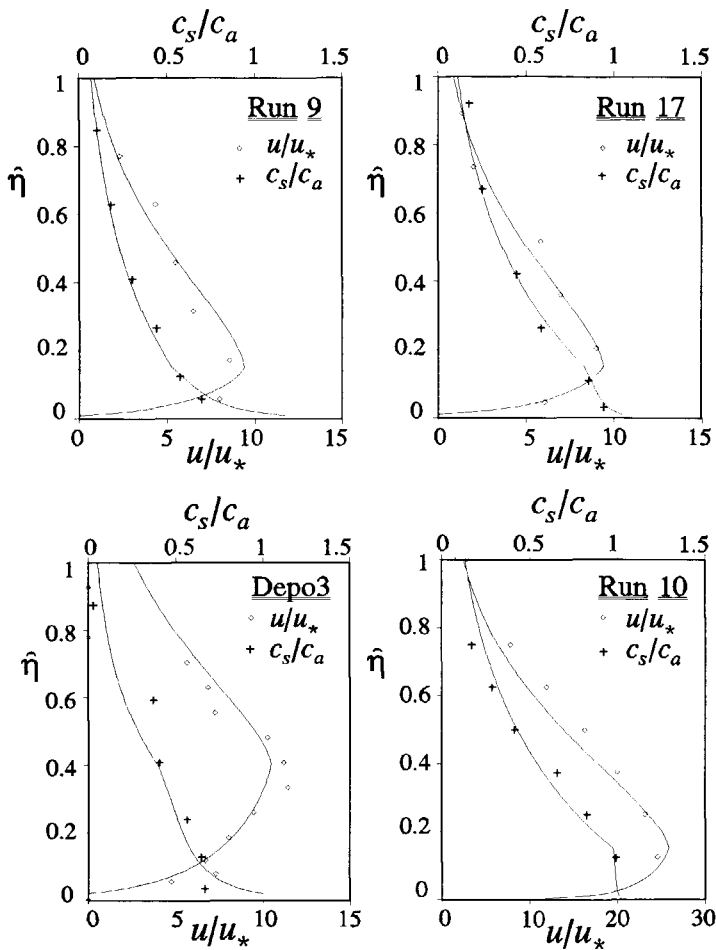


Figure 2.17 Some computed velocities and concentrations compared to Garcia's (1985, 1990) and Cordi & Ophem's (1994) flume experiments.

Run 10 (see section 7.3) carried out by Cordi and van Ophem (1994). All these profiles were measured sufficiently far from the inlet section of the flume such that they reached a practically equilibrium state. In most experiments the profiles are very uniform at the inlet gate. During this verification it was observed that, due to settling and adaptation, in general close to the inlet the concentrations in the upper sub-layer are slightly underestimated using the model, while those far downstream are slightly overestimated. This deviations are within the scatter range of the empirical relation as expected.

The computations are carried out by choosing a value for  $a_2$ ,  $c_a(\hat{\eta}_a)$ ,  $C_D$  and using

Stokes law to compute the fall velocities of the fine sediment. Practically the important  $c_a$  and  $C_D$  values require calibration and empirical closure relations as described in the following section. It is important to realize that this physically based model results in somewhat larger values of  $a_2$  than those proposed by other authors (e.g., Parker, et al., 1987, Garcia, 1990, Stacey & Bowen, 1988a). Their underflow depths are indirectly obtained from the following integrals

$$u_2 a_2 = \int_{z_b}^{h_s} u \, dz \quad ; \quad u_2^2 a_2 = \int_{z_b}^{h_s} u^2 \, dz \quad ; \quad u_2 C_s a_2 = \int_{z_b}^{h_s} u c_s \, dz \quad (2.51)$$

which is based on the slab approximation (sub-section 2.2.1) of Ellison & Turner (1959) which claims that all shape factors can be taken equal to unity. This formulation is consistent with our depth-integrated model, but there is no direct relation to the physical underflow depth. Measurements of profiles and visible interface levels indicate that in most cases our approach results in depths located between the depths observed visually and computed with equation (2.51). Consequently the shape factors originating from the depth integration of convective terms ( $u^2$ ) and sediment transport terms ( $u c_s$ ) are found to be larger than unity (up to 1.3), which contradicts the slab approximation and needs a correction in the basic equations. Essentially the proposed concentration and velocity profiles are used to close Galappatti's equation, and only a small correction of this equation is sufficient to harmonize the model. We have done this by setting  $L_a'$  equal to  $T_a'$  which were found to be differing to an extent equal to the shape factor for sediment-transport (Sloff, 1994a). We did not further examine small effects of this defect, for instance on the equilibrium concentration.

In the following section the closure relations and calibration parameters are discussed which are needed to complete the two-layer model. The effects of bottom friction and the equilibrium reference equation are particularly important in this section, but also the quantification of interfacial mixing and shear is assessed.

## 2.5 Closure relations for the two-layer model

When using a depth-integrated two-layer model the inevitable consequence of schematization is the necessity of quantifying boundary terms each of which gather various physical processes. In principle these boundary terms at bed and/or interface comprise friction, sediment entrainment, sediment concentration, and interfacial mixing. In this section is discussed how these terms are estimated in the model, as proposed in Sloff (1994a).

The roughness length-scale  $\hat{\eta}_0$  is found to be one of the primary calibration

parameters of the presented model, representing the grain and bed-form induced bed-shear stress. It is essential for the model to define an appropriate roughness scale or a relation between roughness scale and hydraulic conditions. We have already shown that this scale can also be expressed in terms of a bed-friction coefficient  $C_D$  or a Chézy value with help of equation (2.50). In a 2-D model we assume similarity in flow profiles in  $x$  and  $y$ -direction and we note that for the bed-shear stresses holds that  $\tau_b = \sqrt{(\tau_{bx}^2 + \tau_{by}^2)}$ . Then we find for the bed-shear stress in  $x$ -direction

$$\frac{\tau_{xb}}{\rho_f} = u_* u_{*x} = C_D u_* \sqrt{u_*^2 + v_*^2} \quad (2.52)$$

A similar form holds for the stress in  $y$ -direction. Note that in a 1-D flow  $v_*$  simply disappears. As we are usually dealing with rough boundaries the roughness scale  $\hat{\eta}_0$  can be expressed in terms of a Nikuradse sand-roughness height. However, experimental observations of turbidity currents on a mobile bed revealed the presence of bed forms which requires a reliable bed-form roughness predictor. Here the literature does not present us many tools to account for these bed forms in relation with turbidity currents. Garcia and Parker (1993) used a method developed by Nelson and Smith (1989) for the removal of form drag due to bed forms for open channel flow. But this method can only be used if bed-form dimensions are known. Also predictors from open-channel flow (e.g., van Rijn, 1984c) are not of much use, since they should be reformulated for the underflow depth for which a large number of data is required. Since data on this phenomena are very scarce it is best to calibrate the  $C_D$  or Chézy value for each application (e.g., on basis of observed velocity profiles). Considering that turbidity currents are characterised by rather constant Froude numbers it is plausible that the bed-form regime (and roughness scale) remains quite similar along the reach.

On the interface boundary a similar friction term can be defined to express the interfacial shear stress. When studying the velocity and concentration profiles according to the model presented in the previous section this stress at the associated interface level can be neglected compared to bed-shear stress. However, since the underflow depth in the two-layer model must be consistent with Ellison and Turner's (1959) slab approximation (equation 2.51, all shape factors are equal to unity) the interface is located at a lower level within the mixing layer. In subsection 2.4.3 it was shown that at this level the interfacial shear-stresses are of the same order of magnitude as bed-shear stresses. In harmony with the bed-shear stress we use the following 2-D equation for  $\tau_{xi}$  (Abraham et al., 1979):

$$\tau_{xi} = \rho_f C_{Di} (u_2 - u_1) \sqrt{(u_2 - u_1)^2 + (v_2 - v_1)^2} \quad (2.53)$$

The result can be written in  $y$ -direction in a similar way. The  $C_{Di}$  coefficient requires calibration again, where it must be smaller than  $C_D$ . In the model

interfacial friction and mixing have a similar impact on the momentum equation although mixing also effects the mass balance and concentration.

So far the effect of friction is assessed in a empirical but fundamental way. Even more uncertain is the quantification of the entrainment velocity which is appearing in the basic equations due to interfacial mixing processes. Basic mechanisms of mixing are studied by Sloff (1994a). It can be concluded that these mechanisms are still poorly understood and only empirical quantification is possible. The present knowledge on basic mixing mechanisms has mainly been provided from laboratory experiments. Usually these experiments are very specific and simplified, and their results cannot be applied for general field situations which differ much from laboratory circumstances. For instance it is shown that vortex-generated mixing behind the front may be much greater in a gravity current which enters a diverging channel or a widening reservoir, than the mixing in a prismatic laboratory flume (section 4.2). It is also possible that different basic entrainment mechanisms can occur simultaneously in the field which interact. It is therefore not surprising that the published empirical relations often show large deviations from the mixing rates in the field.

Mixing between the layers and the governing formation of the mixing layer is determined by shear and turbulence generated interfacial perturbations at the head of the current (e.g. Kelvin-Helmholtz instabilities originating from vortices at the interface). In the following we consider, just like Bo Pedersen (1980), all mixing as entrainment irrespective whether it is a one-way (pure entrainment), an equal two-way process (pure diffusion), or somewhere in between. In sub-section 2.3.1 it is shown that mixing processes occur at the upper edge of the upper sub-layer or mixing layer of the turbidity current, while the mixing layer itself is formed just behind the front (section 2.4). Eventually turbulence and shear-generated instabilities in this layer are the processes which entrain (net) the clear water and determine the entrainment rate. Considering these complex processes, as well as various others (Sloff, 1994a), it is not surprising that a satisfactory relation is not yet formulated.

Existing entrainment relations are based on the hypothesis that the entrainment velocity is proportional to a characteristic velocity, usually defined as a mean velocity or shear velocity of the underflow (Turner, 1986). Furthermore it is, in agreement with the turbulence considerations in section 2.3, considered to be fundamentally dependent on the gradient Richardson number or an equivalent formulation:

$$\frac{w_{ie}}{u_2} = f(Ri) \quad (2.54)$$

It is this parametrization and the regions of validity which generates the differences



in various approaches. In this study we considered a few popular formulas, but we have not made any effort to improve them or to develop alternatives. Often cited are Ellison and Turner's (1959), Bo Pedersen's (1980), Christodoulou (1986a,b), and Parker's (1987) formulas. In figure 2.18 a comparison of data and theory from Sloff (1994a) is presented (for references in this figure see this thesis). It illustrates the uncertainty in predicting the entrainment rate, especially when realizing that both axes have a logarithmic scale, so that the actual scatter is greatly distorted.

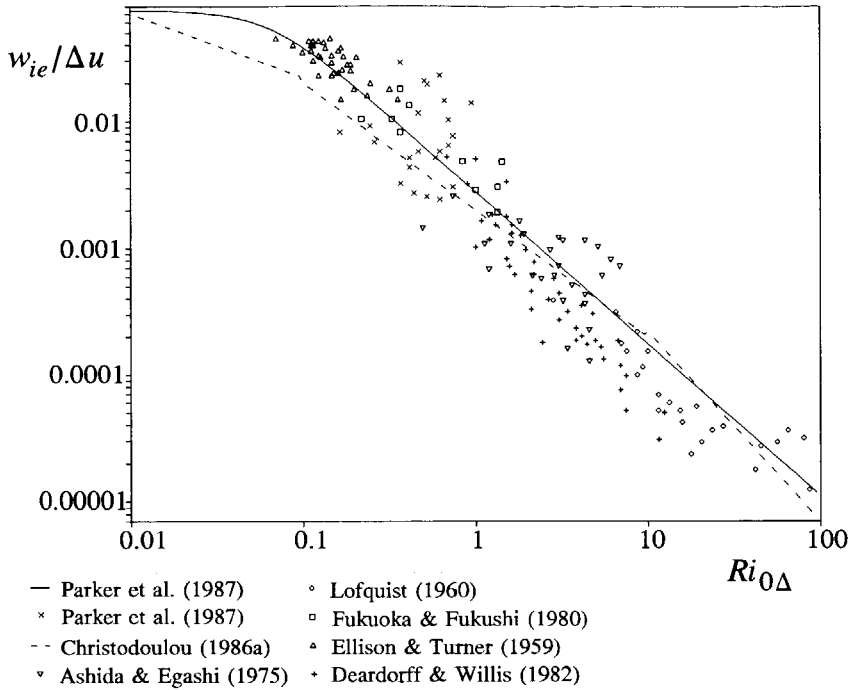


Figure 2.18 Entrainment rate: comparison between theory and data.

The large scatter in this figure is partially due to various uncertainties in measuring and scaling the entrainment rate. Using other length and velocity scales, such as proposed by Christodoulou (1986b) have not shown an appreciable improvement of these results. As an example of a possible source of uncertainty it should be remarked that the values of  $e_w$  from Parker's (1987) experiments were back-calculated from a finite difference form of the following fluid mass balance between two sections:

$$\frac{du_2 a_2}{dx} = e_w u_2 \quad ; \quad e_w = \frac{w_{ie}}{u_2} \quad (2.55)$$

Inevitably an increase in error is involved due to the differentiation of the measured

values for depth and velocity.

Another phenomenon that could militate against the use of the formulations proposed is the possibility of spurious correlations. Benson (1965) has shown that correlating two parameters, each containing the same stochastic variables, may lead to spurious correlation. In the most popular methods the entrainment rate is defined as

$$\frac{w_{ie}}{\Delta u} = f(Ri_{0\Delta}) \quad ; \quad Ri_{0\Delta} = \frac{\sigma' C_s g a_2}{\Delta u^2} \quad ; \quad \Delta u = u_2 - u_1 \quad (2.56)$$

If  $w_{ie}$ ,  $\Delta u$ ,  $a_2$ , and  $C_s$  are stochastic variables it can be shown that the parameters  $y_1 = w_{ie}/\Delta u$  and  $y_2 = (\sigma' C_s g a_2)/\Delta u^2$  a large correlation coefficient can exist although the original variables are not correlated (Sloff, 1994a). To prevent the occurrence of spurious correlations an alternative parameter should be used (e.g.,  $y_1 = w_{ie}/(g\nu)^{1/3}$ ). This possibility is not further studied, mainly because of the unavailability of appropriate data. Alternatively the entrainment rate can be coupled to energy considerations when using Bagnold's approach to compute sediment transport rates. Such an approach was followed by Pallesen (1983) as an extension of Bo Pedersen's (1980) approach.

Clearly the use of these relations demands caution. Under- or overestimation of the actual entrainment rate with a factor of the order of two is possible, which does reduce the predictability of a two-layer model significantly. Although entrainment effects are usually considered of minor importance, it can be shown numerically that these effects can completely modify the behaviour of the underflow. It affects the current in a similar way as the deposition of sediment, which also involves empiricism with a very large uncertainty.

The quantification of the near-bed sediment concentration  $c_a$  (reference concentration) determines completely the value of the equilibrium concentration in Galappatti's model. In quantifying it this large uncertainty is introduced. In previous turbidity-current studies various existing equations for  $c_a$  have been used, which were almost all derived for open-channel flow. The reason therefore is the lack of a specific equation for turbidity currents and the lack of data to derive one. Furthermore the flow conditions below the velocity maximum are comparable to those in open channel flow. Although Parker et al. (1987) tried to fit their data to an empirical relation for open-channel flow, the inaccuracies in the data and the method of computing the entrainment rate of sediment resulted in a large scatter. Experiments of a saline current passing over an erodible bed by Garcia and Parker (1993) yielded more useful results which are more realistic than those found for open-channel equations. Still large scatter in the data is due to the method of computing the sediment entrainment (e.g, by differentiating the concentration and velocities along a section). Garcia (1990) and Garcia and Parker (1991) compared

the performance of some equations for computing  $c_a$  in open-channel flow. One of the equations that performed best on open-channel data is the one proposed by van Rijn (1984b).

For practical purposes or numerical experiments also a more simple power law can be used based on the critical shear-stress approach. For instance by considering that Van Rijn's (1984a) transport stage parameter is proportional to the square of the underflow velocity, the reference concentration can be written as some cubic function of this velocity:

$$c_a = m \cdot u_2^3 \quad (2.57)$$

or in line with van Rijn's approach:

$$c_a = m' \cdot T^{1.5} = m' \cdot \left( \frac{u_*^2 - u_{*cr}^2}{u_{*cr}^2} \right)^{1.5} \quad (2.58)$$

where  $m$  is a parameter related to sediment characteristics and the reference height  $\eta_a$  and  $u_{*cr}$  is the critical shear velocity for initiation of movement.

In combination with these closure relations the presented two-layer model can be applied to simulate various types of turbidity currents. Clearly calibration and empiricism is inevitable in this model, but when applied correctly the results are sufficiently accurate for practical applications. However, at all times the limitations of the model due to shortcomings of the closure relations must be borne in mind. In the following chapter the mathematical model is further studied by using the method of characteristics.



# Chapter 3

## Characteristic analysis

### 3.1 General

To simulate the evolution of flow and bed morphology in a non-prismatic reservoir we have derived a two-dimensional (2-DH) two-layer model. In its complete form it corresponds to an extended form of the model for sediment-laden shallow-water flow on a mobile bed as presented by Sloff (1993a, 1993b). Furthermore it forms a hyperbolic system of first-order partial differential equations characterized by wave-like solutions. A useful tool in analyzing the structure of these complicated solutions, and those of other types of 2-DH hydraulic models, is *the method of characteristics*, which concerns the study of propagation of physical disturbances. Disturbances with infinitely small amplitude propagate along the characteristics in the solution space ( $t,x,y$ -space) as wave fronts, carrying information from initial and boundary conditions. As we show herein, this method supplies us with some essential information for simplifying, and analytically or numerically solving of the equations. It gives us rules for imposing boundary conditions to make the system well posed, and it can be used to formulate a stability criterium for two-layer flow.

The mathematical treatment of the characteristic theory for a general system of partial differential equations is given by Courant and Hilbert (1962). Often their treatment has been used to analyze and solve the 2-D (depth-averaged) shallow-water equations for flow on a fixed bed (without stratification), for example by Daubert and Graffe (1967) and Hirsch (1988). De Vriend (1985,1987a,b) added the influence of a mobile bed into the characteristic analysis of 2-D shallow-water flow. More general applications of the method to 2-D depth-averaged hydraulic models are given by Sloff (1992), where the theory is elaborated starting from simple shallow-water flow to fully coupled two-layer flow on a mobile bed. A further extension of the 2-D theory is given by Sieben (1994) (also Sieben & Sloff, 1994) to analyze models which include morphological changes in mountain rivers with sediment mixtures. A general treatment of 1-D models is given by Abbott (1966).

Application of the method of characteristics is pursued herein for our reservoir model in one and two dimensions. It shows how, and under which conditions, the mobility of the bed and the high sediment concentrations affect the solutions, by

comparison with fixed-bed models for conservative density currents (e.g. saline density underflows). Various simplifications and rules are obtained for further elaboration of the mathematical (and numerical) model, explained from a physical point of view. The theory presented can easily be applied to other type of 2D models.

### 3.2 Characteristic conditions

When initial values are given on an arbitrary surface (or a line in a 1-D model) in the  $t,x,y$ -space then the solution of the corresponding (Cauchy) initial-value problem is obtained by extending this initial data into an integral surface (solution surface) in the characteristic directions. However, when this initial data is given along a characteristic surface such an extension is not possible, and a solution cannot be found. Clearly, as the complete solution is constituted by the characteristics, this theory can be used to analyze propagation properties of the model. One of its features is that regions with different solutions are separated by characteristic surfaces. Therefore, jump discontinuities with infinitely small amplitude are carried along characteristic surfaces and can be interpreted into wave fronts. Likewise characteristic celerities are defined as the propagation velocities of these small disturbances in the solution space. They correspond to the characteristic directions  $dx/dt$  in the 1-D approach, and to the bicharacteristic directions  $dx/dt$  and  $dy/dt$  in the 2-D approach (the directions of the characteristic lines and surfaces). In a 2-D flow the discontinuities propagate along a family of bicharacteristics or rays which envelope the associated wave front in the corresponding characteristic directions. Mathematically the celerities can be obtained from the characteristic equation or characteristic condition as will be shown in this section.

A general mathematical presentation of the method of characteristics can be found in Courant and Hilbert (1962). Here we prefer to summarize the results of such an analysis for our model from a physical viewpoint (see also Hirsch, 1988, 1990). A more elaborate presentation of this study was given in Sloff (1992) and Sloff (1994b). The analysis is applied to the general coupled system of basic equations before utilizing the Boussinesq application and decoupling baroclinic and barotropic flow. The relative effect of these simplifications is of the order of the density difference and therefore irrelevant.

For the characteristic analysis the general 2-DH model (in  $q,a$ -form) is written in the following matrix form

$$A_t \frac{\partial \mathbf{U}}{\partial t} + A_x \frac{\partial \mathbf{U}}{\partial x} + A_y \frac{\partial \mathbf{U}}{\partial y} = \mathbf{b} \quad (3.1)$$

where  $A_j$  are the Jacobian matrices,  $\mathbf{b}$  a column vector of the non-homogeneous source terms, and  $\mathbf{U}$  is the vector of dependent variables i.e.,  $(q_{1x}, q_{1y}, a_1, q_{2x}, q_{2y}, a_2, z_b, C_s)$ . To this system of eight equations (or six if 1-D flow) an identical number of characteristic surfaces can be defined. The formulation of these surfaces can be obtained from the corresponding eigenvalue problem for the wave front surface in which the characteristic condition is expressed as

$$Q(\xi_t, \xi_x, \xi_y) = \det \left\| A_t \xi_t + A_x \xi_x + A_y \xi_y \right\| = 0 \quad (3.2)$$

where each vector  $\vec{\xi}_k$ , which satisfies this equation, is the vector normal to the corresponding characteristic surface  $C_k: \phi_k(x, y, t) = 0$  (phase of the wave front) which can be expressed as

$$\vec{\xi} = (\xi_t, \xi_x, \xi_y) = \left( \frac{\partial \phi}{\partial t}, \frac{\partial \phi}{\partial x}, \frac{\partial \phi}{\partial y} \right) \quad (3.3)$$

The system is hyperbolic, such that simple-wave-like solutions of the type  $\mathbf{U} = \bar{U} \exp(i \cdot \phi_k)$  exist, if all the characteristic normals (or eigenvalues) are real with linear independence of the corresponding left eigenvectors. For each  $\vec{\xi}$  which satisfies equation (3.2) we can define bicharacteristic directions in the  $t, x, y$ -space as

$$\frac{dx}{dt} = \frac{\partial Q / \partial \xi_x}{\partial Q / \partial \xi_t} \quad ; \quad \frac{dy}{dt} = \frac{\partial Q / \partial \xi_y}{\partial Q / \partial \xi_t} \quad (3.4)$$

These celerities are the directions of the (infinite number of) bicharacteristic rays in the  $t, x, y$ -space which envelop the characteristic surfaces. By eliminating  $\vec{\xi}$  from eq. (3.2) by means of eq's. (3.4) the characteristic equation can be expressed in terms of  $dx/dt$  and  $dy/dt$  and is then called the Monge equation. In a 1-D model equation (3.4) reduces to (Hirsch, 1988)

$$\frac{dx}{dt} = - \xi_t / \xi_x \quad (3.5)$$

such that the celerities in the  $t, x$ -plane can be directly obtained from the characteristic condition (3.2).

The characteristic condition for our 2-DH model is an algebraic equation in  $\vec{\xi}$  of the order eight but it can be factorized into two linear and one sixth-order equation:

$$1. \quad Q_1(\vec{\xi}) = \lambda_1 = \xi_t + \frac{q_{1x}}{a_1} \xi_x + \frac{q_{1y}}{a_1} \xi_y = 0 \quad (3.6)$$

for which  $dx/dt = q_{1x}/a_1$  and  $dy/dt = q_{1y}/a_1$ . This is a type of wave, along the stream lines in the upper layer, along which vorticity is transported (Vreugdenhil, 1989). It is a wave only observable in the velocity pattern,

and does not exist in 1-D theory.

$$\underline{2.} \quad Q_2(\bar{\xi}) = \lambda_2 = \xi_x + \frac{q_{2x}}{a_2} \xi_x + \frac{q_{2y}}{a_2} \xi_y = 0 \quad (3.7)$$

for which  $dx/dt = q_{2x}/a_2$  and  $dy/dt = q_{2y}/a_2$ . This is a wave (located along the stream lines) in the lower layer representing convective transport of suspended sediment following from Galappatti's equation with  $L_a' = T_a'$ .

3. An sixth order algebraic equation in  $\bar{\xi}$  is  $Q_3 = 0$ :

$$\begin{aligned} Q_3(\bar{\xi}) = & \xi_x a_2 \lambda_2 (p' - C_s \gamma_s) \left[ (\lambda_1^2 - a_1 g_z \lambda_3) (\lambda_2^2 - a_2 g_z \lambda_3) - a_1 a_2 g_z^2 \lambda_3^2 (1 - \varepsilon) \right] + \\ & + \gamma_s \xi_x \left[ g_z a_2 (\lambda_1 - a_1 g_z \lambda_3 \varepsilon) \left\{ \frac{s_{btot}}{u_{2tot}^3} \lambda_5^2 (\lambda_1^2 - a_1 g_z \lambda_3 - \lambda_2) + \frac{f_b}{u_{2tot}^2} \lambda_4 (\lambda_2 \lambda_4 - \lambda_5^2) \right\} \right] + \\ & - g_z a_2 \lambda_2^2 \left[ \frac{s_{btot}}{u_{2tot}^3} \lambda_5^2 + \frac{f_b}{u_{2tot}^2} \lambda_4^2 \right] (\lambda_1^2 - a_1 g_z \lambda_3 \varepsilon) = 0 \end{aligned} \quad (3.8)$$

where:

$$\begin{aligned} s_{btot} &= \sqrt{(s_{bx}^2 + s_{by}^2)}; \quad s_{bx} = u_2 s_{btot} / u_{2tot}; \quad s_{by} = v_2 s_{btot} / u_{2tot} \\ u_{2tot} &= \sqrt{(u_2^2 + v_2^2)} \\ f_b &= ds_{btot} / du_{2tot} \\ p' &= 1 - \varepsilon_p \quad (\text{bed porosity}) \\ \varepsilon &= \sigma' C_s \quad (\text{density difference: } g_z' = g \varepsilon) \\ \lambda_3 &= \xi_x^2 + \xi_y^2 \\ \lambda_4 &= u_2 \xi_x + v_2 \xi_y \\ \lambda_5 &= v_2 \xi_x - u_2 \xi_y \\ \gamma_s &= \text{dummy equals 0 or 1: unity at high } C_s, \text{ zero at low } C_s. \end{aligned}$$

This irreducible algebraic equation in  $\bar{\xi}$  cannot be solved analytically, and therefore cannot be written as a Monge equation. The six characteristic cones expressed by equation  $Q_3=0$  make up four cones (Monge cones) in the  $t, x, y$ -space.

The cones following from  $Q_3=0$  can be subdivided in two groups: 2 cones generated by circular (or elliptical) wave fronts, and 2 cones generated by star-shaped fronts (at least when  $\gamma_s=1$  as is shown hereafter). An example is given in figure 3.1 which shows how wave fronts develop in time originating from a point disturbance at the origin and how bicharacteristics (rays) envelop the cones. In reality the bicharacteristics are curved since they are dependent on the local values of the dependent variables (depth, discharge, etc.) which also vary in time and space. Due to this curvature wave fronts of different disturbances may intersect and allow for jumps and fronts with finite amplitude (e.g. Courant and Hilbert, 1962). This property plays an evident role in shock-capturing methods for solving the equations as discussed in chapter 6. The physical meaning of each cone is discussed in the following sections.



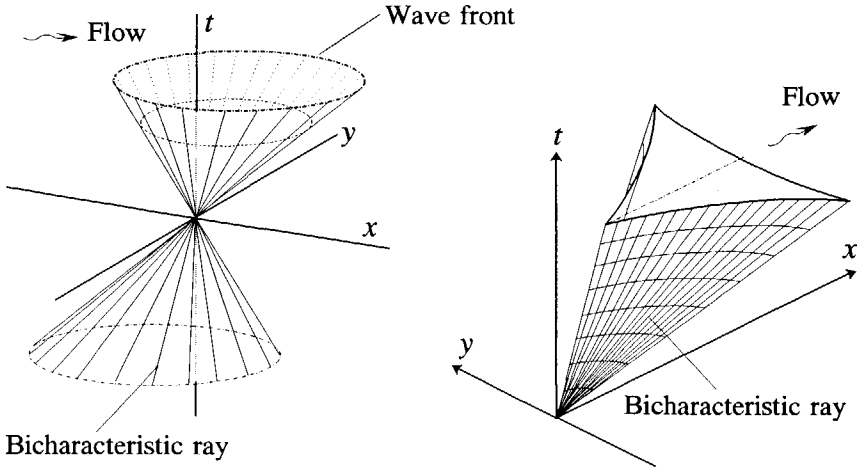


Figure 3.1 Monge cones for 2-DH mobile bed models

We found that one of the star-shaped cones almost coincides with the stream line in the lower layer if concentrations are large (with  $\gamma_s=1$ ), and fully coincides with the stream line if  $\gamma_s=0$  if concentrations are small (then it can simply be shown that  $Q_3$  factorizes into a fifth order and another linear algebraic equation). This wave is associated to transport of vorticity in the lower layer (cf.  $Q_1 = 0$ ).

If the general 2-DH model is integrated over the width, while assuming a wide prismatic channel, the following 1-D characteristic equation is found

$$\begin{aligned}
 & (\phi - u_2) \left[ (\gamma_s C_s - p') \phi a_2 \left\{ (\phi - u_1)^2 - g_z a_1 \right\} \left\{ (\phi - u_2)^2 - g_z a_2 \right\} - g_z^2 a_1 a_2 \frac{\rho_f}{\rho_2} \right] + \\
 & + \gamma_s f_b \phi \left\{ (\phi - u_1)^2 - g_z a_1 \right\} \left\{ (\phi - u_2) u_2 - a_2 g_z \right\} - g_z^2 a_1 a_2 \frac{\rho_f}{\rho_2} \right] + \quad (3.9) \\
 & + g_z a_2 f_b (\phi - u_2) \left\{ (\phi - u_1)^2 - g_z a_1 \left( 1 - \frac{\rho_f}{\rho_2} \right) \right\} \right] = 0
 \end{aligned}$$

where  $\phi = dx/dt$  is the characteristic celerity. Again for low concentrations  $\gamma_s=0$  the result can be simplified notably. Here the celerity  $\phi = u_2$  (first term in eq. 3.9) follows directly from Galappatti's equation with  $L_a' = T_a'$ .

As will be shown later in this chapter, a fundamental difference of the behaviour of the model following these characteristic equations exists for an internal subcritical and internal supercritical density current (e.g., Schijf and Schönfeld, 1953). For relatively low concentrations the flow is internal critical if the densimetric Froude

numbers  $Fr_1$  and  $Fr_2$  satisfy

$$Fr_1^2 + Fr_2^2 = \frac{(u_1^2 + v_1^2)}{g'_z a_1} + \frac{(u_2^2 + v_2^2)}{g'_z a_2} = 1 \quad (3.10)$$

where  $g'_z = g_z \varepsilon = g_z \sigma' C_s$ . If their sum is smaller than unity then the flow is internal subcritical, else supercritical. In a 1-D flow velocities  $v_i$  disappear and condition (3.10) remains unchanged.

### 3.3 Analysis of characteristics for the 1-D 2-layer flow

The characteristic equation of the width-integrated 1-D formulation of our model is given by equation (3.9). It is reducible to a fifth-order algebraic equation and a term  $\phi = u_2$  associated to adaptation of suspended-sediment concentration. The fifth-order equation cannot be solved analytically and is therefore not practical. Still it will be possible to relate the complex mathematical behaviour expressed by this relation to physical phenomena. Later in this section some approximative solutions are proposed, based on the conclusions of a complete numerical analysis of this equation.

In a fixed-bed situation the characteristic condition corresponds to the classical two-layer condition (Abbott, 1979), while in a infinitely deep reservoir with mobile bed the condition reduces to the open-channel flow condition (de Vries, 1959, 1965, Sloff, 1993a, 1993b) with modified gravity acceleration ( $g'$  instead of  $g$ ). To extend and combine the analyses of these classical models we consider a two-layer flow with zero velocity in the upper layer ( $u_1 = 0$ ). Furthermore we define the following dimensionless parameters:

- $Fr_2$  = densimetric Froude number of underflow ( $Fr_1 = 0$ )
- $\lambda_a$  =  $a_1/a_2$  = dimensionless depth parameter
- $\tilde{\phi}$  =  $\phi/u_2$  = dimensionless celerity
- $\psi$  =  $f_b/(a_2 \{p' - \gamma_s C_s\})$  = dimensionless bed-load transport parameter

Rewriting the complete characteristic equation (3.9) yields

$$\begin{aligned} & \tilde{\phi} \left\{ \left[ \varepsilon \tilde{\phi}^2 - \lambda_a Fr_2^{-2} \right] \left[ \varepsilon (\tilde{\phi} - 1)^2 - Fr_2^{-2} \right] - \lambda_a \frac{Fr_2^{-4}}{1 + \varepsilon} \right\} + \\ & - \gamma_s \psi \tilde{\phi} \left\{ \left[ \varepsilon \tilde{\phi}^2 - \lambda_a Fr_2^{-2} \right] \left[ \varepsilon (\tilde{\phi} - 1) - Fr_2^{-2} \right] - \lambda_a \frac{Fr_2^{-4}}{1 + \varepsilon} \right\} + \\ & - Fr_2^{-2} \psi (\tilde{\phi} - 1) \left[ \tilde{\phi}^2 - \lambda_a Fr_2^{-2} \left( 1 - \frac{1}{1 + \varepsilon} \right) \right] = 0 \end{aligned} \quad (3.11)$$

The five roots of this algebraic equation are plotted as a function of the densimetric Froude number in figures 3.2 and 3.3 using  $\gamma_s=1$ . Here the roots  $\tilde{\phi}_1$ ,  $\tilde{\phi}_3$  and  $\tilde{\phi}_5$  are always positive (pos), while  $\tilde{\phi}_2$  and  $\tilde{\phi}_4$  are negative (neg) as shown in the figures.

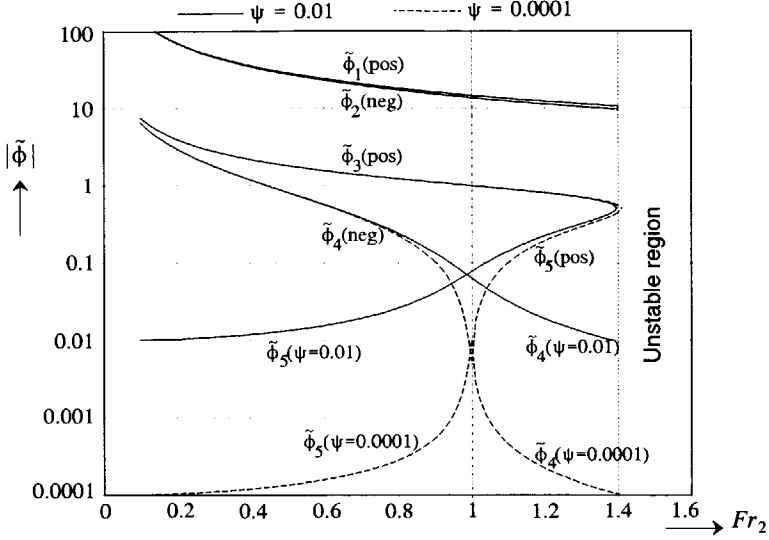


Figure 3.2 Absolute values of dimensionless celerities for different  $\psi$ , using  $\lambda_a=1$ ,  $\varepsilon=0.01$  and  $u_1=0$ .

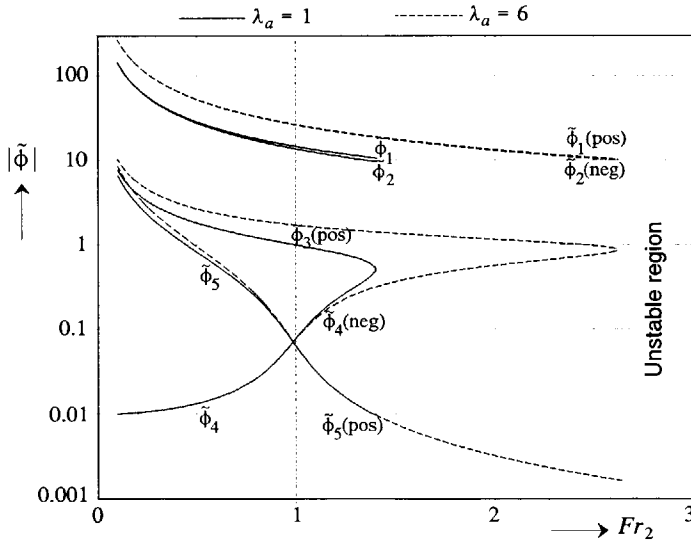


Figure 3.3 Absolute values of dimensionless celerities for different  $\lambda_a$ , using  $\psi=0.01$ ,  $\varepsilon=0.01$  and  $u_1=0$ .

Comparing these celerities to those for conservative two-layer flow and open-channel flow on a mobile bed some important conclusions can be drawn from these figures and from a more general analysis of equation (3.9).

- The critical state  $Fr_2=1$  (or in general equation 3.10) is clearly the point where absolute values of  $\tilde{\phi}_4$  and  $\tilde{\phi}_5$  intersect. It is most important for mathematical and physical behaviour.
- It can be shown that the celerities  $\tilde{\phi}_1$  and  $\tilde{\phi}_2$  correspond to the external celerities of the barotropic flow (celerities of surface waves). The effect of mobile bed (through parameter  $\psi$ ) and baroclinic phenomena (through parameter  $\varepsilon$ ) is negligible for all Froude numbers, permitting a decoupling of the model. In general their magnitude is one order of magnitude larger than  $\tilde{\phi}_3$ , and they depend on the total discharge and depth of the reservoir.
- In an internal subcritical state with  $Fr_2 < 0.8$  the celerity  $\tilde{\phi}_3$  corresponds to the positive celerity of internal waves in the baroclinic flow as found for a two-layer fixed-bed model. Likewise the celerity  $\tilde{\phi}_4$  corresponds to their negative celerity (baroclinic disturbances travel up and downstream). The remaining positive celerity  $\tilde{\phi}_5$  can be associated to disturbances in the bed morphology related to bed-load transport.
- In an internal supercritical underflow with  $Fr_2 > 1.2$  the celerity  $\tilde{\phi}_3$  corresponds again to the positive celerity of internal waves, but also the positive celerity  $\tilde{\phi}_5$  is now associated to internal-wave propagation (no upstream propagation of baroclinic disturbances). The remaining negative celerity is now identified with bed disturbances, for instance the upstream propagation of anti-dunes.
- In a fixed-bed model celerity  $\tilde{\phi}_5$  disappears in these figures for  $Fr_2 < 1$  and  $\tilde{\phi}_4$  disappears for  $Fr_2 > 1$ . Then  $\tilde{\phi}_5 = \tilde{\phi}_4 = 0$  at  $Fr_2 = 1$ . In the non-critical ranges of Froude numbers the internal celerities are practically independent of the mobile bed (allowing a decoupling). Bed mobility is only relevant for the bed celerity. However, in the near-critical region ( $0.8 < Fr_2 < 1.2$ ) the celerities  $\tilde{\phi}_5$  and  $\tilde{\phi}_4$  are fully coupled and dependent on  $\varepsilon$  and  $\psi$ .
- Bed celerities are not affected by the depth parameter  $\lambda_a$  if  $\psi$  is constant for all Froude numbers. Clearly they are independent of the depth.
- For large densities and  $\gamma_s = 1$  (increasing  $\varepsilon$ , not illustrated here) the positive internal-wave and bed-wave celerities are increased, while their negative counterparts are decreased. As a consequence the critical flow condition is slightly shifted to lower values of  $Fr_2$ . This phenomena was described by Sloff (1993a, 1993b) for open-channel flow on a mobile bed.
- A breakdown of the model occurs when  $\tilde{\phi}_3$  and  $\tilde{\phi}_4$  become imaginary. In the figures this is called the unstable region, as for this situation the model becomes elliptic and the 2-layer approach loses its stability. The general stability criterion for 1-D two-layer flow with low concentrations is (Sloff, 1992)

$$(u_2 - u_1)^2 < g'_z(a_1 + a_2) \quad (3.12)$$

where  $g'_z = g_z \varepsilon$ . At larger concentrations this condition still holds provided that the right-hand term is somewhat reduced. This stability criterion practically equals that which can be found by analyzing the Kelvin-Helmholtz instabilities (e.g. Thorpe, 1971) and requiring that the depth of a subsequent developing interfacial mixing layer is less than the total depth or layer depth. Coherently also a consideration of energy of the mixing process due to Kelvin-Helmholtz instability yields the same criterion. Equation (3.12) as well as the figures shows that the two-layer model is more stable in deep-water reservoirs, and becomes superfluous in an infinitely deep reservoir.

- Another type of flow instability arising from the non-linearity of the basic equations (geometry and roughness) are roll waves in steady uniform supercritical flow. Mathematical analysis based on the characteristics for sediment-laden open-channel flow (Sloff, 1993a, 1993b) showed that again the stability criterion at which these instabilities occur is reduced at high concentrations. Due to the analogy with open-channel flow internal roll waves appearing on the density interface can also be observed as interfacial instabilities (Alavian, 1986).

For turbidity currents observed in reservoirs the bed-load transport parameter  $\psi$  is small. Therefore their 1-D characteristic behaviour is not much different from fixed-bed models where the bed-wave celerity does not exist. For these zero-amplitude long waves the effect of suspended sediment does not affect the bed and internal waves (this is different for short waves with a certain amplitude).

Following these conclusions it has been shown that flow in flow situations which are not close to the critical one, i.e., approximately for  $Fr_1^2 + Fr_2^2 < 0.7$  and  $Fr_1^2 + Fr_2^2 > 1.4$ , it is possible to simplify the model and to allow for a quick and analytical solution as follows (Sloff, 1992):

- The propagation velocity of disturbances in the bed is small compared to those in flow. Consequently flow and morphology can be *decoupled*: Use a quasi-steady approach for computing the morphology by neglecting all derivatives to  $t$  except those for  $\partial z_b / \partial t$ , but by still allowing for the time variation of discharges. Consider a fixed bed for computing the unsteady flow phenomena.
- Also the difference in magnitude of the barotropic (internal waves) and baroclinic flow (surface waves) propagation velocities allows us to *decouple* these modes if the density differences between the layers are small ( $\varepsilon \ll 1$ ), which was also shown by Vreugdenhil (1979).

For the 1-D model it can be shown easily that these simplification results in the

following approximative celerities (also shown by Schijf and Schönfeld, 1953):

Internal-wave celerities  $\phi_i$ :

Assume fixed bed ( $f_b=0$ ). Consider the terms  $(\phi_i-u_1)$  and  $(\phi_i-u_2)$  of order  $\sqrt{(\varepsilon ga)}$  in which  $a_1$  and  $a_2$  are of order  $a$  (total depth). Then the terms of order  $(\varepsilon ga)^2$  can be neglected compared to the other terms ( $\varepsilon \ll 1$ ), yielding:

$$\phi_{i,2} \approx \frac{a_1 u_2 + a_2 u_1}{a_1 + a_2} \pm \sqrt{\frac{a_1 a_2}{(a_1 + a_2)^2} [\varepsilon g_z (a_1 + a_2) - (u_1 - u_2)^2]} \quad (3.13)$$

External-wave celerities  $\phi_e$ :

Assume fixed bed ( $f_b=0$ ). Consider the terms  $(\phi_e-u_1)$  and  $(\phi_e-u_2)$  of order  $\sqrt{ga}$  and  $(u_1-u_2)$  of order  $\sqrt{ga}$  in which  $a_1$  and  $a_2$  are of order  $a$ . Then the terms of order  $\varepsilon(ga)^2$  can be neglected compared to the other terms ( $\varepsilon \ll 1$ ). This yields:

$$\phi_{e,2} \approx \frac{a_1 u_1 + a_2 u_2}{a_1 + a_2} \pm \sqrt{g_z (a_1 + a_2)} \quad (3.14)$$

Bed-wave celerity  $\phi_b$ :

Assume steady flow (neglect all derivatives to  $t$  except  $\partial z_b / \partial t$ ) and assume small concentrations. This yields:

$$\phi_b = \frac{f_b u_2 (1 - Fr_1^2)}{a_2 p' (1 - Fr_1^2 - Fr_2^2)} \quad (3.15)$$

These results are quite important but not comprehensive. The characteristic analysis of the 2-DH model provides more insight in the physical behaviour of the model and more support for decisions concerning simplification and decoupling of the model. This will be shown in the following section.

### 3.4 Analysis of characteristics for the 2-DH 2-layer flow

#### 3.4.1 Introduction

Wave fronts (with infinitely small amplitude), originating from a point disturbance, can be obtained from the Monge equations (i.e., characteristic equation rewritten in terms of  $dx/dt$  and  $dy/dt$ ) by means of integration to  $t$ . We suppose that the

disturbance emanates in the origin of the coordinate system. By expressing  $dx/dt = \Delta x/\Delta t$  and  $dy/dt = \Delta y/\Delta t$  we can draw wave fronts developing for each value of  $\Delta t$ . However, for the characteristic condition  $Q_3=0$  (equation 3.8) a Monge equation cannot be formulated and we used the graphical Huygens' method (Courant and Hilbert, 1962) to construct the wave fronts. Taking  $\Delta t=1$  s, the lines  $\lambda - (\alpha_x \cdot \Delta x) - (\alpha_y \cdot \Delta y) = 0$  envelop the wave front, where the values for  $\lambda$  (the eigenvalues) follow (numerically) from  $Q_3(-\lambda, \alpha_x, \alpha_y) = 0$  and where  $\vec{\alpha} = (\alpha_x, \alpha_y)$  is a unit vector which has to be varied over the unit sphere (cf. Hirsch, 1990). These lines are the secants of the bicharacteristic strips and the surface  $t=1$  s. Equation  $Q_3(-\lambda, \alpha_x, \alpha_y) = 0$  gives six roots for the eigenvalues  $\lambda$  relating to the four cones expressed by this equation (Sloff, 1992). Alternatively to this graphical approach Sieben (1994) (also Sieben & Sloff, 1994) proposed the use of polar coordinates to formulate the wave fronts. This results in a more direct numerical description of Huygens' approach.

### 3.4.2 Internal subcritical flow

Consider an internal subcritical two-layer flow. These types of turbidity currents have a low sediment-transport capacity so that we may assume  $\gamma_s=0$ . In figure 3.4 the wave fronts are plotted for a mobile bed derived from condition  $Q_3$  originating from a point disturbance (in the origin at  $t=0$  s) after  $\Delta t=1$  s. We used the fictitious values  $q_{1x}=-0.3\text{ m}^2/\text{s}$ ;  $q_{1y}=q_{2y}=0$   $\text{m}^2/\text{s}$ ;  $q_{2x}=0.5$   $\text{m}^2/\text{s}$ ;  $a_1=3$  m;  $a_2=1$  m; exaggerated  $C_s \approx 0.1$ ;  $s_{\text{tot}}=0.001$   $\text{m}^2/\text{s}$ ;  $Fr_1^2+Fr_2^2 \approx 0.16$ .

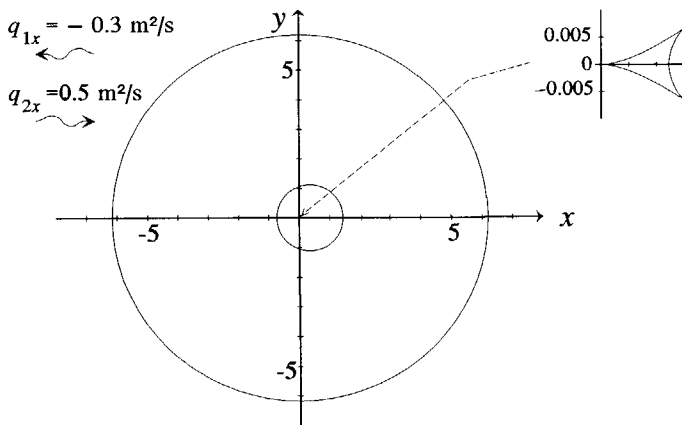


Figure 3.4 Wave fronts internal subcritical flow.

We found that for a fixed bed model ( $\partial z_b/\partial t=0$ ) the two circular fronts are practically identical to those for a mobile bed in figure 3.4, but that the star-shaped

front cannot be found. The wave fronts in figure 3.4 can be associated to the following physical phenomena which were also identified in the 1-D approach:

- The large circular front is associated to *surface waves*. This external flow phenomenon disappears if a rigid lid model is defined. Surface waves have a relatively large propagation speed.
- The small elliptical front is associated to *internal waves* at the density interface, which have a much smaller propagation speed than surface waves. These internal waves only occur in multiple-layer models.
- The small star-shaped front is associated to *bed waves* and is typical for all morphological models. Their propagation speed is very low.

The distinct differences in magnitude of the celerities of these waves, notably for  $Fr_1^2 + Fr_2^2 < 0.8$ , allows us to simplify the model as in the 1-D case to define approximative solutions. By simplifying and reducing the characteristic equation  $Q_3 = 0$  according to these considerations we can define approximate Monge equations for each type of wave front separately. These equations are presented in Sloff (1994b) and show some analogy with the approximative solutions for the 1-D celerities given by equations (3.13) to (3.15). Analogous to the 1-D approach we assumed fixed bed and neglect density differences for the external waves, resulting in a Monge cone practically corresponding to that of open-channel flow on a fixed bed. For internal flow (internal waves) we assumed fixed bed and neglect terms of order  $(\varepsilon g(a_1 + a_2))^2$ , resulting in a somewhat more complicated equation characterised by circular cones (figure 3.1). For the morphology we assume the flow to be quasi-steady and rewrite the system of equations for coordinates in the flow direction ( $s, n$ -axis) of the underflow (we assume the bed morphology to be practically independent of the quiescent ambient flow). This is permitted as characteristic are invariant with respect to arbitrary transformations of independent variables (Courant & Hilbert, 1962). This yields an equation similar to that for quasi-steady flow on a mobile bed as presented by de Vriend (1987a,b) and Sloff (1992). It can be solved, yielding four roots forming two families. These roots compose the star-shaped cone illustrated in figure 3.1. The approximative 1-D celerities of the previous section correspond to the intersections of the wave fronts with the flow axis. For instance the bed celerity corresponds to the downstream point of intersection of the two-dimensional star-shaped bed-wave front with the  $s$ -axis in flow direction. At this point the elementary behaviour of the bottom is identical with the one-dimensional behaviour. Compared to the one-dimensional models it can be noticed that at the edges of the star shaped front the two-dimensional approach yields slightly larger propagation velocities of bed disturbances.

The separate Monge equations presented in Sloff (1994b) can be used to determine the Monge cones for subcritical unsteady density and turbidity currents with small density differences. They are required for numerical methods which are based on the method of characteristics.



### 3.4.3 Internal supercritical flow

Now consider an internal supercritical turbidity current which can be sediment-laden ( $\gamma_s=1$ ). In fig. 3.5 the wave fronts after  $\Delta t=1$  s are plotted for a mobile bed derived from condition  $Q_3$  originating from a point disturbance in the origin (at  $t = 0$  s).

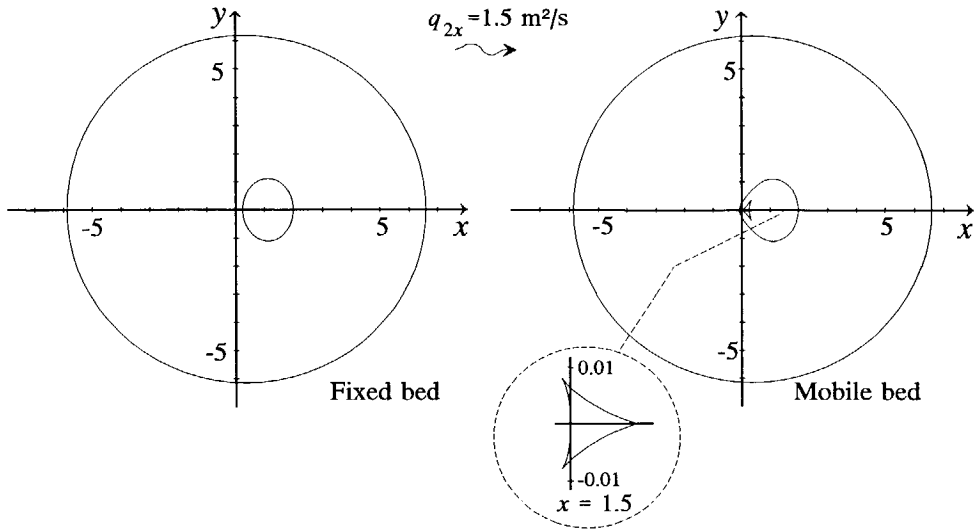


Figure 3.5 Wave fronts internal supercritical flow, left fixed, right mobile bed.

We used  $q_{1x}=q_{1y}=q_{2y}=0$  m<sup>2</sup>/s;  $q_{2x}=1.5$  m<sup>2</sup>/s;  $a_1=3$  m;  $a_2=1$  m;  $C_s \approx 0.1$ ;  $f_b=0.01$  m;  $s_{bot}=0.003$  m<sup>2</sup>/s;  $Fr_2=1.17$ . Clearly the figure for fixed bed resembles that for internal subcritical flow, except for the internal wave front, which is now located fully downstream of the disturbance source (typical for supercritical flow). Furthermore the fixed bed and mobile bed models show a fundamentally different behaviour except for the large circular (external) wave front. These aspects were already observed comparably in the 1-D analysis.

A more detailed plot is given in figure 3.6, which also illustrates how the wave fronts are constructed using Huygens' method. Firstly a small star-shaped front is found near the lower layer streamline (amplified in the dotted circle in figure 3.6), which, as previously stated (section 3.3), we may associate to vorticity. Secondly on a mobile bed the small egg-shaped and star-shaped front near the origin *interact* in such a way that upstream disturbance propagation occurs. In the 1-D analysis this negative propagation was associated to the propagation of anti-dunes on the bed, but that is not evident in a 2-DH model.

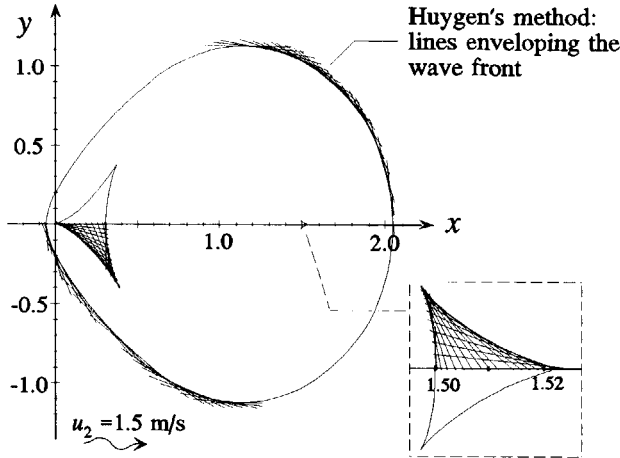


Figure 3.6 Huygen's construction of the internal supercritical wave fronts with  $\gamma_s=1$  and stagnant upper layer (external waves not plotted).

From the strong interaction between the two wave fronts we may conclude that in internal supercritical flow the wave fronts cannot be associated to either internal waves or bed waves, and consequently the processes are fully coupled. A similar behaviour was found for supercritical shallow water flow on a mobile bed without stratification by Sloff (1992) and by Sieben and Sloff (1994). Solving of the equations for this type of flow requires at least a *fully coupled* (numerical) solution method for the internal flow and the bed morphology, whereas the solution becomes sensitive to the boundary conditions. This is contradictory to the results of the 1-D analysis in which is shown that decoupling is allowed for Froude numbers larger than 1.2. External flow may still be decoupled for the same reasons as in subcritical flows. The decoupled equations for the baroclinic and barotropic flow are presented in sub-section 2.3.3.

Accounting for large concentrations by taking  $\gamma_s=1$  causes, besides the formation of a star-shaped vorticity wave, an increase in propagation velocities in the direction of the turbidity current and a decrease in counterflow direction. Similarly to the 1-D flow this phenomenon decreases the critical Froude number and the Froude number at which instability occurs. Also in a 2-DH model instability of the model is found when the Monge equation for the physical relevant wave fronts yields imaginary roots. The stability criterion for a 2-DH flow can be approximated (Sloff, 1994b) as

$$(u_2 - u_1)^2 + (v_2 - v_1)^2 < g_z \varepsilon (a_1 + a_2) \quad (3.16)$$

which is similar to equation (3.12) expressing the stability of long internal waves.

In chapter 2 it was already assumed that for practical situations the low concentration model is favourite. By applying the Boussinesq approximation to simplify the model (sub-section 2.2.2) automatically the dummy variable  $\gamma_s$  is taken equal to zero. The corresponding results of the 2-D and 1-D analyses are therefore most relevant for further application to our model. In the following section the characteristics are used to impose boundary conditions.

### 3.5 Number of boundary conditions

The knowledge on the development of the wave fronts can be used to determine the number of boundary conditions (b.c.) required to make the system well posed. For hyperbolic problems the number of boundary conditions, needed at any particular point at the boundary equals the number of characteristics entering the region at that point (Daubert and Graffe, 1967). In a 2-DH flow boundary conditions have to be given at each instant  $t$  at the contour of a boundary  $\Omega$ . Consider the lower-layer flow-velocity normal to the boundary to be  $u_{nor2}$ ; the upper-layer flow-velocity  $u_{nor1}$ . Furthermore we assume  $u_{nor2} \gg u_{nor1}$ . From the discussed wave fronts (external, internal, bed, sediment convection, and vorticity) the required number of boundary conditions is determined in Table (3.1) for different flow types on a mobile bed as well as on fixed bed (Sloff, 1992, 1994b).

Internal subcritical density current		b. c.		Internal supercritical density current		b. c.	
		mobile	fixed			mobile	fixed
lower layer	inflow $u_{nor2} < 0$	4	3	lower layer	inflow $u_{nor2} < 0$	4	4
	outflow $u_{nor2} > 0$	2	2		outflow $u_{nor2} > 0$	2	1
	solid $u_{nor2} = 0$	2	2		solid $u_{nor2} = 0$	2	2
upper layer	inflow $u_{nor1} < 0$	1	1	upper layer	inflow $u_{nor1} < 0$	1	1
	outflow $u_{nor1} > 0$	0	0		outflow $u_{nor1} > 0$	0	0
	solid $u_{nor1} = 0$	0	0		solid $u_{nor1} = 0$	0	0
susp. transport	inflow $u_{nor2} < 0$	1	-	susp. transport	inflow $u_{nor2} < 0$	1	-
	outflow $u_{nor2} > 0$	0	-		outflow $u_{nor2} > 0$	0	-
	solid $u_{nor2} = 0$	0	-		solid $u_{nor2} = 0$	0	-

Table 3.1 Number of boundary conditions for coupled 2-DH stratified flow.

In a similar way a table can be defined for the decoupled model. Figure 3.7 illustrates the characteristic planes (local approximations of characteristic surfaces)

for an internal supercritical density current at an arbitrary boundary. Note that the cones in this figure are the backward Monge cones, deduced by imaging them in their vertex (point where disturbances originate). On the smooth boundary  $d\Omega$  the conditions have to be imposed according to the incoming characteristics.

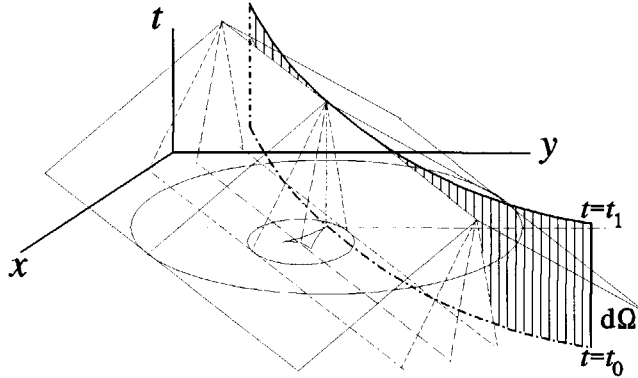


Figure 3.7 Characteristic planes at the boundary (Sloff, 1992).

The type of boundary conditions to be given is usually determined from physical reasoning and additional conditions for well-posedness, as will be shown for 1-D flow in sub-section 6.7.1 (see also Hirsch, 1990).

The number of boundary conditions to be imposed on a 1-D model analogously corresponds to the number of characteristics entering through the boundary. This is summarized in table 3.2 based on the sign of the characteristics. In the fully coupled 1-D two-layer turbid flow on a mobile bed (not critical) always four positive and two negative celerities can be found (section 3.3). In a conservative current (on a mobile bed) the positive suspension characteristic, and a positive  $\tilde{\phi}_3$ , or negative  $\tilde{\phi}_4$  characteristic disappears depending on the flow type. In a decoupled model the number of boundary conditions is split according to table 3.2.

Model type	Mode	Flow type	Upstream inflow b.c.		Downstream outflow b.c.	
			mobile bed	conservative	mobile bed	conservative
Fully Coupled Model		subcritical	4	2	2	2
		supercritical	4	3	2	1
Decoupled Model	Baroclinic	subcritical	3	1	1	1
		supercritical	3	2	1	0
	Barotropic	subcritical	1	1	1	1

Table 3.2 Number of boundary conditions for 1-D stratified flow.

### 3.6 Discussion

The method of characteristics is used to analyze the 2-DH and 1-D depth-averaged two-layer model for simulation of morphological processes in a reservoir with turbidity currents. It shows mathematically how a point-disturbance develops into a number of (characteristic) wave fronts (with infinitely small amplitudes) which are related to physical phenomena. Since information from boundaries and initial conditions is transported along characteristics it is well known that these results are important for numerical and analytical solutions. By comparing conservative two-layer flow on a fixed bed to that on a mobile bed and by comparing low concentration turbidity currents to sediment-laden ones we found that:

- Besides circular wave fronts which can be associated in a coupled 2-DH flow to surface waves (barotropic waves) and internal (baroclinic) waves, and a star-shaped wave front which can be associated to bed waves, two downstream propagating waves are found associated to transport of vorticity in the upper and lower layer respectively. Furthermore another downstream directed wave is associated to the adaptation of suspended sediment. The characteristics found in a 1-D flow correspond to these wave fronts, except for the vorticity waves.
- For 2-DH and 1-D internal subcritical flow ( $Fr_1^2 + Fr_2^2 < 0.7$ ) the wave fronts (or celerities) for surface waves, internal waves and bed waves differ several orders of magnitude and are practically independent. Their interaction is very weak. Therefore morphological computations can be carried out by means of a quasi-steady approach, or unsteady flow computations can be carried out with a fixed bed. Also external and internal flow computation may be decoupled if density differences are small (which is elaborated in the previous chapter). These adjustments greatly simplify the model, and allow for analytical formulations of the wave fronts or celerities.
- For 2-DH internal supercritical flow the internal and morphological processes are fully coupled and require a fully coupled computation. However, in a 1-D model the internal and morphological computation (e.g., anti-dunes) can be decoupled again for  $Fr_1^2 + Fr_2^2 > 1.4$ . Still external and internal flow can be decoupled at all Froude numbers in both 2-DH and 1-D models (if  $C_s \ll 1$ ).
- At high concentrations the propagation speed of disturbances in flow direction increases, while that in counter-flow direction decreases. For that reason the flow may become critical (and also instable) at lower Froude numbers.

- The required number of boundary conditions for numerical or analytical solution directly follow from the number of characteristic entering through the boundary. For a coupled 2-DH and for 1-D models these numbers are summarized in tables 3.1 and 3.2.
- A physically sound stability criterion for two-layer flow follows from the condition for hyperbolicity of the model (equations 3.12 and 3.16). At a certain (high) value of the densimetric Froude number the model becomes elliptic due to imaginary characteristics. In deep-water reservoirs the flow remains stable up to higher Froude numbers than in shallow reservoirs.

The method of characteristics plays an evident role in further mathematical analysis of the model and the solution (analytical and numerical). Sometimes it is useful to rewrite the system of equations in an equivalent form, i.e. the compatibility equations, along the (bi-) characteristics. This transformation to a 2-D characteristic coordinate system is for instance treated by Hirsch (1990) and applied by Sieben (1994). It can be shown that if the system of basic equations (3.1) is rewritten in conservative form (i.e.,  $A_i$  is the identity matrix  $\hat{I}$ ), the characteristics can be considered as the eigenvalues  $\lambda_k$  of the Jacobians as follows:

$$\det \| \lambda \hat{I} - A_x \xi_x - A_y \xi_y \| = \det \| \lambda \hat{I} - \tilde{K} \| = 0 \quad (3.17)$$

In turn we can define left eigenvectors  $\mathbf{I}^k$  as solutions of

$$\mathbf{I}^k \tilde{K} = \lambda_k \mathbf{I}^k \quad \text{or} \quad \mathbf{I}^k (A_x \xi_x + A_y \xi_y) = \lambda_k \mathbf{I}^k \quad (3.18)$$

Then the compatibility equation for  $\lambda_k$  for the 2-DH model becomes

$$\mathbf{I}^k \frac{\partial \mathbf{U}}{\partial t} + \mathbf{I}^k \frac{\partial \mathbf{U}}{\partial x} + \mathbf{I}^k \frac{\partial \mathbf{U}}{\partial y} = \mathbf{I}^k \mathbf{b} \quad (3.19)$$

In compact form this can also be written as

$$\left( L^{-1} \frac{\partial}{\partial t} + L^{-1} \frac{\partial}{\partial x} + L^{-1} \frac{\partial}{\partial y} \right) \mathbf{U} = L^{-1} \mathbf{U} \quad (3.20)$$

where  $L^{-1}$  is a matrix in which each  $k^{\text{th}}$  line is the left eigenvector  $\mathbf{I}^k$  (Hirsch, 1990). Also a matrix of right eigenvectors can be defined as  $R=L$  (inverse of  $L^{-1}$ , each  $k^{\text{th}}$  column is right eigenvector  $\mathbf{r}_k$ ). Right eigenvectors are proportional to the intensity of the propagating disturbance, a property which is used in section 6.6 to decompose the fluxes in simple-wave contributions (in terms of characteristic variables or Riemann invariants). The matrix  $L^{-1}$  can be shown to diagonalize the matrix  $\tilde{K}$  into a diagonal matrix of the eigenvalues as is also used in section 6.6.

The presented elaboration of the theory for characteristic analysis can easily be used for other 2-D models by means of simplification of the model equations and of the results. It is a useful tool in analyzing a complicated model and a first step to be made for numerical solution. It has been shown that the intersection of the characteristic wave fronts plays an evident role in computing shocks and jumps in the solutions, because these discontinuities develop due to intersection of these characteristic wave fronts. This property has been used in the following chapter to define shock relations for the gravity-current front and related discontinuities.





# Chapter 4

## Gravity-current fronts

### 4.1 Introduction

A gravity current advancing at the bottom of a reservoir is preceded by a front (its nose) which is characterized by a raised head and followed by intense mixing. Frontal motion depends on various complicated physical processes causing energy dissipation and dispersion. In general the motion of gravity-current fronts is important for many different hydrodynamical, geophysical, and meteorological processes; for example propagation of oil slicks, toxic gases, dredging disposals, avalanches, turbidity currents in submarine canyons, or downbursts of cold air from a thunderstorm (Simpson, 1987). For venting out turbidity currents from a reservoir the rate of propagation the front is important to predict the arrival of the current at the dam, after which sluices in the dam can be opened. This enables us to prevent unnecessary loss of stored water. A good understanding of the physics is required to develop and understand a model which includes the advance of such a front.

A description of the physical processes is given in section 4.2 which determine the motion of a gravity-current head as reported from observations and interpretations of laboratory experiments. The treat of these processes deals with gravity currents in prismatic flumes (1-D plane gravity currents) as well as 2-DH currents with axisymmetrical spreading.

The theoretical analysis of gravity-current fronts is historically assessed from two different view points. In one approach the characteristics of the front are studied for a gravity current that has already been established and exhibits a practically steady state. These steady-state features have been shown to be quite common in nature, and this type of approach has gained much notice in literature. This has resulted in various relations that must hold at the front. It is Benjamin's (1968) formula which is most often cited due to its good match with the scattered data of various observed fronts. To reduce the discrepancies, i.e. the scatter, a wide range of other formulas and variations to Benjamin's equation have been developed, for instance by adjusting the dissipation rate.

As the alternative approach the front is taken as a solution of the shallow-water equations, for instance evolving from a state of rest. It is considered as a wave that attained maximum steepness which means that it is a shock wave. In this context the turbid underflow can roughly be regarded as a dam-break wave collapsing into an

ambient fluid, which enables us to use some established methods from dam-break modelling.

In this chapter we try to combine the two approaches in a way that the shock-wave solution of the two-layer model matches the well-working and verified steady-state solutions. Theoretical considerations on modelling the front are treated in section 4.3 and further. Starting from our 1-D or 2-DH models the first step in incorporating the motion of the front would be the formulation or reformulation of appropriate balance equations for momentum and energy. To consider the gravity current front as an internal bore is the most attractive approach for mathematical and numerical simulation, especially if the model is two-dimensional. A gravity-current head is assumed to be a special form of an internal bore where downslope of the front depth and velocity of the lower layer are extremely small. The advantage of this approach is the necessity of only one algorithm for computing both internal bores and gravity-current fronts. Numerical shock-fitting or shock-capturing methods can be used. They are already in common use for instance for dam-break flows.

In section 4.4 shock relations are derived from the Rankine Hugoniot conditions for an internal bore in a 1-D two-layer model. These are used to examine the differences between the propagation and development of an internal bore and a real front. On basis of empirical evidence a choice is made with respect to correcting or transforming the basic equations for two-layer flow to account for real fluid effects such that its shock-wave solutions matches the classical steady-state formulations. In the following section 4.5 this approach is further elaborated to a concept model for 2-DH fronts.

## **4.2 Gravity-current fronts in laboratory and in the field**

Before attempting to develop a theoretical model for an intruding gravity current it is important to understand its complex behaviour in nature. Gravity currents can be found in various forms, which are relevant for as many different research fields. As the leading front of the current is often an important control, much research has been carried out to describe its behaviour. Based on the experimental part of some of this research (in laboratory and field) a description of the physics of gravity-current fronts is given in this section.

Most laboratory research concerns gravity currents in flumes which are not subjected to 3-D spreading processes because these currents are confined by the parallel side walls. In figure 4.1 the frontal region of such a plane gravity-current head is sketched. If we want to describe its motion we need to consider all relevant forces and all sources of energy loss. Then the primary forces controlling the unidirectional motion of a head are pressure, gravity and friction. In the following list is described how

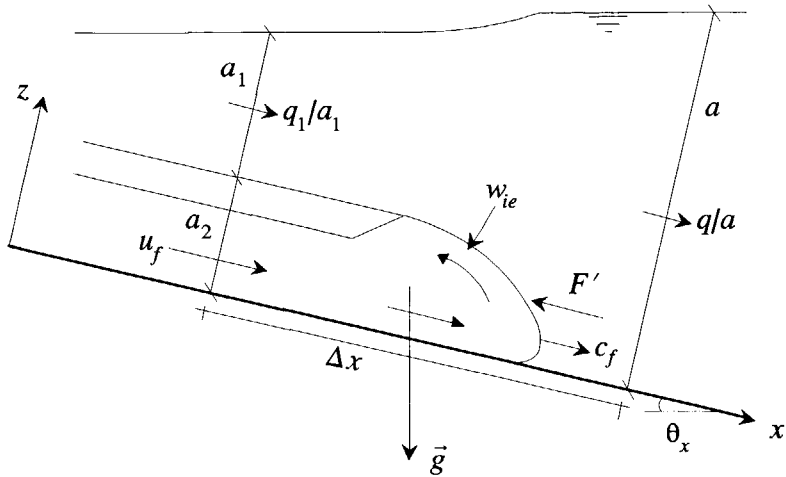


Figure 4.1 Definition sketch of a gravity current head.

these components contribute to this motion, especially if we consider conservation of momentum:

- The pressure balance of sections left and right of the head yields a net driving force. The left side pressure force is higher due to the higher density of the gravity current.
- For gravity currents on an incline an additional driving force exists from the component of the gravity force along the bed. This force tends to dominate the motion of the current at large slopes. On steeply sloping beds the gravity force component is reduced due to entrainment in the head. Britter and Linden (1980) assumed that for slopes  $\theta > 0.34^\circ$  the buoyancy force down the slope counteracts the friction force to produce a steady flow ( $u_f = \text{constant}$ ). For slopes  $\theta > 5^\circ$  the influence of bottom drag is less noticeable, but the flow velocity remains constant because the buoyancy force is now counteracted by increased entrainment (see later in this section).
- The pressure balance in combination with conservation of buoyancy flux yields an increasing front celerity  $c_f$  for decreasing submergence ratio  $a_2/a$ , i.e. a deeper reservoir (Simpson and Britter, 1979). Consequently, in reservoirs with sloping bottom and a finite submergence ratio, a downslope increase of  $c_f$  may occur.
- The wave celerities in the following gravity current are most often larger than the front velocity ( $\phi_3 > c_f$ , section 3.3). Therefore different parts (internal waves) of the current catch up with the front and overtake it, resulting in scatter in measured front velocity data. For instance in Maxworthy's (1983) experiment the front was overtaken by a solitary wave generated by varying the inflow. The dense fluid from the gravity current supplied into the head is added to the head volume together with entrained fluid. Part of the fluid is left behind in the mixing layer.

- Shape factors of velocity and density distributions influence the propagation of the head, but in theoretical analyses they are usually neglected.
- Bottom drag and interfacial friction become important if propagation processes over longer distances are considered. Interfacial friction causes shear instability at the interface (billows) and subsequent entrainment of less dense water (see later in this section). Furthermore interfacial and bottom shear increase the turbulence rate in the head region.
- The depression of the free surface above the gravity current is very small compared to effects of viscosity and interfacial instability (Benjamin, 1968).

A significant difference in propagation speed can be noticed if we compare gravity-current fronts to related fronts in open channel flow, submerged in the atmosphere (Simpson, 1987). The front velocity of a gravity current advancing into an ambient fluid with a one percent lesser density will be only of the order of one percent of the front velocity for equivalent dam-break flows in the atmosphere. The effective driving force of the intruding front is of the order of only one percent of the open-channel flow situation when considering that the main driving forces are gravitational and inertial (i.e. caused by the displacement of ambient fluid).

Benjamin (1968) showed that energy dissipation must be present near the head. Some of these energy losses may be compared with losses occurring in internal bores, or in bores and hydraulic jumps in open channel flow. Locally energy losses and entrainment are associated with the flow in the head, i.e. increased turbulence and shear generated instabilities. The instabilities generated at the head are described by Simpson & Britter (1979), Simpson (1987) and Sloff (1994) in relation to interfacial mixing processes controlled by the head.

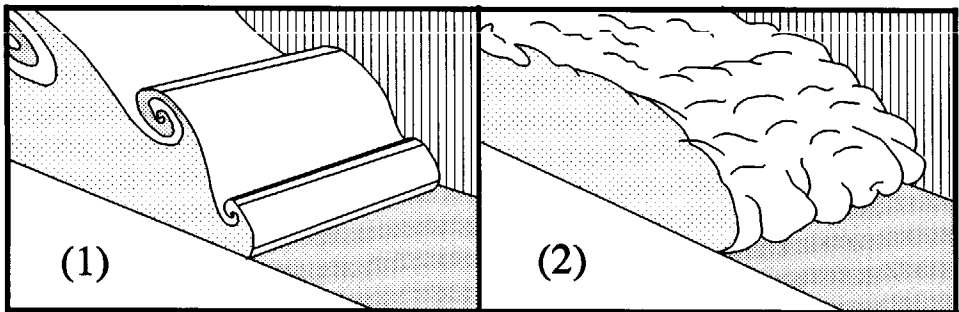


Figure 4.2 Instabilities of a gravity current head after Simpson (1987): (1) billows; (2) lobes and clefts.

The two major forms of instability at the front of a fully turbulent gravity current, which cause energy loss and entrainment, are (after Simpson, 1987, Sloff 1994):

- Billows associated to Kelvin-Helmholtz instabilities forming at the front (see

figure 4.2, part (1)).

- Gravitational instabilities in the head caused by rising less dense fluid which is overrun by the head. This type of instability only occurs due to the effect of bottom friction. It is responsible for the non-steady lobe and cleft structure illustrated in figure 4.2, part (2). The Kelvin-Helmholtz billows on the head are then broken up in a complicated 3-D form.

Beside for the gravitational instabilities, bottom friction is also important for shear related turbulence generation and associated energy losses in the gravity current (Abraham and Vreugdenhil, 1971)

Interfacial mixing due to K-H instabilities increases when the bottom slope increases. The front speed however remains constant for increasing slopes because the larger gravitational force is counterbalanced by the increased entrainment in the head and the flow behind it. Interfacial mixing cause momentum to be imparted to less dense reservoir fluid entrained into the head (Britter and Linden, 1980). Furthermore it causes (together with dense inflow from behind) a growth of the head volume and head height. Although for large slopes  $c_f$  remains constant, it has been observed that the front behaviour is extremely sensitive to the slope as it approaches the horizontal.

Not only shear related instabilities and buoyancy and gravity related forces affect the motion of the head, but also turbulence related properties of the ambient fluid can be important:

- The propagation of gravity currents in co-flowing and counter-flowing fluids is affected by the boundary structure (velocity profile) of the downstream ambient fluid. Furthermore a loss of energy in the continuous upper layer may occur in the decelerating flow just behind the head wave (Kranenburg, 1993a, Abraham and Vreugdenhil, 1971).
- Background turbulence in the ambient fluid, in the continuous layer, significantly influences the entrainment mechanism (e.g. Noh & Fernando, 1992, Simpson, 1987, and Sloff, 1994), and consequently the head height and head velocity.

Turbidity currents do not significantly differ from saline density currents if the concentration is not extremely large. However, if the sediment concentration decreases due to settlement, the motion of the head and the flow behind is affected:

- Settling of suspended sediment can decrease the buoyancy flux of the gravity current head Altinakar et al. (1990). However, the increased turbulence rate locally in the head may often prevent settling and can even cause erosion of bed sediments (Simpson, 1987). Velocities in the head are larger than the celerity of the head wave. Then settling of sediments is more likely to occur in the following gravity current body.
- Turbidity currents with coarse sediment show an increase of the height of the head wave. This is caused by conversion of kinetic energy into potential energy due to a more important loss of the buoyancy flux on a horizontal bed

(Altinakar et al., 1990).

If a gravity current is not laterally confined by side walls the current is subjected to spreading. For instance, if a turbidity current is not running through a bottom channel, e.g. the former river channel in a storage reservoir, then it will spread over the bottom as a boundary-attached plume or as a jet. Its development depends on reservoir geometry, friction, bottom slope, initial buoyancy flux, and interfacial mixing (Alavian, 1986). Buoyancy related forces drive the rate of lateral spreading, but it can be reduced by the downslope driving force.

One striking difference between plane 1-D and 2-DH (axi-symmetric) spreading gravity current in shallow reservoirs is the intensity of rotational motion, and the related mixing rate (Rottman & Simpson, 1984, Sloff, 1994). The majority of the gravity-current fluid becomes concentrated at the front in deep reservoirs or in multiple fronts in shallow reservoirs, leaving only a thin layer of heavy fluid near the ground. Plane gravity currents are more uniform in depth shortly after release. The formation of this leading edge vortex, which occupies almost the full depth of the dense fluid, is associated to the formation of Kelvin-Helmholtz vortices at the head: see figure 4.3.

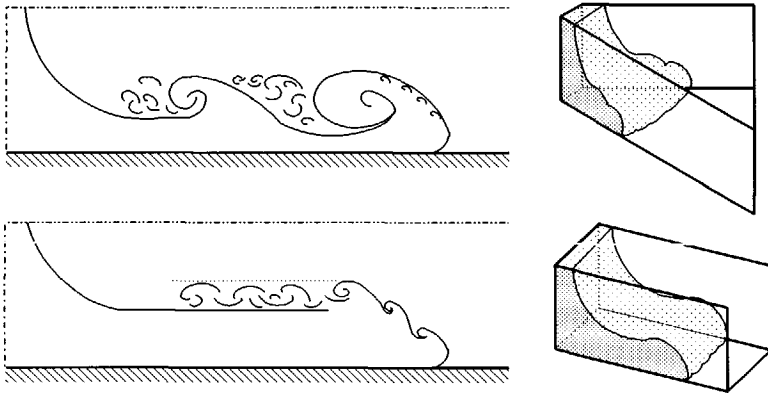


Figure 4.3 Comparison of gravity currents in a sector tank and in a prismatic channel after Rottman & Simpson (1984), Simpson (1987).

Due to conservation of angular momentum and by entrainment of fluid the intensity of the vortices is increased if they are stretched, notably near rapid expansions (e.g. near the source). An increased intensity gives an increased entrainment. This vortex formation is also reported by McClimans (1978) and Garvine (1984) for a fresh surface-current entering coastal waters.

The derivation of shock relations for these 2-DH spreading currents, and the adaptation of the mathematical model to satisfy observed behaviour, are treated in

section 4.5. These theories are conceptual as they are not calibrated and verified yet. The actual difference in the plume shape of 1-D and 2-DH currents due to the frontal condition is discussed in the following chapter, illustrating causes and effects of the increased mixing rate and the raised edge of the plume.

In the following sections a theoretical model is presented which can be applied to simulate the front within our 2-layer model.

### **4.3 Theoretical considerations on shock relations for front-propagation in a one-dimensional 2-layer flow.**

In the introduction to this chapter is explained that two approaches in treating gravity-current fronts are possible. Considering the front as the mathematical solution of a developing two-layer flow, or considering it as a dissipating edge of a steady-state current are usually not compatible. The only way to match the latter approach to the former is by taking the steady-state formula as a local internal boundary condition to the two-layer flow.

Internal bores, fronts and hydraulic jumps may be considered as discontinuous solutions of the two-layer flow which is described by the coupled system of basic equations. In the principle part of the reservoir the system is conservative with respect to mass, momentum, energy and entropy. However, locally at the jump the established assumption is that only mass and momentum are conserved. The latter follows from the Second Law of Thermodynamics (nature always proceeds to a less ordered situation). At a discontinuity mechanical energy is lost into turbulent motion, but this process is irreversible and entropy is increased by an increase in random molecular motions. It is supposed that at a discontinuity, such as a hydraulic jump, energy is lost to just the extent that is needed to satisfy the laws of conservation of mass and momentum.

In general the discontinuities can be expressed by shock relations. Considering the coupled 2-layer model, where the barotropic and baroclinic computation is not decoupled, locally at a discontinuity the basic equations (based on hydrostatic pressure) do not hold. Therefore discontinuities can be considered as internal boundaries, where shock relations can be considered as internal boundary conditions. These relations can either be obtained directly from the chosen set of equations (as will be shown later) or they can be obtained from the steady-state theory. In chapter 5 is shown that developing gravity currents exhibit a self-similar behaviour with steadily propagating fronts, justifying the application of steady-state theory.

Most of the existing steady-state theories for gravity-current fronts are based on

Benjamin's (1968) inviscid-fluid theory, i.e. viscous forces are assumed to be completely absent. The frictional effect of ground and interface disappears but instability, which leads to formation of billows, still remains provided that Reynolds numbers are large. Benjamin's model was developed for ideal fluids, notably for a cavity flow, which is an air intrusion in a long closed water-filled channel. The equations for conservation of momentum and volume through the transition are formulated in a frame of reference moving with the front. Furthermore energy conservation along a streamline is formulated (Bernoulli's equation) for streamlines passing through the stagnation point (or nose) of the current. For steady energy-conserving flows (energy loss=0) the advancing layer fills half the channel ( $a_2/a=0.5$ ). This is the singular loss-free solution of the model. In practical situations the front is lower due to energy dissipation and entropy limitations ( $a_2/a < 0.5$ ). Benjamin's theory has been extended by many researchers for the real fluid effects which are described in section 4.2, which for instance affect the propagation of a front at the bottom.

The primary differences in models based on Benjamin's theory occur in the parametrization of these real fluid effects and of the energy dissipation. They were all developed to eliminate the discrepancies between predicted and observed front celerities and to generalize Benjamin's approach. For instance the introduction of the nose elevation above the bottom by Simpson and Britter (1979) yielded slower propagation speeds  $c_f$ . Also Kranenburg (1978) predicted a decrease of  $c_f$  by introducing an energy loss coefficient for dissipation in the head. The parametrizations used are all empirical and calibration and verification is inevitable. It should be remarked that discrepancies between predicted and observed fronts are not all due to defects in Benjamin's model but also the definition of depths, densities and front celerities from measurements to verify the formula are highly inconsistent in literature. Klemp et al. (1994) demonstrated that not the uncertainty in the front conditions is responsible for these variations, but that other effects, such as interfacial mixing and friction in the following underflow explain them.

Although this kind of models seems to yield promising results, they have not been applied thoroughly for spreading turbidity currents with intense vortex development. The direct application of the results of these theories in two-layer numerical models requires the application of difficult shock-fitting techniques or moving boundaries with previously defined conditions (e.g. see Bonnetcaze et. al., 1993).

An alternative approach to steady-state formulas can be obtained directly from the basic equations for the continuous two-layer model. The underlying idea is that the integral conservation law must still be satisfied at a discontinuity. Therefore a more general integral relation can be deduced for which its solution is called a weak solution (e.g. see Lax, 1954, or Abbott, 1975), and which does not require differentiability. In the following is described how discontinuities occur and how weak solutions result into appropriate shock relations. Initially we consider discontinuous solutions in 1-D



2-layer flow which provides us with an essential foundation for computing discontinuities in 2-DH flow.

It can be shown that weak solutions of conservation laws are not necessarily unique. to choose the physically relevant solution it is necessary to impose an additional condition. Mathematically this condition can be derived from the requirement that a shock must have characteristics going into it. In figure 4.4 three types of possible weak solutions are plotted originating from an initial state with a discontinuity separating two constant states.

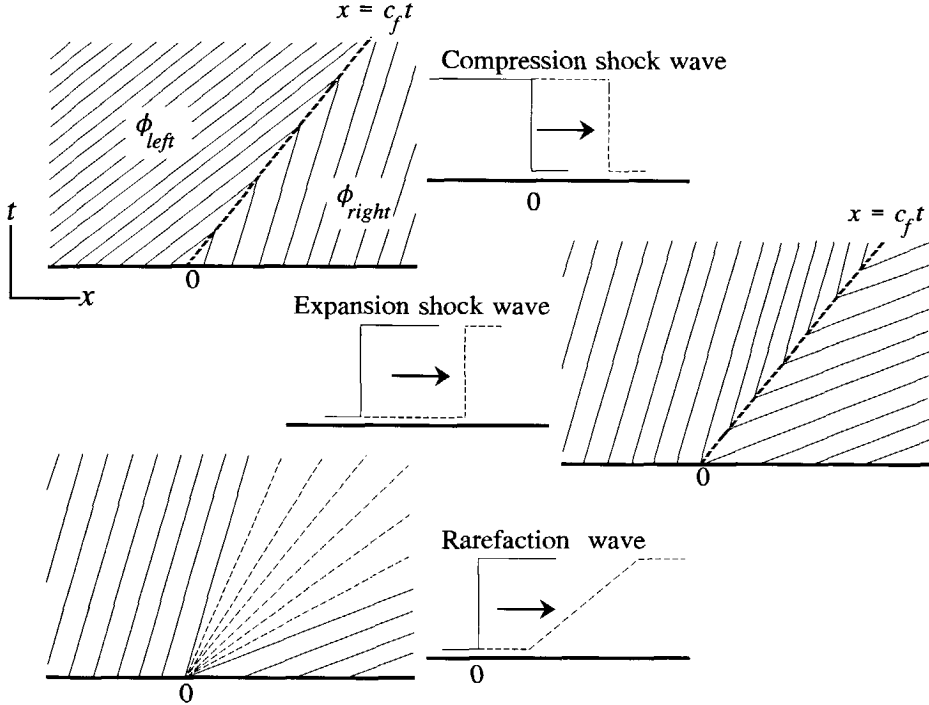


Figure 4.4 Upper and lower plot: entropy satisfying shocks; Middle plot: entropy violating shock (unstable shock).

The upper plot shows the unique weak solution in which characteristics from both sides enter the shock as time advances. In analogy with gasdynamics this is usually called a compression shock (compression of gas molecules). The middle plot is a physically incorrect one, and mathematically it represents a non-unique solution (in fact there are infinite solutions). As the characteristics go out of this expansion shock the solution is unstable to perturbations. For this shock it can be shown that the entropy condition is violated, the shock changes to a rarefaction wave by adding a little (physical) viscosity. The latter type of wave, also called a centred simple wave, is physically admissible and unique. Due to the fanning out of the characteristics the

initial discontinuity is smeared and satisfies entropy. The arguments above with respect to physically admissible shocks can be summarized in a type of mathematical 'entropy' condition (Lax, 1957, Courant and Hilbert, 1962, Le Veque, 1990). For 1-D models and a shock moving in  $x$ -direction from left to right we can write this criterion as:

$$\phi_{1, \text{left}} \geq c_f \geq \phi_{1, \text{right}} \quad (4.1)$$

where  $\phi_1 = dx/dt$  is the positive characteristic celerity of the continuous flow on left and right side of the shock respectively, and where  $c_f$  is the celerity of the front. Clearly this condition can also be used to judge whether a shock is stable. Kranenburg (1978) showed that the stability of the front requires the two-layer flow behind the front to be internally subcritical or critical at most within a frame of reference moving with the front. Effectively it reduces the maximum admissible front height to about  $0.35a$  which is consistent with the observations.

Now consider the two alternative systems of coupled 1-D Boussinesq equations (after width integration) for a 2-layer flow on a fixed-bed ( $z_b = \text{const.}$ ) as presented in section 2.2. The original system in  $q, a$  form obtained from momentum conservation is called **system QA**. The system in  $u, a$  form obtained from combination of the mass and momentum equations of system QA is called **system UA** (see also sub-section 2.2.3 for decoupled equations). Both systems give identical solutions in continuous flows. The gravity current is assumed to be propagating in a smooth prismatic channel ( $\partial z_b / \partial x \approx 0$  relative to the average bottom slope) with quiescent ambient fluid, with constant and low sediment concentrations, and with a prismatic cross section.

Due to the presence of friction forces, entrainment, horizontal gravity forces and residual pressure forces (e.g.  $g_2 a_1 \partial a_2 / \partial x$  and  $g_2 a_2 \partial a_1 / \partial x$ ) both systems cannot be written in conservation form. However, if we consider the piece-wise continuous solution of the system in a physically small region at the shock (i.e. the support of the discontinuity), it is usually assumed that these force terms may be neglected or averaged over the shock. Under these assumptions the system of equations reduces into the following semi-conservation form (which is called semi-conservative since quantity  $\mathbf{U}$  is not fully conserved due to the presence of a source term  $\mathbf{Q}_R$  containing force and entrainment terms):

$$\frac{\partial \mathbf{U}}{\partial t} + \frac{\partial \mathbf{f}(\mathbf{U})}{\partial x} = \mathbf{Q}_R \quad (4.2)$$

where  $\mathbf{U} = (q_1, a_1, q_2, a_2)$  or  $\mathbf{U} = (u_1, a_1, u_2, a_2)$  and  $\mathbf{f}(\mathbf{U}) =$  momentum and mass fluxes.

If we now consider the support of the discontinuity, which we may assume to be restricted to the limit to a single point, the physical situation can be described by the weak solution of eq. (4.2) which is defined as (from the integral conservation law)

$$\int_0^{\infty} \int_{-\infty}^{\infty} \left[ \frac{\partial \mathbf{U}}{\partial t} + \frac{\partial \mathbf{f}(\mathbf{U})}{\partial x} - \mathbf{Q}_R \right] \mathbf{w} \, dx dt = 0 \quad (4.3)$$

or after integration by parts

$$\int_0^{\infty} \int_{-\infty}^{\infty} \left[ \mathbf{U} \frac{\partial \mathbf{w}}{\partial t} + \mathbf{f}(\mathbf{U}) \frac{\partial \mathbf{w}}{\partial x} + \mathbf{w} \mathbf{Q}_R \right] dx dt + \int_{-\infty}^{\infty} \mathbf{w}(0, x) \mathbf{U}_0(x) \, dx = 0 \quad (4.4)$$

where  $\mathbf{w}(t, x)$  is a test function which tends rapidly to zero as  $|x| + t$  increases (the support of  $\mathbf{w}$ , outside which  $\mathbf{w} = 0$ , covers a neighbourhood of the discontinuity in the  $t, x$ -plane), and where  $\mathbf{U}_0 = \mathbf{U}(0, x)$  is the initial value of  $\mathbf{U}$ . Integrate over the two subdomains (left and right) of the support of  $\mathbf{w}$ , which are separated by the discontinuity curve in the  $t, x$ -plane. Subtraction of these two integrals with  $\mathbf{Q}_R = 0$  gives (e.g. see Abbott, 1975)

$$c_f [\mathbf{U}_{left} - \mathbf{U}_{right}] = [\mathbf{f}_{left} - \mathbf{f}_{right}] \quad \Leftrightarrow \quad c_f [\mathbf{U}_l - \mathbf{U}_r] = [\mathbf{f}_l - \mathbf{f}_r] \quad (4.5)$$

where  $\mathbf{U}_l$  and  $\mathbf{U}_r$  are the solutions on the respective subdomains, and  $c_f = dx_f/dt$  is the propagation speed of the discontinuity in  $x$ -direction. This eq.(4.5) is the *Rankine-Hugoniot jump condition*. It has to be satisfied for the solutions  $\mathbf{U}_l$  and  $\mathbf{U}_r$  to constitute a weak solution.

Elaboration of this theory for either of the two systems *UA* and *QA* shows that their weak solution and jump conditions are different. Lax (1954) already noticed that this non-uniqueness is not paradoxical but a consequence of the nonlinear transformation which is used to derive system *UA* from system *QA*. Derivation of one system from the other requires manipulating derivatives in a manner that is valid only when  $\mathbf{U}$  is smooth. The selection of a meaningful weak solution, and hence a meaningful system of basic equations, can only be based on physical considerations. From the classical theories on hydraulic jumps and bores in open-channel flow it can be easily shown that for this type of flow the only genuine weak solutions are those which follow from basic equations in the form of system *QA*, governing momentum and mass conservation (e.g. Abbott, 1979). In line with these classical ideas a major part of this study is carried out after an early rejection of system *UA*. Although the results with respect to internal bores seemed meaningful, it appeared to give a poor representation of a real front. This effect is also known in dam-break models (e.g., Stoker, 1957) for which the leading front approaches zero depth and propagates with a speed which is about twice the observed one. Initially this was corrected by introducing an additional force to the basic equations but later it was found that these problems could be tackled much simpler by using system *UA*. Both of these equally important approaches are treated in the following section.

#### 4.4 Shock relations for front-propagation in a one-dimensional 2-layer flow.

For numerical computation of a gravity-current front by means of a shock-capturing technique it is most convenient to consider the front as an internal bore with very small finite depth and discharge in the downstream lower layer. In figure 4.5 a schematic representation of a front or bore moving with speed  $c_f$  at the bed is given, in which all relevant parameters are summarized. The discharge of the undisturbed ambient flow is  $q_{1r}$  and its depth  $a_{1r}$ . Before arrival of the bore the lower layer is assumed to have a small finite depth  $a_{2r}$ , discharge  $q_{2r}$  and concentration  $C_{sr}$ . Clearly this formulation allows also for regular internal bores.

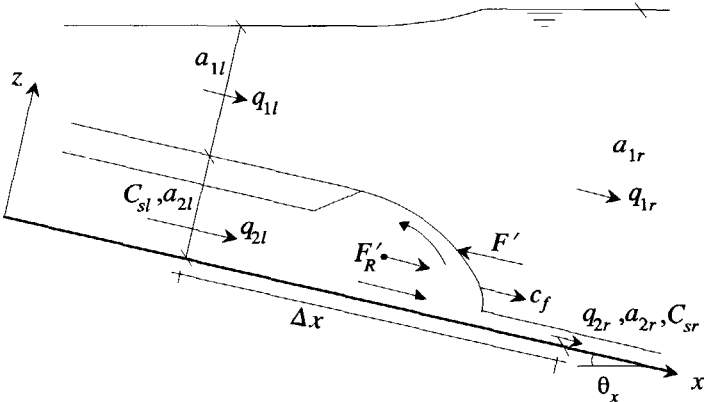


Figure 4.5 Schematic representation of the computation of a front at the bottom

Locally near the shock we neglect external forces acting in the overall (barotropic/external) flow, such as bottom friction and net gravity forces. Also local entrainment is neglected. This is required to obtain conservation of mass and momentum. It implies that eventual internal mass- and momentum-sink/source terms of the baroclinic flow are balanced by both layers (e.g. forces acting on the interface). Initially we got round the necessity of the latter assumption by collecting external forces into a small force  $F_R$  resisting the underflow. It may be cancelled to obtain momentum conservation of the barotropic system afterwards. The local internal / baroclinic forces, balanced by both layers, are collected and called  $F'$  also resisting the underflow.

Now we can write shock relations as the four Rankine-Hugoniot conditions (eq. 4.5) for the weak solutions of the four basic differential equations in (semi-) conservative form. Therefore  $\mathbf{Q}_R$  in eq. (4.2) is composed of forces  $F'$  and  $F_R$ . The baroclinic force  $F'$  disappears by adding the momentum equations. In this derivation we consider  $q_{1l}$ ,  $a_{1l}$ ,  $q_{2l}$ , force  $F'$  and the front celerity  $c_f$  to be unknown. Others are known, for

instance determined by the characteristics directed towards the shock. With five unknowns, a system of five equations is required to close the problem. Following Benjamin (1968) the fifth equation may be Bernoulli's equation along the streamlines over  $\Delta x$  close to the bottom. This approach has been used also by Kranenburg (1978, 1993a), to account for energy losses in a front on a horizontal channel. For further elaboration of equations we use their results to determine the unknown force  $F'$ .

In line Kranenburg's analysis the following transformations of variables can be applied ( $i=1,2$ , and  $a$  is the total depth of the undisturbed reservoir:  $a=a_{1l}+a_{2r}$ ):

$$\bar{c} = \frac{c_f}{\sqrt{g'_z a}} \quad ; \quad \bar{q}_{il,r} = \frac{q_{il,r}}{a \sqrt{g'_z a}} \quad ; \quad \bar{u}_{il,r} = \frac{u_{il,r}}{\sqrt{g'_z a}} \quad ; \quad \bar{F} = \frac{F'}{g'_z a^2}$$

$$\bar{a}_f = \frac{a_{2l}}{a} \quad ; \quad \alpha_r = \frac{a_{2r}}{a} \quad ; \quad \bar{a}_{1l} = \frac{a_{1l}}{a} \quad ; \quad r = \sigma' C_s$$

By taking  $g' = g\sigma' C_s$  we assumed a constant concentration. This does not affect the results if the part of the lower layer right of the bore disappears when dealing with a front at the bed. After substitution of these dimensionless parameters, and after eliminating  $q_{1l}$  and  $q_{2l}$  in system  $QA$  and  $u_{1l}$  and  $u_{2l}$  in system  $UA$  (by substituting mass equations into momentum equations) the following shock-relations remain:

- For system  $QA$ :

$$\begin{aligned} & \sigma' C_s [\bar{c}(1-\alpha_r) - \bar{q}_{1r}]^2 (1-\bar{a}_{1l}-\alpha_r) + \\ & - (1-\alpha_r) \left[ \frac{1}{2} \bar{a}_{1l} (1+\bar{a}_{1l}-\alpha_r) (1-\bar{a}_{1l}-\bar{a}_f) - \bar{a}_{1l} \sigma' C_s \bar{F} \right] = 0 \end{aligned} \quad (4.6)$$

$$\begin{aligned} & \sigma' C_s (\bar{a}_f - \alpha_r) \left[ 2(\bar{c}\alpha_r - \bar{q}_{2r})^2 - \bar{a}_f \alpha_r (\bar{a}_f + \alpha_r) \right] - \bar{a}_f \bar{a}_{1l} \alpha_r (\bar{a}_f + \alpha_r) + \\ & + 2\bar{a}_f \alpha_r \sigma' C_s (\bar{F} + \bar{F}_R) + \bar{a}_f \alpha_r (\bar{a}_f + \alpha_r) (1-\bar{a}_f) = 0 \end{aligned} \quad (4.7)$$

- For system  $UA$ :

$$\begin{aligned} & \sigma' C_s (\bar{c} - \bar{u}_{1r})^2 (1-\bar{a}_{1l}-\alpha_r) (1+\bar{a}_{1l}-\alpha_r) + \\ & + 2\bar{a}_{1l}^2 \sigma' C_s \bar{F} a - 2\bar{a}_{1l}^2 (1-\bar{a}_f - \bar{a}_{1l}) = 0 \end{aligned} \quad (4.8)$$

$$\begin{aligned} & \sigma' C_s (\bar{a}_f - \alpha_r) \left[ (\bar{c} - \bar{u}_{2r})^2 (\bar{a}_f + \alpha_r) - 2\bar{a}_f^2 \right] + 2\bar{a}_f^2 (1-\bar{a}_f) + \\ & + 2\bar{a}_f^2 \sigma' C_s (\bar{F} + \bar{F}_R) - 2\bar{a}_{1l} \bar{a}_f^2 = 0 \end{aligned} \quad (4.9)$$

Equations (4.7) and (4.9) can be used to eliminate  $\bar{a}_{1l}$  from equation (4.6) and equation (4.8) respectively. Then for each system one equation remains with two unknowns:  $\bar{c}$  and  $\bar{F}$ ;  $\bar{a}_r$ ,  $\alpha_r$ ,  $q_{2r}$ ,  $u_{2r}$ ,  $q_{1r}$ ,  $u_{1r}$  and  $\bar{F}_R$  are the dependent variables. For a decoupled system the shock-relations for the baroclinic flow are identical to the equations presented above if  $C_s \ll 1$ .

The rejection of either system *QA* or *UA* can be well reasoned by comparing these shock relations to experimental data. In the following this exercise is carried out for internal hydraulic jumps, internal bores, and real gravity-current fronts. For a steady internal hydraulic jump in a very deep reservoir ( $\bar{c}=0$ ;  $\bar{F}=0$ ;  $\bar{F}_R=0$ ;  $a \rightarrow \infty$ ; and small  $C_s$ ) the shock relation for *system QA* reduces to:

$$\frac{a_{2r}}{a_{2l}} = \frac{1}{2} \left[ \sqrt{1 + 8 Fr_{Dl}^2} - 1 \right] \quad (4.10)$$

and for *system UA*:

$$\frac{a_{2r}}{a_{2l}} = \frac{1}{4} \cdot Fr_{Dl} \left[ \sqrt{8 + Fr_{Dl}^2} + Fr_{Dl} \right] \quad (4.11)$$

A densimetric Froude number  $Fr_{Dl}$  is defined as  $u_{2l} / \sqrt{(\sigma' C_s g a_{2l})} > 1$ .

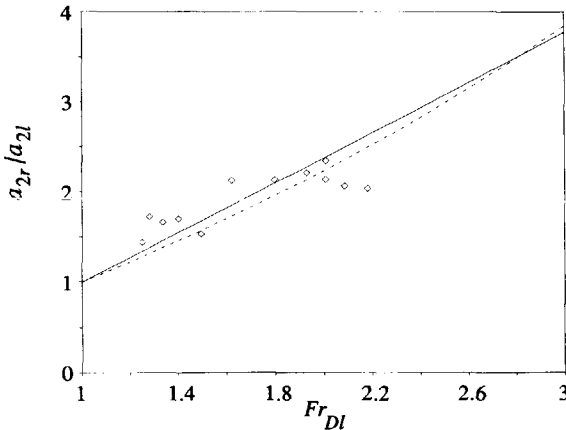


Figure 4.6 Depth ratio  $a_{2r}/a_{2l}$  for a steady internal hydraulic jump; drawn line: eq. (4.10); dashed line: eq.(4.11); diamonds: Garcia's (1993) measurements.

Eq. (4.11) shows a discrepancy with eq. (4.10), especially at large values of  $Fr_{Dl}$ . Plots of these equations for  $Fr_{Dl}$  less than 3 are given in figure 4.6. This figure shows that eq. (4.10), which is the classical hydraulic jump relation, does not favour eq. (4.11) if compared to Garcia's (1993) experiments.

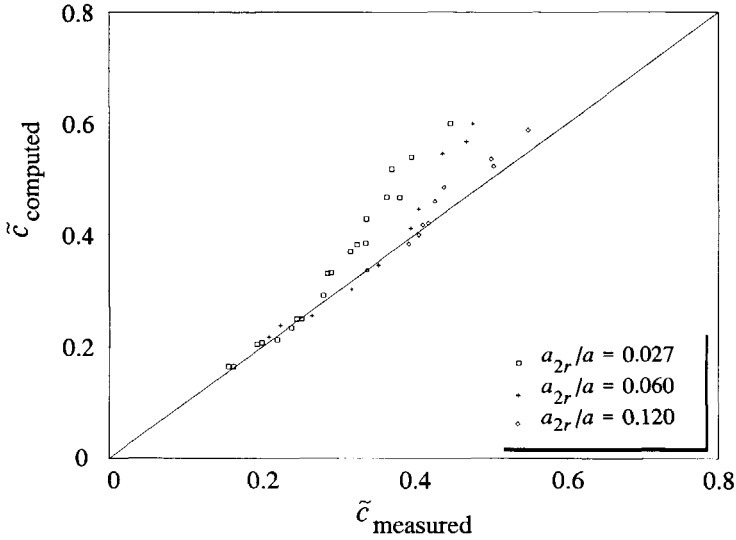


Figure 4.7 Internal bore: experiments versus theory: *system QA*; eq.(4.10).

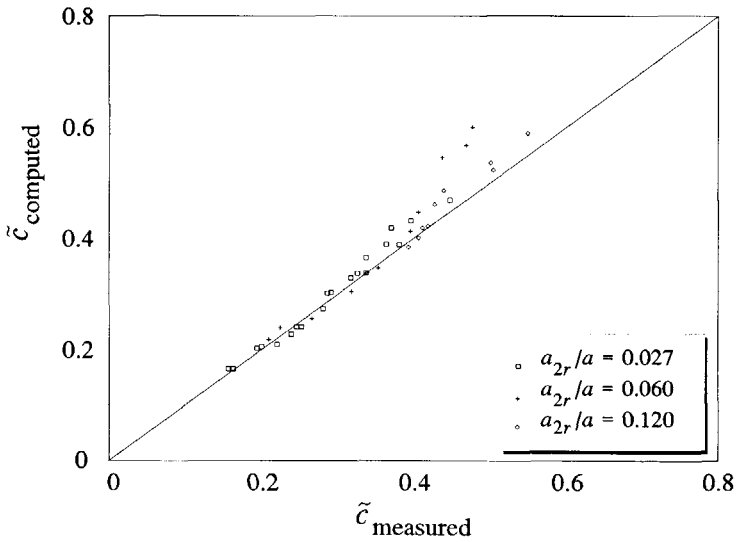


Figure 4.8 Internal bore: experiments versus theory: *system UA*; eq.(4.11).

A more obvious difference can be obtained from comparison of computed and measured celerities of internal bores. In figure 4.7 and 4.8 the theoretical  $\tilde{c}$  values from eq. (4.10) and (4.11) respectively, with  $\tilde{F} = \tilde{F}_R = 0$ , are compared to experimental values from Wood & Simpson (1984) for internal bores in 2-layer miscible fluids. A close look to both figures demonstrates the superiority of *system UA* (eq. 4.11),

although at higher values of  $\bar{c}$  the computations still overestimate the measured results. Wood and Simpson showed that those experiments are characterized by more intensive mixing and related energy losses, compared to those with a lower value of  $\bar{c}$ .

The most striking evidence for the superiority of using system *UA* for computing internal fronts in 2-layer flows, can be obtained from real fronts. Taking  $\alpha_r=0; q_{2r}=0; \bar{F}_R=0$  and  $C_s \ll 1$ , eq. (4.6) and eq. (4.7) reduce to

$$(\bar{c} - \bar{q}_{1r})^2 + 2\bar{F} \frac{(1 - \bar{a}_f)}{\bar{a}_f^2} - \frac{1}{2}(2 - \bar{a}_f)(1 - \bar{a}_f) = 0 \quad (4.12)$$

while eq.(4.8) and eq.(4.9) reduce to

$$\left( \frac{1}{1 - \bar{a}_f} \right)^2 (\bar{c} - \bar{u}_{1r})^2 + 2\bar{u}_{1r}(\bar{c} - \bar{u}_{1r}) + 4\bar{F} + \bar{u}_{1r}^2 - 2\bar{a}_f = 0 \quad (4.13)$$

Note that for this situation  $\bar{q}_{1r}$  equals  $\bar{u}_{1r}$ , since  $a_{1r}=a$  and  $u_{1r}=q_{1r}/a_{1r}$ .

Kranenburg (1993a) showed and verified, starting from conservation equations for mass and momentum for a control volume, and Bernoulli's theorem along the stream line, how the front velocity can be expressed as above corrected with an empirical energy-loss coefficient  $k$ . Therefore he considered a coordinate system moving along with the front. Kranenburg's relation can be written as

$$\left( \frac{1 + \bar{a}_f}{1 - \bar{a}_f} + k \right) (\bar{c} - \bar{q}_{1r})^2 + (1 + k)\bar{q}_{1r}(\bar{c} - \bar{q}_{1r}) - \bar{a}_f(2 - \bar{a}_f) = 0 \quad (4.14)$$

Originally the coefficient  $k$  was introduced by Kranenburg (1978) and was found approximately equal to zero for surface currents, and 0.6 for bottom currents. Furthermore Kranenburg showed, demanding that energy-loss in the upper layer is non-negative and applying eq. (4.1) respectively, that the following two restrictive conditions should be added:

$$\bar{c} - \bar{q} \leq 1 - \bar{a}_f \quad (4.15)$$

$$\bar{c} - \bar{q} \leq (1 - \bar{a}_f)^{3/2} \quad (4.16)$$

The front is unsteady and will flatten if the latter condition, which is more restrictive than the former, is not satisfied.

Figure 4.9 with stagnant ambient fluid  $\bar{q}_{1r}=\bar{u}_{1r}=0$  and  $k=0.6$  shows the behaviour of the presented relations, e.g., for a lock-exchange flow. In this figure some



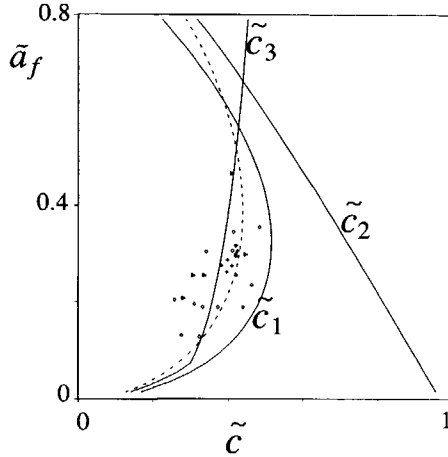


Figure 4.9 Front-celerities for system UA:  $\tilde{c}_1$ ; system QA:  $\tilde{c}_2$ ; Kranenburg (1978) with  $k=0.6$ : dashed line; Huppert & Simpson (1980):  $\tilde{c}_3$ .

experimental data are plotted from Altinakar et al. (1990), Abraham & Vreugdenhil (1971) and Bühler et al. (1991) for comparison. Also the often cited empirical steady-state relations proposed by Huppert and Simpson (1980) are plotted. In terms of parameters  $\tilde{a}_f$  and  $\tilde{c}$  these relations are

$$\begin{aligned} \tilde{c} &= 1.19 \sqrt{\tilde{a}_f} & \text{if } 0 \leq \tilde{a}_f \leq 0.075 \\ \tilde{c} &= 0.5 \cdot (\tilde{a}_f^{-1/3}) \sqrt{\tilde{a}_f} & \text{if } 0.075 < \tilde{a}_f \leq 1 \end{aligned} \quad (4.17)$$

Figure 4.9 clearly illustrates the superiority of *system UA* over *QA*. Actually it can be shown easily that a front, computed with *system QA*, which satisfies restrictive conditions (4.15) and (4.16), can only exist if its height is zero. This corresponds to the theoretical (non-physical) height of a dam-break wave on a dry bed treated by Stoker (1957).

For  $k=0$  and  $\bar{q}_{1r}=0$  Kranenburg's equation (4.4) reduces exactly to Benjamin's (1968) formula. A comparison of this relation with the *UA* relation in figure 4.10 shows that the latter performs remarkably well, especially when recalling the verification of Benjamin's equation by Klemp et al. (1994). Note that the experimental data in this plot indeed satisfy the restrictive condition (4.16).

The celerities from *system UA* seem still systematically too large, but adequate for practical applications, especially if the effect of bottom friction and entrainment is added to the model which is shown later in this thesis. Even if the original ambient fluid is flowing moderately, the results of *system UA* are still satisfactory. This is illustrated in figure 4.11 for an ambient co-flow with  $\bar{q}=\bar{q}_{1r}$ , comparing Kranenburg's

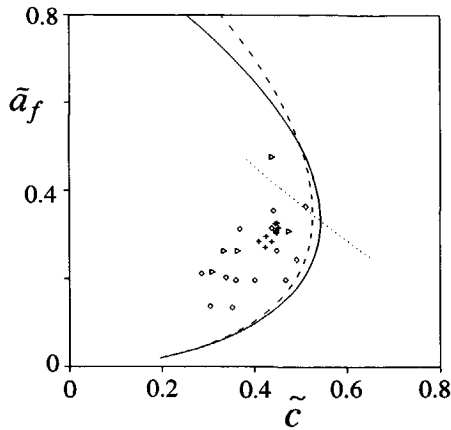


Figure 4.10 Front-celerities for system UA: drawn line; Benjamin (1968) : dashed line. Symbols represent experimental data, dotted line is eq. (4.16).

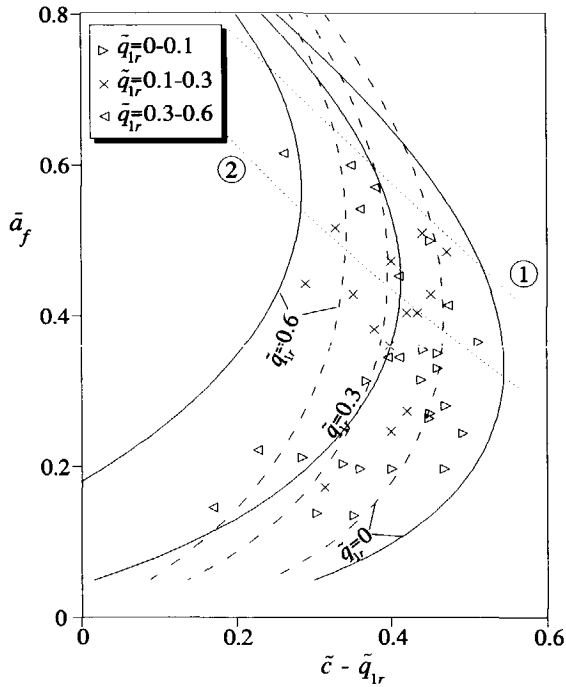


Figure 4.11 Front-celerities in ambient flow. System UA: drawn lines, Kranenburg (1993a): dashed lines; eq.(4.15): line 1; eq.(4.16): line 2.

result (eq. 4.14) to system UA (eq. 4.13) and data published by Bühler et al. (1991) and Abraham & Vreugdenhil (1971).

Rejection of system  $QA$  obviously implies that at a gravity-current front momentum is not conserved. Momentum and energy is lost by friction and entrainment of upper-layer fluid, as described in section 4.2, to such an extent that velocity is conserved. This is shown in experiments (e.g. Britter and Linden, 1980) where, even at large bottom slopes, the front celerity  $c_f$  remains practically constant due to the action of mixing. In shallow water the velocity difference  $u_2 - u_1$  is conserved which agrees with the observed dependence of front celerities on the relative depth  $a_2/a$ .

Although these examples give sufficient argument to choose for system  $UA$ , an attempt was made to extend system  $QA$  such that it would resolve into the correct shock relation for a gravity current at the bed ( $\alpha_r=0$ ). This attempt originated after a preliminary rejection of system  $UA$  on basis of the classical shock theories as mentioned before. Instead of taking  $\tilde{F}=0$  in the shock relations (as we did above), a relation for this unknown force (to enable momentum loss) is found by using Kranenburg's (1993a) relation for closure: eliminate  $\tilde{c}$  from eq. (4.12) using eq. (4.14) to describe  $\tilde{F}$  as a function of  $\tilde{a}_f$ ,  $\tilde{q}_{1r}$  and  $k$ . A very simple (approximate) result can be derived if  $\tilde{q}_{1r} = 0$ :

$$\tilde{F}_{\tilde{q}_{1r}=0} \approx \frac{1}{4} \tilde{a}_f (1+k) \tilde{c}^2 \approx \frac{1}{4} \tilde{a}_f^2 \left[ \frac{(1+k)(2-\tilde{a}_f)(1-\tilde{a}_f)}{1+\tilde{a}_f+k(1-\tilde{a}_f)} \right] \quad (4.18)$$

If  $\tilde{q}_{1r} \neq 0$  the following approximate result can be derived

$$\tilde{F}_{\tilde{q}_{1r} \neq 0} \approx \frac{1}{2} \tilde{a}_f^2 \left[ \frac{2(\tilde{c}-\tilde{q}_{1r})^2 - (1-\tilde{a}_f)(2-\tilde{a}_f)}{2\sigma' C_s (\tilde{c}-\tilde{q}_{1r})^2 + 3\sigma' C_s \tilde{a}_f (2-\tilde{a}_f) - 2(1-\tilde{a}_f)} \right] \quad (4.19)$$

where  $\tilde{c}-\tilde{q}_{1r}$  follows from eq. (4.14). These equations for  $\tilde{F}$  are slightly different if the front is computed as an internal bore with a finite depth of the lower layer downstream of the front. For computing a gravity-current front as an internal bore the resisting force if  $\tilde{q}_{1r}=0$  can be written as

$$\tilde{F}_{\tilde{q}_{1r}=0} = (\tilde{a}_f - \alpha_r) \left[ \frac{1}{2} (\tilde{a}_f + \alpha_r) - \frac{(2-\tilde{a}_f)(\tilde{a}_f^2 - 2\tilde{a}_f\alpha_r + \alpha_r(2-\alpha_r))}{(2-\tilde{a}_f-\alpha_r)[k(1-\tilde{a}_f) + 1 + \tilde{a}_f]} \right] \quad (4.20)$$

The variation of  $\tilde{F}$  with  $\tilde{a}_f$ ,  $k$  and  $\tilde{q}_{1r}$  from eq.(4.19) is plotted in figure 4.12. In this figure also the restrictive conditions to  $\tilde{a}_f$  are plotted expressed by eq. (4.15) and eq. (4.16). Clearly (figure 4.12) the value of  $\tilde{F}$  (opposing the frontal motion) increases as the ambient co-flow increases, tempering the frontal motion by an increased energy loss in the ambient flow layer. On the other hand an ambient counterflow decreases this value. Also differences between the figures for  $k=0$  (surface current) and  $k=0.6$  (bottom current) are evident. The increased losses in the bottom current result in a

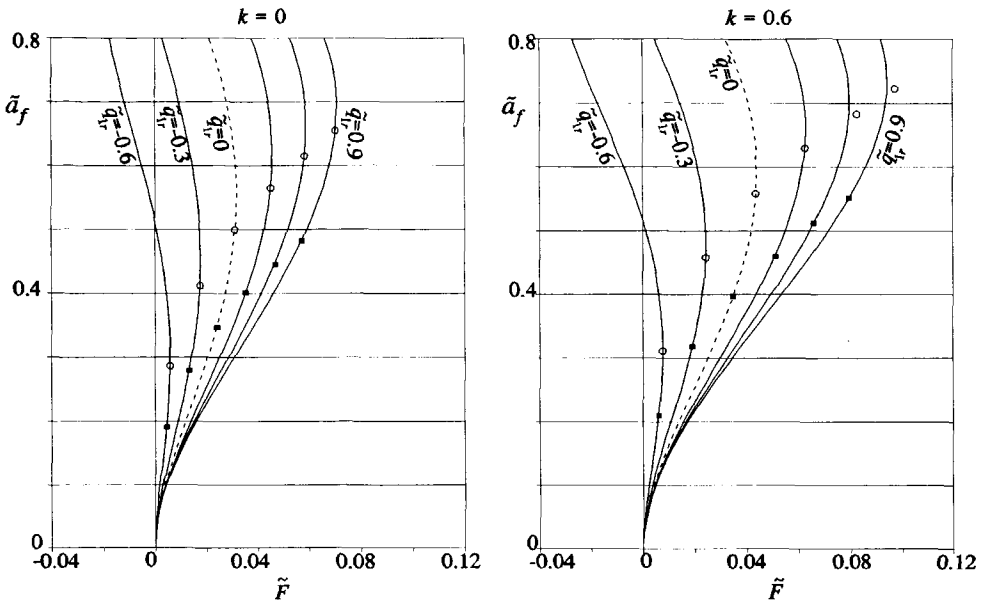


Figure 4.12 Variation of  $\tilde{F}$  with  $\tilde{a}_f$  and  $\tilde{q}$  for  $k=0$  and  $k=0.6$ ;  $\circ$  = condition (4.15);  $\blacksquare$  = condition (4.16).

larger resisting force  $\tilde{F}$  and a higher admissible front height.

In this section we have formulated the shock relations for a 1-D fixed-bed two-layer model. It is shown that the formulation of the system of basic equations in terms of  $u$  and  $a$  (system  $UA$ ) can be used to compute discontinuities in the internal flow. If the system is formulated in terms of  $q$  and  $a$  (system  $QA$ ) a resisting force should be added locally near the front to enable momentum loss. For coupled as well as decoupled models the derived relations are identical provided that  $C_s \ll 1$ . The actual error in front celerity using the decoupled model is of the order of 1 % depending on  $g' = g\sigma' C_s$  (deduced by comparing numerical results of equations 4.8 and 4.9 to equation 4.13). This is a logical consequence of the insignificance of the local surface depression for the behaviour of the baroclinic flow. In general gravity-current fronts are found to be velocity conserving such that balance of forces on the head (which cause momentum and energy losses) allow for constant front celerities.

#### 4.5 Conceptual model for 2-DH front propagation.

The results from the 1-D model can be extended to 2-DH fronts considering that only quantities normal to the front suffer a jump, while in tangential direction all quantities

remain continuous. In a radial (axi-symmetric) flow situation on a horizontal bed a simple transformation of the 2-DH flow equations to a 1-D model the previously defined shock relations can be applied without modification. For instance chapter 5 (section 5.3) this approach is followed to define an analytical model for axi-symmetric plumes. However, in more complex 2-DH flow situations the 1-D shock relations have to be adopted to model some typical 2-DH physical processes. In this section a conceptual model is derived to add some additional information to shock relations which are based on  $q, a$  basic equations (system  $QA$ ) for conservation of mass and momentum.

In appendix A the shock relations are derived from the Rankine-Hugoniot condition for the 2-DH baroclinic basic equations. By means of a coordinate transformation of the basic equations to coordinates  $s, n$  respectively tangential and normal to the front these Rankine-Hugoniot conditions reduce to an equivalent 1-D formulation with only one celerity  $c_f$  of the front in the normal ( $n$ ) direction:

$$c_f(\mathbf{W}'_l - \mathbf{W}'_r) = (\mathbf{H}'_l - \mathbf{H}'_r) - F'' \quad (4.21)$$

where  $\mathbf{W}'$  is the vector of dependent variables and  $\mathbf{H}'$  is the (discontinuous) flux vector in  $n$  direction. Besides the regular forces such as friction and gravity, the force vector  $F''$  also contains the continuous tangential flux vector  $\partial \mathbf{G}' / \partial x$ . Again we neglected the effect of these force terms compared to the strong discontinuous terms in the equations.

At the foremost point of the advancing plume the shock relation in the  $s, n$ -system equals that of a 1-D plane current (as in the previous sections). However, this is not necessarily true at its sides by the presence of tangential velocity components. In fact, as contrasted with the 1-D approach, the parametrization of additional (front-related) energy losses in Bernoulli's equation must involve this tangential velocity to model in some way the physical processes related to it. To underpin this argument, and to underline the difference with 1-D fronts, the following physical properties of the flow near a 2-DH front must be considered:

- Due to the increased vorticity in the head, as mentioned in section 4.2, the local friction losses are expected to be larger than in a 1-D flow.
- Experimental results from unbounded density currents on a sloping floor (Alavian, 1986) show that just below the narrow inflow channel a region appears with rapid spreading of the plume (near zone), while further downstream the spreading ceases and the plume width remains practically constant (far field) as the side-fronts are arrested. For small density differences this width was found to be smaller than for higher density differences. The latter type of density current behaves more like a spreading plume due to the dominance of buoyancy over momentum, while the former behaves more like

a jet due to the opposite reasoning.

The experiments showed that these processes were rather insensitive to the slope, which implies that gravity is not the only essential force in arresting a front with a finite depth. The experiments of Lüthi (1981) and Hauenstein and Dracos (1984) (see figure 4.13), and the experiments of Johnson et al. (1987) in a horizontal diffuser, revealed the same phenomena, although their basins were not long enough to reach a state with a constant plume width.

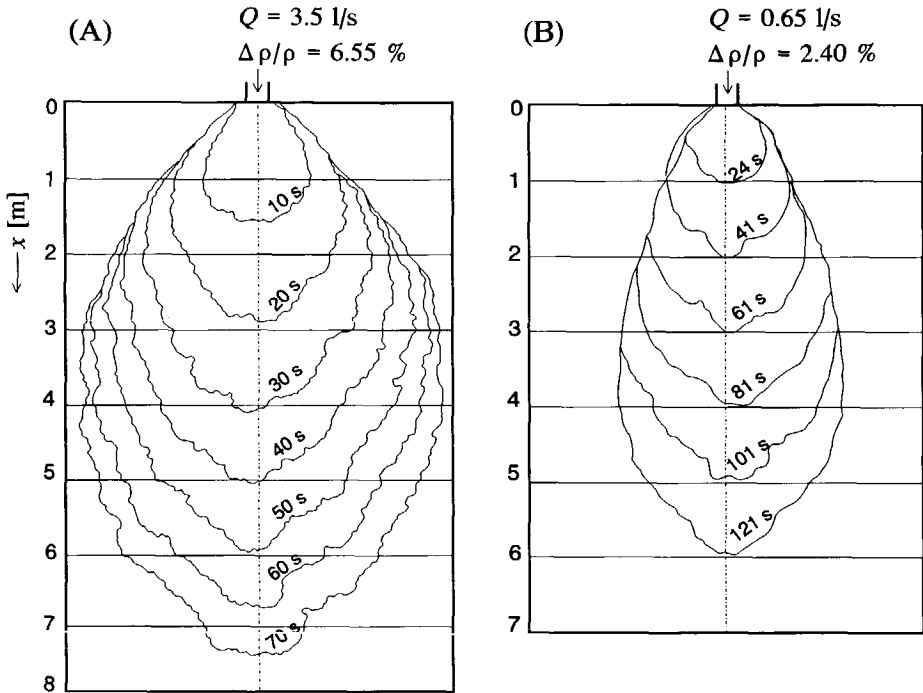


Figure 4.13 Propagation of 3-D turbidity current: front contours; Experiment (A) Lüthi (1981); (B) Hauenstein and Dracos (1984).

The processes which are able to temper the speed of a front are again friction, gravity, and entrainment. The processes which drive the front are pressure differences and momentum inflow as well as gravity. From the previous considerations it became clear that the parametrization of energy losses must allow for arresting the front to prevent it from spreading indefinitely in all directions. The experiments mentioned above showed that momentum of the flow and notably momentum (or velocity) in downstream direction is able to generate forces which can counteract the net pressure force normal to the arrested front, i.e. the sides of the plume. Firstly downstream (tangential) flow affects bottom-generated turbulence and associated energy losses in the head. Secondly shear stresses acting on the face of the front (between front and

ambient fluid) drive horizontal eddies in the ambient flow and generate a flow towards the inward of the plume (due to the water level differences generated by the frontal friction). Furthermore ambient fluid is entrained along the face of the front (e.g. see McClimans, 1978). Since these processes are all associated to velocities parallel to the front we introduce them into the parametrization of the energy losses in the front, adding up to the force  $F''$  in the momentum balances.

In appendix A the force  $F''$  is eliminated using Bernoulli's equation along a stream line passing through the front as proposed by Benjamin (1968) for the 1-D front. Additional energy losses  $\Delta E_1$  and  $\Delta E_2$  in this equation represent the effects of bottom generated turbulence in the ambient flow, and of the flow in the head of the turbidity current respectively. Following Kranenburg's approach these losses can be parametrized with the square of the head velocity ( $u_f^2$  or  $c_f^2$ ) using a loss coefficient  $k_1$  (Kranenburg's  $k$ ) as defined in the previous section. For the 2-DH front we add to this parametrization a term with the square of the tangential velocity ( $u_{2s}^2$ ) with an empirical loss coefficient  $k_2$ . After transforming the shock-relations and Bernoulli equation to their equivalent dimensionless variables (similar to those in section 4.4) the following shock relation for the case without ambient flow is derived if  $C_s \ll 1$  and  $\tilde{q}_{2s}$  is small:

$$\tilde{c} \approx \sqrt{\frac{(1 - \tilde{a}_f) \left[ (2 - \tilde{a}_f) \tilde{a}_f^3 - k_2 \tilde{q}_{2s}^2 \right]}{\tilde{a}_f^2 \left[ \tilde{a}_f (1 - k_1) + 1 + k_1 \right]}} \quad (4.22)$$

Here  $k_2$  has to be obtained from experiments. The variation of  $\tilde{c}$  with  $\tilde{a}_f$  following this equation for a few values of  $k_2 \tilde{q}_{2s}^2$  is illustrated in figure 4.14.

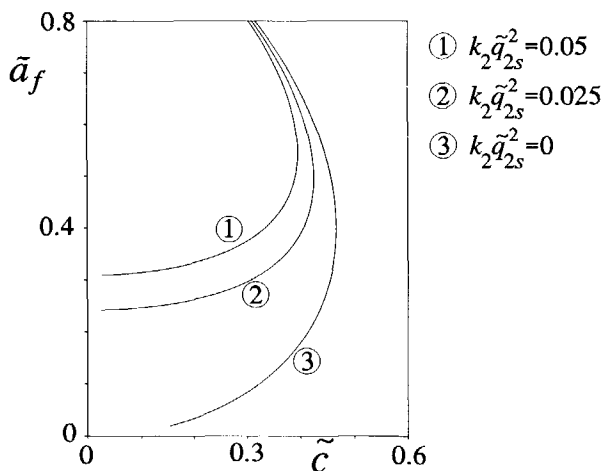


Figure 4.14 Variation of normal front celerity  $\tilde{c}$  with front height  $\tilde{a}_f$  for different energy-loss coefficients  $k_2$ .

It can be seen how front celerities are reduced significantly due to the presence of tangential flow velocities. The maximal value of  $k_2$  for which the front is arrested, i.e.  $c_f = 0$  is

$$k_{2,\max} \cdot \tilde{q}_{2s}^2 = \bar{a}_f^3 (2 - \bar{a}_f) \quad (4.23)$$

For higher values a front cannot be found from this shock relation.

Similar shock relations are derived in appendix A for the case with ambient flow (also quite similar to 1-D relations), and the corresponding relations for the force acting on the front  $F''$  are deduced from these results. Note that for all these results the tangential flow velocity (or  $\tilde{q}_{2s}$ ) is a governing parameter.

The relations which have been derived so far represent the frontal celerities and the dissipating forces of 2-DH frontal motion. By introducing the energy loss coefficient  $k_2$  to the originally 1-D model based on Benjamin's (1968) theory some physical processes typical for 2-DH fronts are parametrized in concept. At this point the theory can be calibrated for  $k_2$  and  $k_1$ , and it can be verified by means of experimental data. However, this theory presented here is not further elaborated, and further (experimental) research is required. One could think of numerical shock-fitting calculations or laboratory experiments of a release of salt water in a horizontal fresh water tank. The initial momentum and buoyancy of the plume can be varied, and at different locations near the (intruding) front samples can be taken of velocity vectors and density. These types of calculations and experiments are quite ambitious and for the present research and engineering applications redundant. Again with numerical shock-capturing techniques, in which the front is computed as an internal bore, satisfactory results for engineering applications are expected, if calculations are based on the  $u, a$ - basic equations (for which conservation of velocity instead of momentum is achieved).



## Chapter 5

### Analytical similarity solutions

#### 5.1 Introduction

So far the shock relations for an intruding gravity current are mathematically formulated. However, the front is just an internal boundary for the integral flow field. As its speed and height are function of the contiguous unsteady flow, the solution to this problem can only be obtained by considering the full gravity-current development.

Although this is tackled in a numerical way in the following chapters, it can be shown that a simple analytical solution can be derived under certain restrictions. That is, for a two-layer flow in a horizontal channel without bed friction, interfacial mixing and horizontal density gradients. As a result of these assumptions the system of basic equations reduces to such an extent that the model allows for a similarity or self-similar solution. In such a self-similar motion the distributions of flow variables remain similar to themselves with time, and vary only as a result of changes in scale. Therefore the flow can be described with only one independent variable, and the original system of partial differential equations changes into a system of ordinary differential equations.

This type of solution has a wide range of applications in gas and fluid dynamics, for instance see Sedov (1991) and Zel'dovich & Raizier (1966,1967). Dam-break waves in river channels, intense gas explosions, flame propagation, and supernova flare-ups are some striking examples of self-similar motions with a great theoretical analogy to our problem. Self-similar solutions for gravity currents have been studied for instance by Grundy & Rottman (1985,1986), Kranenburg (1993b), and Gratton & Vigo (1994). The last two papers deal only with plane (1-D) gravity currents, while the first papers deal also with radial spreading (2-D) gravity currents.

Since self-similarity provides us with a simple analytical solution, this theory can be used to verify numerical computations, and to gain important insight in the mathematics and physics of gravity current development. Consequently, in Chapter 6 self-similar solutions are applied to verify numerical results to compensate for the scarcity of appropriate and accurate data.

For the derivation of a self-similar solution for our two-layer model the dimensional

methods described by Zel'dovich & Raizer (1966) or Sedov (1993) can be followed. For a one-layer model with variable inflow this approach was used by Grundy & Rottman (1985, 1986) and Gratton & Vigo (1994). They applied a phase-plane analysis to construct a wide range of solutions, and to determine their validity and uniqueness. However, by starting the derivation from some relevant physical examples a large number of these solutions can be discarded. Here, the latter approach for finding physically relevant solutions is followed for our two-layer model, in analogy to Kranenburg (1993b).

Our one-dimensional gravity currents are described by shallow-water equations so that the analogy with collapsing dam-break waves and other Riemann-type problems can be used. With respect to this type of waves the analytical solution of Stoker (1957) is often cited. Stoker and Kranenburg's (1993b) self-similar solutions, which greatly coincide in their appearance, are the keys to matching different parts of the self-similar solution. In section 5.2 this is shown for a steady two-layer flow by presentation and discussion of the results.

Starting from these results, the 1-D (plane) self-similar solution is extended quite simply to a 2-D solution for radial axi-symmetrical flow. This type of plume can be observed for instance due to a vertical release of dense fluid in a horizontal basin. A one-layer example of numerical solution of this type of flow can be found in Garvine (1984), and a self-similar solution can be found in Grundy & Rottman (1985). In section 5.3 is demonstrated how the solution to this problem, shows some remarkable differences with 1-D gravity currents.

## 5.2 1-D self-similar solutions

### 5.2.1 Introduction and derivation

Considering the rather hypothetical horizontal 2-layer flow without friction and mixing, the source terms in the baroclinic equations for mass and momentum (eq. 2.19, 2.20, 2.7) disappear. These equations are made dimensionless by a similar transformation used for the derivation of shock relations in section 4.4, i.e.:

$$a_j = a\tilde{a}_j ; u_j = \tilde{u}_j\sqrt{g'_z a} ; q = \tilde{q} a\sqrt{r g'_z a} \quad (j=1,2) \quad (5.1)$$

The independent variables transform as

$$x = \tilde{x} a ; t = \tilde{t} \sqrt{a/g'_z} \quad (5.2)$$

Kranenburg (1993b) showed that this transformed system of equations is governed by four independent parameters: two densimetric inflow Froude numbers which we take constant, a parameter of the scale of vertical accelerations which disappears for hydrostatic flow, and a parameter  $\zeta = \bar{x}/\bar{t}$ . The flow is now called self-similar in  $\zeta$  because there are in this problem only two constant dimensional parameters ( $a$  and  $g_2'$ ) with independent dimensions, so that only one dimensionless combination can be formed from  $x$  and  $t$  (Sedov, 1993). Parameter  $\zeta$  becomes the only independent similarity variable. The system of equations for our model reduces to the following (see also Kranenburg, 1993b)

$$(\bar{u}_2 - \zeta) \frac{d\bar{u}_2}{d\zeta} - (\bar{u}_1 - \zeta) \frac{d\bar{u}_1}{d\zeta} + \frac{d\bar{a}_2}{d\zeta} = 0 \quad (5.3)$$

$$(\bar{u}_2 - \zeta) \frac{d\bar{a}_2}{d\zeta} + \bar{a}_2 \frac{d\bar{u}_2}{d\zeta} = 0 \quad (5.4)$$

$$\frac{d\bar{a}_1}{d\zeta} + \frac{d\bar{a}_2}{d\zeta} = 0 \quad (5.5)$$

$$\frac{d\bar{u}_1 \bar{a}_1}{d\zeta} + \frac{d\bar{u}_2 \bar{a}_2}{d\zeta} = 0 \quad (5.6)$$

For this type of quasi-linear homogeneous system of differential equations two solutions can be defined (see also Zel'dovich and Raizer, 1966, for the motion of a piston in a gas):

- A trivial solution, corresponding to a constant state or uniform flow, is found if all derivatives are zero.

$$\frac{d\bar{a}_1}{d\zeta} = \frac{d\bar{a}_2}{d\zeta} = \frac{d\bar{u}_1}{d\zeta} = \frac{d\bar{u}_2}{d\zeta} = 0 \quad (5.7)$$

- A non-trivial solution is found if the determinant of the coefficient matrix of the system is zero, making the equations indeterminate.

$$\frac{(\bar{u}_1 - \zeta)^2}{\bar{a}_1} + \frac{(\bar{u}_2 - \zeta)^2}{\bar{a}_2} = 1 \quad (5.8)$$

In a frame of reference travelling with speed  $\zeta$  in positive  $x$ -direction, relation (5.8) implies that in this frame the flow is critical. This means that one of the two internal-wave celerities disappears, and a centred simple-wave or rarefaction wave is found.

These solutions are the general solutions to various cases of Riemann problems, which can be considered as the development of shock-waves from an initial flow condition in which two different constant states are separated by a single discontinuity (e.g. Le Veque, 1990)

Kranenburg (1993b) continued the analysis by fitting and matching both solutions for gravity currents with a relatively high inflow rate. However, it is not possible to extend his theory to smaller flows. At this point Stoker's (1957) dam-break solution blends into the derivation, providing the required knowledge for matching the low-flow trivial and non-trivial solutions. In figure 5.1 two alternatives are given for matching the solutions to obtain physically relevant solutions.

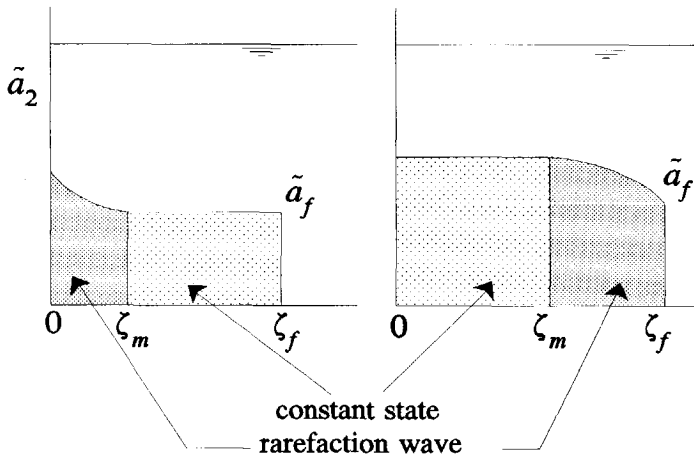


Figure 5.1 Self-similar solutions for low and high discharge respectively.

On the left side of this figure the self-similar solution for a low inflow rate resembles Stoker's solution for dam-break waves, which also satisfies Gratton & Vigo's (1994) results. The right-side solution is Kranenburg's solution for high inflow rates, also described by Klemp et al. (1994).

To construct and evaluate the proper self-similar solution we considered three hypothetical experiments in a laboratory flume, successively illustrated in figure 5.2. These are partial lock-exchange, regular lock-exchange (or dam break), and sluicing. A lock exchange (or dam break) is initiated by removing a gate which separates a reservoir which is fully or partially filled with a dense fluid, from a reservoir filled with lighter fluid. Two waves are generated, travelling in opposite directions. A (dam-break) wave travels downstream with speed and height determined by its shock relation. A wave near the surface or interface travels into the undisturbed upstream reservoir. Due to the intruding gravity current a reverse flow is generated in the upper layer with  $|\bar{u}_1(0)| \leq |\bar{u}_2(0)|$ .

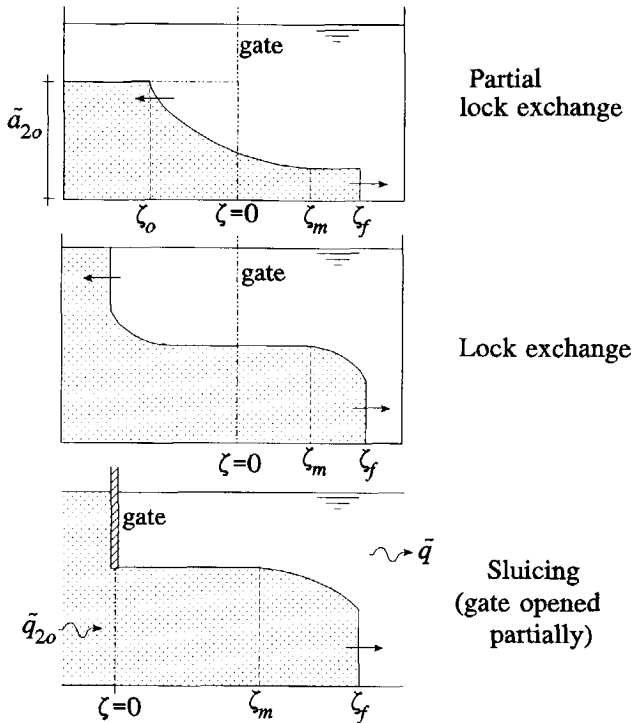


Figure 5.2 Hypothetical experiments with self-similar flow

If the gate is only partially lifted, a reverse flow cannot develop if the interface remains attached to the gate. This means that light fluid cannot flow under the gate in reverse direction. As a result, a total water depth increase in the flume can only be prevented if the discharge of light fluid, released at the downstream end of the flume, equals the discharge of dense fluid entering under the gate, i.e.  $\bar{q} = \bar{q}_2(0)$ . This experiment can be considered as a rough representation of a sluicing operation in a reservoir where the gate corresponds to a stationary plunge point.

Essentially the differences in these three experiments with steady inflow and outflow are only caused by the initial condition which has to be imposed as a Riemann problem (i.e. a discontinuity separating sections with a constant state). This initial state can be imposed by inflow discharge, boundary Froude numbers (or the inflow depth and density) and the total water depth. These are the constant abstract parameters which, combined with the front relation, determine the final shape of the current. In the following sub-sections is shown for each case how they determine the way of matching non-trivial and trivial solutions, and the propagation of the front.

### 5.2.2 Self-similar solutions for lock-exchange flows

A graphical representation of the downstream part of a partial lock-exchange flow resulting in a low-discharge gravity current is given in figure 5.3.

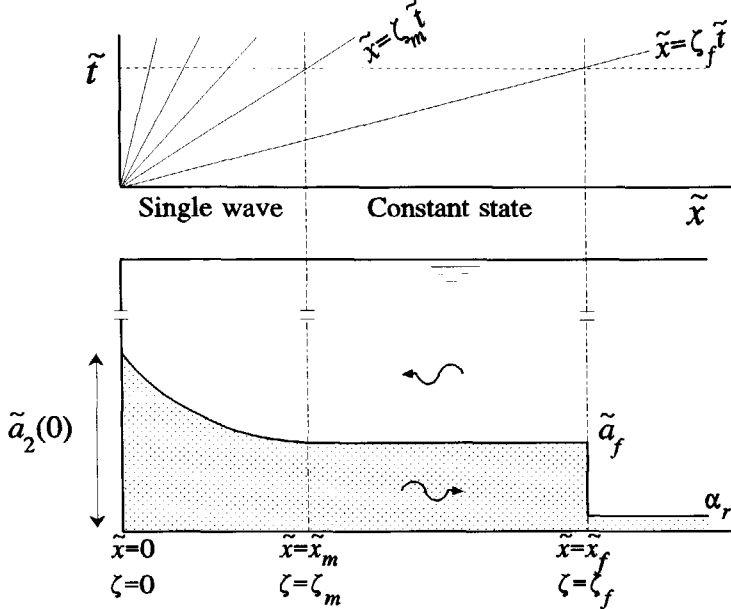


Figure 5.3 Self-similar solution for partial lock-exchange flow:  $\tilde{x}$ - $\tilde{t}$  diagram and physical presentation.

As we have seen earlier, this 1-D baroclinic approach has two real characteristic celerities  $\phi_{1,2}$  with  $\phi_1 \geq \phi_2$ . The solution of an imposed Riemann problem will therefore result in at most two jumps, since a jump can only exist by a mutual intersection of characteristics belonging to the same family (either the  $\phi_1$  or the  $\phi_2$  family). In this example the initial discontinuity at  $\zeta=0$  indeed generates two jumps: a front with speed  $\zeta_f$  induced by  $\phi_1$  characteristics, and a rarefaction wave induced by  $\phi_2$  characteristics. In figure 5.3 is shown how the  $\phi_2$  characteristics fan out in the rarefaction region, such that the flow accelerates and the depth decreases. In terms of gas molecules this implies a spreading of the fluid such that it becomes rarified. The velocity and depth in the constant state part of the solution remains constant in time. With this situation disturbances near the front cannot propagate back to the gate and the critical condition at  $x=0$  maintains control over the downstream propagating gravity current. Disturbances originating upstream can take over the front during propagation.

If at the upstream boundary  $\zeta=0$  (the gate) the non-trivial solution holds, then the flow

is critical (eq.5.8). Imposing a constant discharge  $q_2(0)$  or depth  $a_2(0)$  the boundary discharge and depth are defined, and by using equation (5.8) and (5.2) the flow profile can be obtained numerically for consecutive values of  $\zeta$  starting from this boundary. For a very deep reservoir this profile can be expressed analytically as

$$\bar{a}_2^*(\zeta^*) = \left( -\frac{1}{3}\zeta^* + \sqrt{\bar{a}_2^*(0)} \right)^2 \tag{5.9}$$

with  $\zeta_m^* \approx 0.364$ ,  $\bar{a}_2^*(\zeta_m^*) = \bar{a}_f^* \approx 0.772$ , and  $\zeta_f^* \approx 1.243$ . Here superscript \* indicates that variables are made dimensionless according to equation (5.1) in which  $a$  is replaced by  $a_2(0)$ .

If the relative depth of the dense fluid before removal of the gate is  $\bar{a}_{2o}$  then the resulting depth  $\bar{a}_2(\zeta=0)$  after removal is constant and approximately equal to  $(4/9)\bar{a}_{2o}$  if  $\bar{a}_{2o} < 0.2$ . Then the simple wave region extends from  $\zeta_o = -\sqrt{(\bar{a}_{2o}\{1-\bar{a}_{2o}\})}$  to  $\zeta = \zeta_m$  (see figure 5.2). At  $\zeta_m$  equation (5.8) satisfies the shock relation for the front. From this point it is possible to match the trivial solution to the non-trivial solution. This downstream constant state can be found by considering mass conservation over the full gravity current expressed as

$$\bar{q}_2(0) = \int_0^{\zeta_m} \bar{a}_2 d\zeta + \bar{a}_f(\zeta_f - \zeta_m) - \zeta_f \alpha_r \tag{5.10}$$

This equation states that the net inflow of mass equals the mass of the non-trivial and the trivial solution minus the initial mass (at  $t=0$ ). The location of the front  $\zeta_f$  follows from this equation after integrating the non-trivial solution from  $\zeta=0$  to  $\zeta=\zeta_m$ .

The effect of the boundary condition  $\bar{a}_2(\zeta=0)$  or  $\bar{a}_{2o}$  on the solution is illustrated in figure 5.4. It shows how for increasing values of  $\bar{a}_2(0)$ , and correspondingly increasing values of  $\bar{q}_2(0)$ , the solution reaches a transitional state for which  $\zeta_m$  equals zero. This transitional solution (for partial lock-exchange flows with  $\bar{q}=0$  and  $u,a$  front, i.e., a front computed with shock relations obtained from basic equations system UA in chapter 4) can be described with the following parameters:

$$\bar{a}_2(0) = \frac{1}{3} \quad ; \quad \bar{q}_2(0) = \frac{1}{3} \left( \frac{2}{3} \right)^{3/2} \approx 0.181 \quad ; \quad \zeta_f = \left( \frac{2}{3} \right)^{3/2} \approx 0.544 \tag{5.11}$$

It is obtained by combining eq. (5.8) for  $\zeta_f$ , with the shock relation. Doing this the critical front condition for existence of a front, equation (4.16) in the preceding chapter, is exactly satisfied:

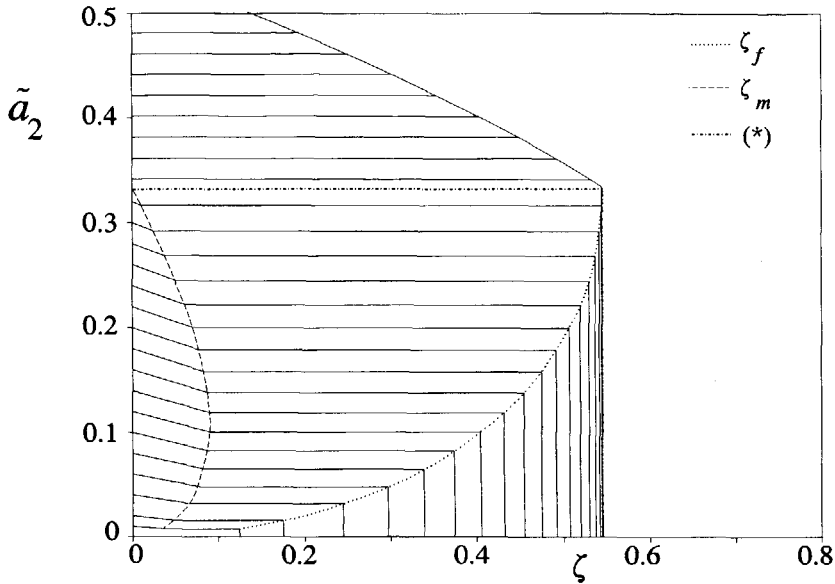


Figure 5.4 Self-similar solutions for a partial lock-exchange flow, varying  $\bar{a}_2(\zeta=0)$  with steps of 0.02. Line (\*) is the transitional solution.

$$\zeta_f = (1 - \bar{a}_f)^{3/2} \quad (5.12)$$

For fronts with higher depths this entropy condition is violated and the front becomes unsteady. In section 4.3 it is shown that it is physically correct to replace this shock by a rarefaction wave. Therefore the only possible high-discharge solution is the one shown in figures 5.1 and 5.4. The transitional solution now forms the boundary between low-discharge and high-discharge solutions, and the height  $\bar{a}_f$  and location  $\zeta_f$  of the front for the high-discharge solutions is constant and equal to that of the transitional solution.

The high-discharge solutions are typical for gravity currents intruding into ambient fluid with finite depth, and is not found in dam-break waves intruding the atmosphere. For high values of  $\bar{a}_2$  the celerity of disturbances travelling along the positive characteristics falls below the front speed, resulting in a subcritical state. Now the behaviour of the flow becomes more complex since the front affects the upstream reservoir, while upstream variations in this reservoir affect the front. Usually this effect of finite channel depth is largely ignored in gravity-current models.

High discharge solutions for a given value of  $\bar{a}_2(0)$  are constructed starting from the front relations given above. The non-trivial solution is solved until  $\bar{a}_2(\zeta) = \bar{a}_2(0)$ . From this point  $\zeta = \zeta_m$  to the upper boundary the trivial solution holds (uniform flow). The



maximal admissible value for  $\bar{a}_2(0)$  is about 0.54, for which the trivial solution disappears and the solution is non-trivial from boundary to front. The self-similar solution with  $\bar{a}_2(0)=0.5$  corresponds to a complete lock-exchange with  $\bar{a}_{2o}=1$ . This is the second hypothetical experiment presented in figure 5.2.

A major benefit of these simple analytical solutions for partial and full lock-exchange flows is the possibility of gaining insight into the sensitivity of the computations to variations in the controlling variables  $C_s$ ,  $a$  and  $q_2(0)$ . By means of some examples this dependence is illustrated.

Self-similar solutions with different concentrations  $C_s$  are plotted in figure 5.5 for a partial lock-exchange flow intruding into a 10 m deep stagnant reservoir with  $q_2(0)=1$  m<sup>2</sup>/s.

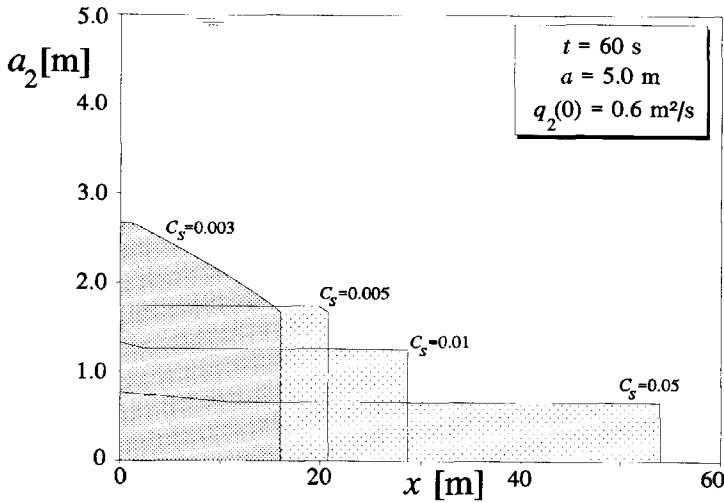


Figure 5.5 Self-similar solutions in physical coordinates, for a partial lock exchange with different values of concentration  $C_s$ .

The results are transformed to the physical coordinates at time  $t=60$  s, using the transformation

$$x = t \cdot \zeta \sqrt{\sigma' C_s g a} \quad (5.13)$$

As expected an increase of concentration results in an increase of front celerity, although the value of  $\zeta_f$  decreases in the dimensionless coordinate system. By making the constant discharge  $q_2(0)$  dimensionless using  $C_s$ , a decreasing density results in an increase of  $\tilde{q}_2(0)$  and the transition from low to high-discharge solutions can be seen.

The sensitivity of velocities and discharges to the increase of concentration for this

example is illustrated in figure 5.6 (in a physical coordinate system at  $t = 60$  s). In a turbidity current on an erodible bed this behaviour is responsible for the ignitive auto-suspension principle treated for instance by Pantin (1979) and Parker et al. (1986). If sediment is picked up from the bed the concentration increases, resulting in an increase of velocity and so on. This type of self-accelerating turbidity current can be found on steep slopes such as in submarine canyons. The self-similar solution presented here cannot be used for suspensions with concentration gradients; therefore this principle is not further analysed here.

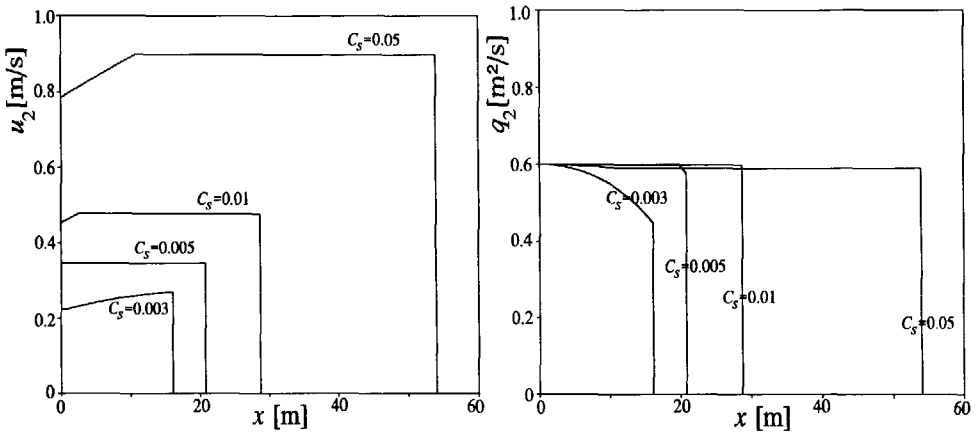


Figure 5.6 Velocities and discharges for self-similar solutions of partial lock-exchange flows with different values of  $C_s$ .

An important, previously mentioned result can be demonstrated by the internal Froude numbers of the  $x,t$  system: the high-discharge solution (low  $C_s$ ) is internally subcritical, and the low-discharge solution (high  $C_s$ ) is internally supercritical. The transitional state corresponds to critical flow. Also Kranenburg (1993b) and Klemp et al. (1994) concluded that therefore, in agreement with laboratory experiments, the high-discharge solution as a whole acts as a control to the flow at  $\zeta=0$ . For numerical modelling this is crucial knowledge for imposing boundary conditions. Note that internal Froude numbers for both types of solutions are close to unity, which already indicates the importance of using a coupled model for computing flow and morphology for turbidity currents.

The sensitivity of the self-similar solution to the total water depth  $a$  is illustrated in a similar way as above by means of an example in figure 5.7 with  $C_s=0.005$  and constant discharge  $q_2(0)=1$  m<sup>2</sup>/s. As the reservoir depth decreases the front is slowing down,  $a_2(x)$  increases, and the dimensionless discharge  $\tilde{q}_2(0)$  increases. For reservoir depths less than about 5.2 m the high-discharge solution must be used and the gravity current becomes fully subcritical. These results emphasize the importance of accounting for upper-layer flow when computing density currents in shallow

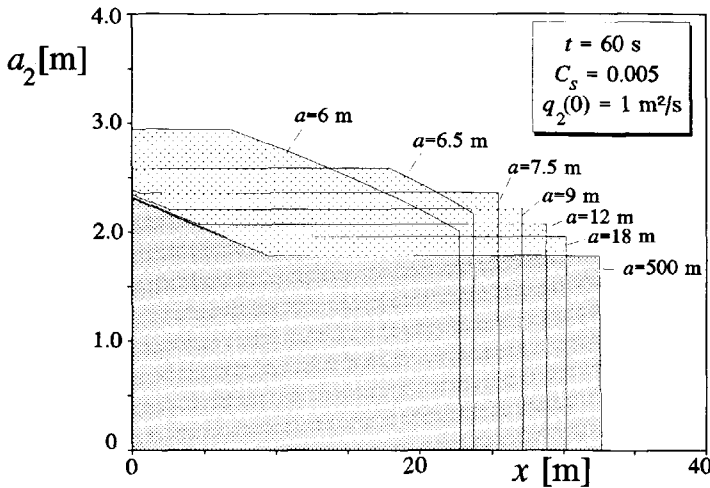


Figure 5.7 Self-similar solution for a density current with different reservoir depths.

reservoirs.

To conclude these analyses of self-similar solutions for lock-exchange flows the sensitivity of the solutions to the shock relations is illustrated. Again it is possible to distinguish between a model described by basic equations in  $q, a$  form (*system QA*), and a model described by equations in  $u, a$  form (*system UA*). So far only results computed for UA models are presented. However, it is quite easy to show the effect of differences in their shock relations. Firstly for both systems the non-trivial solution, expressed by eq.(5.8), is identical. Secondly the appearance of the trivial solution is equal for both systems, but their values deviate since the shock relations are different. In figure 5.8 (left side) two examples of self-similar solutions for low-discharge flows are plotted for identical flow conditions with model A and B respectively, illustrating their difference.

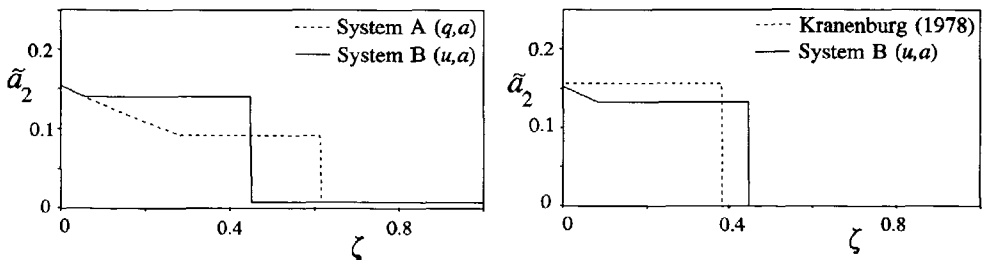


Figure 5.8 Comparison of solutions computed with different shock relations.

In this figure (right side) also a comparison is given of solutions using Kranenburg's (1978) shock relation (with  $k=0.6$ ) and using the shock-relation of System UA. These

results confirm the findings from the previous chapter, and they show that density currents computed with system UA have a lower depth with higher velocities than those computed with the help of Kranenburg's shock relations. The latter effect is slightly reduced if friction and entrainment are taken into account in the basic equations.

In figure 5.9 a similar comparison is presented for a high-discharge flow. In this figure also some visual data (obtained from shadowgraphs) for an experimental small-scale lock-exchange flow from Rottman and Simpson (1983) are plotted.

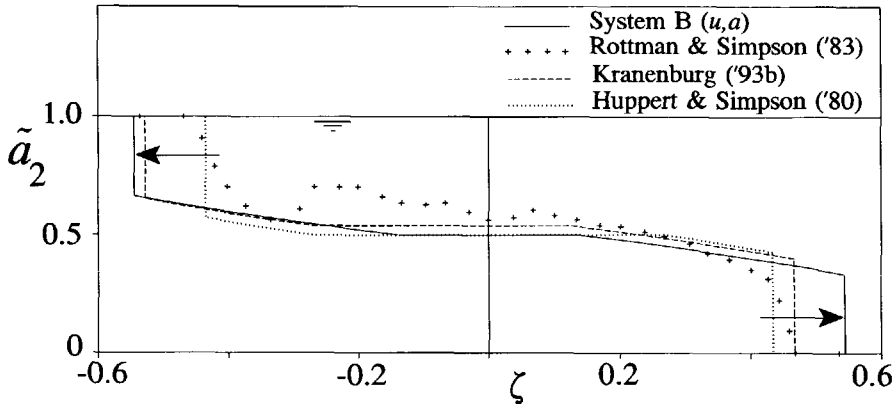


Figure 5.9 Self-similar solution for lock exchange flows using different shock relations.

Clearly the presented solution reproduces qualitatively the data set which shows a wedge shaped gravity current. Note that for Kranenburg's (1993b) solution the surface front is defined with  $k=0$ , the bottom front with  $k=0.6$ . Therefore  $a_2(0) \approx 0.54 \cdot a$  instead of half the channel depth. With respect to depths and velocities the conclusions for low-discharge flows still hold.

### 5.2.3 Self-similar solutions for sluicing operations

The third hypothetical experiment which can be expressed by the previously defined self-similar solutions is the sluicing experiment shown in figure 5.2. In this experiment the elevation of the gate is adjusted at its highest possible level at which no ambient fluid escapes to upstream. The discharge of ambient fluid downstream is defined as  $\bar{q} = \bar{q}_2(0)$ , and  $\tilde{a}_2(0)$  defines the discharge  $\bar{q}_2(0)$ . In figure 5.10 the resulting self-similar solutions are plotted for various elevations of the gate.

Due to the presence of ambient flow the shock relation is altered. Effectively, due to

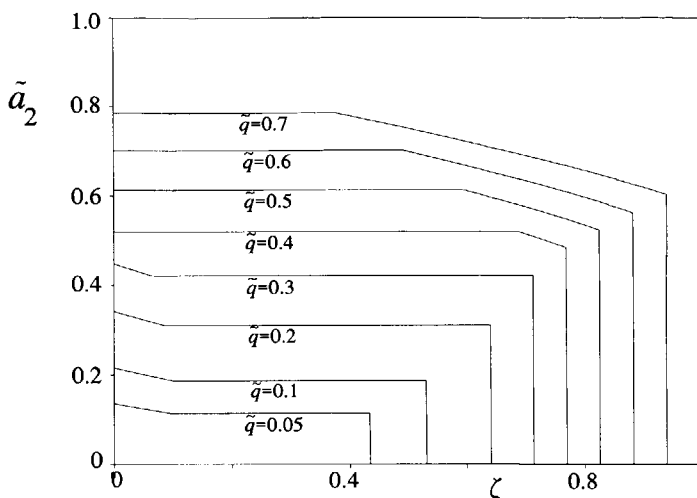


Figure 5.10 Self-similar solution for a sluicing operation with different inflow discharges, or different gate elevations.

the ambient flow, front propagation speeds, as well as admissible inflow discharges and heights increase significantly. Theoretically the value  $\tilde{a}_{2,\max}(0) \approx 1$  is admissible, for which the non-trivial solution extends over the full current (in lock-exchange flows  $\tilde{a}_{2,\max}(0) \approx 0.55$ ). However, for this extreme situation the Froude numbers range from  $\zeta=0$  to  $\zeta=\zeta_f$  from unity to a value of three, which is highly supercritical and violates the assumption of negligible entrainment at the interface.

For all the solutions in figure 5.10 the flow is internally supercritical with Froude numbers near unity. The subcritical state at high inflow discharges cannot be found, also if other shock relations are used. Furthermore the transition from low to high-inflow solutions occurs at higher inflow discharge and depth, than for lock-exchange flows.

With respect to the sensitivity to total depth, density and shock relations the results for lock-exchange flows presented in previous sub-sections also apply to the sluicing case.

#### 5.2.4 Discussion

In this section analytical solutions are presented for 1-D intruding gravity currents in a horizontal channel. These self-similar solutions are used to describe three hypothetical experiments: partial and full lock-exchange and sluicing operations. Although the model is severely simplified (e.g. entrainment neglected), an analysis of

these solutions has learned us a lot about the behaviour and sensitivity of the two-layer model, and provided us with verification material for the numerical model.

So far the analysis is restricted to gravity currents with a constant inflow discharge and inflow Froude numbers determined by the chosen experiments. However, it seems worthwhile to extend the more general derivations of Gratton & Vigo (1994) for one-layer gravity currents (i.e. very deep reservoirs) to two-layer flows. They showed, by adapting phase-plane formalism of gas dynamics (Sedov, 1993), that self-similar solutions also exist for gravity currents with an inflow discharge defined by the following power law

$$q_2(x=0, t) = \alpha \cdot q_2(x=0, t=0) \cdot t^{\alpha-1} = \alpha \cdot q_{20} \cdot t^{\alpha-1} \quad (5.14)$$

A constant inflow is obtained if  $\alpha=1$ , spreading of a constant volume is obtained if  $\alpha=0$ , while all other positive values of  $\alpha$  represent variable inflows. The independent (similarity) variable of this approach becomes

$$\zeta' = \frac{x}{(g'q_{20})^{1/3} t^\delta} \quad (5.15)$$

where  $\delta=(2+\alpha)/3$  for plane flow. The phase variables  $\tilde{V}$  and  $\tilde{A}$  are defined by

$$u_2 = (g'q_{20})^{1/3} t^{\delta-1} \cdot \delta \cdot \zeta' \cdot \tilde{V}(\zeta') \quad ; \quad a_2 = (g'q_{20})^{2/3} t^{2\delta-2} \cdot \delta^2 \cdot (\zeta')^2 \cdot \tilde{A}(\zeta') \quad (5.16)$$

In the phase plane  $(\tilde{V}, \tilde{A})$  the solutions to the problem are represented by integral curves. Self-similar solutions, characterized by the boundary conditions, are constructed by taking appropriate pieces of these curves. In fact this phase-plane analysis is just another (graphical) way of the representing the theory described in this chapter, and therefore it is not further discussed here. For instance a quite clear introduction to the use of phase-plane analyses to general Riemann problems is given by Le Veque (1990). Phase-planes for more than two variables become multi-dimensional and therefore difficult to present graphically. The theoretical approach described in this section does not have this disadvantage.

By varying the inflow Froude number Gratton and Vigo (1994) obtained a wide range of self-similar solutions with sub- and supercritical flow and internal hydraulic jumps. For instance it is possible to manage the gate elevation and discharge in the sluicing experiment (sub-section 5.2.3) such that the inflow Froude number is much higher than unity. In some experiments this will generate a (moving) internal hydraulic jump.

For the derivation of self-similar solutions in this section the effects of bottom friction and entrainment are neglected. However, this assumption must be verified for real gravity currents, especially those which are highly supercritical. For a full lock-exchange flow (as performed by Rottman & Simpson, 1983) a comparison is made

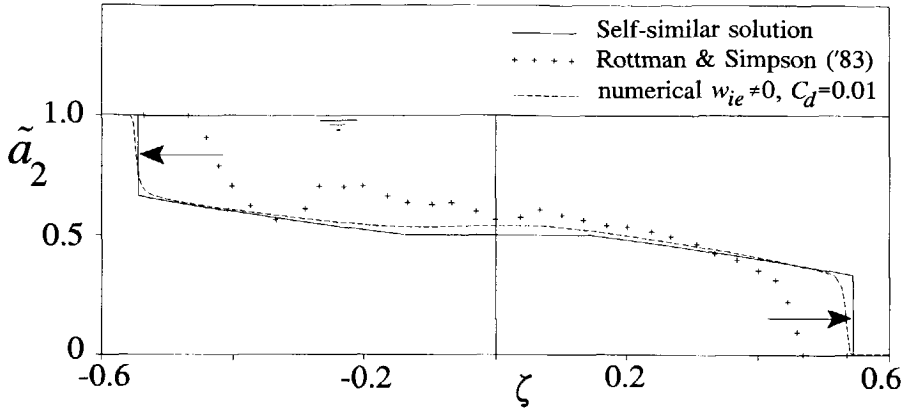


Figure 5.11 Lock-exchange flow: comparison of the self-similar solution to a numerical solution with friction and entrainment.

between the self-similar solution and a numerical solution (chapter 6), accounting for friction and using the entrainment relation defined by Parker et al. (1987). The results are presented in figure 5.11 in dimensionless coordinates. By considering also the numerical solution without friction and entrainment (not presented in this figure) the assumption above is easily verified. The only noticeable difference, although very small, is found at  $\zeta=0$  where  $\tilde{a}_2(0)$  is slightly larger than 0.5 (this is primarily due to the entrainment effect). Reduction of front celerities by these mechanisms is only effective for currents flowing over long distances or for non-conservative density currents. Also for 2-D axi-symmetric flows in the following section a comparison with and without entrainment is presented.

### 5.3 Axi-symmetric 2-DH radial flows

#### 5.3.1 Construction of 2-DH self-similar solutions

In the previous section the similarity principle is successfully used to derive an analytical solution for 1-D gravity currents. The question arises whether this type of similarity can also be found in 2-DH gravity currents. Therefore it is again necessary to reduce the basic equations of the system to a form which allows for a simple mathematical treatment. In this section this reduction is obtained by considering radially developing flow in a very deep ambient fluid. Examples are plumes generated by vertical releases of dense fluid on a horizontal surface in a deep tank, riverine fresh water plumes on the surface of coastal waters, or a collapse or explosion of a volume

of dense gas into the atmosphere (e.g. Garvine, 1984, McClimans. 1978).

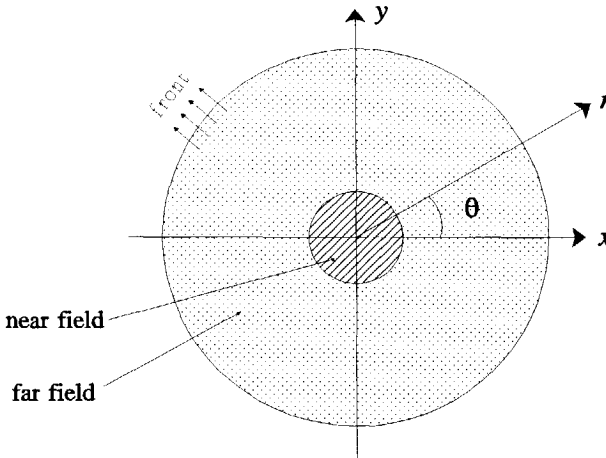


Figure 5.12 Definition sketch for a radial flow.

For radial flow on a horizontal surface, defined in figure 5.12, the system can be transformed to polar coordinates:

$$x = r \cdot \cos(\theta) \quad ; \quad y = r \cdot \sin(\theta) \quad ; \quad u = \sqrt{u_2^2 + v_2^2} \quad (5.17)$$

The flow field is split into a near-field region with radius  $r_0$  and a far-field region. Physically the near-field region is either characterized by 3-D hydrodynamic processes which cannot be represented by a layer model, or it is the boundary at which dense fluid is released. The inflow discharge  $q_2(r_0)$  or the inflow depth  $a_2(r_0)$  is taken constant again. The far field region is the part of the flow where the layer model applies. Due to the transformation the 2-DH system of three p.d.e. in  $x$  and  $y$  reduces to an equivalent 1-D system of two p.d.e.:

$$\frac{\partial u}{\partial t} + u \frac{\partial u}{\partial r} + g_z' \frac{\partial a_2}{\partial r} = 0 \quad (5.18)$$

$$\frac{\partial a_2}{\partial t} + \frac{\partial a_2 u}{\partial r} = - \frac{a_2 u}{r} \quad (5.19)$$

The only difference to the 1-D equations for a plane current is the right-hand term  $a_2 u / r$  in the mass-balance equation which acts as a sink and represents the spreading effect. Clearly for  $r \rightarrow 0$  this term and simultaneously the underflow depth goes to infinity, which underlines the necessity of a near-field region.



In a similar manner as in sub-section 5.2.1 the variables can be transformed as follows:

$$a_2 = a_2(r_0) \bar{a}_2 ; \quad u = \bar{u} \sqrt{g'_z a_2(r_0)} ; \quad q = \bar{q} a_2(r_0) \sqrt{g'_z a_2(r_0)} \quad (5.20)$$

The independent variables transform as

$$r = \bar{r} a_2(r_0) ; \quad t = \bar{t} \sqrt{a_2(r_0)/g'} \quad (5.21)$$

Again the problem is determined by two constants  $a_2(r_0)$  and  $g'$  with independent dimensions. Additionally to 1-D motion the near-field coordinate  $r_0$  enters the derivation which is represented by a dimensionless parameter  $\zeta_0 = \bar{r}_0/\bar{t}$ . For similarity of the 2-DH motion it is necessary that only one similarity variable can be constructed, and that other parameters are constant. Therefore parameter  $\zeta_0$  must satisfy

$$\zeta_0 = \frac{\bar{r}_0}{\bar{t}} = \text{Constant} \quad (5.22)$$

Hence the radius  $r_0$  of the near-field region must increase linearly with time. The similarity variable  $\zeta_r$  can be defined as

$$\zeta_r = \frac{(\bar{r} - \bar{r}_0)}{\bar{t}} = \frac{\bar{r}}{\bar{t}} - \zeta_0 = \frac{r - r_0}{t \sqrt{g' a_2(0)}} \quad (5.23)$$

The similarity variable for axi-symmetric flows defined by Grundy and Rottman (1985, 1986) slightly differs from equation (5.23) as they assumed the inflow discharge to increase proportionally with  $t^\alpha$  ( $\alpha \geq 0$ ) while they assumed a fixed near-field boundary  $r_0$ . Although this approach is inverse to ours, they also concluded that for the case where  $r_0$  as well as  $q_2(r_0)$  are constant, similarity cannot exist.

The basic p.d.e. transform to the following set of ordinary differential equations:

$$(\bar{u} - \zeta_r) \frac{d\bar{u}}{d\zeta_r} + \frac{d\bar{a}_2}{d\zeta_r} = 0 \quad (5.24)$$

$$(\bar{u} - \zeta_r) \frac{d\bar{a}_2}{d\zeta_r} + \bar{a}_2 \frac{d\bar{u}}{d\zeta_r} + \frac{\bar{a}_2 \bar{u}}{(\zeta_r + \zeta_0)} = 0 \quad (5.25)$$

The system is indeterminate if again the flow is critical in a frame of reference travelling with speed  $\zeta_r$ , i.e. if  $(\bar{u} - \zeta_r)^2/\bar{a}_2 = 1$ . However, the resulting non-trivial solution (rarefaction wave) is not required for the self-similar solution presented in this

section.

Equations (5.24) and (5.25) are solved numerically (using the Runge Kutta method) for  $\tilde{u}$  and  $\tilde{a}_2$ . For the upper boundary a constant discharge  $q_2(r_0)$  and a value for the densimetric Froude number  $Fr_2(r_0) = \tilde{u}(r_0)^2 / \tilde{a}_2(r_0) \geq 1$  are imposed (corresponding to physical considerations by Garvine, 1984, with respect to fresh-water plumes). At the lower boundary, the front, the boundary condition is represented by the shock relation as derived in chapter 6 and rewritten for deep water reservoirs:

$$\zeta_r = \zeta_f : \quad \tilde{u}_f^2 = 2 \tilde{a}_f ; \quad \zeta_f = u_f \quad (5.26)$$

Starting integration from the upper boundary it is found that the 'moving' densimetric Froude number  $Fr^2(\zeta_r) = (\tilde{u} - \zeta_r)^2 / \tilde{a}_2$  increases in downstream direction with values exceeding unity, i.e. supercritical in a moving reference. However, from equation (5.26) follows that at the front the flow is subcritical in a moving reference with  $Fr^2(\zeta_f) = 0$ . Clearly a transition from supercritical to subcritical flow must exist in the plume. Indeed, numerical computations carried out with the model presented in chapter 6 show a well defined moving internal jump (internal bore), and also studies of Rottman & Simpson (1984), Garvine (1984) and Grundy & Rottman (1986) reveal this phenomenon. In neither of these studies rarefaction-wave regions or non-trivial solutions were found.

The construction of the appropriate self-similar solution is carried out similarly to open-channel hydraulic jumps (e.g., Chow, 1959). The internally 'supercritical' curve is obtained by integration in positive  $\zeta_r$ -direction starting from the upstream boundary. An internally 'subcritical' curve is obtained by integration in negative  $\zeta_r$ -direction starting from the front with a chosen value for  $\zeta_f$ . For the internal bore the following shock-relation can be defined (cf. section 4.4):

$$\frac{\tilde{a}_{2l}}{\tilde{a}_{2r}} = \frac{1}{4} \cdot Fr_r \left[ \sqrt{Fr_r^2 + 8} + Fr_r \right] \quad \text{with} \quad Fr_r = \sqrt{\frac{(\tilde{u}_r - \zeta_r)^2}{\tilde{a}_{2r}}} \quad (5.27)$$

where  $\tilde{a}_{2l}$  is the depth left of the jump and  $\tilde{a}_{2r}$ ,  $\tilde{u}_r$  and  $Fr_r$  are defined right of the jump. The jump is located where both profiles satisfy this shock relation. In figure 5.13 a conjugate curve is constructed by applying equation (5.27) on all the computed values of the subcritical curve. The location of the jump is now found where the conjugate and the supercritical curve intersect.

For the example in figure 5.13 we used  $r_0/t = 0.1$  m/s;  $C_s = 0.005$ ;  $Fr_2(r_0) = 1$ ;  $a_2(r_0) = 1$  m. The resulting profile must satisfy the following mass-balance, which follows from integration of equation (5.25) over the plume:

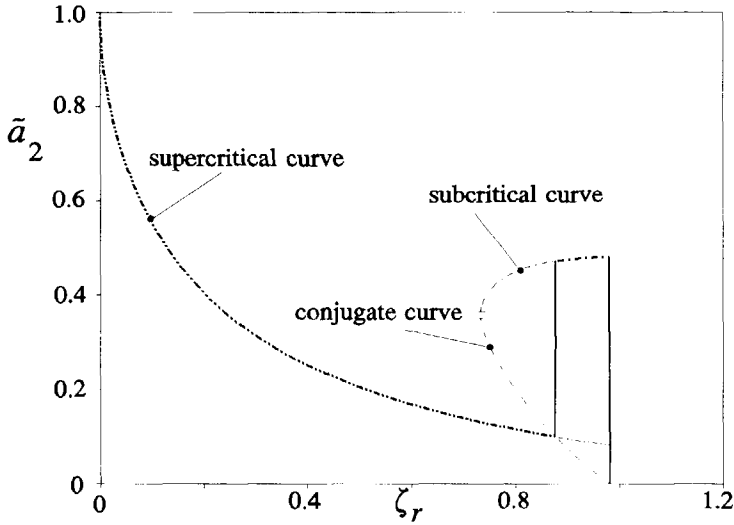


Figure 5.13 Construction of a self-similar solution for radial flow.

$$\tilde{a}_2(\zeta_0) \zeta_0 = \int_{\zeta_0}^{\zeta_f} (2\zeta + \zeta_0) \tilde{a}_2(\zeta) d\zeta \quad (5.28)$$

Iteratively the chosen value of  $\zeta_f$  must be corrected until this equation is satisfied.

The presence of an internal bore, and the absence of a rarefaction wave in these results already indicate the differences between 1-D plane currents and 2-DH axisymmetric flows. These differences are all determined by the sink term  $a_2 u/r$  in the mass-balance equation (5.19). In the following sub-section the characteristics of 2-DH self-similar solutions and the comparison to 1-D self-similar solutions are presented by means of some examples.

### 5.3.2 Analysis of 2-DH self-similar currents

In the previous sub-section a mathematical similarity solution for radial flow is derived. However, the questions arise whether this solution is realistic with respect to real spreading plumes, and to what extent this solution deviates from the 1-D self-similar solutions. By means of some examples is tried to elucidate these issues.

For the example of figure 5.13 we have plotted the resulting 3-D state 30 seconds after initiation in figure 5.14. The results show how a major part of the current gets concentrated in a narrow rim at the spreading front.

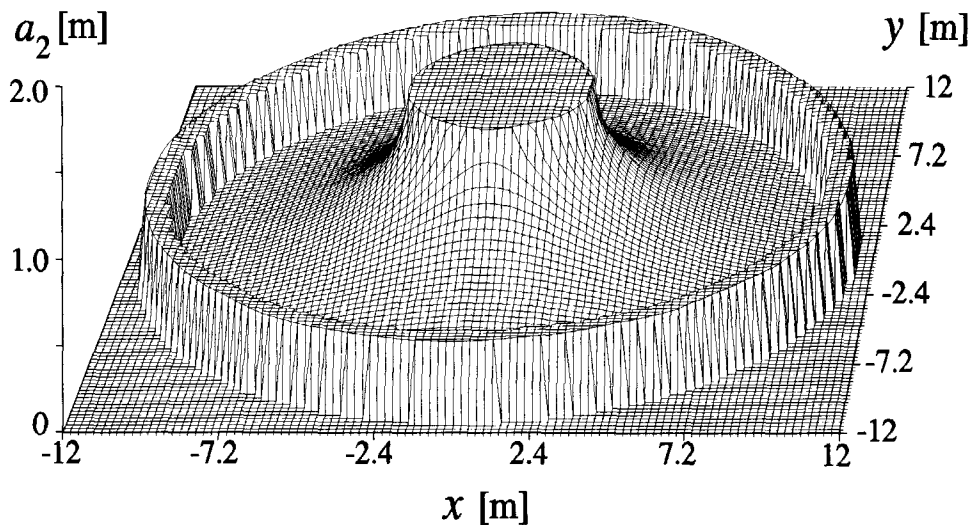


Figure 5.14 3-D representation of a self-similar axisymmetric flow.

This mathematical result was also found by others, for instance by Garvine (1984). For comparison we used data deduced from Garvine's paper to compute the next examples. These data are:  $r_0 = 1$  m if  $t = 33.4$  s;  $a_2(0) = 0.72$  m;  $Fr_2(0) = \sqrt{2}$ ;  $C_s = 0.005$ .

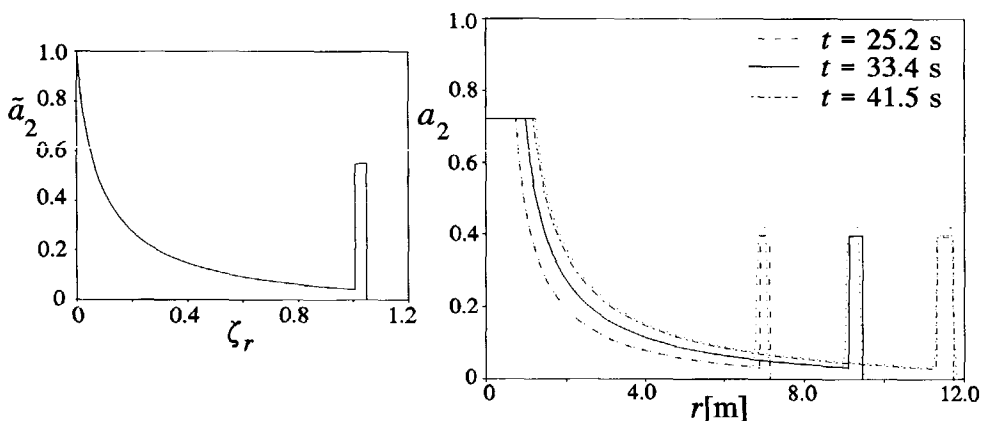


Figure 5.15 Time evolution of the 2-DH self-similar solution in physical coordinates. Dotted line is the numerical solution (Garvine's '84 data).

To illustrate the time-evolution of the presented self-similar solution, results computed with these data are plotted in figure 5.15. On the left side of this figure the solution is plotted in dimensionless coordinates; on the right side in physical coordinates. Additionally we added numerical results computed with the shock-capturing model

presented in chapter 6. Besides the good agreement between numerical and analytical results, this figure also shows how the rim behind the front remains relatively narrow compared to the traversed distance. Also the linear growth of  $r_0$  with time is visible.

The differences to the 1-D (deep-water) self-similar solution becomes apparent if they are visualized for a case with identical inflow conditions. Consider a self-similar partial lock-exchange flow in a 2 m wide flume and a comparable release in a sector

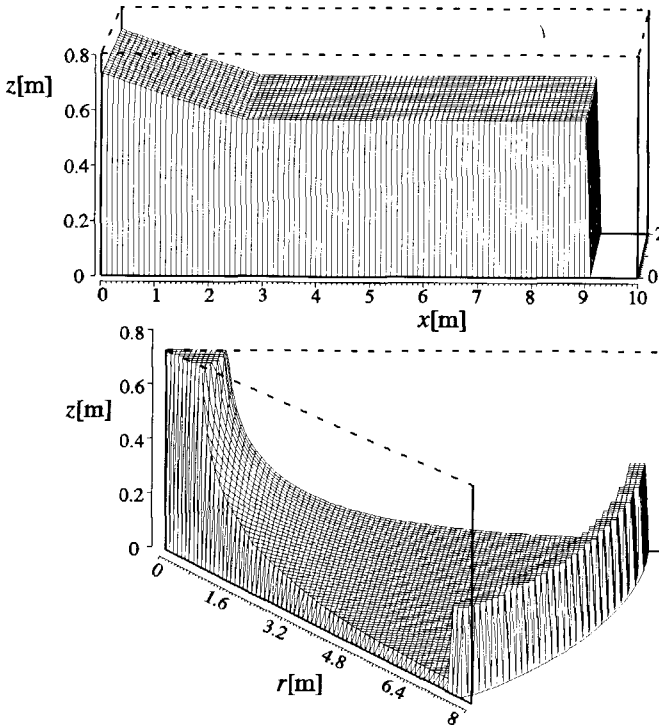


Figure 5.16 3-D representation of self-similar flow in a flume and a sector tank, using identical inflow parameters.

tank which allows for development of self-similar radial flow. In figure 5.16 a 3-D representation of these examples is given, using data as given above for  $t=30$  s with  $Fr_2(0)=1$ . Although both figures are computed with identical inflow parameters, they differ substantially. For the 1-D plane current this solution is composed of a rarefaction wave and a uniform current, without any internal shocks. Its depth remains large compared to the radial flow, and its front celerity is somewhat larger (see also figure 5.17). A notable difference can also be found if the densimetric Froude numbers for these currents are compared. A plot of these Froude numbers in figure 5.17 shows that they become extremely large for the spreading part of the 2-D flow

(a maximum value of about 8.5 for radial flow as against about 1.4 for 1-D flow).

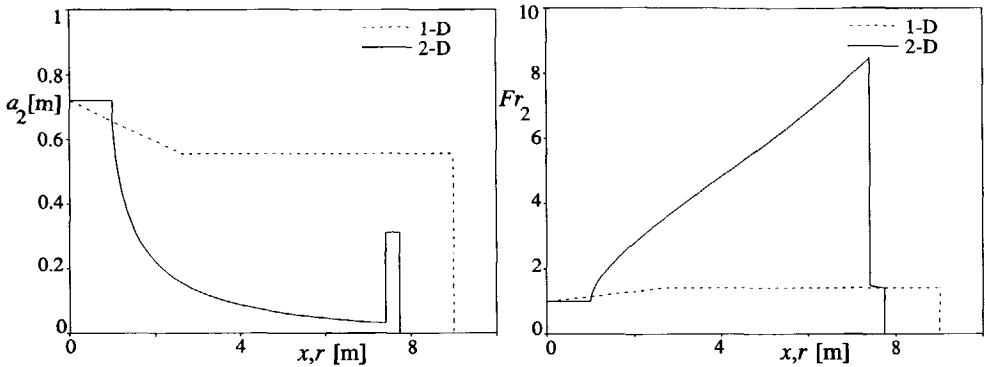


Figure 5.17 Comparison of depths and densimetric Froude numbers for a 1-D plane current and a 2-D axisymmetric current.

Due to this large value the interfacial-mixing rate must be correspondingly large. This phenomenon was observed in laboratory in a salt-water current collapsing in a sector tank by Rottman and Simpson (1984). Their experiments showed how multiple fronts are formed by means of stretching of large amplitude Kelvin-Helmholtz vortices which are generated by the greater shear in these flows. This process results in an increased mixing rate and a larger mixing-layer depth. Also McClimans (1978) reported this vortex formation at the front of a riverine fresh-water plume entering a saline fjord. Clearly this effect is not accounted for in the analytical solution presented here, and therefore it cannot be used for an exact representation of these experiments.

Using our numerical model (chapter 6), computing the entrainment velocity by the relation of Parker et al. (1987), we attempted to simulate the experiments of Rottman and Simpson in their sector tank. From sequential shadowgraphs of two experiments of a collapsing volume of salt water, contours are drawn and compared to numerical results. The experiment is initiated by removing a gate between fresh and salt water located at  $r=0.6$  m. The total water depth  $a$  in the tank is 0.4 m,  $g'$  is  $0.47$  m/s<sup>2</sup>, and the ratio between initial depth and total depth is given by:

$$\begin{aligned} \text{Experiment 1:} & \quad a_{2o}/a = 1 \\ \text{Experiment 2:} & \quad a_{2o}/a = 0.375 \end{aligned}$$

Time scales of numerical computations are adjusted to enable a reasonable fit with the shadowgraphs (Rottman & Simpson did not report time scales). In figure 5.18 results are plotted for experiment 1 (comparable to a full lock-exchange flow). Although the formation of multiple fronts rules out the possibility of defining an accurate interface level, it is shown that on the average a good agreement exists between the computed and observed depths. For experiment 2 (comparable to a partial lock-exchange flow), presented in figure 5.19, this conclusion still holds.

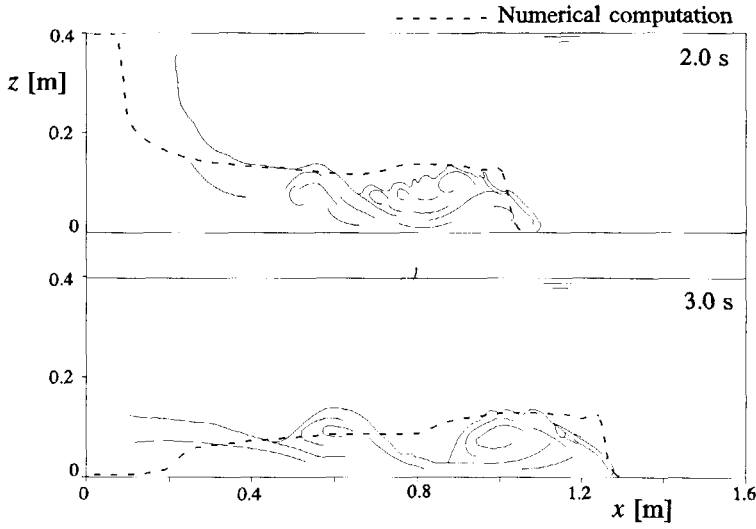


Figure 5.18 Comparison visual data (Simpson & Rottman, 1984) with numerical data for a radial flow in a sector tank, Experiment 1:  $a_{20}/a=1$ .

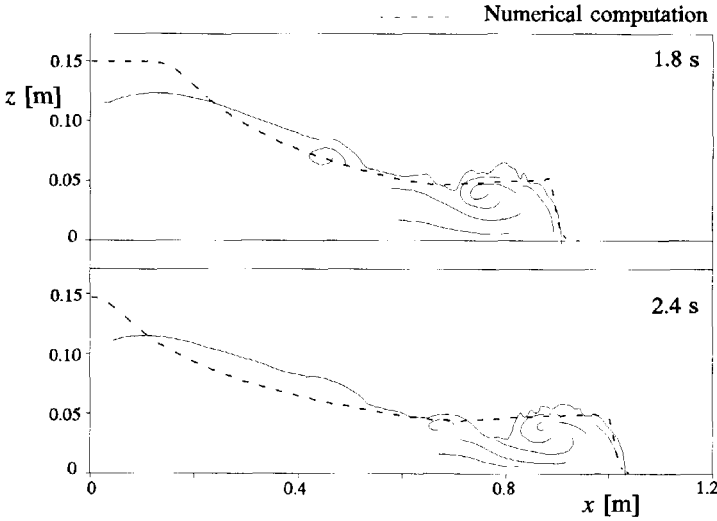


Figure 5.19 Comparison visual data (Simpson & Rottman, 1984) with numerical data for a radial flow in a sector tank, Experiment 2:  $a_{20}/a=0.375$ .

Comparing the structure of the currents for both experiments, it can be seen that the vortex formation in experiment 1 is more significant. Simpson & Rottman explained this difference by the greater shear at the interface of the fluids. As this shear-effect is governed by the overall Richardson number  $Ri_0$  which is equal to  $Fr_2^{-2}$ , these

parameters must reveal this effect.

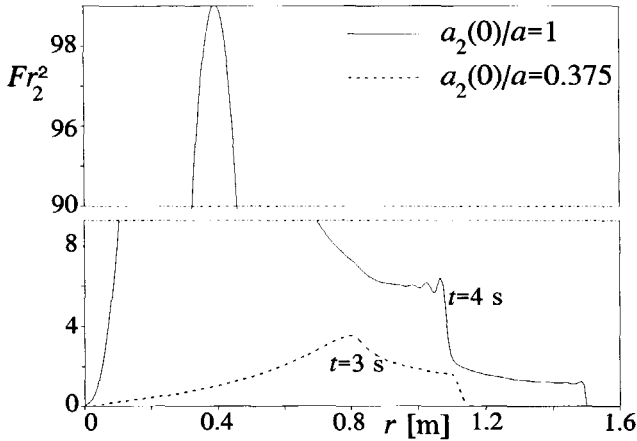


Figure 5.20 Numerically computed densimetric Froude numbers for the two-experiments without accounting for entrainment.

Indeed, a plot of  $Fr_2$  in figure 5.20 computed for the respective experiments without accounting entrainment shows that for experiment 1 the Froude numbers are significantly larger ( $Ri_0$  is much smaller). Consequently entrainment will be much larger in this experiment (see also chapter 2).

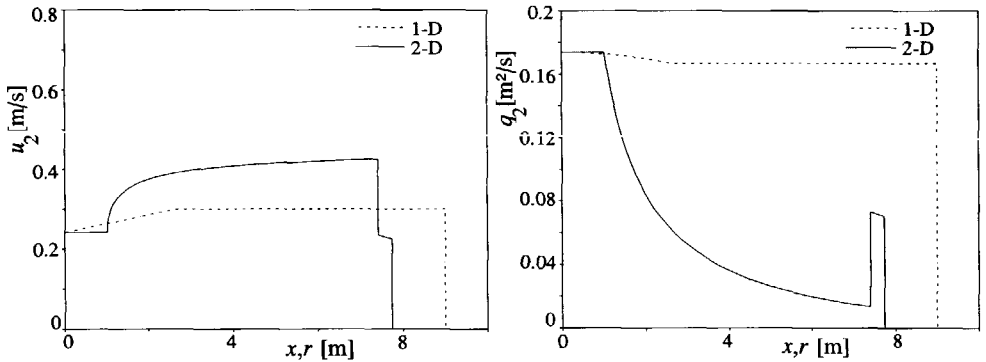


Figure 5.21 Comparison of velocities and discharges for a 1-D plane current and a 2-D axis-symmetric current (Garvine's '84 data).

Besides the notable difference in interfacial mixing between 1-D plane and 2-D radial currents, more deviations of parameters can be distinguished by analysing the self-similar solutions. Looking back at the example of figures 5.16 and 5.17 it has been shown that a significant difference exists in depths, Froude numbers and flow structure. Furthermore, as illustrated in figure 5.21, discharges vary in a similar



manner as underflow depths, but velocities remain quite constant. All velocity related processes, such as bottom friction and erosion are not that different in magnitude for both experiments.

A numerical example illustrating the effect of entrainment  $w_{ie}$  on the frontal region of the plume is given in figure 5.22 for  $t=33.4$  s.

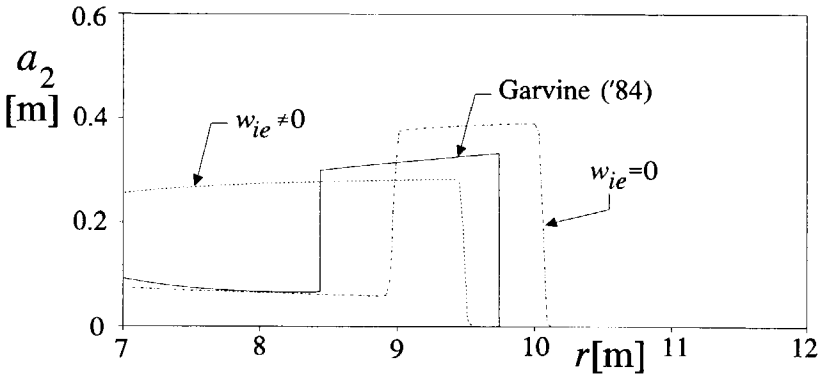


Figure 5.22 Computed effect of entrainment on a radially developing plume, and comparison to numerical solution of Garvine (1984).

For the computations a fixed value of  $r_0$  ( $=1$  m) is used for all time steps, so the current in this example is not self-similar. Due to entrainment the head of the current is lowered and widened, and its celerity is affected. Not surprising is the good agreement between our numerical result (with  $w_{ie}=0$ ) and the numerical result of Garvine. Although Garvine used a finite-difference form of the characteristic equations, the basic equations and internal-jump relations are identical to ours. Therefore any appropriate numerical solution method will always converge to the solutions presented in figure 5.22. Only a minor difference between Garvine's and our results is caused by the different shock-relation at the front. Garvine used a shock-fitting approach where the shock-relation is a boundary condition for the numerical solution, and contains some empirical coefficients to account for 3-D physical processes at the front.

In figure 5.23 these computations are extended even more by incorporating bottom friction. As entrainment clearly lowers the head and raises the body of the current, bottom friction only lowers the head. Also the front celerity is reduced by the effect of friction on the following current. Reduction or increase of front celerities by friction and entrainment is not as noticeable in 1-D plane currents as in 2-D axisymmetric currents (e.g. compare the 1-D results in sub-section 5.2.3).

The magnitude in which 1-D and 2-D results deviate is greatly determined by the ratio between the radius of the near-field region  $r_0$  and the boundary depth  $a_2(0)$ . By

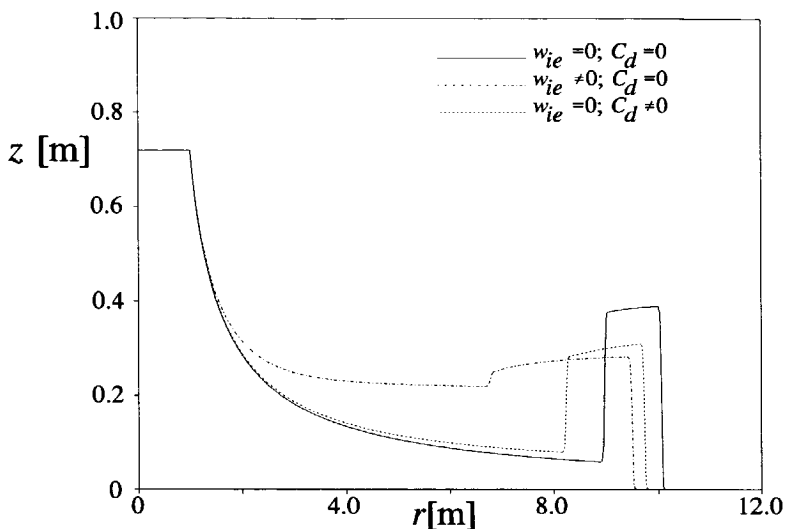


Figure 5.23 Numerically computed effects of entrainment and bottom friction on a 2-D radial flow ( $t=33.4$  s).

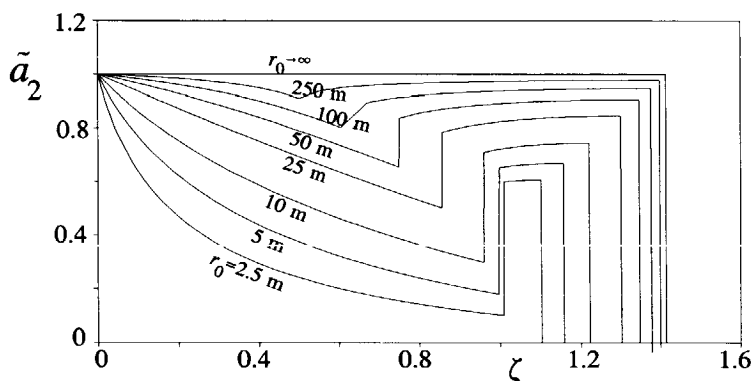


Figure 5.24 Dependence of 2-D self-similar solutions on the ratio  $r_0/a_2(0)$ .

increasing this ratio  $\bar{r}_0$  the 2-D self-similar solution approaches the corresponding 1-D self-similar solution. In figure 5.24 this is illustrated by increasing  $r_0$  for Garvine's data as presented before. The 1-D self-similar solution for this example consists of a uniform flow with  $\zeta_f = \sqrt{2}$  and  $a_2(r) = a_2(0)$ .

The other parameters which determine the shape of the self-similar solution can also be varied to illustrate the dependence. For instance  $Fr_2(0)$  can be raised (starting from unity), or  $C_s$  (or  $g'$ ) can be varied. To some extent the dependence presented for 1-D plane currents in the previous section also applies for these 2-D currents. It does not

add many new insights in the physical behaviour of these currents by presenting these analyses again for the 2-D self-similar solution. Furthermore it is possible to find a wider range of self-similar solutions by introducing other similarity variables. For instance the approach of Grundy & Rottman (1986) using the phase-plane method can be used to achieve this target. These extensions of the theory might be topics for further research.

The 2-D analytical solution in this section is developed for a gravity current intruding into a very deep ambient fluid, i.e. represented by a one-layer model. The extension of this theory to two-layer flow with shallow ambient flow will result a in higher and slower front due to the ambient flow effect on the shock-relation as described for the 1-D self-similar flow. Numerical calculations based on Garvine's data with  $r_0 = 1$  are carried out to illustrate this effect in figure 5.25. At the upper boundary the total discharge  $q(r_0)$  is set equal to the underflow discharge  $q_2(r_0)$  to prevent a return flow into the near field (which is physically not admissible).

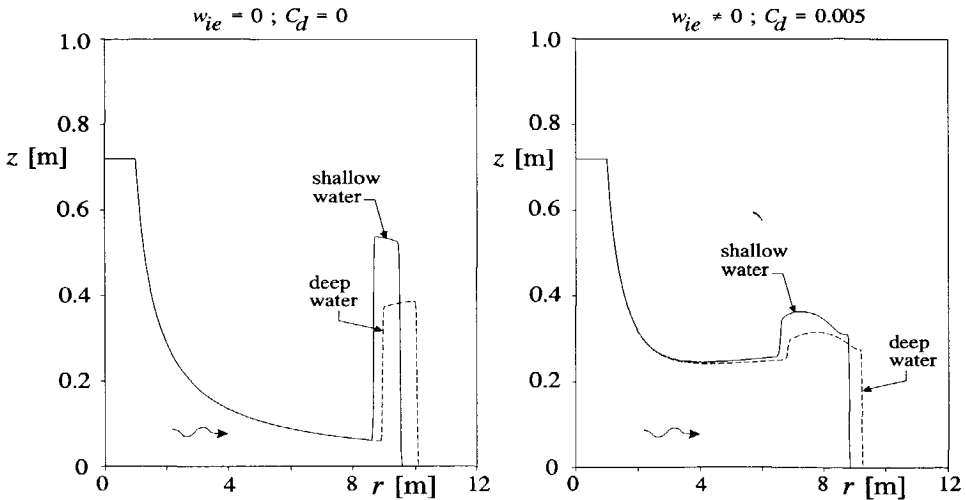


Figure 5.25 Numerically computed radial underflow (after  $t=33.4$  s) in an ambient fluid with depth  $a=3.0$  m compared to a deep ambient fluid ( $a \rightarrow \infty$ ).

Clearly the left plot shows how, without friction and entrainment, the front becomes higher and the interface slope at the rim is reversed. Here an analogy to 1-D high discharge solutions emerges. In the right plot is shown how in shallow reservoirs the underflow with entrainment and friction reveals a similar trend. Analogous a comparison can be made between the self-similar conservative underflow and a turbidity current with sediment deposition. In figure 5.26 numerical results are given for a turbidity current based on the previously used data with sediment particles of  $160 \mu\text{m}$  with a fall velocity of  $0.018$  m/s, computed with  $C_D=0.005$  and with entrainment. Due to deposition the density of the turbidity current is rapidly decreased, and the

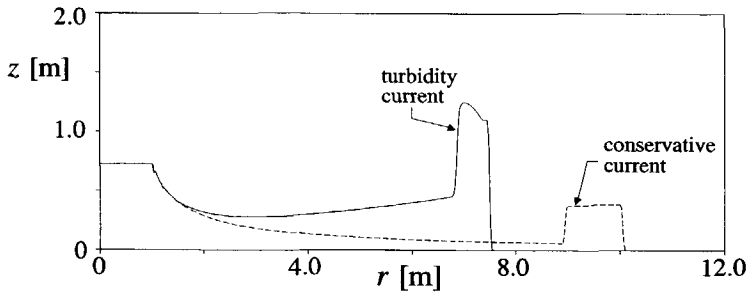


Figure 5.26 Numerically computed radial turbidity current (after  $t=33.4$  s) compared to a self-similar density current.

front decelerates and rises. On the other hand dilution by interfacial mixing is less intense due to lower velocities in the following current. In figure 5.27 the particle concentration is plotted for this example and compared to dilution effects only by entrainment in the deep water computation of figure 5.25.

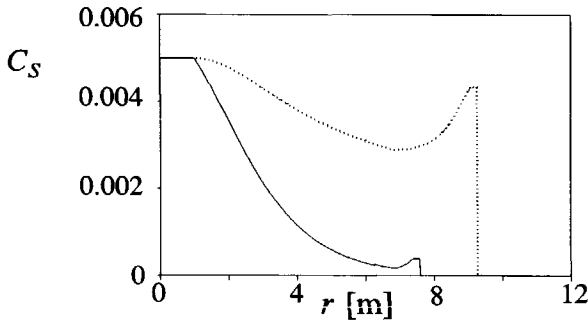


Figure 5.27 Computed volumetric concentrations for turbidity current (drawn line) and conservative current with entrainment (dotted line).

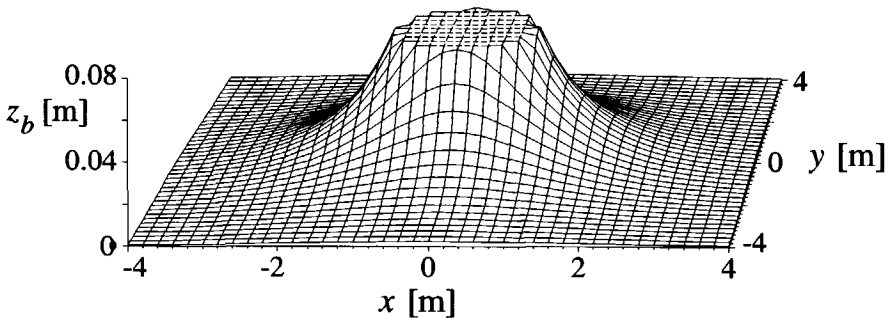


Figure 5.28 Bed-morphology computation for a radial depositing turbidity current.

As expected the density loss by settling of sediment is more pronounced, and results in a radial bed-level variation as plotted 3-D in figure 5.27.

Reviewing the latter examples it is clear that the 2-D self-similar solution cannot be used generally to explain the behaviour of all observed density currents. The sensitivity of the exact solution to friction, sedimentation, interfacial mixing and reservoir depth is an important argument to switch from the limited analytical approach to more complete numerical solutions. A similar reasoning holds for the 1-D model in section 5.2. The construction of the numerical model used for some of the examples in this section is the topic of the following chapter.



# Chapter 6

## Numerical model

### 6.1 Introduction

The solution of the presented 2-layer mathematical model for sedimentation and turbidity current simulation in a reservoir has to be found by means of integration in time and space. Due to the complexity and non-linearity and non-homogeneity of the basic equations, and the presence of discontinuities this solution requires a numerical integration method. In chapter 5 it is shown that only in strongly simplified situations the use of analytical methods is justified. In general situations a finite difference solution can be derived which approximates the exact solution if the model is discretized by appropriate finite-difference operators. The choice of such a numerical scheme and the solution algorithms for the chosen approach is the topic of this chapter.

In the field of computational fluid dynamics (CFD) there is a large number of numerical tools available to select from. Since the rise of the digital computers this number has grown enormously. Often it seems that for every new group of applications a new numerical scheme is invented. Then such a new generation of schemes and algorithms is usually an improved form of an already successful one. With respect to discontinuous flows, we owe the development of computational methods to the fluid dynamics branch emerging from the aeronautical science. CFD codes for the design and analysis of transonic flow past airfoils and wings have become standard tools of the aircraft industry. At this point the engaging field of aerodynamics links up with that of hydraulic engineering, proceeding from the analogy between compressible flows in gas dynamics and open-channel flow. Notably the last decade the progress of CFD in computing discontinuous shallow water flows has increased significantly.

The first representatives in the field of CFD for discontinuous flows were perhaps the first-order explicit schemes of Lax or Lax-Friedrichs (1954). Some of their variants are still in use. Later a family of second order space-centred explicit schemes were derived from the basic Lax-Wendroff (1960, 1964) scheme. For instance the two-step, i.e. predictor corrector, Richtmyer (Richtmyer and Morton, 1967) and MacCormack (1969) schemes, or the more general  $S_x^{\beta}$  schemes by Lerat and Peyret (1974, 1975). These schemes are still very popular, especially for

discontinuous fluids and gasses. To overcome the limitations on the time step for stability imposed by the CFL condition (Courant-Friedrichs-Lewis condition), a variety of schemes with implicit properties has been developed. For instance we may think of the widely used Preissmann's (1960) scheme, the Beam-Warming (1976, 1978) scheme, or the very popular Alternative Direction Implicit (ADI) method for 2-D implicit schemes. A treatment of various schemes can be found in textbooks for CFD, such as Abbott and Basco (1989), Hirsch (1990), Vreugdenhil (1989, 1994), and Tan Weiyan (1992). Furthermore an overview of some relevant numerical methods is given in section 6.2.

The choice of the numerical solution method for our model is determined by the following considerations (in random order):

- 1 - The numerical computations are primarily considered as a tool for simulating the physical behaviour of the model as derived herein. We are not aiming for a new computational method.
- 2 - Robustness of the method is required. A method has to be chosen which has proved its applicability and suitability for models similar to ours.
- 3 - The computational effort required for computation is only a weak constraint.
- 4 - The propagating front of a turbidity current requires the computation of a shock wave. This is usually considered as a Riemann problem defined as an initial value problem in which two constant states are separated by a discontinuity at time  $t=0$ . However, from an engineering point of view we only need to estimate the approximate position and speed of the shock, and not the details of the transition. For morphological computations the continuous flow regions are often far more important.
- 5 - It must be possible and simple to extend the numerical scheme used for 1-D flows to 2-DH flows.
- 6 - The mathematical 2-layer model is essentially similar to 1-D (and 2-DH) shallow water models. Consequently also the numerical treatment of the model can be derived from experience in shallow water flow.

In the following section 6.2 an overview is given of numerical methods which are studied whether they can be used to compute our discontinuous flow. At the end of that section MacCormack's scheme (MacCormack, 1969) is selected from these alternatives judging from the criteria listed above. A description of this scheme and the discretization of the 1-D model is the topic of sections 6.3 and 6.4. This involves the discretization of the decoupled barotropic and baroclinic flow equations separately. Generally the method results in very small errors and high accuracy, but near discontinuities these errors intensify and result in oscillations without any physical meaning. In section 6.5 and 6.6 is shown how these disturbing oscillations can be damped or eliminated by adding a viscosity term to the numerical equations.

In section 6.7 special attention is given to the implementation and numerical



treatment of the boundary conditions. This is actually a very important subject since the boundary information along with its errors will eventually cover the full computational domain (i.e., spreading out along the characteristics). The overall accuracy and stability of the model is therefore highly dependent on the correct boundary treatment. In a similar way the initial condition, which can also be considered as a type of boundary condition, has a significant impact on the final solution. In section 6.8 some alternative initial conditions are given and evaluated.

Using artificial viscosity and optimizing the boundary scheme still does not fully guarantee high accuracy and prevent instability. Therefore an analysis of accuracy and stability of the numerical equations is made in section 6.9 by considering the local truncation error and solutions in terms of Fourier series (von Neumann analysis). These results revealed some important restrictions and advantages of MacCormack's as well as Lax-Wendroff's (1960, 1964) scheme.

In section 6.10 is shown that for robustness and a better convergence to realistic solutions some additional conditions have to be added to the model. In particular this means the inclusion of a shock tracking technique and a lower limit to the dependent variables. Furthermore the methodology of computing decoupled flow and morphology is presented for the proposed model. This chapter is concluded in section 6.11 with a review of the most important results.

## **6.2 Overview of numerical methods for discontinuous flows**

### **6.2.1 Introduction**

The mathematical model consists of six (1-D) or eight (2-DH) first-order quasi-linear partial differential equations, while the barotropic (external) and baroclinic (internal) parts of flow are considered to be decoupled. The most important constraint we impose on the numerical model, is the ability to compute shocks in the internal flow (external flow is assumed to be continuous). A selection of the numerical methods can already be done by considering the two possible basic techniques to compute the front of the turbidity current numerically:

- Shock fitting (see figure 6.1): The method is most accurate (e.g., see Moretti, 1975, Tan Weiyan, 1992). The front is considered as an internal moving boundary condition in the computational domain which is continuous for the rest. The internal boundary conditions are the Rankine-Hugoniot conditions as defined in chapter 4. In 1-D models a Lagrangian (sub-) coordinate system is usually defined moving with the shock, since the location of the front is not explicit and may otherwise lose its sharp profile.

This usually involves a deforming grid. In 2-DH models the method may encounter large difficulties due to complexity of the shocks and their mutual interactions. Therefore it is rarely applied for in 2-D cases.

Shock capturing (see figure 6.1): Continuous flow and shocks are all solved by means of the same scheme without using the shock relations. This technique has already a long history of applications for aeronautics and aerospace gas dynamics as well as for hydraulics, and due to its merits it is now commonly used. The discontinuity is smeared over at least one grid cell (cf. fig. 6) and is therefore less sharp. For the propagation of the turbidity current front, which has a much smaller length scale than the reservoir, it is sufficient to use a reliable and simple shock-capturing scheme.

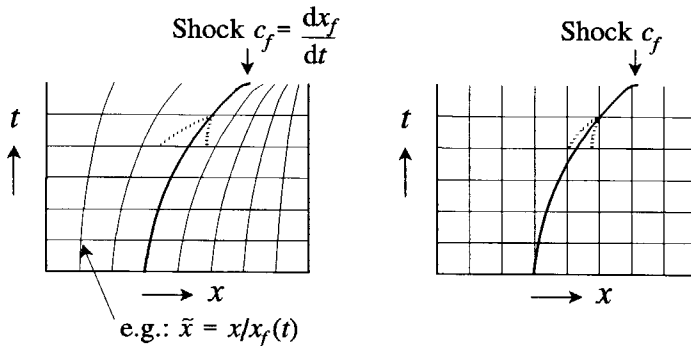


Figure 6.1 Shock-fitting (left) versus shock-capturing (right) for a moving jump. Dashed lines represent pos. celerities  $\phi^+$  at each side of the jump. In a deformed grid the right  $\tilde{\phi}^+ < 0$ .

For 1-D models with a moving turbidity current front the shock-fitting technique can be used for its high accuracy and the possibility to introduce additional energy-loss parameters in the shock relation for the front, according to chapter 4 (e.g. see Bonnacaze et al., 1993). However, if during the computation other shock waves appear in the flow, such as internal hydraulic jumps, this technique soon becomes disordered and loses its robustness due to the requirement of additional (moving) internal boundary conditions, and deforming grids. By using shock-capturing techniques the organization of the computations is not affected by the existence of various discontinuities in the computational domain, even if they are interacting. As mentioned above this organizational aspect is even more significant for 2-DH CFD codes. Eventually a blend of shock-capturing and shock-fitting techniques can be used to keep control. For instance the model for a 'lock-exchange' turbidity current by Bonnacaze et al. (1993) computed the front as a moving boundary (i.e. shock-fitting) and the trailing internal jump was captured using a two-step Lax-Wendroff scheme (see next section).

These arguments already indicate that shock-capturing techniques are favourite for

the present application, even more if we consider that for engineering purposes the robustness and ease of them greatly compensate the loss of accuracy. The benefit of shock-fitting techniques for our case is the possibility of introducing an additional energy-loss effect at the front of the turbidity current. However, it is shown in chapter 4, that by using appropriate basic equations the front can be computed with reasonable accuracy without additional empirical loss terms (hence without additional calibration coefficients).

An essential property of shock-capturing techniques is the addition or presence of pseudo-viscosity for damping the parasitical numerical oscillations ('wiggles') near the shock. Pseudo viscosity has a smoothing effect near the jump, while in the gradually varied flow region it is at least one order of magnitude smaller than the order of the numerical scheme. Some techniques require a significant additional term in the momentum (and often in the continuity) equation, called artificial viscosity. Others (modern schemes) take the advantage of their numerical dissipative mechanism, e.g., coming from even-order terms in the truncation error of the scheme. The latter is called scheme or numerical viscosity.

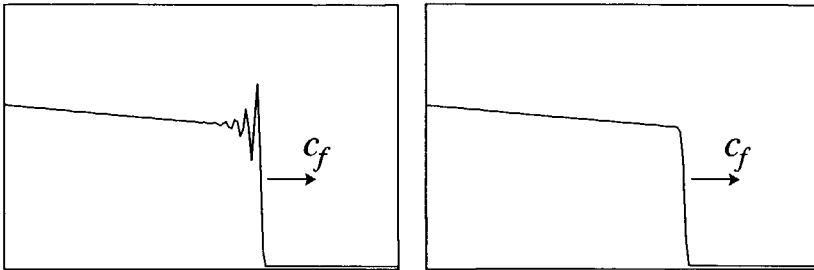


Figure 6.2 Front computed with MacCormack's scheme without pseudo-viscosity with wiggles (left), and with TVD-viscosity without wiggles (right).

In figure 6.2 two identical computational examples are shown to illustrate the inevitable occurrence of wiggles and the subsequent disappearance of these wiggles by using artificial viscosity with TVD properties (see section 6.3). Often the introduction of artificial viscosity is also required to satisfy the entropy condition to prevent the occurrence of non-physical shocks (Hirsch, 1990). The latter requirement can be seen as an introduction of a dissipative mechanism in the model to stimulate the energy losses associated with the shocks.

The origin of the wiggles lies in the numerical treatment of shocks. The replacement of a derivative by a differential quotient generates an error much larger than the truncation error. Then the solution strongly oscillates (over- and undershooting) because the discontinuity becomes a fixed source continuously emanating disturbances. Expanding a difference equation into a Taylor series, we obtain again the original equation with on the right side higher-order terms added

(e.g. originating from the convective terms). Even-order derivative terms cause physical dissipation (wave-amplitude attenuation) while odd-order derivative terms cause dispersion (phase velocity of the various waves are altered). The orders of these dissipation and dispersion errors are determined by the scheme. A first-order scheme has dissipation and dispersion errors of order 2 and 3 respectively. A second-order scheme has fourth-order dissipation and third-order dispersion. When dissipation is dominant (e.g. order-1 schemes) the solution is smoothed, but if dispersion is significant (e.g. order-2 schemes) parasite oscillations occur near the shock. Furthermore a shift of energy occurs into higher wave numbers near the jump, but due to the finite mesh size the real high frequency waves are treated as low frequency ones resulting in dispersion. We may conclude that oscillations occur when the viscosity term is not present or small and an odd-order dispersive term appears in the differential approximation. An analytical explanation of this conclusion is given in section 6.9 for the chosen numerical scheme.

In section 6.4 we pointed out that the equations are casted in their conservative form. Similarly, to ensure the discretization technique to correctly represent the integral form of these conservation laws, it is important that the scheme is conservative. In other words this means (Hirsch, 1990) that the time derivative of the integral of  $\mathbf{U}$  (the vector of primitive variables) over a given space domain only depends on the boundary flux and not on the fluxes within this domain. Then a unified formulation (Lax, 1957) of all conservative explicit schemes can be written as (here in 2-D form)

$$\mathbf{U}_{ij}^{n+1} - \mathbf{U}_{ij}^n = - \frac{\Delta t}{\Delta x} (\mathbf{f}_{i+1/2,j}^* - \mathbf{f}_{i-1/2,j}^*) - \frac{\Delta t}{\Delta x} (\mathbf{g}_{i,j+1/2}^* - \mathbf{g}_{i,j-1/2}^*) \quad (6.1)$$

For consistency of the scheme the following condition must be satisfied:

$$\begin{aligned} \mathbf{f}^*(\mathbf{U}_j, \dots, \mathbf{U}_{j+k}) &= \mathbf{f}(\mathbf{U}) && \text{when all } \mathbf{U}_j = \mathbf{U} \\ \mathbf{g}^*(\mathbf{U}_j, \dots, \mathbf{U}_{j+k}) &= \mathbf{g}(\mathbf{U}) && \text{when all } \mathbf{U}_j = \mathbf{U} \end{aligned}$$

where  $\mathbf{f}^*$  and  $\mathbf{g}^*$  are the respective discretized numerical flux vectors. For equations with source terms such as friction their discretized equivalents are added to equation (6.1), not to the numerical fluxes.

The different types of schemes with shock-capturing abilities, which have been developed in the past, especially for solving the Euler equations in aerodynamics, can be subdivided into the following groups (after Hirsch, 1990):

- *Space-centred schemes*, such as the Lax-Wendroff (1960, 1964) and Lax-Friedrichs (1954) explicit schemes. Or the two-step explicit schemes of MacCormack (1969) or Lerat and Peyret (1974). Or the implicit schemes by Lerat (1983) and MacCormack (1981).
- *Upwind schemes*, such as the flux vector splitting methods by Moretti (1979) or Steger and Warming (1981). Or the exact Riemann solvers such as the first-order Godunov (1959) scheme and second-order Van Leer (1979)

scheme, and the approximate Riemann solvers such as Harten et al. (1983).

- *High resolution TVD (total variation diminishing) schemes*, such as the explicit TVD upwind schemes by Boris and Book (1973) and Van Leer (1974, 1979) and Harten (1983,1984). Or the implicit TVD upwind scheme by Yee et al. (1985), or the central TVD schemes by Yee (1987).

Each of these groups of schemes are treated in the following sub-sections for 1-D and 2-DH models. We have restricted the overview to explicit methods although there are in each group a number of implicit tools available. For more details on the presented techniques the cited papers and textbooks as Hirsch (1990), Finlayson (1992), Tan Weiyan (1992) and Vreugdenhil (1994) are recommended.

### 6.2.2 Space-centred schemes

Most of the schemes which may be relevant for our model, are based on the second-order accurate scheme of Lax Wendroff, which is centred in space and time, and based on Taylor-expansions. In linearized 1-D conservative form the numerical flux in eq. (6.1) can be written for Lax Wendroff as

$$\mathbf{f}_{i+1/2}^* = \frac{1}{2}(\mathbf{f}_i + \mathbf{f}_{i+1}) - \frac{1}{2} \frac{\Delta t}{\Delta x} A_{i+1/2}(\mathbf{f}_{i+1} - \mathbf{f}_i) \quad (6.2)$$

where  $A$  is the Jacobian matrix of the fluxes .

When accounting for the non-linear fluxes in the equations, many variants exist which are generally structured as explicit predictor-corrector algorithms. Also some implicit variants have been developed in this Lax-Wendroff family of schemes. Although nearly all these schemes have been developed and analyzed for 1-D models, most of them can be easily extended to the 2-D case. An important property of these schemes, as follows from eq. (6.2) is that they are conservative. Furthermore they require a form of artificial viscosity in the vicinity of a shock.

One of the most popular schemes is the second-order accurate two-step version of MacCormack (1969). Examples of the application of MacCormack's method to 1-D shallow-water flow are for instance Fennema & Chaudry (1986), García-Navarro et al. (1992) and Valiani (1993). Applications to 2-DH shallow water flow with shocks were for instance presented by Fennema and Chaudry (1990) and Jiménez and Chaudry (1988). Its merits are impressive simplicity, compactness, easy to use in 2-D cases, order 2 accurate both in space and time, applicability to both continuous and discontinuous flows, and simplicity in the boundary condition procedure as it is not involved with time  $t_{n+1}$ . Its drawbacks are asymmetry (using forward and backward differences in each semi step), the necessity of artificial

viscosity, and sensitivity to the boundary condition procedure adopted. For the latter reasons many modified forms have been proposed. For instance a 2-D form of MacCormack's scheme can be defined in which the scheme is formulated in split form by products of 1-D operators (e.g. see Hirsch, 1990). An implicit version of this scheme was proposed by MacCormack (1981, 1982) by adding an implicit adjustment step to the predictor and corrector steps of the original scheme. The amount of computations increased with a factor of two, but the time-step can be increased up to a factor of three.

By using the centred difference the physical propagation along characteristics is not considered (no distinction of upstream and downstream influences). For continuous functions the Taylor series expansions (the basic concept behind space-centred schemes) can be applied for correct reconstruction, but if a discontinuity appears information is destroyed, and oscillations appear. In the next sub-section the class of upwind schemes is treated which account for physical propagation.

### 6.2.3 Upwind schemes

The class of non-space-centred schemes classified as upwind schemes establish a relation between characteristic propagation properties and the differencing. That means directional space discretizations are applied in accordance with the physical behaviour of the flow. The first upwind scheme was introduced by Courant et al. (1952), followed by a large group of variants (e.g., second-order accurate or implicit upwind schemes) impelled by their good performance in aerodynamics. In the following an overview is given of the different types of upwind schemes which can be used to compute discontinuous flows.

#### *Godunov-type schemes*

A group of upwind schemes, which is based greatly on the physical properties of the model, is the family of Godunov-type schemes. The original Godunov's (1959) method includes the solution of the Riemann problem (solution of Riemann invariants along characteristics near a shock wave) at each time step for each computational cell to find the fluxes through the interfaces of these cells. By introducing the properties of these exact local solutions into the scheme, a very elegant and admirable method is obtained. Various extensions to this approach for more general or more accurate results are usually referred to as flux-difference splitting methods, most of them which use approximate Riemann solvers (e.g., Glaister, 1988, 1990, Roe, 1981a,b, and Osher, 1981). Approximate Riemann solutions are often used since the solution of the Riemann problem is difficult due to non-linearity of the governing equations, which requires an iteration technique.

Often such a time consuming iteration approach is exuberant as only first-order accuracy can be achieved. An example of one of the approximation techniques to speed up things, and which is becoming most popular, is Roe's (1981b) local linearization of the non-linear equations (see also section 6.6).

Although the Godunov-type methods are very strong and physically sound techniques for solving 1-D discontinuous flows, it is quite a job and requires quite a computational effort to solve 2-DH discontinuous flows.

### *Characteristic difference schemes*

In 1-D and 2-D flows the method of characteristics can be used for constructing physically-based schemes. Therefore the compatibility equations are used which hold on the (bi)characteristics. An example of a characteristic difference method is the Moretti (1979, 1987)  $\lambda$  scheme and the dam-break flood-wave model of Katopodes and Strelkoff (1978). Since these methods use the compatibility equations in non-conservative form, they require the shock relations (some sort of shock fitting) to capture shocks. Upwind schemes in (bi-)characteristic direction are used to approximate the characteristic relations. In 2-D flows these methods are mainly used to design characteristic-based schemes rather than a characteristic difference scheme (e.g., increasing accuracy by flux splitting and controlling the numerical dependency domain).

### *Characteristic-based splitting*

The characteristic-based splitting techniques involve flux-vector splitting (FVS) and flux-difference splitting (FDS). The FVS group is formed by directional discretization of flux derivatives (e.g., Steger and Warming, 1981, Van Leer, 1982). For instance the system of 1-D conservative equations is written as

$$\frac{\partial \mathbf{U}}{\partial t} + \frac{\partial \mathbf{f}^+}{\partial x} + \frac{\partial \mathbf{f}^-}{\partial x} = \mathbf{0} \quad (6.3)$$

where  $\mathbf{f}^+$  and  $\mathbf{f}^-$  are associated to fluxes with positive and negative Jacobian eigenvalues respectively (positive and negative characteristic directions). Then  $\mathbf{f}^+$  and  $\mathbf{f}^-$  can be discretized using a backward and forward difference. This approach is more reasonable than a simple upwind scheme where the difference direction is based on the flow direction. The first-order result is dissipative (no artificial viscosity required) and always converges to a physical solution. In gas dynamics there are many alternatives available for splitting the Jacobian matrix of the 1-D Euler equations (e.g., see Tan Weiyan, 1992). Both splitting-first differencing-last, and differencing-first splitting-last are feasible. The latter technique, with limiting after the first step, was posed by Van Leer (1979) and called the MUSCL

technique (Monotone Upwind Schemes for Conservation Laws). It performs better near shocks than the former technique (in getting a smooth transition). Another property of MUSCL technique is the variable extrapolation for the generation of second-order high-resolution upwind schemes. It is possible to rewrite MacCormack's scheme as a FVS scheme if fluxes are split properly.

The approximate Riemann solver developed by Roe (1981a,b) is a FDS scheme, based on the characteristic decomposition of the flux differences over a cell. It extends the linear wave decomposition, which is the exact linear solution to Riemann's problem, to non-linear equations. More details on this splitting technique is given in section 6.6, applied to our non-linear system of equations. Roe's method and that of Osher (1981) are usually classified as approximate Riemann solvers in relation with Godunov-type schemes.

#### **6.2.4 High-resolution schemes: FCT and TVD algorithms**

The flux-corrected transport (FCT) and total variation diminishing (TVD) methods are both based on flux limiters. The governing schemes can be classified as high-resolution schemes in their capability of limiting a shock to a range of 1-2 mesh cells. By replacing the first-order upwind schemes by second-order schemes again oscillations are generated around discontinuities (for the same reasons as in the central schemes). To obtain correct oscillation free solutions the scheme must satisfy the concept of monotonicity (introduced by Godunov, 1959: no creation and amplification of local extremes) or for 2-order schemes the concept of bounded total variation (introduced by Harten, 1983: if the equations are non-linear with non-TVD exact solutions). Also an entropy condition must be satisfied to obtain physically acceptable solution. For second-order schemes to satisfy these conditions a non-linear component, different from artificial viscosity, can be introduced in discretizations: flux limiters (e.g., Van Leer, 1973,1974) which prevent the appearance of over- and undershoots. In general, upwind schemes cannot avoid wiggles without flux limiters. Except for first-order upwind schemes, where they are usually removed by the intrinsically monotonicity of the 1-order scheme. In contrast with artificial viscosity, which allows oscillations to develop but subsequently damps them, flux limiters prevent the generation of oscillations.

FCT algorithms (anti-diffusive two-step methods) were proposed by Boris and Book (1973) and are designed to avoid the occurrence of negative density when solving mass continuity equations with steep gradients, i.e. guarantee positivity. Therefore a diffusive term (with numerical viscosity  $\nu$ ) is added to the order-1 predictor, while an anti-diffusive term (with coefficient  $\mu$ ) is introduced in the corrector to obtain second-order accuracy and to cancel that part of numerical viscosity which exceeds the demand of positivity. By limiting the anti-diffusive flux



(limiting  $\mu$ ), so that no new maxima and minima can appear or that the existing ones cannot be amplified, the requirement of limiting is exactly monotonicity preserving. Hence stability can be ensured by preventing the occurrence of spurious oscillations. The corrected anti-diffusive term is called the corrected flux. The main disadvantage of FCT is the necessity of adjusting the values of the parameters.

Since conservative monotonic schemes for non-linear equations can only be order-1 accurate, a class of high resolution schemes is developed satisfying the condition of total variation boundness (Harten, 1983,1984), which is a weaker and more general condition than monotonicity. This class of 1-D TVD schemes is based on the total variation of a discrete numerical solution given by

$$TV(u) = \sum_i |u_{i+1} - u_i| \quad \left( \text{if } TV = \int \left| \frac{\partial u}{\partial x} \right| dx \right) \quad (6.4)$$

The 1-D numerical scheme is TVD if

$$TV(u^{n+1}) \leq TV(u^n) \quad (6.5)$$

Therefore all monotone schemes are TVD, and all TVD schemes are monotonicity preserving ( $u^{n+1}$  remains monotone if  $u^n$  is monotone, hence no overshoots can be created). However, the above conditions can only result in an order-2 scheme if the scheme is non-linear (Hirsch, 1990). For instance this can be done by using more than three points (e.g. 5 points) in a non-linear way in the definition of numerical fluxes. The methodology for defining a high-resolution scheme is (after Hirsch, 1990):

- 1) Select a first-order monotone numerical flux.
- 2) Extend the numerical flux to second-order accuracy.
- 3) Use non-linear limiter functions  $\Psi$  to ensure TVD conditions (restricting the amplitude of gradients appearing in second-order terms).
- 4) Select time integration procedure (best suited for unsteady flows is the combined space-time methods in line with the Lax-Wendroff technique). Some adaptation may be required of the fluxes to ensure TVD conditions.
- 5) Check the entropy condition for the 'limited' higher-order scheme, since TVD cannot guarantee that the solution satisfies this condition.

Analyses of  $\Psi$  limiters were given by Sweby (1984, 1985) and Roe (1985). By using these limiters the Lax-Wendroff type schemes (also MacCormack) can be made TVD under certain constraints of  $\Psi$ . Various limiters have been reported in literature, for instance Van Leer (1974) or Roe's (1985) 'Superbee' limiter. Harten (1983) introduced a modified flux to an order-1 upwind flux, leading to order-2 accuracy and followed by TVD limiting (see also Yee et al. 1985). Sweby (1984) proposed a flux limiter to modify the FCT method into a family of high-resolution

schemes.

The TVD approach can be considered as a kind of artificial viscosity continuously dissipating energy (e.g. see Hirsch, 1990), avoiding the adaptation of 'empirical' viscosity. Consequently solutions become first-order near strong gradients, while remaining second-order in smooth regions. TVD can be used with any two-step Lax-Wendroff type schemes resulting in sharp oscillation free profiles. For instance the 1-D computation of discontinuous flows in open channels with a TVD MacCormack scheme was carried out with satisfactory results by García-Navarro et al. (1992) and Valiani (1993). Although strictly speaking the TVD property only holds for homogeneous scalar non-linear conservation laws and homogeneous systems of equations with constant coefficients, García-Navarro's and Valiani's results indicate an accurate performance on the non-linear system of shallow-water equations with non-homogeneous terms (friction). Possibly the effects of external forces and interacting waves, which might increase the solution and hence increase the total variation, are not dominant for these cases.

Formally TVD is a 1-D concept, but nevertheless it is applicable to the 2-D case as well. In the 2-D case the total variation may be defined as

$$TV(u) = \int_{\Omega} \|\nabla u\| dx dy = \int_{\Omega} (|u_x| + |u_y|) dx dy = TV_x(u) + TV_y(u) \quad (6.6)$$

where

$$TV_x(u) = \Delta y \sum_{i,j} |u_{i+1,j} - u_{ij}| \quad (6.7)$$

Although a 2-D TVD scheme with a specific 2-D flux limiter is at best order-1 accurate (Goodman and Le Veque, 1985), the combined use of space-splitting technique and a 1-D order-2 TVD scheme can provide approximately second order accuracy and sharp resolution. The TVD schemes proposed by Yee (1987) were used to solve the 2-D Euler equations and the Navier Stokes equations. Yang and Hsu (1993b) extended the 1-D TVD and ENO (essentially non-oscillatory scheme proposed by Harten and Osher, 1987) schemes as presented by Yang et al. (1993a), to compute 2-D discontinuous shallow water flow. Therefore they adopted Van Leer's (1982) flux vector splitting and the Strang-type (Strang, 1968) dimensional splitting method. Still these TVD techniques are in a stage of development and have not fully proved their robustness for 2-DH flows in open channels. Furthermore the additional number of algebraic operations make the approach rather costly.

### 6.2.5 Choice of the numerical solution method

In the previous sub-sections a large number of alternatives is presented which can be used for solving our model with a turbidity-current front. To choose from these alternatives they have been tested with the conditions proposed in the introduction (section 6.1). Summarizing these conditions which we impose on the numerical technique: No ambition to develop a new method, robustness is required, computational effort is of minor importance, approximative shock capturing must be possible, computation of continuous flow regions must be accurate, one method must be used for all computations and it must be extendable to 2-DH cases for future research.

To satisfy a reasonable accuracy in continuous flow regions a numerical method must be chosen with at least order-2 accuracy in these regions. Furthermore it must satisfy the conservation property to enable shock capturing. For instance the Lax-Wendroff type or second-order upwind schemes perform well here. Other methods, although they may have a very good shock resolution, do not necessarily perform better. This is an important argument to choose from a simple group of schemes which has proved its robustness in computing shallow-water flow with bores and dam-break waves.

In line with the modelling approach a motivation can be given for choosing an explicit scheme in favour of an implicit scheme. Firstly, notably in situations with nearly critical internal flow, there are no significant differences in characteristic celerities in each of the decoupled computation steps (external flow, or internal flow with morphology). For each computation a space and time step can be chosen according to desired accuracy and stability. Secondly there are discontinuities in the flow for which implicitly obtained solutions often do not satisfy conservation requirements (Tan Weiyan, 1992) due to linearization. Overall can be concluded that due to accuracy limitations (only low Courant numbers allowed), and also due to the presence discontinuities, the computational effort per time step required for an implicit solution are not compensated, and in that respect simple explicitly obtained solutions are superior.

As stated before the MacCormack (1969) scheme, although it is slightly old-fashioned, is a very simple and robust centred scheme with order-2 accuracy. It suits the accurate computation of the continuous flow sections (in which characteristics are positive and negative), as well as the approximative computation of the turbidity-current front. Artificial viscosity is required to prevent parasitic oscillations (sections 6.5, 6.6). It has proved its applicability to 2-DH shallow-water flow, and it has shown to compute shocks which are sufficiently accurate for engineering purposes. For instance Van Leer et al. (1987) demonstrated with applications the superior behaviour of the MacCormack scheme over FDS and FVS

methods in continuous regions. Comparisons made by Fennema and Chaudry (1986, 1990) between the performance of Moretti's (1979)  $\lambda$ -scheme, Gabutti's (1983) scheme, Preissmann's (1961) scheme, and MacCormack's scheme also revealed the excellent performance of the latter. This conclusion was also supported by the results of Jiménez and Chaudry (1988) in comparison with measurements. Nevertheless the use of this scheme requires caution with respect to accuracy and stability as is shown in section 6.9.

The description and application of the MacCormack scheme to the reservoir sedimentation model is treated in the following sections.

### 6.3 MacCormack scheme

The numerical scheme proposed by MacCormack (1969) is a Lax-Wendroff type scheme. It differs from other Lax-Wendroff type schemes in its simple and straightforward treatment of non-linear fluxes by means of a two-step (predictor and corrector) approach. For linearized equations the MacCormack method can be reformulated as the original Lax-Wendroff scheme. This allows us to adopt the results from linear numerical analyses of the Lax-Wendroff scheme with respect to stability and accuracy.

Consider the general 2-DH formulation of the model in conservative form with source vector  $\mathbf{Q}$  (which contains for example friction and entrainment terms):

$$\frac{\partial \mathbf{U}}{\partial t} + \frac{\partial \mathbf{f}(\mathbf{U})}{\partial x} + \frac{\partial \mathbf{g}(\mathbf{U})}{\partial y} = \mathbf{Q}(\mathbf{U}) \quad (6.8)$$

Its quasi-linear form, with associated Jacobian matrices  $A_x$  and  $A_y$ , becomes

$$\frac{\partial \mathbf{U}}{\partial t} + A_x(\mathbf{U}) \frac{\partial \mathbf{U}}{\partial x} + A_y(\mathbf{U}) \frac{\partial \mathbf{U}}{\partial y} = \mathbf{Q}(\mathbf{U}) \quad (6.9)$$

In a 1-D formulation (eliminate  $\partial/\partial y$  terms) MacCormack's scheme is then defined as follows

$$\begin{aligned} \bar{\mathbf{U}}_i &= \mathbf{U}_i^n - \frac{\Delta t}{\Delta x} [\mathbf{f}_{i+1}^n(\mathbf{U}_{i+1}^n) - \mathbf{f}_i^n(\mathbf{U}_i^n)] + \Delta t \mathbf{Q}_i^n(\mathbf{U}_i^n) + \frac{\Delta t}{\Delta x} (\mathbf{D}_{i+1/2}^n - \mathbf{D}_{i-1/2}^n) \\ \bar{\bar{\mathbf{U}}}_i &= \mathbf{U}_i^n - \frac{\Delta t}{\Delta x} [\bar{\mathbf{f}}_i(\bar{\mathbf{U}}_i) - \bar{\mathbf{f}}_{i-1}(\bar{\mathbf{U}}_{i-1})] + \Delta t \bar{\mathbf{Q}}_i(\bar{\mathbf{U}}_i) + \frac{\Delta t}{\Delta x} (\bar{\mathbf{D}}_{i+1/2} - \bar{\mathbf{D}}_{i-1/2}) \\ \mathbf{U}_i^{n+1} &= 1/2(\bar{\mathbf{U}}_i + \bar{\bar{\mathbf{U}}}_i) \end{aligned} \quad (6.10)$$

Vector  $\mathbf{U}_i^n$  is the vector of primitive variables defined at grid point  $[i \cdot \Delta x, n \cdot \Delta t]$

while  $\mathbf{U}_i^{n+1}$  is defined on an advanced time level  $[i \cdot \Delta x, (n+1) \cdot \Delta t]$ . Vector  $\bar{\mathbf{U}}_i$  is the predictor solution of  $\mathbf{U}$ , and  $\bar{\bar{\mathbf{U}}}$  is the corrector solution of  $\mathbf{U}$ . Vector  $\mathbf{D}$  is an eventual artificial viscosity term which can be added to the scheme to prevent the occurrence of spurious oscillations. More about this term can be found in section 6.5 and 6.6. Term  $\mathbf{f}$  is the discretized flux vector applied to local values of  $\mathbf{U}$ . Note the numerical fluxes for the scheme can be written as

$$\mathbf{f}_{i+1/2}^* = \frac{1}{2}(\mathbf{f}_{i+1}^n + \bar{\mathbf{f}}_i) \quad ; \quad \mathbf{f}_{i-1/2}^* = \frac{1}{2}(\mathbf{f}_i^n + \bar{\mathbf{f}}_{i-1}) \quad (6.11)$$

such that the numerical method can be formulated as

$$\begin{aligned} \Delta \mathbf{U}_i = \mathbf{U}_i^{n+1} - \mathbf{U}_i^n = & -\frac{\Delta t}{\Delta x}(\mathbf{f}_{i+1/2}^* - \mathbf{f}_{i-1/2}^*) + \frac{\Delta t}{2}(\mathbf{Q}_i^n + \bar{\mathbf{Q}}_i) + \\ & + \frac{1}{2} \frac{\Delta t}{\Delta x}(\mathbf{D}_{i+1/2}^n - \mathbf{D}_{i-1/2}^n + \bar{\mathbf{D}}_{i+1/2} - \bar{\mathbf{D}}_{i-1/2}) \end{aligned} \quad (6.12)$$

which shows that the scheme is in conservation form ( $\mathbf{D}$ -terms also add up to flux).

Here the predictor step is a first-order forward scheme, while the corrector is a backward first-order scheme. The overall combined scheme is stable and of second order due to cancellations of the truncation errors in each step. The above sequence of forward and backward schemes was found to be sufficiently accurate and most successful in resolving the turbidity current front. Changing the sequence of backward and forward schemes in consecutive time-steps, to avoid a bias by an eventual accumulation of errors, does not greatly improve the overall performance of the method for this particular application.

For completeness the 2-D form of MacCormack's scheme is given to illustrate the similarity to the 1-D scheme and the simplicity of the transition from 1-D to 2-D. The following 2-D six-point version of MacCormack's scheme can be defined (with source term  $\mathbf{Q}$  and artificial viscosity terms  $\mathbf{D}_x, \mathbf{D}_y$ ):

$$\begin{aligned} \bar{\mathbf{U}}_{ij} &= \mathbf{U}_{ij}^n - \frac{\Delta t}{\Delta x}[\Delta_x \mathbf{f}_{ij}^n] - \frac{\Delta t}{\Delta y}[\Delta_y \mathbf{g}_{ij}^n] + \Delta t \mathbf{Q}_{ij}^n + \frac{\Delta t}{\Delta x} \mathbf{D}_x^n + \frac{\Delta t}{\Delta y} \mathbf{D}_y^n \\ \bar{\bar{\mathbf{U}}}_{ij} &= \mathbf{U}_{ij}^n - \frac{\Delta t}{\Delta x}[\nabla_x \bar{\mathbf{f}}_{ij}] - \frac{\Delta t}{\Delta y}[\nabla_y \bar{\mathbf{g}}_{ij}] + \Delta t \bar{\mathbf{Q}}_{ij} + \frac{\Delta t}{\Delta x} \bar{\mathbf{D}}_x + \frac{\Delta t}{\Delta y} \bar{\mathbf{D}}_y \\ \mathbf{U}_{ij}^{n+1} &= \frac{1}{2}(\bar{\mathbf{U}}_{ij} + \bar{\bar{\mathbf{U}}}_{ij}) \end{aligned} \quad (6.13)$$

where  $\bar{\mathbf{f}}_{ij} = \mathbf{f}(\bar{\mathbf{U}}_{ij})$ ,  $\bar{\mathbf{g}}_{ij} = \mathbf{g}(\bar{\mathbf{U}}_{ij})$ , and  $\bar{\mathbf{Q}}_i = \mathbf{Q}(\bar{\mathbf{U}}_{ij})$ , and where  $\Delta_x, \Delta_y$  and  $\nabla_x, \nabla_y$  are order-1 forward and backward difference operators respectively, defined as follows

$$\begin{aligned}
 \Delta_x \mathbf{f}_{ij}^n &= \mathbf{f}_{i+1,j}^n - \mathbf{f}_{ij}^n & ; & & \Delta_y \mathbf{g}_{ij}^n &= \mathbf{g}_{i,j+1}^n - \mathbf{g}_{ij}^n \\
 \nabla_x \mathbf{f}_{ij}^n &= \mathbf{f}_{ij}^n - \mathbf{f}_{i-1,j}^n & ; & & \nabla_y \mathbf{g}_{ij}^n &= \mathbf{g}_{ij}^n - \mathbf{g}_{i,j-1}^n
 \end{aligned}
 \tag{6.14}$$

Four different versions can be written for equation (6.11) by combinations of the one-sided differences  $\Delta_x, \Delta_y$  and  $\nabla_x, \nabla_y$  on the flux components  $\mathbf{f}$  and  $\mathbf{g}$ . The corresponding computational molecules are plotted in figure 6.3.

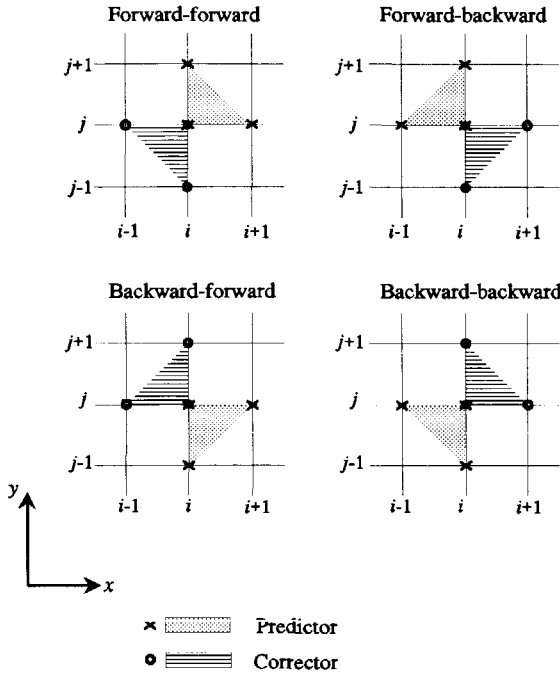


Figure 6.3 Alternatives computational molecule for 2-D MacCormack's scheme.

Again, to avoid a bias, it is often recommend to cycle between the four possibilities during a computation.

The following sections focus on the 1-D model discretization, the associated numerical properties of the model, the solution algorithm, boundary conditions and the formulation of artificial viscosity terms.

## 6.4 1-D model discretization using MacCormack's scheme

### 6.4.1 Baroclinic flow

Starting from the equations in their (quasi-) conservative form the model can be discretized using the proposed forward and backward difference operators. It has been shown so far that a decoupling of the barotropic and baroclinic part can be adopted since density differences are relatively small. The baroclinic part of a 1-D flow is described by the width-integrated form of equations (2.19) to (2.20) etc. and will be treated in this section. The barotropic part is treated in sub-section 6.4.2 as a much simpler method suffices.

To reformulate the internal-flow equations in a form which allows a straightforward solution we defined a new variable

$$\Omega = u_2 - u_1 \quad (6.15)$$

such that  $u_2$  and  $Q_2$  are replaced by

$$u_2 = \Omega \left(1 - \frac{a_2}{a}\right) + \frac{Q}{aB_2} \quad ; \quad Q_2 = B_2 u_2 a_2 \quad (6.16)$$

As a consequence the following system makes up the 1-D internal flow model:

$$\begin{aligned} \frac{\partial \Omega}{\partial t} + \frac{\partial}{\partial x} \left[ \frac{1}{2} \Omega \left\{ \frac{2Q}{aB_2} + \Omega \left(1 - 2\frac{a_2}{a}\right) \right\} \right] + g\sigma' \frac{\partial (C_s a_2)}{\partial x} - \frac{1}{2} g\sigma' a_2 \frac{\partial C_s}{\partial x} + \\ + g\sigma' C_s \frac{\partial z_b}{\partial x} = -C_D \frac{u_2^2}{a_2} + w_{ie} \left[ \frac{u_1}{a_1} + \frac{u_2}{a_2} \right] \end{aligned} \quad (6.17)$$

$$\frac{\partial (a_2 B_2)}{\partial t} + \frac{\partial Q_2}{\partial x} = -B_2 w_{ie} \quad (6.18)$$

$$\frac{\partial C_s}{\partial t} + \left\{ \frac{L'_a u_2}{T'_a} \right\} \frac{\partial C_s}{\partial x} = \left\{ \frac{w_s}{(a_2 T'_a)} \right\} (C_{se} - C_s) \quad (6.19)$$

$$B_2 \frac{\partial(\{1 - \epsilon_p\}z_b + C_s a_2)}{\partial t} + \frac{\partial S_s}{\partial x} + \frac{\partial S_b}{\partial x} = 0 \quad (6.20)$$

Here  $B_2 = B_2(x)$  is not a function of time as the banks are fixed, and it is not a function of depth as we assumed a rectangular cross-section. Furthermore values and gradients in the total discharge  $Q$  and the total reservoir depth  $a$  are independently obtained from the external flow module (sub-section 6.4.2). In the following the discretization of the model is presented.

### Predictor step

Firstly predictor values are computed, secondly a corrector step is used to obtain second-order accuracy. The predictor variations of  $\mathbf{U}$  are obtained in the following order (top to bottom) from the values of the primitive variables  $\Omega$ ,  $a_2$ ,  $C_s$ ,  $z_b$  at each grid point at the present time level ( $n \cdot \Delta t$ ):

$$\begin{bmatrix} \overline{\Delta \Omega}_i \\ \overline{\Delta a_{2,i}} \\ \overline{\Delta C_{s,i}} \\ \overline{\Delta(\{1 - \epsilon_p\}z_b + C_s a_2)_i} \end{bmatrix} = - \frac{\Delta t}{\Delta x} \begin{bmatrix} \Delta_x f_{\Omega,i}^n \\ \Delta_x f_{a,i}^n \\ \Delta_x f_{C,i}^n \\ \Delta_x f_{z,i}^n \end{bmatrix} + \Delta t \begin{bmatrix} Q_{R,i}^n + w_{iem,i}^n \\ -w_{ie,i}^n \\ \omega_{s,i}^n (C_{se,i}^n - C_{s,i}^n) \\ 0 \end{bmatrix} + \frac{\Delta t}{\Delta x} \begin{bmatrix} D_{1,i+1/2}^{n,\Omega} - D_{1,i-1/2}^{n,\Omega} \\ D_{1,i+1/2}^{n,a} - D_{1,i-1/2}^{n,a} \\ D_{1,i+1/2}^{n,C} - D_{1,i-1/2}^{n,C} \\ D_{1,i+1/2}^{n,z} - D_{1,i-1/2}^{n,z} \end{bmatrix} \quad (6.21)$$

where  $\Delta_x f_i = f_{i+1} - f_i$  is again the forward difference operator, which is applied to the respective flux terms in the equations. At grid point  $(i+1) \cdot \Delta x$  these fluxes are defined consistent with equations (6.17) to (6.20) as

$$\begin{bmatrix} f_{\Omega,i+1}^n \\ f_{a,i+1}^n \\ f_{C,i+1}^n \\ f_{z,i+1}^n \end{bmatrix} = \begin{bmatrix} \Omega_{i+1}^n \left[ \frac{2Q}{B_{2,i+1} a_{i+1}} + \Omega_{i+1}^n \left( 1 - 2 \frac{a_{2,i+1}^n}{a_{i+1}} \right) \right] + g \sigma' \left( C_{s,i+1}^n a_{2,i+1}^n - \frac{a_{2,i}^n C_{s,i+1}^n}{2} + C_{s,i}^n z_{b,i+1}^n \right) \\ \frac{Q_{2,i+1}^n}{B_{2,i}} \\ \left( \frac{u_2 L_a'}{T_a'} \right)_i^n C_{s,i+1}^n \\ \frac{(S_{b,i+1}^n + S_{s,i+1}^n)}{B_{2,i}} \end{bmatrix} \quad (6.22)$$

There corresponding values at grid point  $i \cdot \Delta x$  are obtained by replacing all



quantities with index  $(i+1)$  with quantities at  $i$ . Note that  $\omega_{s,i}^n = w_{s,i}(a_2 T_a')_i^n$ .

Friction and entrainment terms in (6.21) are linearized and written explicitly as

$$Q_{R,i} = -C_D (u_2/a_2)_i^n u_{2,i}^n \quad (6.23)$$

$$w_{iem,i}^n = w_{ie,i}^n (\Omega_i^n, a_{2,i}^n, C_{s,i}^n) \left[ \frac{u_{2,i}^n}{a_{2,i}^n} + \frac{u_{1,i}^n}{(a_i - a_{2,i}^n)} \right] \quad (6.24)$$

Transport terms can be directly deduced from the application of transport formulae

$$S_{b,i+1}^n = B_{2,i+1} \cdot s_b (u_{2,i+1}^n, a_{2,i+1}^n) \quad ; \quad S_{s,i+1}^n = B_{2,i+1} C_{s,i+1}^n a_{2,i+1}^n \quad (6.25)$$

From the presented discretization the predictor bed-level change can be obtained by

$$(1 - \epsilon_p) \overline{\Delta z}_{b,i} = \overline{\Delta \{ (1 - \epsilon_p) z_b + C_s a_2 \}_i} - (C_{s,i}^n + \overline{\Delta C}_{s,i}) (a_{2,i}^n + \overline{\Delta a}_{2,i}) + C_{s,i}^n a_{2,i}^n \quad (6.26)$$

The discretization of the viscosity terms  $D_1$  can be chosen afterwards and is discussed in sections 6.5 and 6.6.

### Corrector step

In the corrector step the numerical fluxes are obtained by reversing the direction of differentiation (from forward to backward) and by using the new values of the primitive variables obtained from the predictor step. Therefore we define the vector of these new predicted variables as

$$\overline{\mathbf{U}}_i = \mathbf{U}_i^n + \overline{\Delta \mathbf{U}}_i \quad (6.27)$$

Corrector variations are then computed conformal the predictor step as follows

$$\begin{bmatrix} \overline{\overline{\Delta \Omega}}_i \\ \overline{\overline{\Delta a}}_{2,i} \\ \overline{\overline{\Delta C}}_{s,i} \\ \overline{\overline{\Delta \{ (1 - \epsilon_p) z_b + C_s a_2 \}_i}} \end{bmatrix} = - \frac{\Delta t}{\Delta x} \begin{bmatrix} \nabla_x \bar{f}_{\Omega,i} \\ \nabla_x \bar{f}_{a,i} \\ \nabla_x \bar{f}_{C,i} \\ \nabla_x \bar{f}_{z,i} \end{bmatrix} + \Delta t \begin{bmatrix} \overline{Q}_{R,i} + \overline{w}_{iem,i} \\ -\overline{w}_{ie,i} \\ \omega_{s,i}^n (\overline{C}_{se,i} - \overline{C}_{s,i}) \\ 0 \end{bmatrix} + \frac{\Delta t}{\Delta x} \begin{bmatrix} \overline{D}_{1,i+1/2}^\Omega - \overline{D}_{1,i-1/2}^\Omega \\ \overline{D}_{1,i+1/2}^a - \overline{D}_{1,i-1/2}^a \\ \overline{D}_{1,i+1/2}^C - \overline{D}_{1,i-1/2}^C \\ \overline{D}_{1,i+1/2}^z - \overline{D}_{1,i-1/2}^z \end{bmatrix} \quad (6.28)$$

where  $\nabla_x f_i = f_i - f_{i-1}$  is the backward difference operator applied to the flux. A discretization of flux terms at grid point  $(i-1) \cdot \Delta x$  yields

$$\begin{bmatrix} \bar{f}_{\Omega,i-1} \\ \bar{f}_{a,i-1} \\ \bar{f}_{C,i-1} \\ \bar{f}_{z,i-1} \end{bmatrix} = \begin{bmatrix} \frac{\bar{\Omega}_{i-1}}{2} \left[ \frac{2Q}{B_{2,i-1} a_{i-1}} + \bar{\Omega}_{i-1} \left( 1 - 2 \frac{\bar{a}_{2,i-1}}{a_{i-1}} \right) \right] + g \sigma' \left( \bar{C}_{s,i-1} \bar{a}_{2,i-1} - \frac{\bar{a}_{2,i} \bar{C}_{s,i-1}}{2} + \bar{C}_{s,i} \bar{z}_{b,i-1} \right) \\ \bar{Q}_{2,i-1} / B_{2,i} \\ (\bar{u}_2 \bar{L}'_a / \bar{T}'_a)_i \bar{C}_{s,i-1} \\ (\bar{S}_{b,i-1} + \bar{S}_{s,i-1}) / B_{2,i} \end{bmatrix} \quad (6.29)$$

There corresponding values at grid point  $i \cdot \Delta x$  are obtained by replacing all quantities with index  $(i-1)$  with quantities at  $i$ . Note that predicted values of derived variables, such as  $u_2$  and  $S_s$ , are calculated directly from the primitive variables in equation (6.27).

In order to preserve the order and stability of the scheme it is necessary to write the source terms in the following linearized way

$$Q_{R,i} = - C_D \left( \frac{u_2}{a_2} \right)_i^n \bar{u}_{2,i} \quad (6.30)$$

$$w_{iem,i}^n = w_{ie}^n(\Omega_i^n, a_{2,i}^n, C_{s,i}^n) \left[ \frac{\bar{u}_{2,i}}{a_{2,i}^n} + \frac{\bar{u}_{1,i}}{(a_i - a_{2,i}^n)} \right] \quad (6.31)$$

$\downarrow$   
 $w_{ie,i}^n$

Although this linearization appears quite rough, it follows the predictor step and satisfies consistency and stability. Sometimes semi-implicit discretizations are proposed for this term to prevent it from causing numerical instability. However, as is shown in section 6.9, for practical application of our model this is not essential. Another discretization of the source terms can be based on Roe's (1981b) characteristic decomposition of the source terms for a better performance near shocks. This method is used for instance by Glaister (1988) in combination with Roe's numerical scheme.

During the development of the baroclinic part of the model a preliminary version was written for a two-layer flow with fixed concentration ( $C_s = \text{const.}$  for all  $x$  and  $t$ ) on a fixed bed. The discretization is based on the momentum and continuity equations as above, after eliminating gradients in  $C_s$ . The algorithm written for solving these two remaining equations was extended to the full system of equations

after solving most programming problems and after carrying out numerous test runs. The original fixed bed model is retained in the final model.

### 6.4.2 Barotropic flow

Decoupling the barotropic (external) and baroclinic (internal) part of the flow is shown to be beneficial for the size of the computational time step. The basic equations for the barotropic flow are the traditional Saint Venant equations for long waves in the reservoir. Their numerical solution is classical and treated extensively in literature. Realizing that flows in reservoirs with density currents must be quiescent with low Froude numbers these equations can be significantly simplified and allow for a simple numerical solution. In an attempt to speed up these numerical calculations we have chosen for the possibility of approximating the barotropic flow with a quasi-steady approach. This approach is commonly used in computing bed-variations in 1-D or 2-DH subcritical open-channel flow (e.g. de Vries, 1993).

External waves are assumed to have a propagation speed which is much higher than that for internal waves (especially in very deep reservoirs). On the time scale of these internal events the effects of changes in boundary conditions for external flow (e.g. a flow hydrograph) can be assumed to be felt instantaneously over the total reservoir. Hence they propagate with an infinite speed and the flow is computed as a sequence of steady surface profiles. External quasi-steady flow allows us to use an increased time step adjusted to the stability condition for internal flow, which is much less restrictive than that for unsteady external flow. The error in the baroclinic flow due to this approximation is of the order of the density difference or less since the interaction between external and internal flow is very weak and Froude numbers for external flows are small. For practical applications this is an acceptable error.

In a 1-D approach the remaining model consists of ordinary differential equations which can be solved quite easily for each time-level  $t_n$ :

$$\frac{d}{dx} \left( \frac{Q^2}{A} \right) + g_z A \frac{d(a+z_b)}{dx} = -BC_D u_2^2 + g_x A$$

$$\frac{dQ}{dx} = 0$$

where  $a$  is the total depth,  $Q$  is the total discharge,  $B$  the width and  $A$  the cross-sectional area ( $=a \cdot B$ , i.e., we assumed a rectangular cross section). As boundary

conditions for the integration we use

$$t = t_n : Q(x=0) = Q(t_n) \quad \text{and} \quad a(x_{\text{end}}) = a_{\text{dam}}(t_n) \quad (6.34)$$

Bed-levels and widths (either irregular or smooth) are supposed to be known at each grid point, while inflow discharge  $Q(t_n)$  follows from the flow hydrograph, and the downstream depth  $a_{\text{dam}}$  follows for instance from a head-discharge relation (e.g. see sub-section 7.5.1). The differential equation is solved using a standard fourth-order Runge-Kutta method (e.g. Sloff, 1990) starting from the lower boundary ( $x_{\text{end}}$ ). The step-size for this integration is taken as a fraction of the computational step-size  $\Delta x$  to obtain high accuracy. Still the computational effort remains negligible compared to an unsteady external-flow computation.

In a 2-DH approach the model is more complicated since it cannot be reduced to an ordinary differential equation. The characteristic equation of the 2-DH Saint-Venant equations in the  $x,y$ -plane can be written as

$$(u - v\phi)[(u - v\phi)^2 - g_z a(1 + \phi^2)] = 0$$

where  $u$  and  $v$  are depth-averaged flow velocities in  $x$  and  $y$  direction respectively. For this equation the following characteristics are found

$$\phi_1 = u/v$$

$$\phi_{2,3} = \frac{uv}{v^2 - g_z a} \pm \sqrt{g_z a(u^2 + v^2 - g_z a)}$$

This system is hyperbolic (real  $\phi$ ) if the external flow is subcritical. It is parabolic if the flow is critical and elliptic if the flow is supercritical.

Considering the possibility of extending the presented 1-D model to a 2-DH numerical model one must realize that the straightforward discretization and solution of these 2-DH equations on a fine mesh involves the extremely costly solution of an enormous matrix. Therefore it is more common to use the unsteady flow equations and let the solution iteratively converge to the steady-state solution (e.g., to model the bed topography in river bends, Olesen, 1987). In solving the potential flow equations this approach has been used for decades, and various 'relaxation' methods have been proposed (e.g., see Abbott and Basco, 1989, Hirsch, 1990). The number of iterations can be held under control, for instance below the order of ten, by using an implicit numerical scheme and an ADI solution algorithm. Nevertheless, considering that the maximum time step for computing unsteady external flow is of the order of ten times smaller than that for internal flow, the computational effort for the quasi-steady approach is of the same order of

that for the fully unsteady approach. Furthermore, by increasing the mesh-size for the unsteady external flow computation relative to the original grid, a proportional increase of the time step can be achieved, with a loss of accuracy comparable to that induced by the steady flow approach. Consequently a quasi-steady external flow equation is not appropriate for a 2-DH approach.

## 6.5 Conventional artificial viscosity approach

In sub-section 6.2.1 it is shown that near a shock the truncation error of a second-order scheme generates dispersive errors in the form of parasitic oscillations. These high-frequency oscillations are indicated by a large mass flux error. When using the MacCormack scheme these oscillations can be damped by using locally near the shock some type of artificial viscosity. The most simple methods in this respect are the conventional artificial viscosity methods, which are based on an explicit addition of diffusion terms (second-order derivatives) to the flux terms. Their diffusion coefficient is often a non-linear function of the data multiplied with an empirical coefficient which must be calibrated. In this way the discontinuity is smeared (smoothing according to the amount of viscosity) and continuous flow is hardly affected. An additional advantage of artificial viscosity is the possibility to prevent the computation of non-physical solutions (which violate the entropy condition) during shock capturing.

There are many specific forms of the artificial viscosity method, which was firstly introduced by Von Neumann and Richtmeyer (1950) for the 1-D gas-flow problems. As mentioned above these additional terms should simulate the effect of physical viscosity on the scale of the mesh near discontinuities, but should be of the order of the truncation error in continuous regions. In 2-DH flows a complete artificial viscosity should be of order-2 tensor form yielding both normal and tangential stresses. However, on a rectangular grid a more simple form can also be used by discretizing

$$\frac{\partial}{\partial x} \left( v_x \frac{\partial U}{\partial x} \right) + \frac{\partial}{\partial y} \left( v_y \frac{\partial U}{\partial y} \right) \quad (6.38)$$

where

$$\frac{v_x}{\rho_x^2} = \frac{v_y}{\rho_y^2} = \frac{\nu}{\rho^2} \quad \text{with} \quad \rho_x = \frac{\Delta t}{\Delta x} \quad ; \quad \rho = \sqrt{\rho_x^2 + \rho_y^2} = \frac{\sqrt{\Delta x^2 + \Delta y^2} \Delta t}{\Delta x \Delta y} \quad (6.39)$$

and  $\nu$  is a constant or a variable, as follows from the alternatives hereafter. In a 1-D approach this term is identical to eq. (6.38) with  $\partial/\partial y$  eliminated.

The first alternative to introduce the artificial viscosity is the generalized version of the original method applied by Von Neumann and Richtmeyer (1950). The addition of these terms to the MacCormack scheme corresponds to a modification of numerical fluxes in such a way that the conservation property of the scheme is not distorted. The dissipation terms are generally added both at the predictor and the corrector level. The 1-D formulation becomes

$$\begin{aligned}\bar{U}_i &= U_i^n - \frac{\Delta t}{\Delta x}(\Delta_x \mathbf{f}_i^n) + \Delta t \mathbf{Q}_i^n + \frac{\Delta t}{\Delta x}(\delta_{i+1/2}^v \cdot \Delta_x U_i^n - \delta_{i-1/2}^v \cdot \nabla_x U_i^n) \\ \bar{\bar{U}}_i &= U_i^n - \frac{\Delta t}{\Delta x}(\nabla_x \bar{\mathbf{f}}_i) + \Delta t \bar{\mathbf{Q}}_i + \frac{\Delta t}{\Delta x}(\bar{\delta}_{i+1/2}^v \cdot \Delta_x \bar{U}_i - \bar{\delta}_{i-1/2}^v \cdot \nabla_x \bar{U}_i) \\ U_i^{n+1} &= \frac{1}{2}(\bar{U}_i + \bar{\bar{U}}_i)\end{aligned}\quad (6.40)$$

which corresponds to discretization of the system of equations

$$\frac{\partial \mathbf{U}}{\partial t} + \frac{\partial \mathbf{f}}{\partial x} = \mathbf{Q} + \frac{\partial}{\partial x} \left( \Delta_x \cdot \delta^v \frac{\partial \mathbf{U}}{\partial x} \right) \quad (6.41)$$

Here  $\Delta_x$  and  $\nabla_x$  are forward and backward difference operators respectively.

When adopting the generalized Von Neumann and Richtmeyer (1950) method we add non-linear artificial viscosity only to the momentum equations. Function  $\delta^v$  can then be written for the momentum equation in  $x$ -direction as

$$\delta_{i+1/2}^v = \alpha |\Delta_x \Omega_i^n| \quad ; \quad \delta_{i-1/2}^v = \alpha |\nabla_x \Omega_i^n| \quad (6.42)$$

This formulation can be easily extended to 2-DH viscosity and eventually it can be generalized for application to other equations (e.g. continuity) as well. The coefficient  $\alpha$  is of the order of unity, and has to be adjusted empirically.

In generally for a steep front better results can be expected using the MacCormack and Baldwin (1975) artificial viscosity. Originally they proposed to make  $\delta^v$  proportional to a second derivative of the pressure field to enhance the effect of dissipation in presence of strong pressure gradients and to reduce it in smooth flow regions. In shallow water flow it is more convenient to replace the pressure by the flow depth to account for strong depth gradients. The factor  $\delta^v$  then becomes

$$\delta^v = \alpha \Delta x^2 \frac{\phi_{max}}{a_2} \left| \frac{\partial^2 a_2}{\partial x^2} \right| \quad (6.43)$$

where  $\phi_{max}$  is the maximum celerity, which can be computed numerically in the following discretized form

$$\delta_{i+1/2}^v = \max(\epsilon_i, \epsilon_{i+1}) \quad ; \quad \delta_{i-1/2}^v = \max(\epsilon_{i-1}, \epsilon_i) \quad (6.44)$$

with

$$\epsilon_i = \alpha (\Phi_{max})_i \left( \frac{|a_{2,i+1}^n - 2a_{2,i}^n + a_{2,i-1}^n|}{a_{2,i+1}^n + 2a_{2,i}^n + a_{2,i-1}^n} \right) \quad (6.45)$$

The adjustable constant  $\alpha$  is usually set to 1/4 or, especially for this model, it can be given a higher value which will be in the order of unity.

Again the approach can be extended easily to 2-DH cases. For instance MacCormack-Baldwin viscosity has been used by Fennema and Chaudry (1990) to compute 2-DH transient shallow-water flow. However, they added these terms only after a predetermined number of time steps. Jameson et al. (1981) added to the MacCormack-Baldwin dissipation a linear fourth-order dissipation which provides background dissipation in smooth parts of the flow (damps high-frequency modes). Since near a shock this fourth difference generates overshoots it is usually switched off in its neighbourhood.

Neumann-Richtmyer as well as MacCormack-Baldwin viscosity were implemented in our numerical model in the predictor (using variables from the preceding time level) and in the corrector step (using the predictor variables). In algorithm 6.1 this procedure is summarized.

<p>Compute : <math>\mathbf{D}_{i+1/2}^n = \delta_{i+1/2}^{v,n} (\Delta_x \mathbf{U}_i^n)</math> ; <math>\mathbf{D}_{i-1/2}^n = \delta_{i-1/2}^{v,n} (\nabla_x \mathbf{U}_i^n)</math></p> <p style="text-align: center;">↓</p> <p>Compute : <math>\Delta \bar{\mathbf{U}}_i = -\frac{\Delta t}{\Delta x} [\Delta_x \mathbf{f}_i^n] + \Delta t \mathbf{Q}_i^n + \frac{\Delta t}{\Delta x} (\mathbf{D}_{i+1/2}^n - \mathbf{D}_{i-1/2}^n)</math> (predictor)</p> <p style="text-align: center;">↓</p> <p>Compute : <math>\bar{\mathbf{D}}_{i+1/2} = \bar{\delta}_{i+1/2}^v (\Delta_x \bar{\mathbf{U}}_i)</math> ; <math>\bar{\mathbf{D}}_{i-1/2} = \bar{\delta}_{i-1/2}^v (\nabla_x \bar{\mathbf{U}}_i)</math></p> <p style="text-align: center;">↓</p> <p>Compute : <math>\Delta \bar{\bar{\mathbf{U}}}_i = -\frac{\Delta t}{\Delta x} [\nabla_x \bar{\mathbf{f}}_i] + \Delta t \bar{\mathbf{Q}}_i + \frac{\Delta t}{\Delta x} (\bar{\mathbf{D}}_{i+1/2} - \bar{\mathbf{D}}_{i-1/2})</math> (corrector)</p> <p style="text-align: center;">↓</p> <p>Compute : <math>\mathbf{U}_i^{n+1} = \mathbf{U}_i^n + \frac{1}{2} [\Delta \bar{\mathbf{U}}_i + \Delta \bar{\bar{\mathbf{U}}}_i]</math></p>
---

Algorithm 6.1 MacCormack algorithm (repeat this cycle for  $t=0, t_{end}-\Delta t$ )

To illustrate the performance of these respective viscosities a comparison is given

between an analytical and numerical solution of a self-similar partial lock-exchange flow (with constant concentration, and without friction and entrainment). The results are generalized by using the dimensionless coordinates  $\zeta$  and  $\tilde{a}_2$  as defined in sub-section 7.2.1 (equations 7.1 and 7.2). Only the part downstream of the gate is presented here.

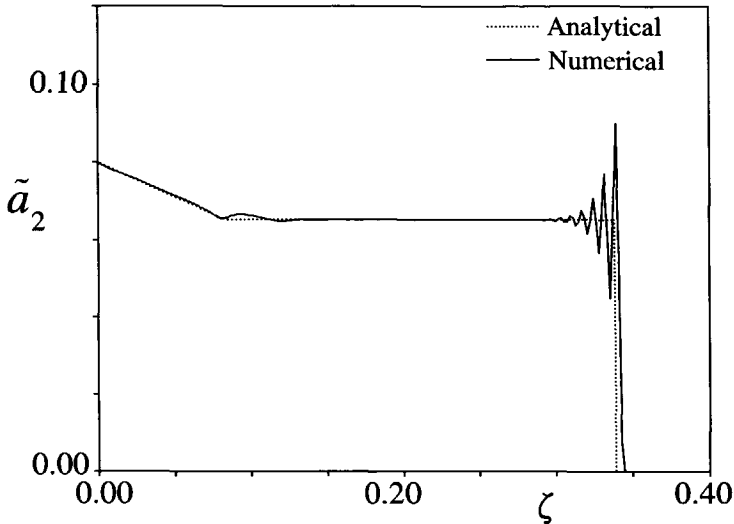


Figure 6.4 Partial lock-exchange flow computed without any artificial viscosity compared to its analytical self-similar solution.

In figure 6.4 the results are given for a computation without artificial viscosity. Large oscillations are generated near the shock, which are often affecting the stability unfavourably. Still the front celerity is accurately resolved as a consequence of the conservative property of the scheme.

Now the computation is repeated using Neumann and Richtmyer's artificial viscosity to the momentum equation. The results of this computation with  $\alpha=0.5$  and  $\alpha=1.5$  are presented in figure 6.5 and 6.6 respectively. They show that oscillations are significantly damped but not fully eliminated. A further increase of  $\alpha$  does not significantly ameliorate the results. The results also show that the expansion wave near  $\zeta=0$  is more accurately approximated. The latter evolves from the expected convergence to entropy-satisfying weak solutions.

It was found that the best performing conventional artificial viscosity method for our model is the MacCormack and Baldwin method. The computed results for the particular example presented here, are plotted in figure 6.7 and 6.8. It was necessary to replace  $\phi_{max}$  in equation (6.45) by unity to limit the value of  $\alpha$  while retaining sufficient viscosity especially near the gravity-current front. Viscosity is now added to all the basic equations, while allowing for attunement of each of the



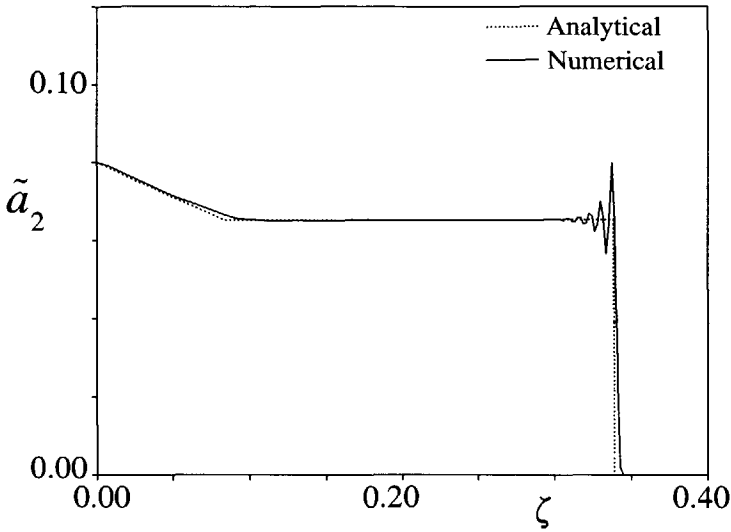


Figure 6.5 Partial lock-exchange flow computed with Neumann and Richtmyer's viscosity with  $\alpha=0.5$ .

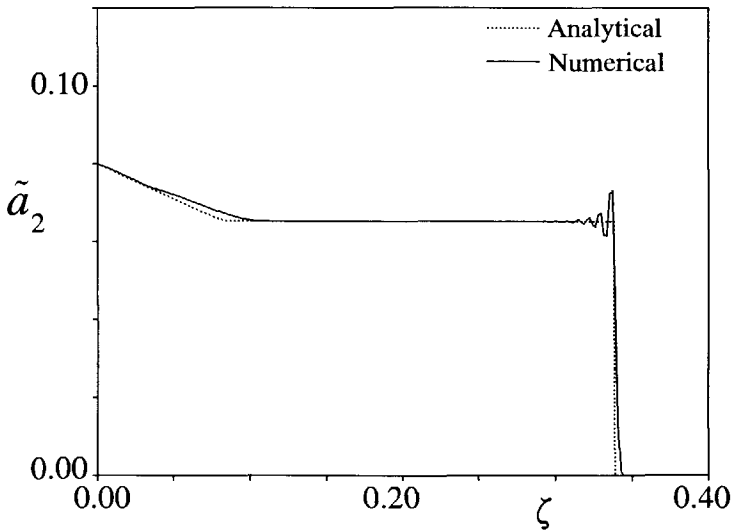


Figure 6.6 Partial lock-exchange flow computed with Neumann and Richtmyer's viscosity with  $\alpha=1.5$ .

viscosity terms by using different  $\alpha$  values for each equation (i.e.  $\alpha_1$  for momentum,  $\alpha_2$  for continuity,  $\alpha_3$  for suspended sediment, and  $\alpha_4$  for morphology). In the example above  $\alpha_1=\alpha_2=0.25$  and  $\alpha_1=\alpha_2=1.0$  are used respectively. Clearly the amplitude of the oscillations near the front can be reduced satisfactory by

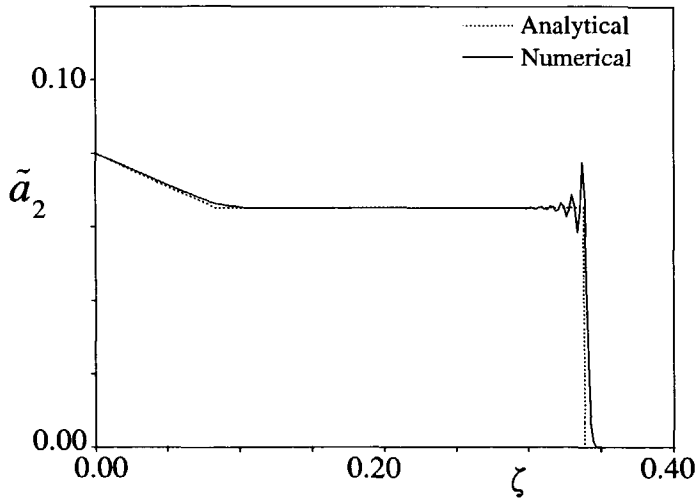


Figure 6.7 Partial lock-exchange flow computed with MacCormack and Baldwin viscosity with  $\alpha=0.25$ .

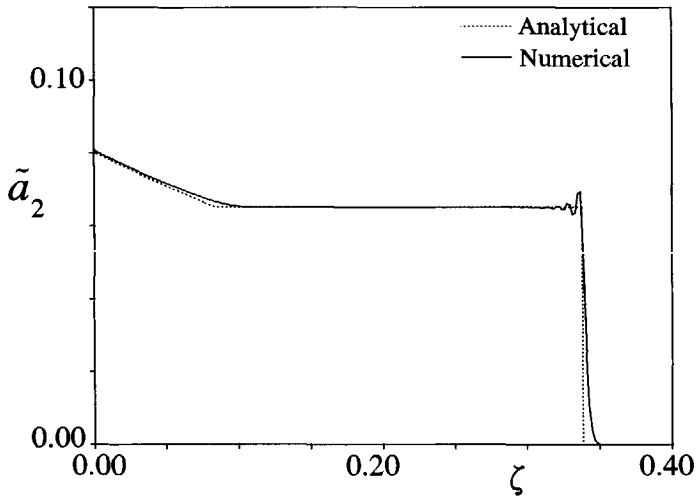


Figure 6.8 Partial lock-exchange flow computed with MacCormack and Baldwin viscosity with  $\alpha=1.0$ .

increasing  $\alpha$ . Small differences in the height of the constant part of the solution is due to a slight difference in initial conditions in numerical and analytical solutions and is not due to a systematic error (e.g., in these numerical computations  $q \neq 0$ , lower depth  $\neq 0$ ).

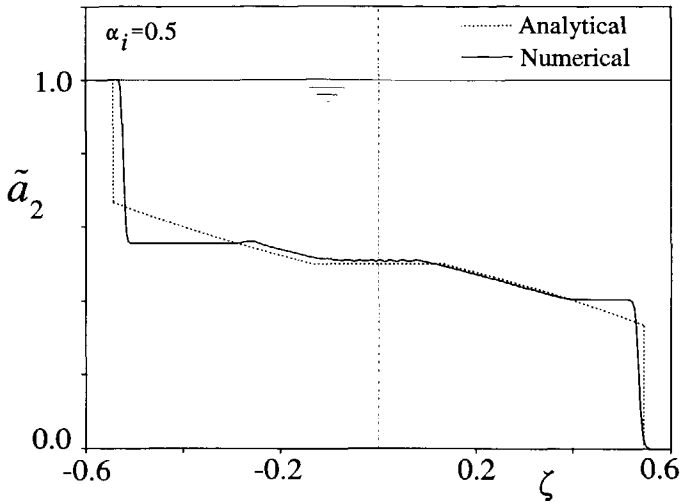


Figure 6.9 Self-similar full lock-exchange flow computed with MacCormack and Baldwin's viscosity with  $\alpha_1 = \alpha_2 = 0.5$ .

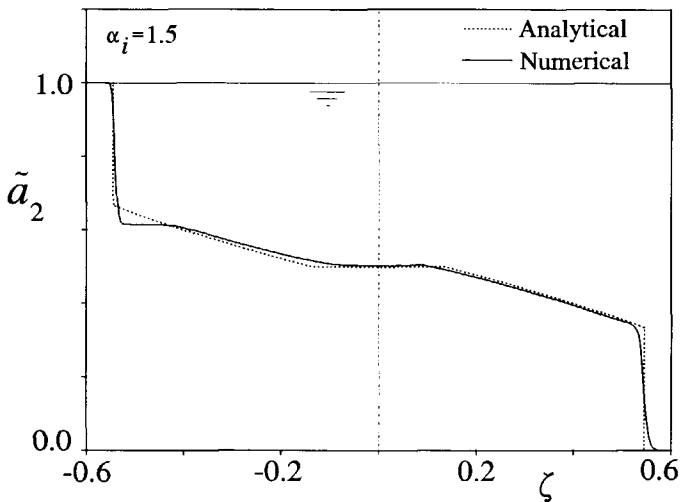


Figure 6.10 Self-similar full lock-exchange flow computed with MacCormack and Baldwin's viscosity with  $\alpha_1 = \alpha_2 = 1.5$ .

The primary disadvantage of the presented conventional artificial viscosity methods is the necessity to calibrate  $\alpha$ -coefficients for each application. A most striking example of this aspect can be obtained from the computation of a full lock-exchange flow instead of a low discharge partial lock-exchange flow. In figures 6.9 and 6.10 an example is given of a full lock-exchange flow in dimensionless

coordinates using the proposed form of MacCormack and Baldwin's viscosity with  $\alpha_1=\alpha_2=0.5$  and  $\alpha_1=\alpha_2=1.5$  respectively. For comparison the exact analytical solution is added to these plots. The results show that  $\alpha=0.5$ , which is sufficient for partial lock-exchange flows, does not provide enough dissipation here. The numerical solution does not approximate correctly the exact solution for instance due to erroneous behaviour near  $\zeta=0$  near  $t=0$ . Although this problem is partially fixed by increasing  $\alpha$  to a value of 1.5 the results show that the rarefaction region in the surface front (on the left) is mistaken. Most likely this effect is caused by the Courant-number ( $\sigma=\phi_{\max}\cdot\Delta t/\Delta x$ ) dependence of the strain exerted by the viscosity (section 6.9), and the dependence of the viscosity on the underflow depth  $a_2$  through equation (6.45). By carrying out some more experiments on this typical case, it is found that the contribution of the viscosity term in the continuity equation is dominant. For instance taking  $\alpha_1=0$  in both computations does not significantly worsen the results, but by taking  $\alpha_2=0$  the difference between numerical and analytical results increases drastically. Clearly Neumann & Richtmyer's viscosity performs very poor in this example as it only acts on momentum.

Besides the mobile-bed case the full lock-exchange flow is a rather severe test problem which has somewhat tempered our enthusiasm on the conventional artificial viscosity methods. Later, in section 6.9 is shown that by increasing the time step, close to the stability range, the amount of viscosity can be reduced and sometimes eliminated as wiggles disappear. It is also shown that the amount of viscosity reduces the stability limit of the model (again related on the computational time step). A careless choice of viscosity coefficients may therefore lead to instabilities by amplification of the wiggles instead of damping. Although the conventional artificial-viscosity approach can be extended simply to 2-DH models, its inaccuracy and calibration requirements are prejudicial. In the following section an alternative artificial viscosity approach is presented which makes the computations TVD and gets rid of major disadvantages of conventional viscosity methods.

## 6.6 TVD artificial viscosity approach

As conventional artificial viscosity methods cannot satisfactory eliminate the oscillatory behaviour near discontinuities, and as they require calibration, it is worthwhile to search for a more robust method. In sub-section 6.2.4 it is shown that for this purpose, especially for 1-D flows, the more advanced TVD (Total Variation Diminishing) approach can be applied. It actually prevents the occurrence of oscillations instead of damping them afterwards. In this section is shown how artificial viscosity terms are defined which make the MacCormack scheme TVD.

The elaboration of the underlying theory is presented in appendix B.

It has been shown that the numerical generation of oscillations is due to the second-order approximation, as first-order approximations are free of wiggles. It can be shown that the second-order effect can be attributed to the slope of the state variables or fluxes in each cell (e.g. Hirsch, 1990). If this slope exceeds the difference of adjacent mean values oscillations are generated. By keeping these gradients within their proper bounds it is possible to prevent the creation of new local extremes which makes the method TVD (see sub-section 6.2.4). The control of gradients in the solution can be accomplished by means of flux limiters.

The TVD concept is originally based on scalar equations, but can be extended to non-linear systems by using a type of local linearization. For linear systems the compatibility equations form a set of scalar equations. The flux limiter can then be applied to each of these decoupled scalar problems. This is shown later in this section.

Having a linearized problem, we can start with reformulating MacCormack's scheme as the Lax-Wendroff scheme. The second order Lax-Wendroff numerical flux (equation 6.2) can be written as an first-order upwind flux plus a correction, using the flux splitting method (equation 6.3, decompose fluxes and Jacobians into their positive and negative parts):

$$\mathbf{f}_{i+1/2}^* = \mathbf{f}_i^+ + \mathbf{f}_{i+1}^- + \frac{1}{2} \left( 1 - \frac{\Delta t}{\Delta x} A_{i+1/2}^+ \right) \Delta_x \mathbf{f}_{i+1/2}^+ - \frac{1}{2} \left( 1 + \frac{\Delta t}{\Delta x} A_{i+1/2}^- \right) \Delta_x \mathbf{f}_{i+1/2}^- \quad (6.46)$$

upwind flux correction

By applying the flux limiter method, the magnitude of the correction term is limited dependent on the data. Hence, with a limiter function  $\Phi$  applied to positive and negative components respectively, the numerical flux becomes:

$$\mathbf{f}_{i+1/2}^{*\text{TVD}} = \mathbf{f}_i^+ + \mathbf{f}_{i+1}^- + \frac{1}{2} \Phi^+ \left( 1 - \frac{\Delta t}{\Delta x} A_{i+1/2}^+ \right) \Delta_x \mathbf{f}_{i+1/2}^+ - \frac{1}{2} \Phi^- \left( 1 + \frac{\Delta t}{\Delta x} A_{i+1/2}^- \right) \Delta_x \mathbf{f}_{i+1/2}^- \quad (6.47)$$

In smooth regions the limiter function  $\Phi$  has to be close to unity to preserve second-order accuracy, while near discontinuities  $\Phi$  should be near zero to utilize the dissipation of the first-order scheme. Consequently the order of the scheme is reduced near discontinuities. The difference between the original Lax-Wendroff numerical flux and the limited flux can now be considered as an 'intelligent' artificial viscosity term (to be added to the original flux)

$$\mathbf{f}_{i+1/2}^{*\text{TVD}} = \mathbf{f}_{i+1/2}^* - \mathbf{D}_{i+1/2} \quad (6.48)$$

where

$$\mathbf{D}_{i+1/2} = \frac{1}{2}(1 - \Phi^+) \left( 1 - \frac{\Delta t}{\Delta x} A_{i+1/2}^+ \right) \Delta_x \mathbf{f}_{i+1/2}^+ - \frac{1}{2}(1 - \Phi^-) \left( 1 + \frac{\Delta t}{\Delta x} A_{i+1/2}^- \right) \Delta_x \mathbf{f}_{i+1/2}^- \quad (6.49)$$

As stated before this result can be extended for MacCormack's scheme for the non-linear system, if a local linearization is applied, for instance in the neighbourhood of each cell interface  $x_{i+1/2}$ . A very simple and popular way to achieve this is to use Roe's (1981) characteristic decomposition of the fluxes obtained from Roe's approximate Riemann solver (e.g., see also Hirsch, 1990 and Le Veque, 1990). In appendix B is shown how Roe's decomposition is defined, and how fluxes for our model are decomposed. Essentially the linear-wave decomposition is used which is the exact linear solution to Riemann problems. Any variation in  $\mathbf{U}$  can be expressed as a sum of simple wave contributions as follows

$$\Delta_x \mathbf{U} = \sum_{k=1}^m (\Delta_x \omega_k) \mathbf{r}_k \quad (6.50)$$

where

- $m$  = number of characteristic eigenvalues (celerities)
- $\mathbf{r}_k$  = right-eigenvector of the linearized Jacobian  $\hat{A}$ , associated to celerity  $\phi_k$
- $\omega_k$  = Riemann variable or characteristic variable associated to celerity  $\phi_k$

The vector of characteristic variables for the linear case is defined by

$$\bar{\omega} = \mathbf{R}^{-1} \mathbf{U} \quad (6.51)$$

where  $\mathbf{R}$  is a matrix which columns are the right eigenvectors  $\mathbf{r}_k$  ( $k=1, m$ ) of  $\hat{A}$ . In terms of these characteristic variables the system of equations can be written as a set of compatibility equations

$$\frac{\partial \bar{\omega}}{\partial t} + \Lambda_e \frac{\partial \bar{\omega}}{\partial x} = 0 \quad (6.52)$$

where  $\Lambda_e$  is the diagonal matrix of eigenvalues. Flux limiters can now be applied to each of these decoupled scalar equations.

The higher-order correction of Lax-Wendroff's fluxes can also be written in terms of these scalar equations using the proposed eigenvector expansion to these fluxes:

$$(1 - \Phi^+) \left( 1 - \frac{\Delta t}{\Delta x} A^+ \right) \Delta_x \mathbf{f}^+ = \sum_{k=1}^m \hat{\phi}_k^+ (1 - \Phi_k^+) \left( 1 - \frac{\Delta t}{\Delta x} \hat{\phi}_k^+ \right) (\Delta_x \omega_k) \hat{\mathbf{r}}_k \quad (6.53)$$

$$-(1 - \Phi^-) \left( 1 + \frac{\Delta t}{\Delta x} A^- \right) \Delta_x \mathbf{f}^- = \sum_{k=1}^m -\hat{\phi}_k^- (1 - \Phi_k^-) \left( 1 + \frac{\Delta t}{\Delta x} \hat{\phi}_k^- \right) (\Delta_x \omega_k) \hat{\mathbf{r}}_k \quad (6.54)$$

Here  $\hat{\phi}^+$  and  $\hat{\phi}^-$  denote positive and negative characteristic celerities respectively, and  $\Delta_x \omega_k = \omega_{k,i+1} - \omega_{k,i}$ . All quantities with circumflex ( $\hat{\phantom{x}}$ ) are obtained from the linearized Jacobian given in appendix B. Note that a flux limiter is now defined for each decoupled wave contribution individually.

As these equations indicate a full characteristic analysis must be performed on the linearized Jacobian  $\hat{A}_{i+1/2}$ . For reasons of conservation, consistency and hyperbolicity Roe proposed three properties of  $\hat{A}$  which have to be satisfied. Generally this requires a special square root type of averaging on primitive variables, but for our model the averaging can be linear (see appendix B). This can be traced back to the different choice of basic equations in  $u,a$ -form (System UA), as opposed to more classical applications which usually use equations in  $q,a$ -form (System QA). The convective terms in the momentum equations for these two forms are different as the latter introduces a division of conservative variables ( $q/a$ ) in the Jacobian. Roe's linearization applied to this division results in the mentioned square-root averaging.

In the decomposed artificial viscosity terms the flux limiters can now be defined. Generally TVD conditions are expressed as a function of ratios of consecutive variations of fluxes or variables. Therefore limiters should also be defined as function of these ratios (Hirsch, 1990). For the presented model two types of ratios  $\theta$  can be defined for each wave contribution associated to celerity  $k$  ( $k=1,m$ )

$$\theta_{i+1/2}^{k,1} = \frac{(\Delta_x \omega_k)_{i+1/2-j}}{(\Delta_x \omega_k)_{i+1/2}} ; \quad \theta_{i+1/2}^{k,2} = \frac{\left[ \hat{\phi}_k \left| 1 - \frac{\Delta t}{\Delta x} \hat{\phi}_k \right| (\Delta_x \omega_k) \right]_{i+1/2-j}}{\gamma' + \left[ \hat{\phi}_k \left| 1 - \frac{\Delta t}{\Delta x} \hat{\phi}_k \right| (\Delta_x \omega_k) \right]_{i+1/2}} \quad (6.55)$$

where  $j = \text{sign}(\hat{\phi}_k)$  to assure that  $\theta$  is the ratio of slopes in upwind direction;  $\gamma'$  is a small number (e.g.  $1 \cdot 10^{-8}$ ) to prevent division by zero. The most simple ratio  $\theta^{k,1}$  is usually applied in literature (e.g., Le Veque 1990, García-Navarro et al. 1992), and only accounts for differences in amplitudes of Riemann variables. An alternative is given by ratio  $\theta^{k,2}$  which considers the amplitude of the correction part in the Lax-Wendroff flux (equation 6.46). A third alternative might be the multiplication of the associated eigenvectors with the numerator and denominator of either of these two types of ratios, but this option is not further studied. We experienced that for most computations the ratio  $\theta^{k,2}$  is superior to  $\theta^{k,1}$  when computing gravity-current shocks.

There are different flux-limiter functions available in literature. One of the additional demands following from the application of these limiters to the Lax-Wendroff flux is symmetry (Hirsch, 1990). All limiters are non-linear functions of the slope ratio and satisfy the following condition

$$0 \leq \frac{\Phi(\theta)}{\theta} \leq 2 \quad \text{and} \quad \Phi(\theta) \leq 2 \quad (6.56)$$

Some of the popular limiters which are incorporated in the numerical model are summarized in appendix B, and can also be found in Hirsch (1990) and Le Veque (1990). The most important limiters from these are the 'minmod' function, the smooth limiter function by van Leer (1974), and the 'superbee' limiter of Roe (1985). While the superbee limiter is slightly overcompressive which makes gradients steeper, the minmod and van Leer limiters are slightly diffusive making gradients smoother. Choosing either one of these limiters must be based on experience or numerical experiments since there are no additional guidelines.

In the non-linear case Roe's decomposition is only applied to determine the artificial viscosity term, which is added to the MacCormack fluxes at each time step. Summarizing the theory above the viscosity term is computed at the begin of each time for each cell interface  $x_{i+1/2}$  by

$$\mathbf{D}_{i+1/2}^n = \frac{1}{2} \sum_{k=1}^m \{1 - \Phi_k(\theta_k)\} \cdot |\hat{\phi}_k| \cdot \left(1 - \frac{\Delta t}{\Delta x} |\hat{\phi}_k|\right) \cdot (\Delta_x \omega_k) \cdot \hat{\mathbf{r}}_k \quad (6.57)$$

and implemented in the algorithm as given by the algorithm 6.2.

<p>Compute : <math>\mathbf{D}_{i+1/2}^n(\text{TVD}) = \frac{1}{2} \sum_{k=1}^m \{1 - \Phi_k(\theta_k)\} \cdot  \hat{\phi}_k  \cdot \left(1 - \frac{\Delta t}{\Delta x}  \hat{\phi}_k \right) \cdot (\Delta_x \omega_k) \cdot \hat{\mathbf{r}}_k</math></p> <p style="text-align: center;">↓</p> <p>Compute : <math>\Delta \bar{\mathbf{U}}_i = -\frac{\Delta t}{\Delta x} [\Delta_x \mathbf{f}_i^n] + \Delta t \mathbf{Q}_i^n</math> (predictor)</p> <p style="text-align: center;">↓</p> <p>Compute : <math>\Delta \bar{\bar{\mathbf{U}}}_i = -\frac{\Delta t}{\Delta x} [\nabla_x \bar{\mathbf{f}}_i] + \Delta t \bar{\mathbf{Q}}_i</math> (corrector)</p> <p style="text-align: center;">↓</p> <p>Compute : <math>\mathbf{U}_i^{n+1} = \mathbf{U}_i^n + \frac{1}{2} [\Delta \bar{\mathbf{U}}_i + \Delta \bar{\bar{\mathbf{U}}}_i] + \frac{\Delta t}{\Delta x} (\mathbf{D}_{i+1/2}^n - \mathbf{D}_{i-1/2}^n)</math></p>
---

Algorithm 6.2 TVD MacCormack algorithm (repeat this cycle for  $t=0, t_{end}-\Delta t$ )

In the mobile bed routine the addition of this type of viscosity increases the computational effort drastically as the eigenvectors and characteristic variables are



large terms, although it is worth it. Therefore, unlike algorithm 6.1 for conventional artificial viscosity, we have knowingly chosen not to repeat the computation of the TVD viscosity before the correction step. The model appeared to work sufficiently well in this way. In appendix B is shown that for a fixed bed routine with constant concentration the amount of work can be reduced significantly.

One of the disadvantages of Roe's linearization is the incapacity of computing rarefaction waves. Therefore the proposed TVD method might yield entropy violating shocks. This problem can be overcome by using an entropy fix as proposed in literature (e.g., Hirsch 1990, Le Veque, 1990). Although relevant numerical experiments revealed that it is rarely encountered, and even then it is often solved by choosing a different limiter or a different slope ratio as defined in eq.(6.55), we have implemented such an entropy fix in the model. In appendix B the chosen method as proposed by Harten and Hyman (1983) is presented.

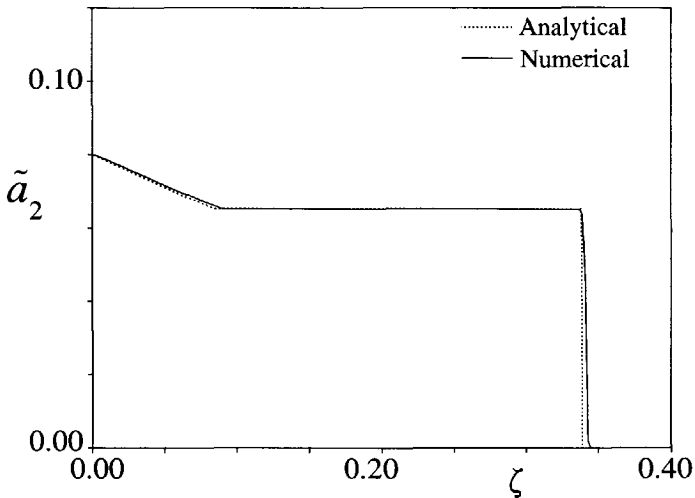


Figure 6.11 Partial lock-exchange flow computed with TVD scheme with superbee limiter, compared to its analytical self-similar solution.

To illustrate the performance of the TVD scheme the two examples for a self-similar partial and full lock-exchange flow from the previous section are recomputed here. Figure 6.11 shows that the solution for the partial lock-exchange is oscillation free as expected, and the rarefaction-wave region is reproduced accurately. For this case the superbee limiter appeared to give the best fit to the analytical profile, although the results of other limiters are hardly a match for it. The computations of a full lock-exchange flow in figure 6.12 give even stronger evidence for the superiority of TVD artificial viscosity over the conventional artificial viscosity methods. In the previous section it was shown (figures 6.9 and

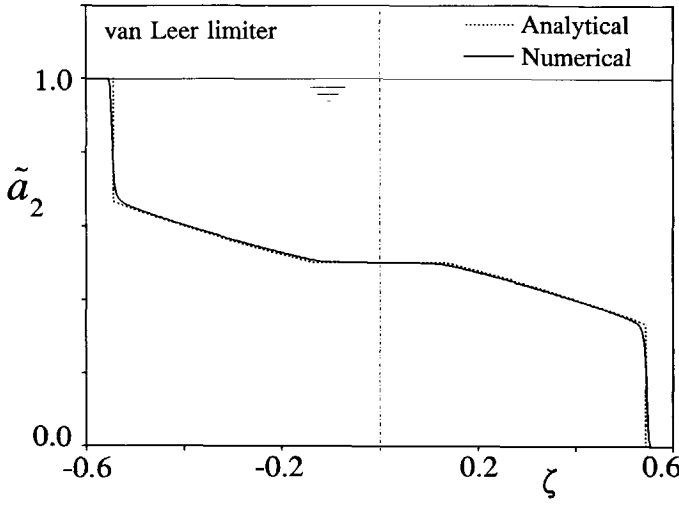


Figure 6.12 Self-similar full lock-exchange flow computed with TVD scheme using van Leer's limiter and  $\theta^{k,1}$ .

6.10) that, even with a large diffusion coefficient, the results did not fully converge to the exact (discontinuous) solution. By using the TVD method this convergence problem is eliminated, which greatly improves the accuracy and stability of the model. In figure 6.12 results are given obtained with van Leer's limiter and  $\theta^{k,2}$ . Excellent results are also found if the minmod limiter is used, giving a little more viscosity near the front. However, slightly less appropriate is the superbee limiter since it does not provide sufficient smearing. A detail of this computation for these three limiters is illustrated in figure 6.13.

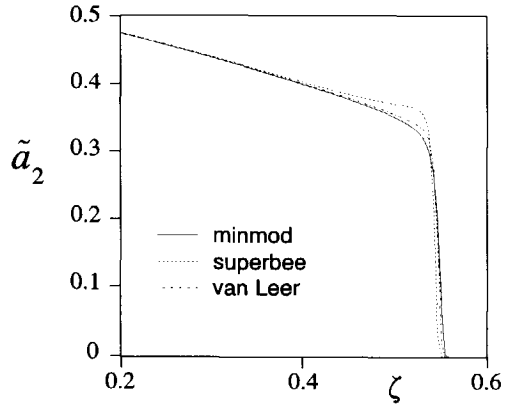


Figure 6.13 Comparison of three TVD limiters applied to a lock-exchange flow.

Not using an entropy fix for this lock-exchange flow appeared to cause failure near  $\zeta=0$  due to the development of a small entropy violating shock (more specific: an expansion with transcritical point). The application of the TVD method presented in this section is not restricted to our model. It can be applied to various shallow-water type equations, for instance to fixed-bed open-channel flow as studied by García-Navarro et al. (1992). In the following chapter results are shown with respect to mobile bed cases and turbid underflows.

Total Variation Diminishing artificial viscosity increases the accuracy and stability of the model on a local level, but it is not sufficient to guarantee them globally. Much more important for the total performance of the model is the boundary-value treatment. This is the topic of the next section.

## **6.7 Boundary conditions**

### **6.7.1 Type of boundary conditions and well posedness**

An essential part of the numerical model is the treatment of boundary conditions (further abbreviated as b.c.). Its effects are often underestimated, resulting in unrealistic or unstable results. Every type of numerical model (1-D or 2-DH) used to compute shallow-water problems has to deal with its boundaries since a numerical grid is always bounded. The hyperbolic propagation property of these equations causes the information from the boundaries to eventually cover the full computational area, overriding the initial boundary values.

Using the method of characteristics it has been shown in chapter 3 that the number of physical b.c., which have to be imposed at a certain boundary, corresponds to the number of characteristics entering through it. On the other hand the remaining outgoing characteristics also affect these boundaries. Here the number of characteristics (ingoing and outgoing) exactly corresponds to the number of dependent variables. Imposed boundary conditions may have different appearances dependent on physical considerations: they may be values of dependent variables or combinations of them (dirichlet type), or they may be gradients of certain variables (Neumann type).

Although we are quite free in taking any type of b.c. (of physical origin) there is an important limitation: the problem should be well posed such that full information on the ingoing and outgoing characteristics can be recovered from the imposed conditions, leading to a bounded solution. In numerical practice this means that at least all the values of dependent variables at the boundary can be computed

from a combination of imposed b.c. and the information coming from the interior along the outgoing characteristics as will be shown hereafter (e.g., see Hirsch, 1990). This must be achieved in a way consistent with the physical properties of the flow, and compatible with the discretized equations.

The types of b.c. that are appropriate and general applicable to the 1-D internal flow model are summarized in table 6.1, where  $\Delta q_2(t) = q_2^{n+1} - q_2^n$ , and  $\phi_k$  ( $k=1,4$ ) are the characteristic celerities at these boundaries. Positive celerities enter the domain through the inflow boundary, and leave through the outflow boundary, negative celerities do the opposite.

		Fixed bed	Mobile bed
Inflow	Subcritical	$(\phi_1 > 0, \phi_2 < 0)$ $\Delta q_2(t)$	$(\phi_1, \phi_3, \phi_4 > 0, \phi_2 < 0)$ $\Delta q_2(t), \Delta C_s(t), \Delta z_b(t)$
	Supercritical	$(\phi_1, \phi_2 > 0)$ $\Delta q_2(t), \Delta a_2(t)$	$(\phi_1, \phi_2, \phi_4 > 0, \phi_3 < 0)$ $\Delta q_2(t), \Delta a_2(t), \Delta C_s(t)$
Outflow (e.g. dam)	Subcritical	$(\phi_1 > 0, \phi_2 < 0)$ $\Delta a_2(t)$ or $\Delta q_2(t)$	$(\phi_1, \phi_3, \phi_4 > 0, \phi_2 < 0)$ $\Delta a_2(t)$ or $\Delta q_2(t)$
	Supercritical	$(\phi_1, \phi_2 > 0)$ -	$(\phi_1, \phi_2, \phi_4 > 0, \phi_3 < 0)$ $\Delta z_b(t)$

Table 6.1 Boundary conditions for the internal-flow model.

In figure 6.14 an example is given of the theory with a  $x,t$ -diagram for an internally subcritical fixed-bed flow.

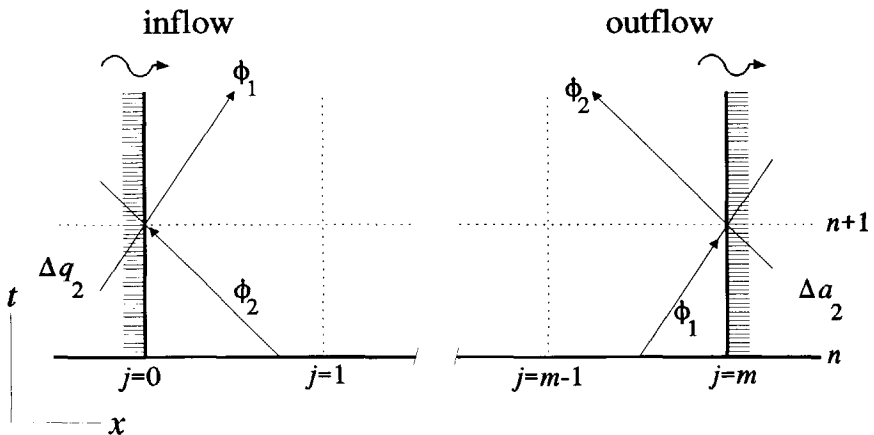


Figure 6.14 Boundary conditions for a subcritical underflow on a fixed bed.

For the chosen set of b.c, it can be shown that the numerical approach is well posed by looking at the characteristics of the linearized homogeneous problem. In the previous section on TVD methods the flux transport through cell boundaries is split in simple-wave components which are transported along characteristics in a decoupled way. These results can also be used to decouple the information from the boundaries entering the domain, and the information from the interior leaving the domain. Consider the model where b.c. are perturbations  $\Delta \mathbf{U}$  around the local boundary values  $\mathbf{U}^n$ . The perturbations can now be decomposed in characteristic variables or simple-wave components as shown in appendix B:

$$\mathbf{U}^{n+1} = \mathbf{U}^n + \Delta \mathbf{U} \quad ; \quad \Delta \bar{\omega} = \mathbf{R}^{-1} \Delta \mathbf{U} \quad (6.58)$$

Here  $\mathbf{R}^{-1}$  is the inverse of the eigenvector matrix with constant coefficients equal to their value on the boundary (with  $\mathbf{U}^n$ ). Each characteristic variable  $\omega_k$  is transported along a characteristic  $\phi_k$ , and is known in advance. In table 6.1 the number of dependent variables given at the boundary corresponds to the number of incoming characteristics. Then the remaining variables are the numerical b.c., which can be defined from the part of system (6.58) for outgoing characteristics if the problem is well posed. For the mobile bed model the decomposition (6.58) is given in appendix B, yielding

$$\Delta \omega_1 = \frac{\gamma_{11} \Delta \Omega + \gamma_{21} \Delta a_2 + \gamma_{31} \Delta C_s + \gamma_4 \Delta z_b}{(\phi_1 - \phi_2)(\phi_1 - \phi_3)} \quad \text{for } \phi_1 \quad (6.59)$$

$$\Delta \omega_2 = \frac{-\gamma_{12} \Delta \Omega - \gamma_{22} \Delta a_2 - \gamma_{32} \Delta C_s - \gamma_4 \Delta z_b}{(\phi_1 - \phi_2)(\phi_2 - \phi_3)} \quad \text{for } \phi_2 \quad (6.60)$$

$$\Delta \omega_3 = \frac{\gamma_{13} \Delta \Omega + \gamma_{23} \Delta a_2 + \gamma_{33} \Delta C_s + \gamma_4 \Delta z_b}{(\phi_1 - \phi_3)(\phi_2 - \phi_3)} \quad \text{for } \phi_3 \quad (6.61)$$

$$\Delta \omega_4 = \Delta C_s \quad \text{for } \phi_4 \quad (6.62)$$

where  $\gamma_{ij}$  are coefficients computed from  $\mathbf{U}^n$  (see appendix B). Here  $\Delta \Omega$  can be written in terms of  $q_2$  and  $a_2$  as

$$\Delta \Omega \approx \left[ \frac{a}{a_1^n a_2^n} \right] \Delta q_2 - \left[ \frac{a q_2^n (a_1^n - a_2^n)}{(a_1^n a_2^n)^2} \right] \Delta a_2 \quad (6.63)$$

Using those relations associated to outgoing characteristics, together with the given physical b.c., a system of equations is obtained which must be solvable for the

numerical b.c. For instance in table 6.1 the physical b.c. for a subcritical outflow may be given by  $\Delta q_2$ , while along the outgoing characteristics equations (6.59), (6.61) and (6.62) hold. It can now be shown easily that, in combination with equation (6.63) and after substitution of the value of  $\Delta q_2$ , a system of 3 linear equations has to be solved to find the numerical b.c.  $\Delta a_2$ ,  $\Delta C_s$  and  $\Delta z_b$ . Elaboration of these results for this case, as well as for the other mobile-bed cases in table 6.1 shows that the numerical b.c. can always be solved. With these b.c. the model is well posed.

In a fixed-bed model the number of equations in system (6.58) reduces to two and is also given in appendix B (by replacing  $\Delta_x$  by  $\Delta$  in equation B.35). Since both relations for the characteristic variables (for  $\phi_1$  and  $\phi_2$ ) contain  $\Delta q_2$  and  $\Delta a_2$ , it makes no difference which of them is chosen as a physical b.c. The other one can always be recovered from these relations, and the model is always well posed.

Some alternatives to the b.c. from table 6.1 can be defined for the dam boundary. The outflow from the reservoir is determined by the structure: a combination of turbines, spillways and bottom outlets can be used to manage the reservoir level and eventually to control sedimentary processes. For these structures head-discharge relations can be defined and implemented in the model. Most important for venting out the turbid underflows are the bottom outlets. A type of hydraulically short underflow gate with free outflow is given in figure 6.15 for the external flow boundary.

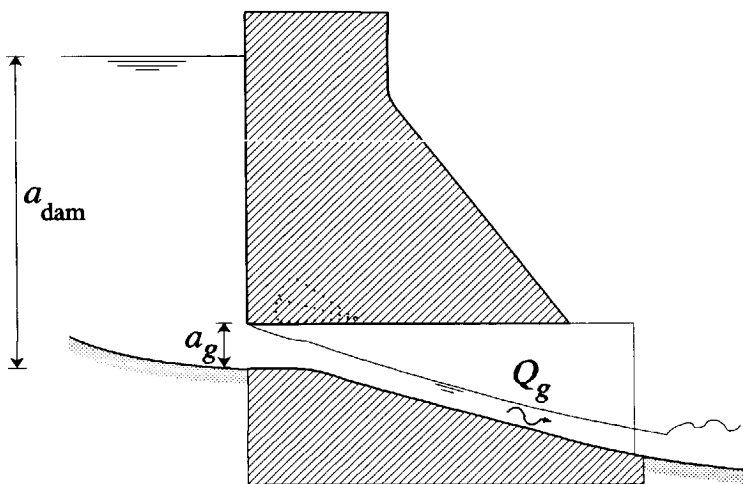


Figure 6.15 Bottom outlet with free outflow (schematic).

The following head-discharge relation expresses its outflow if the  $u/(2g)$  upstream is small (e.g. Chow, 1959):

$$Q_g = B_g \cdot \mu_g \cdot a_g \sqrt{2g a_{\text{dam}}} \quad ; \quad 0.5 < \mu_g < 0.6 \quad (6.64)$$

where  $a_g$  is the depth of the gate,  $B_g$  its width,  $Q_g$  its discharge, and  $\mu_g$  a discharge coefficient. The coefficient  $\mu_g$  depends on many factors, such as the size, entrance geometry, slope, etc. Sometimes the bottom-outlet is a hydraulically long tunnel, which acts as a culvert. It may flow full as a pipe flow and sediment clogging is possible (see section 1.3). Still the head-discharge (6.64) relation can be used with adapted  $\mu_g$  to compute the external flow, and subsequently the internal flow. Note that for a quasi-steady approach also holds (at both boundaries) that  $\partial q/\partial x=0$ .

When the turbid underflow reaches the dam it is sucked in by the bottom outlet. The effect of the increased gravity on the head-discharge relation is small (order of  $\sigma' \cdot C_s$ ), hence equation (6.64) still applies for the external flow computation. The underflow discharge at this point now has an upper limit equal to  $Q_g$  since it is unlikely that clear water is flowing back through the outlet into the reservoir. Therefore in a subcritical outflow condition the flow b.c. should be chosen as  $q_2 = Q_g/B_g$ , in a supercritical state it suffices to verify that  $q_2 \leq Q_g/B_g$ .

For morphological b.c. it is possible to impose the bed-load gradient  $\partial s_b/\partial x (t)$  instead of the bed-level variation. Using the discretized form of the mass-balance equations (section 6.4) it can be shown that this gradient can be reformulated in terms of  $\Delta z_b$ , proving its equivalence to imposing the bed level directly. This option is less relevant for turbidity currents as they are dominated by suspended-sediment.

Besides these alternatives, many others can be formulated as combinations of b.c. from table 6.1 (eventually by using the discretized basic equations). An additional check to the well-posedness of the system can be carried out by analyzing the energy growth of the system. In a well posed problem energy remains bounded, which can be verified theoretically after reformulating the compatibility equations to an energy equation. For more details we refer to Vreugdenhil (1994).

During the model development of the model we have restricted ourselves to b.c. from this table, and applied them to attune the boundary treatment. In the following sub-section is shown how the b.c., satisfying the well-posedness condition, have to be formulated and have to be adjusted to the interior flow model.

## 6.7.2 Discretization of boundary conditions

Application of MacCormack's space-centred scheme to the interior flow field requires a special treatment at the boundary points ( $j=0, j=m$ ) whereas values

outside the domain ( $j=-1, j=m+1$ ) are unknown. It is shown before that by giving the correct number of physical b.c. the remaining (numerical) boundary values should be defined from the information from the interior, transported along outgoing characteristics. Various alternatives can be formulated to determine numerical b.c. ranging from simple extrapolation to one-sided differences or adoption of imaginary points outside the domain, so called 'ghost' points. A review on this subject and the associated theory can for instance be found in Hirsch (1990) and Vreugdenhil (1989, 1994). Although most of the alternatives perform well with smooth flows, our experience showed that their behaviour during passage and reflection of strong shocks is a most critical constraint.

The importance of choosing the best method is obvious with respect to global accuracy and stability of the model. In the previous section it is shown that information as well as discretization errors from b.c. are transported into the interior due to the hyperbolicity of the model. This effect will eventually cover the full computational domain, and determines the solution to the difference equation. An erroneous boundary treatment may cause undesirable reflections of outgoing waves, or creates a source which emanates wiggles which may grow and lead to numerical instability. Basically the boundary discretization must be consistent and in harmony with the physical and numerical problem (e.g., stable, conservative and no under- or overspecification with respect to well posedness). Additionally it must provide sufficient accuracy to maintain the global order of accuracy of the complete model. As a rule of thumb Gustafsson's (1975) theorem proves that, for linear equations, the boundary scheme can be one order lower than the interior scheme. For MacCormack's method it may therefore be a first-order scheme.

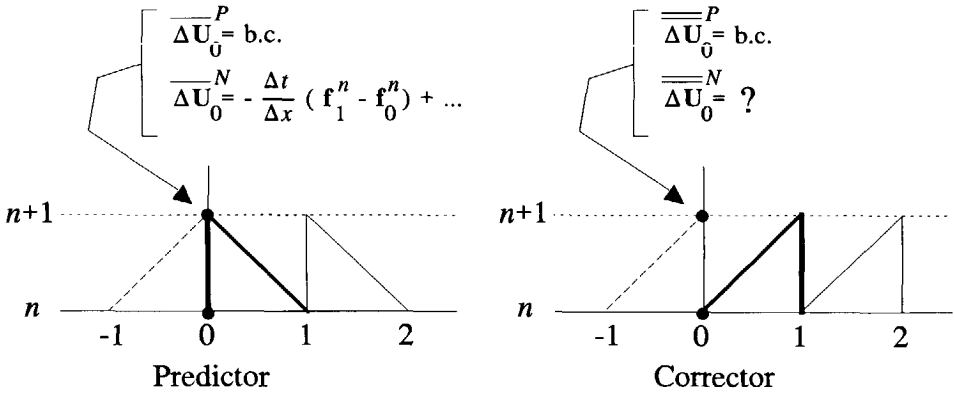


Figure 6.16 MacCormack's scheme near an inflow boundary ( $x,t$  diagram).

The implementation of boundary conditions is relatively simple as MacCormack's method is composed of forward and backward (one-sided) differences in predictor



and corrector step respectively. In figure 6.16 is illustrated how predicted and corrected values are computed near the inflow boundary. Values with superscript  $P$  are prescribed boundary values, while those with superscript  $N$  are the numerical boundary values which have to be determined. In the predictor step the numerical boundary values follow directly from the forward difference, but in the corrector step an extrapolation is required. At the outflow boundary the opposite situation occurs. The various alternatives for extrapolation are discussed briefly hereafter. A comprehensive discussion of some extrapolation methods applicable to this approach is given for instance by Hirsch (1990).

The most simple approach to find the numerical boundary values in figure 6.16 in the corrector step is a simple linear (first-order) variable extrapolation in space. Firstly compute all the corrected values in the interior, secondly compute unknown boundary values using a Taylor-series based extrapolation (e.g., see Roache, 1972, Hirsch, 1990):

$$\bar{U}_0^{N,n+1} = 2 \cdot \bar{U}_1^{N,n+1} - \bar{U}_2^{N,n+1} \quad \text{or} \quad \Delta \bar{U}_0^N = 2 \cdot \Delta \bar{U}_1^N - \Delta \bar{U}_2^N \quad (6.65)$$

Similarly a predictor solution for numerical boundary values at the downstream boundary can be defined by means of a space extrapolation of predicted values from the interior:

$$\bar{U}_m^N = 2 \cdot \bar{U}_{m-1}^N - \bar{U}_{m-2}^N \quad \text{or} \quad \Delta \bar{U}_m^N = 2 \cdot \Delta \bar{U}_{m-1}^N - \Delta \bar{U}_{m-2}^N \quad (6.66)$$

Numerical experiments showed that this approach worked well for our model, but during passage of shocks a large overshoot (or undershoot) occurs which results in a strong reflection and sometimes a break down of the computations. Higher-order (non-linear) space extrapolations do not noticeably improve the approach. Nevertheless for a majority of the experiments the (first-order) method seemed to be sufficiently stable and accurate.

To improve these results we attempted to extend this simple variable extrapolation to a characteristic extrapolation method. Recalling that the numerical boundary values are determined by the information (simple-wave components) carried along outgoing characteristics it is possible to decompose them into characteristic variables after linearization. In the previous sub-section a simple-wave component  $\Delta \omega_k$  is formulated for each characteristic  $\phi_k$  as function of physical variables (eq.'s 6.59 to 6.63). It has been shown that if those relations associated to outgoing waves in combination with the impose b.c. is solvable, the problem is well posed. If we consider the example of figure 6.16 with a subcritical inflow we have one equation (6.60) (after rewriting  $\Delta \Omega$  in terms of  $\Delta q_2$  and  $\Delta a_2$ ) for the outgoing characteristic  $\Delta \omega_2$  and three imposed boundary values  $\Delta q_2^P$ ,  $\Delta C_s^P$ , and  $\Delta z_b^P$ :

$$\overline{\overline{\Delta \omega_2^N}}(0) = \frac{-\gamma_{12b}^n(0)\overline{\overline{\Delta q_2^P}}(0) - \gamma_{22b}^n(0)\overline{\overline{\Delta a_2^N}}(0) - \gamma_{32}^n(0)\overline{\overline{\Delta C_s^P}}(0) - \gamma_4^n(0)\overline{\overline{\Delta z_b^P}}(0)}{(\phi_1^n(0) - \phi_2^n(0))(\phi_2^n(0) - \phi_3^n(0))} \quad (6.67)$$

where

$$\overline{\overline{\Delta q_2^P}} = 2 \cdot \Delta q_2^P(0) - \overline{\overline{\Delta q_2}}(0) \quad ; \quad \overline{\overline{\Delta C_s^P}}(0) = 2 \cdot \Delta C_s^P(0) - \overline{\overline{\Delta C_s}}(0) \quad \text{etc.} \quad (6.68)$$

Coefficients  $\gamma_{ij}$  are defined in appendix B and are obtained from the flow state  $U^n(0)$ . The solution for  $a_2(0)$  can now be obtained from this equation using extrapolation of  $\Delta \omega_2$  for instance by

$$\overline{\overline{\Delta \omega_2^N}}(0) = 2 \cdot \overline{\overline{\Delta \omega_2}}(1) - \overline{\overline{\Delta \omega_2}}(2) \quad \text{or} \quad \overline{\overline{\Delta \omega_2^N}}(0) = \overline{\overline{\Delta \omega_2}}(0) \quad (6.69)$$

A similar result can be written for the outflow boundary. Note that the system is linearized around the values at the previous time level ( $n$ ) but these can be replaced by values from the predictor level. For more details on this elaboration see for instance Hirsch (1990). Again the performance of the method is studied experimentally. For continuous flows the behaviour is comparable to the previously presented variable extrapolation method, but with rapid flow changes notably at shocks the approach is failing. Again over- and undershoots occur and near critical flow (Froude numbers near unity) the method often converges to the wrong solution. The overall performance to our model is slightly worse than a simple variable extrapolation.

Some methods which are more comprehensive can be based on first-order one-sided differences of the basic equations at the boundary. Most natural with respect to the example of figure 6.16 is replacing the backward difference in the corrector step by a forward difference to obtain the corrector boundary value. However, this is incorrect since the final boundary scheme is unstable. This can easily be shown by applying a Neumann stability analysis to a forward difference of simple frictionless 1-D shallow water equations with convection and pressure included (e.g. section 6.9). For this elementary model, which is essentially similar in behaviour as our model, the following stability criterion must hold for all celerities  $\phi_k$ :

$$\phi_{1,2} \frac{\Delta t}{\Delta x} \leq 0 \quad \text{or} \quad (u \pm \sqrt{ga}) \frac{\Delta t}{\Delta x} \leq 0 \quad (6.70)$$

Clearly this condition is satisfied for the negative celerity (with  $u < \sqrt{\{ga\}}$ ), but never for the positive celerity.

The correct procedure in this case is to split the system into its compatibility equations which express the upwind propagation of simple waves along the characteristics. Such a decomposition of the model has been presented in appendix B (section B.1). The equations corresponding to outgoing characteristics are discretized using the forward (or backward) difference, which is then a correct upwind scheme. As a matter of fact the characteristic extrapolation method presented before is an equivalent (simplified) formulation of this approach, and the computational performance is therefore comparable. Again the computation of strong shocks and near critical flow (when characteristics change sign and other compatibility equations become operative) is insufficient. Theoretically the use of compatibility equations for this model is dissuaded as the equations are non-conservative and require a strong linearization which makes the discretization inconsistent with the internal model. A significant effort is required to ameliorate the behaviour round discontinuities. Note that if the TVD artificial viscosity method is used in the computation (section 6.6) the characteristic decomposition of the model is already implemented.

So far the presented methods are operative but lack robustness with respect to computing discontinuities. Various alternatives were defined to improve the boundary treatment. For instance: higher-order variable extrapolation methods to include more points from the interior, using Roe's (1981) first-order upwind scheme at the boundary (using the information available from the TVD algorithm), upwind differencing of compatibility equations rewritten in terms of  $\mathbf{U}$  instead of  $\omega$ , iterative solution of Riemann invariants along outgoing characteristics, etc. However, most of them were rejected quickly as their performance did not justify the effort if compared to simple first-order variable extrapolation methods.

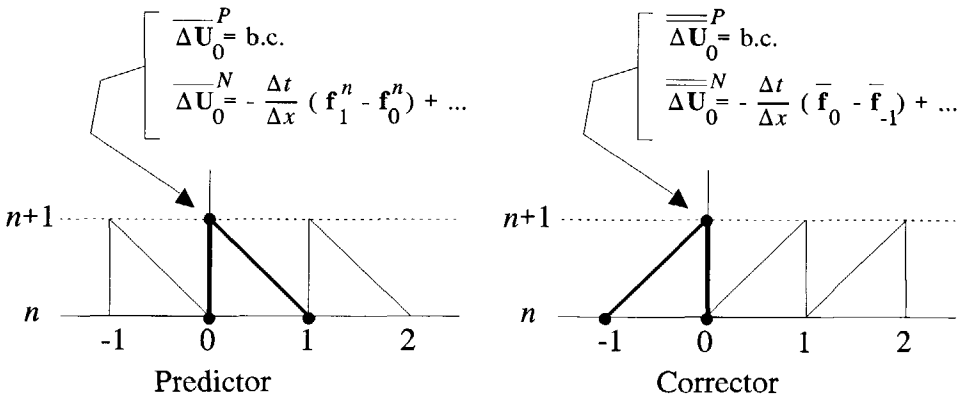


Figure 6.17 MacCormack's scheme using ghost points near an inflow boundary ( $x,t$  diagram).

Robustness of the computations could only be obtained using additional points

outside the region such that MacCormack's scheme can be used including the boundary. Numerical values at these 'ghost' points ( $j=-1$  upstream, and  $j=m+1$  downstream) are obtained from linear extrapolation from the boundary and the interior (according to eq.'s 6.65 and 6.66) or a zero-order extrapolation ( $U_{-1}=U_0$ ). Every time that new values at the boundary are computed (as well as in the predictor as in the corrector step) they are corrected according to the specified boundary conditions. Ghost-point values can also be adjusted at each level to newly computed interior values. In figure 6.17 this procedure is illustrated for the inflow boundary similarly to figure 6.16. With the proposed extrapolation the resulting boundary scheme is at least first-order accurate, hence global accuracy remains second-order. The solution near the boundary is free of wiggles and undesirable reflections of strong shocks are significantly reduced. These good results came up to the expectation as the boundary discretization is fully consistent with the interior scheme, which is stable and accurate. In this way the boundary treatment is composed of three steps, to be applied at both the predictor and the corrector level:

1. Extrapolate boundary values to ghost points (linearly:  $U_{-1}^n = 2 \cdot U_0^n - U_1^n$ ).
2. Compute predictor or corrector values (algorithm 6.1 or 6.2) of the interior flow field, and include in this computation the boundary points.
3. If necessary then rewrite the computed boundary values according to the prescribed b.c.

With respect to step 3 it has been shown in the previous sub-section that different boundary conditions have to be prescribed depending on the flow type, i.e., internally sub- or supercritical flow. Since the flow type at the boundary may change during a computation a detector routine is added to the model. A well functioning approach was found to be a check of near-boundary internal Froude numbers computed from the preceding computational level. At the predictor step we compute Froude numbers from the preceding time-level; at the corrector step we compute them from the predictor level. Changes in flow type at the boundary usually occur rapidly by the passage of shocks, which were located in the first mesh cell next to the boundary at the previous time level. To conduct the shock through the boundary it is necessary to check the densimetric Froude numbers of the mesh point on either side of the boundary cell for the choice of b.c. It is found that this can be achieved by taken a subcritical inflow b.c. only if

$$Fr_{D1}^2(j=0) + Fr_{D2}^2(j=0) \leq 1 \quad \text{or} \quad Fr_{D1}^2(j=1) + Fr_{D2}^2(j=1) \leq 1 \quad (6.71)$$

and a subcritical outflow b.c. only if

$$Fr_{D1}^2(j=m) + Fr_{D2}^2(j=m) \leq 1 \quad \text{and} \quad Fr_{D1}^2(j=m+1) + Fr_{D2}^2(j=m+1) \leq 1 \quad (6.72)$$

on a computational mesh with  $m+1$  gridpoints in  $x$ -direction ( $x=j \cdot \Delta x$ ,  $j=0$  to  $m$ ).

If the conditions above are not satisfied then an internally supercritical b.c. is chosen. The type of b.c. is taken from table 6.1.

Experimental results show that the numerical computation is stable and accurate for various types of underflows. Although this conclusion is entirely empirical, it can be supported by theoretical consideration. For instance tools to prove stability of the computation with the chosen boundary discretization can be obtained by using an energy method or an normal mode analysis (as described by Vreugdenhil, 1994). The latter can be considered as an (complicated) extension of Von Neumann's stability analysis (section 6.9) to non-harmonic normal modes generated at the boundaries.

Reviewing these results it has been shown that the boundary treatment imposes severe demands to the numerical model, especially when dealing with shocks. With respect to well posedness of the model the type of b.c. is best taken from table 6.1, while sufficient stability and accuracy can be obtained if ghost points are used in combination with a Froude number check. In the following section the boundary treatment is completed by considering the initial state which may be considered as a special type of boundary.

## 6.8 Initial conditions

The solution of the hyperbolic system has been shown to be determined by the information carried along the characteristics starting from an initial state and from the boundaries. For the time integration the initial state can therefore be considered as an additional boundary which determines the final solution of the model. In case of a Riemann problem it can be shown easily that the evolution of the solution into multiple shocks is mainly dependent on the initial (single) discontinuity prescribed. Only in very long runs the effect of (erroneous) initial conditions is overridden by the effect of boundaries and of external forces.

The fully coupled unsteady internal-flow model requires prescription of values of all dependent variables at each grid point. In fact, for every computational step, all previously computed variables can be considered as the initial condition. The choice of an appropriate initial condition must be made from physical considerations. At least we are looking for the state which evolves into the physical one we are interested in.

As an example we computed two comparable cases of an underflow over a forward-facing step with height  $\Delta z_b = 1$  m (frictionless flow over a fixed bed with a fixed concentration  $C_s = 0.005$ ). The first starts with a constant depth  $a_2 = 2.2$  m,

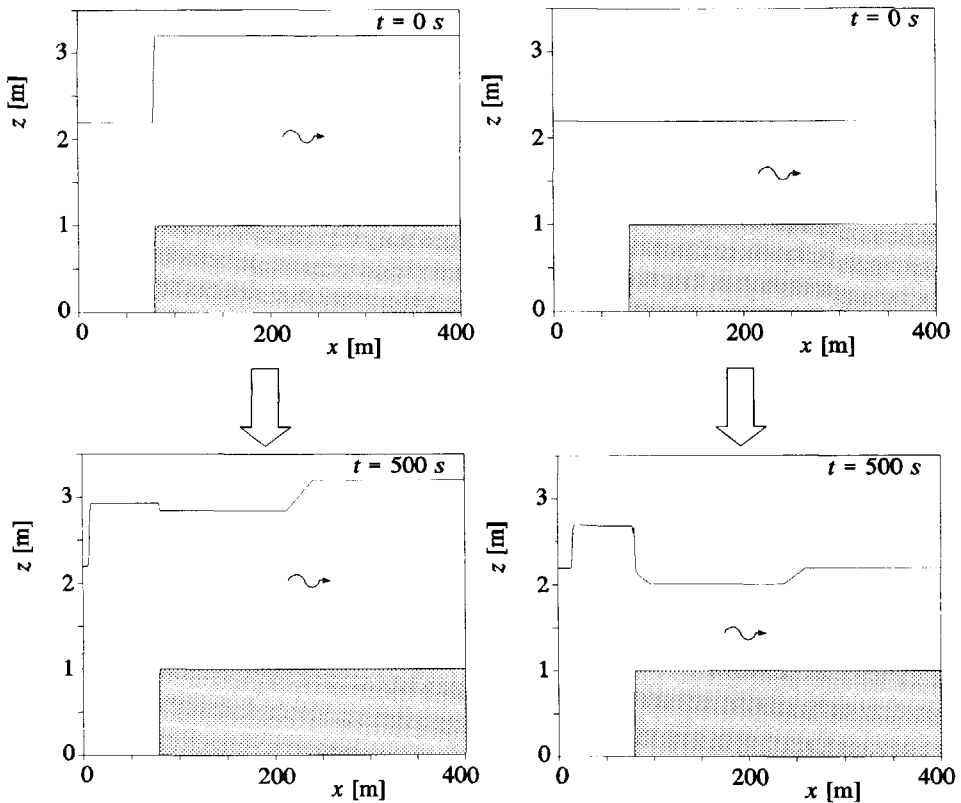


Figure 6.18 Density current over a forward facing step with two-different initial states: left  $a_2 = \text{constant}$ , right  $h_2 = a_2 + z_b = \text{constant}$ .

the second with a constant level  $h_2 = 2.2$  m. In both cases a constant  $q_2 = 0.5$   $\text{m}^2/\text{s}$  is used such that in the constant depth case the initial flow is internally subcritical, while in the constant level case the flow is internally subcritical on the left but supercritical on the right. The results show, figure 6.18, that (after 500 s) these initial Riemann problems are significant different, which can be directly traced to the initial state. For instance the flow type (internally sub- or supercritical) on both sides of the step remains unchanged, and the resulting underflow velocities  $u_2$  in the affected regions are larger in the constant level case.

Although this example illustrates the relevance of choosing a correct initial condition it is not a physically realistic initial state as it cannot occur in laboratory or field. A more appropriate state is a steady underflow with a prescribed bed-level, or a 'zero'-flow depth can be taken as initial condition. The interface profile of a steady underflow can be obtained by means of (numerical) integration of the system of basic equation with  $\partial/\partial t$  terms equal to zero. Therefore it is necessary to

prescribe an initial bed profile, and sufficient boundary conditions on the upper and lower boundary. When shocks (e.g. internal hydraulic jumps) are present in the steady underflow it is often more convenient to run the unsteady model with an arbitrary initial state (with correct b.c. and a fixed bed) until it converges to the steady solution. From that point the actual computations can commence. It should be remarked that this is sometimes a time-consuming procedure as it may take a long period to establish a steady profile. For example the previously described example (fig. 6.18) with a constant initial depth needs at least two hours (physical time) to stabilize (with a constant level this is even worse). In figure 6.19 the computed steady state for this example is plotted, which shows that the final state is far from the initial condition. A faster convergence can be achieved by choosing an initial condition closer to the final steady state.

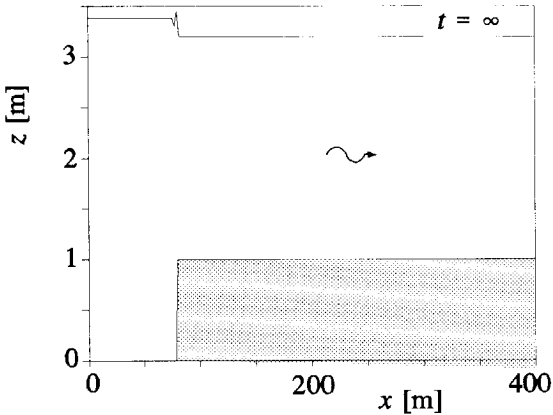


Figure 6.19 Steady state for a dense underflow on a forward step.

The choice of a 'zero' underflow depth as initial state is usually the best alternative when computing the development of a turbidity current into a reservoir. More specifically this state consists of a very small uniform underflow layer with a prescribed bed profile, considering the necessity of a finite depth along the full section to use a shock-capturing technique. Depths  $a_2$  and concentrations  $C_s$  of this layer are much smaller than those of the expected turbidity current, and its discharge is preferably taken in such a way that the densimetric Froude numbers along the section remain below unity. It is an essential requirement that this layer is much smaller than the following turbidity current front (generated by the b.c and running over the layer) to prevent significant violation of the 'dry'-bed front relation. Most of the calculations during this research are carried out using this approach.

Figure 6.20 gives an example of a front running over such a small layer together with a summary of the properties of this particular initial state. To preserve this state in the undisturbed region (before passage of the front) conditional statements

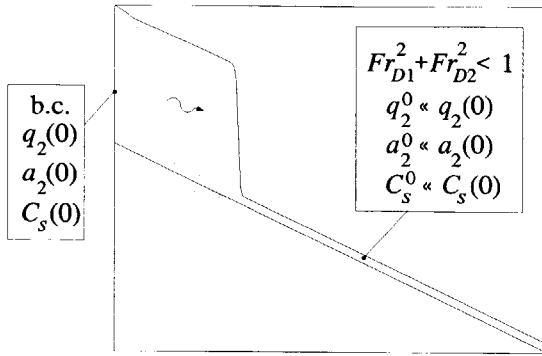


Figure 6.20 Example of an initial state with 'zero' underflow depth.

are added to the model which force the flow to maintain its initial properties. Without these statements there can be a small but noticeable increase of depth and discharges travelling rapidly ahead of the gravity-current front, changing the initially internal subcritical flow into an internal supercritical one. Through this effect the gravity-current front can be significantly flattened and accelerated, again distorting the robustness of the model. A simple solution lies in the fact that any discontinuity always travels slower than the largest celerity. The CFL-condition (section 6.9), which applies to this model, states that the information on this characteristic may not travel over more than one space step  $\Delta x$  during one time step  $\Delta t$ . Clearly also a gravity-current front moves over a distance which is less than  $\Delta x$ , and regions outside this range remain undisturbed. A conditional statement then follows from the values of the previous time level. Values on the new time level are undisturbed if the former flow situation one step  $\Delta x$  upstream (and downstream) is also undisturbed, e.g.

$$\text{if } \left\{ a_{2,i-1}^n = a_2^0 \text{ and } a_{2,i+1}^n = a_2^0 \right\} \text{ then } a_{2,i}^{n+1} = a_2^0 \quad (6.73)$$

In order to fully eliminate the non-physical propagation phenomena ahead of the front a second condition must be satisfied:

$$a_{2,i} \geq \alpha_i \cdot a_2^0 ; \quad q_{2,i} \geq \alpha_i \cdot q_2^0 ; \quad C_{s,i} \geq \alpha_i \cdot C_s^0 \quad (6.74)$$

otherwise the flow is assumed undisturbed and equal to the initial state. Here  $\alpha_i$  is a coefficient slightly larger than unity (e.g.  $\alpha_i = 1.01$ ). This condition does not only settle with small disturbances on the initial state, but also guarantees positivity of all computed values. In this way automatically the stability of the model is improved since the occurrence of negative variables causes a break down of the computations. Coefficient  $\alpha_i$  must be chosen as close to unity as possible, but large enough to preserve the initial state. An intermediate check during the computations is recommended.



Although the small-layer initial condition is most practical, there are other initial conditions possible determined by the physical state. For instance a lock-exchange flow (full or partial) requires a finite underflow depth on one side, and a 'zero'-depth on the other side of the gate. Even a wider range of general initial Riemann problems can be defined as the initial state is composed of two (or more) different states separated by a discontinuity. Note that every initial state yields different computational results, disregarding the influence of boundaries and wave damping by friction. As an extension of the conclusions of the previous section, it can therefore be concluded that the accuracy and stability of the solution is for a significant part determined by the correct treatment of the initial condition. Of course the treatment is only correct if the condition selected from those presented in this section reproduces the expected physical state. If an incorrect initial condition is deliberately prescribed, it is for instance necessary to run the model until the influence of these data is sufficiently reduced (check it) before the actual calculations may commence.

So far it has been concluded that the accuracy and stability of the computational results are greatly determined by the treatment of boundary and initial conditions. However, for this conclusion assumptions are used considering the accuracy and stability of the numerical scheme applied to our model. In the next section a short treatment of this subject is given.

## **6.9 Stability and accuracy**

Using finite difference techniques to solve the original system of differential equations only an approximative solution can be obtained. Therefore, to ensure some level of accuracy, the numerical results must converge to the exact ones as close as possible. This can be achieved by satisfying certain concepts of numerical analysis in order to control and minimize the errors. In this section the application of a few of the most relevant methods and their results for our model are discussed, which can be used for a qualitative analysis of computations and a reliable operation of the model. The error is assessed by examination of the local truncation error, as well as by examination of exact and numerical wave-like solutions of a simple advection equation in terms of Fourier series.

Assuming that the problem is well posed (e.g., satisfies existence, uniqueness) the numerical approach can be examined for instance on consistency, convergence, global errors, truncations errors, and stability. Qualitatively and quantitatively this can be carried out by comparing the original (exact) and the discretized equations and by comparing their respective solutions. For this, various approaches are available for both the linearized and non-linearized system. A first good indication of the behaviour of errors can be obtained for instance from the local truncation

error of the discretized equations. This is usually the first classical step in analyzing the model and provides valuable information as will be shown hereafter.

The local truncation error is obtained by substituting the exact solution into the finite difference equations (e.g. Hirsch 1990, Vreugdenhil, 1989). By expanding all terms of each (non-linear) difference equation into Taylor series relative to a central point  $i$ , the *modified equation* is obtained. The difference between the original differential equations and the modified equations is the local truncation error  $E_i(x,t)$ . It is the error in the equation, not in the solution although there is an analogy. Note that the numerical method is shown to be consistent if

$$\int_{-\infty}^{\infty} |E_i(x,t)| dx \rightarrow 0 \quad \text{as} \quad \Delta x, \Delta t \rightarrow 0 \quad (6.75)$$

For MacCormack's scheme applied to the model without source terms the truncation error is found to be of second order in  $\Delta x$  and  $\Delta t$ . This can be seen by expanding the local truncation error for our model. After assuming a deep reservoir ( $\Omega = u_2$ ) and neglecting entrainment, the truncation error for the momentum equation can be summarized after some effort in the following form

$$E_i = -\frac{1}{2} \Delta t^2 \left[ \frac{\partial^3(\dots)}{\partial x^3} + C_D \frac{\partial^2(\dots)}{\partial x^2} + C_d^2 \frac{\partial(\dots)}{\partial x} - \frac{1}{3} C_D^3 u_2^4 + \omega_s \frac{\partial^2(\dots)}{\partial x^2} + \omega_s^2 \frac{\partial(\dots)}{\partial x} + \dots \right] + \quad (6.76)$$

$$-\frac{1}{2} \Delta x^2 \frac{\partial^3(\dots)}{\partial x^3} - \frac{1}{2} \Delta t \Delta x \left[ \frac{\partial^3(\dots)}{\partial x^3} + C_D \frac{\partial^2(\dots)}{\partial x^2} + \omega_s \frac{\partial^2(\dots)}{\partial x^2} + \dots \right] + \text{h.o.t}$$

Here  $C_D$  and  $\omega_s = w_s / (a_2 T_w')$  are associated to the source terms in momentum and concentration equation respectively. Dots in parentheses denote terms which are combinations of dependent variables, while higher-order terms (h.o.t) are terms of the order three and higher in  $\Delta x$  and  $\Delta t$ . A similar truncation error can be written for the other equations as well. Note that this result proves that the method is consistent since  $E_i$  disappears for vanishing step size. Without the source terms (e.g.,  $C_D = \omega_s = 0$ ) the truncation error only contains second-order terms with  $\Delta x^2$ ,  $\Delta t^2$ ,  $\Delta x \cdot \Delta t$  or higher order. The third-order derivatives to  $x$  appearing in these terms cause dispersion which have been shown to cause wiggles near discontinuities. The dispersion coefficients depend on flow and step-size as expected. On the other hand, if source terms are not discarded, lower-order derivatives to  $x$  appear in the truncation error causing more dispersion (odd-order derivative) and diffusion (even-order derivative). This combination may cause a distortion of the solution. However, the coefficients of these terms are proportional to  $C_D$  and  $\omega_s$ , which are usually quite small so that the generated error is limited.

The truncation error does not provide direct information on the error in the

solution, i.e. the discretization error. Whether the solution is accurate can be evaluated experimentally by computing the solution with different step sizes, or analytically by studying harmonic wave propagation with linearized equations. Although the latter can give a good indication of the discretization error, as will be shown later in this section, it does not provide information on the accuracy of non-linear cases with discontinuities relevant to our case. Therefore we checked the accuracy experimentally after various numerical test. For smooth flows the error is only a fraction of the result and therefore sufficiently accurate. When computing a front the error is usually increased by the extrapolation of concentrations near the jump (section 6.10), hence it is not due to the numerical scheme. This may cause relative errors of a few percent in amplitudes and propagation speeds, but usually these errors remain within acceptable bounds. In all cases the total mass of the system remains conserved according to the in and outflow of mass through the boundaries. Mass-conservation is of fundamental importance for the model and leakage or accretion of mass would lead to high inaccuracy.

Of course stability of the numerical scheme must be guaranteed for accuracy and convergence of the computation. Since MacCormack's scheme is an explicit numerical scheme stability criteria impose time-step limitations. Generally these criteria are obtained using a von Neumann analysis on the linearized differential equations for which MacCormack's scheme corresponds to Lax-Wendroff's scheme. For Lax-Wendroff's scheme without artificial viscosity this theory is well elaborated in literature, e.g. Lax & Wendroff (1960,1964), Hirsch (1990), Finlayson (1992). In the following an extension is given for the model with artificial viscosity. Although the approach can be applied to the full system it usually suffices to consider only a scalar-type linear advection equation for the exact solution and a linear convection-diffusion equation for the numerical solution with artificial viscosity. The problem, excluding source terms, is defined as

$$\frac{\partial u}{\partial t} + \phi_0 \frac{\partial u}{\partial x} - \Delta x \cdot \delta^v \frac{\partial^2 u}{\partial x^2} = 0 \quad ; \quad u(x,0) = u_0 \cdot \exp(ikx) \quad (6.77)$$

where  $\phi_0$  is the wave celerity and  $\delta^v$  is the artificial viscosity coefficient as defined in section 6.5 and taken as a constant here. Changes of a single general Fourier component are considered (initial oscillation) since any wave-like solution can be composed by linear superposition of these terms. Here we define  $-k \cdot x = -k \cdot j \Delta x = -2\pi x/L = j \cdot \xi$  ( $0 \leq \xi \leq \pi$ ) where  $k$  is the wave number for a wave with length  $L$ .

The amplification factor of MacCormack's scheme applied to eq. (6.71) becomes

$$R = 1 - (\sigma^2 + \lambda_N) \cdot [1 - \cos(\xi)] + \frac{1}{4} \lambda_N^2 [\cos(2\xi) - 4\cos(\xi) + 3] + \\ - i \sigma \left\{ \sin(\xi) + \frac{1}{2} \lambda_N [\sin(2\xi) - 2\sin(\xi)] \right\} \quad (6.78)$$

where

$$\sigma = \frac{\Delta t}{\Delta x} \phi_0 = \frac{\Delta t}{\Delta x} |\phi_{\max}| \quad ; \quad \lambda_N = 2 \delta^v \frac{\Delta t}{\Delta x} \quad (6.79)$$

Here  $\lambda_N$  is a viscosity parameter and  $\sigma$  is the Courant number, which is for general models (systems of advection equations) usually determined with the largest eigenvalue of the system ( $\phi_{\max}$ ). Every time step the numerical solution is multiplied with this complex factor. To illustrate the result we plotted  $R$  in the complex plane in figure 6.21 with  $\sigma=0.6$  with and without viscosity term. If  $\lambda^N=0$  the diagram is elliptical, and if  $\lambda^N>0$  it is deformed and egg-shaped.

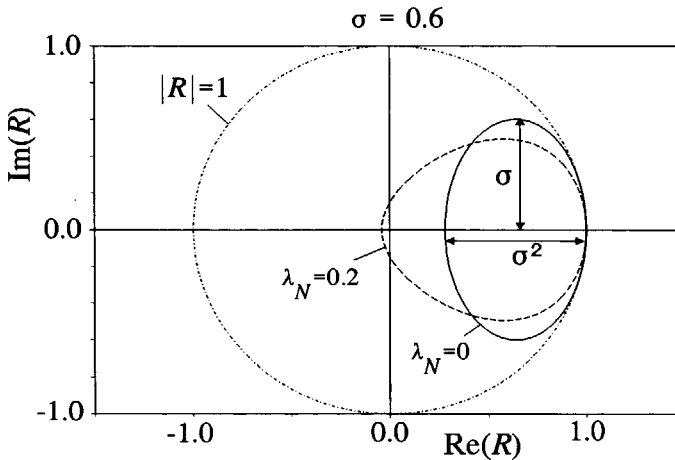


Figure 6.21 Amplification factor ( $R$ ) and stability region ( $|R| \leq 1$ ) of MacCormack's scheme in a complex plane.

Since amplification causes instability (the exact solution does not suffer amplification or attenuation) the stability criterium is  $|R| \leq 1$ . From figure 6.21 and equation (6.78) follows that for the wave with the largest amplification factor (i.e.,  $\xi = \pi$ ) this leads to

$$0 \leq \sigma \leq \sqrt{\lambda_N^2 - \lambda_N + 1} \quad \text{or} \quad 0 \leq \sigma \leq 1 \quad \text{if} \quad \lambda_N = 0 \quad (6.80)$$

This corresponds greatly to the CFL condition (Courant et al., 1928) which can also be viewed as the demand that the characteristics must fall within the computational triangle, or that for the computation of a point at level  $n+1$  the domain of dependence on the previously level  $n$  must fall within the computational stencil of the scheme (e.g. Vreugdenhil, 1989). It is important to notice that by using artificial viscosity the Courant number limit is lowered instead of increased (e.g.,  $\lambda_N = 0.2$  then  $\sigma \leq 0.9$ ). In smooth areas with very small viscosities this is

hardly noticeable, but it becomes pronounced near discontinuities. Later in this chapter we will show how this effect is reflected in the accuracy of the solution.

A similar result can be found if a linearized friction term  $fr_0 u$  is added to the basic equation (6.77) instead of the viscosity term. Here  $fr_0$  is for instance defined as  $C_D(u_0/a_{20})$  which is usually a small factor. By approximation (small  $fr_0$ ) the CFL condition can be written as

$$0 < \sigma < \frac{(fr_0 \Delta t)^4 - 12(fr_0 \Delta t)^2 + 16fr_0 \Delta t - 8}{4[(fr_0 \Delta t)^3 - 4(fr_0 \Delta t)^2 + 4fr_0 \Delta t - 2]} \quad \text{or} \quad 0 \leq \sigma \leq 1 \quad \text{if} \quad fr_0 = 0 \quad (6.81)$$

Only with large source terms or large time steps this condition becomes significantly restrictive, but this is generally not the case.

In smooth flows the presented CFL conditions are sufficient for stability as linearization is justified. However, this is not necessarily true in discontinuous flows where non-linear instability can become important. This type of instability can for instance be triggered by the wiggles near the front or by the non-linear source terms in the basic equations, but a theoretical prove can only be given for simple cases (such as scalar problems, Le Veque 1990). A major part of this instability is automatically taken care of by the addition of artificial viscosity and notably the TVD type which ensures total-variation stability (section 6.6). Another part, that from the source terms and notably from friction, can be considered as one of the drawbacks of the explicit formulation. The appearance of lower-order derivatives in the truncation error and the limitation to the CFL condition already warn for difficulties. For instance Huang and Song (1985) showed for flood waves in a river that a bottom-friction term in an explicit model imposes a severe limitation to the maximum time step. For an underflow in a deep reservoir this limitation can be approximated by

$$\Delta t \leq a_{20} \left( \frac{\sqrt{1 + 2Fr_0} - 1}{C_D u_{20} Fr_0} \right) \quad (6.82)$$

Fortunately a check of this condition for a wide range of possible underflows revealed that this condition is far less restrictive than the presented CFL conditions. Therefore an implicit treatment of the friction term to relax this condition is not required. Also numerical experiments did not indicate any problems. It should be noted that the friction term can also be responsible for physical non-linear instabilities such as roll waves (Sloff, 1993), but these cannot be simulated correctly with the presented model and are therefore irrelevant. Other sources of instability such as those generated by boundary scheme and initial condition are already discussed and removed in the previous sections.

When pushing the previous Fourier analyses somewhat further it is possible to get more information on *accuracy* for initial value problems by looking at differences in exact and numerical (wave-like) solutions (Vreugdenhil, 1989). The exact (convection) and numerical (convection-diffusion) solutions for equation (6.77) become respectively

$$u(x, t) = u_0 \cdot \exp[ik(x - \phi_0 t)] \quad ; \quad u(x_j, t_{n+1}) = u_0 |R|^n \exp[ikx + ni\psi] \quad (6.83)$$

where  $t_n = n \cdot \Delta t$ ,  $x_j = j \cdot \Delta x$  and  $\psi = \arg(R)$ , all based on equation (6.78). To compare the performance of the numerical to the exact solution two parameters can be defined (e.g. Vreugdenhil, 1989, Finlayson, 1992). The ratio of amplitudes can be defined as a damping factor which approaches unity for increasing accuracy:

$$\hat{d} = |R| \quad (6.84)$$

The ratio of phase angles can be defined as a relative (dimensionless) velocity of propagation or a relative phase error, also approaching unity for increasing accuracy:

$$\hat{c}_r = \frac{-\psi}{k \Delta x \sigma} = \frac{-\psi}{\sigma \xi} = \frac{-\psi \cdot m}{2 \pi \sigma} \quad (6.85)$$

Here  $m$  is the number of grid points per wave length, for which the lowest values of  $m$  correspond to the shortest waves in the system. In figure 6.22 plots are given to illustrate the effect of the Courant number ( $\sigma$ ) on the damping factor. In this figure the damping error is greatest at the low  $m$ -values, with a maximum error (without artificial viscosity) if the Courant number satisfies

$$\sigma = \frac{1}{2} \sqrt{2} \quad (6.86)$$

The error gradually decreases for lower or higher values of  $\sigma$ . Damping errors fully disappear for  $\sigma = 1$  and  $\sigma = 0$ , as the method then exactly integrates along the characteristic  $\phi = \phi_0$  (e.g. Finlayson, 1992).

In figure 6.23 the effect of artificial viscosity ( $\delta^\nu$ ) is added to illustrate the effect on the damping factor. These plots verify that all modes are damped depending on the magnitude of  $\delta^\nu$ . The right-hand side of figure 6.23 shows that, if  $\sigma$  is increased (here  $\sigma = 0.9$ ) and the stability criterium is approached, an increase in viscosity yields a decrease of damping at the shortest waves. This may eventually lead to instability when the damping factor exceeds unity, appearing as oscillations on the grid scale (wave length  $2 \cdot \Delta x$ ).

In the same way plots are given of relative velocities of propagation in figure 6.24. Again the errors (i.e., differences from unity) are greatest for the shortest waves.

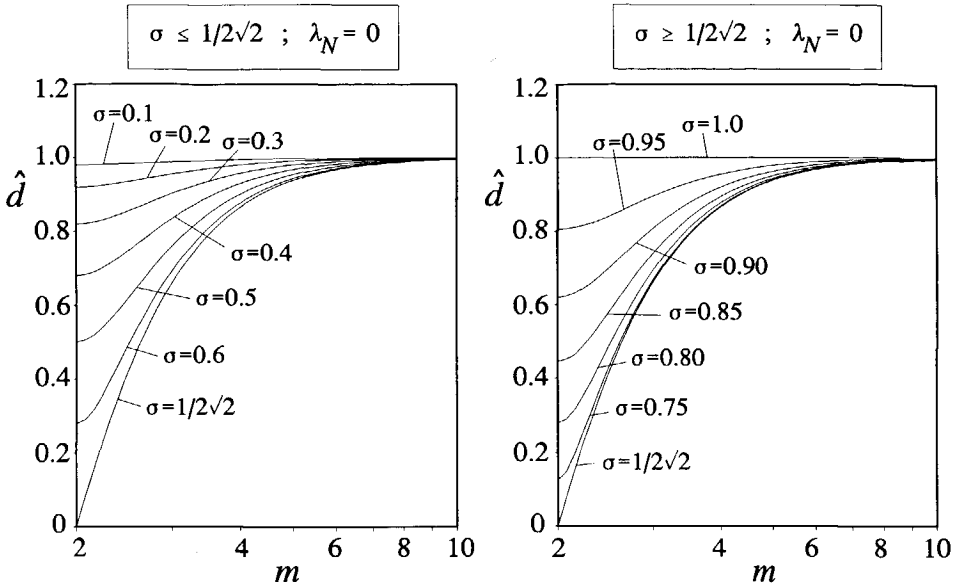


Figure 6.22 Amplitude factor as function of points per wave length ( $m$ ) for various low (left) and high Courant numbers (right).

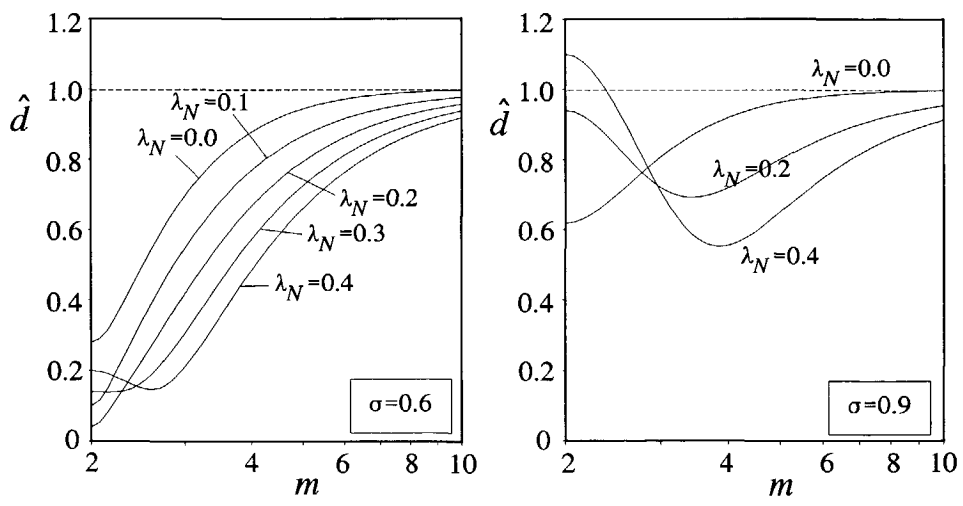


Figure 6.23 Amplitude factor as function of points per wave length for various viscosity coefficients (both low and high values of  $\sigma$ ).

The relative velocity of propagation for Courant numbers  $\sigma \leq 1/2\sqrt{2}$  lies mostly below unity, which indicates a dominating lagging phase error (numerical waves lag compared to analytical waves). This effect tends to accumulate the high-

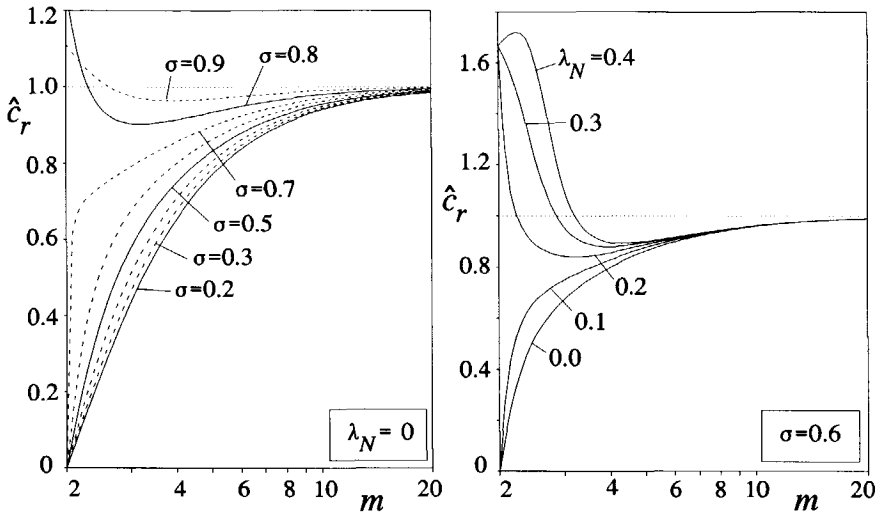


Figure 6.24 Relative velocity of propagation as function of points per wave length for various Courant numbers (left) and various viscosities (right).

frequency errors generated at a discontinuity, and causes the wiggles. For Courant numbers  $\sigma \geq 1/2\sqrt{2}$  (and  $\delta^v=0$ ) the relative velocity of propagation is much closer to unity or just above it, resulting in just a small leading phase error. Fortunately the damping factor imposes a stronger damping on the shortest waves than on long waves, preventing a total collapse of the wiggles.

The effect of artificial viscosity on the phase error is illustrated in the right part of figure 6.24. Comparing the left plot (sensitivity to  $\sigma$ ) and the right plot it can be seen that an increase of viscosity  $\delta^v$  has an equivalent effect to the phase error as an increase of the Courant number  $\sigma$ . To prevent an increase of wiggle production compensation of this phase error must follow from an increase of damping at these high modes, but figures 6.22 and 6.23 show that this is not a trivial fact for high viscosities.

To conclude this analysis it can be assumed that with respect to the accuracy of the numerical scheme the time step should be chosen that the expected Courant number is as close to unity as possible to minimize the damping and phase errors. Furthermore to avoid large errors in relevant physical waves (e.g. internal waves) it is necessary to choose the spatial step  $\Delta x$  significantly smaller than their wave length, e.g.  $m > 5$  to 10. To illustrate and verify these conclusions we have computed a density current entering a deep reservoir without friction, entrainment and deposition. The inflow conditions are:  $q_2 = 1 \text{ m}^2/\text{s}$ ,  $a_2 = 1 \text{ m}$  and  $C_s = 0.01$ . In figure 6.25 the effect of the Courant number is illustrated for a numerical computation with  $\Delta x = 1 \text{ m}$  after 50 s. Time step  $\Delta t = 0.2$  yields near the shock  $\sigma$



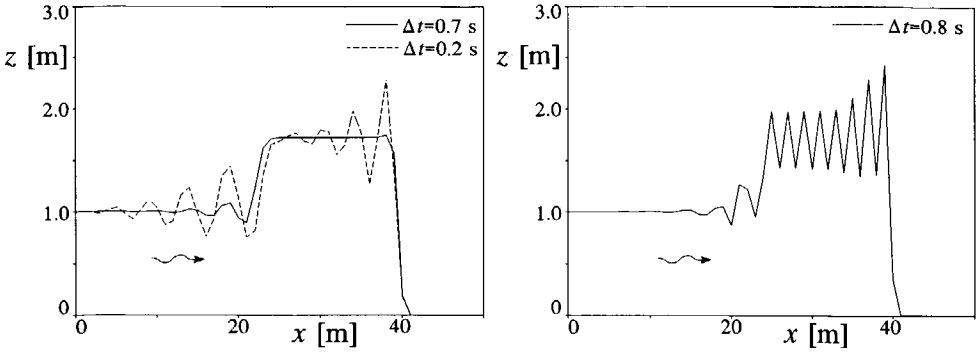


Figure 6.25 Accuracy of a density current front computed without artificial viscosity, with varying time step and  $\Delta x = 1$  m.

$\approx 0.56$ ,  $\Delta t = 0.7$  yields  $\sigma \approx 0.97$ , and  $\Delta t = 0.8$  yields  $\sigma \approx 1.1$ . On the left is clearly shown how phase errors, generating wiggles, disappear as  $\sigma = 1$  is approached. On the right is shown that violation of the CFL condition generates instabilities of the shortest waves on the grid.

For the previous case the computations are also carried out with MacCormack and Baldwin's (1975) artificial viscosity as presented in section 6.5. The viscosity coefficient in this method is scaled using the adjustable coefficient  $\alpha$  (eq. 6.45).

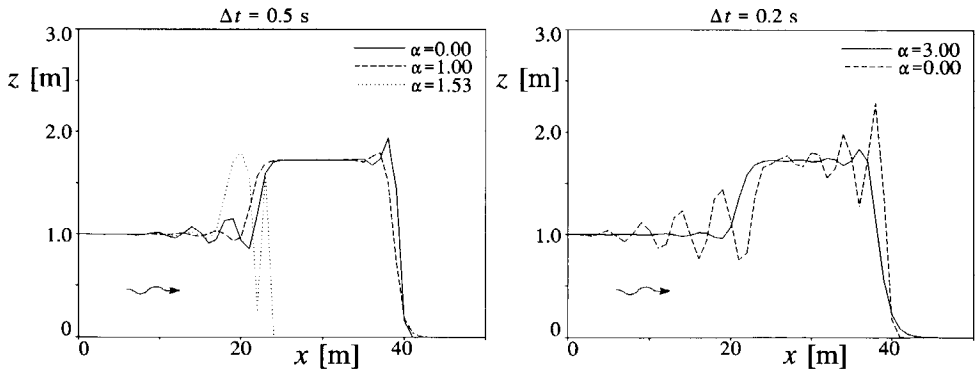


Figure 6.26 Accuracy of a density current front computed *with* artificial viscosity, with varying time step and with  $\Delta x = 1$  m.

For the  $\Delta t = 0.5$  s ( $\sigma \approx 0.7$ ) the effect of an increasing viscosity (increasing  $\alpha$ ) results in a suppression of the wiggles, until  $\alpha \approx 1.53$  when the equation breaks down as predicted by the adapted CFL condition (6.80). This condition also proves that for a lower Courant number a higher viscosity coefficient is allowed, which is shown in the second plot in figure 6.26 for  $\Delta t = 0.2$  s ( $\sigma \approx 0.56$ ). However, at these lower Courant values the wiggles are more pronounced, so that the net effect

is not more significant than for high Courant numbers.

Although these results are derived for the simple linear advection equation it can be shown that they are similar to results from a more complete analysis of the full turbidity-current model. For the 1-D baroclinic flow model on a mobile bed it is shown in section 6.6 that the solution can be decomposed into four characteristic waves advected with their corresponding celerity  $\phi_k$ . The analyses above can therefore be repeated for each of these waves, all having their own Courant number  $\sigma_k$ . Since the celerities and Courant numbers of these waves usually differ significantly in magnitude the different waves are subjected to different phase and damping errors according to figures 6.22 and 6.23. Especially when dealing with bed-morphology the Courant number related to bed-disturbances is very low (if  $\Delta t$  is chosen such that the fastest waves have a Courant value near unity). As an example the numerical results for the bed-evolution of a backward-facing step due to bed-load transport in a subcritical ( $Fr \approx 0.4$ ) open-channel flow are presented qualitatively in figure 6.27. Due to the low Courant-number of the bed-disturbances ( $\sigma_b \approx 4 \cdot 10^{-3}$ ) large phase errors yield large oscillations in  $z_b$ , while the time-step is adjusted to the largest celerity ( $\sigma_{max} \approx 0.9$ ). Likewise the computed results with TVD artificial viscosity are added to this figure (using the Superbee limiter). Using the TVD concept the amount of viscosity added to each characteristic wave component is adjusted to the respective Courant number and can therefore fully eliminate the wiggles.

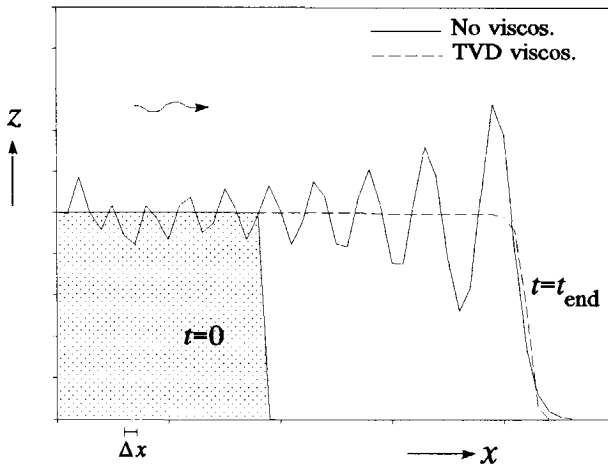


Figure 6.27 Morphological computation of a backward-facing step in an open channel with subcritical flow using MacCormack's scheme.

These results prove that, especially in case of morphological computations with a fully coupled model, the use of an adjusted (or self-adjusting) artificial viscosity term is essential to obtain physically realistic results with a Lax-Wendroff type

numerical scheme.

## 6.10 Shock tracking

Using MacCormack's scheme with artificial viscosity, the intruding front of a conservative density current (i.e., with a constant density) can be computed with sufficient accuracy. However, when the current is not conservative, for instance due to entrainment and settling, the approach is failing. This problem is caused by the application of the shock-capturing technique to the concentration equation and can only be solved by a correction of the solution near the front, or by using a shock-fitting technique. In this section is shown how this failure arises, and how the model can be fixed by tracking the shock.

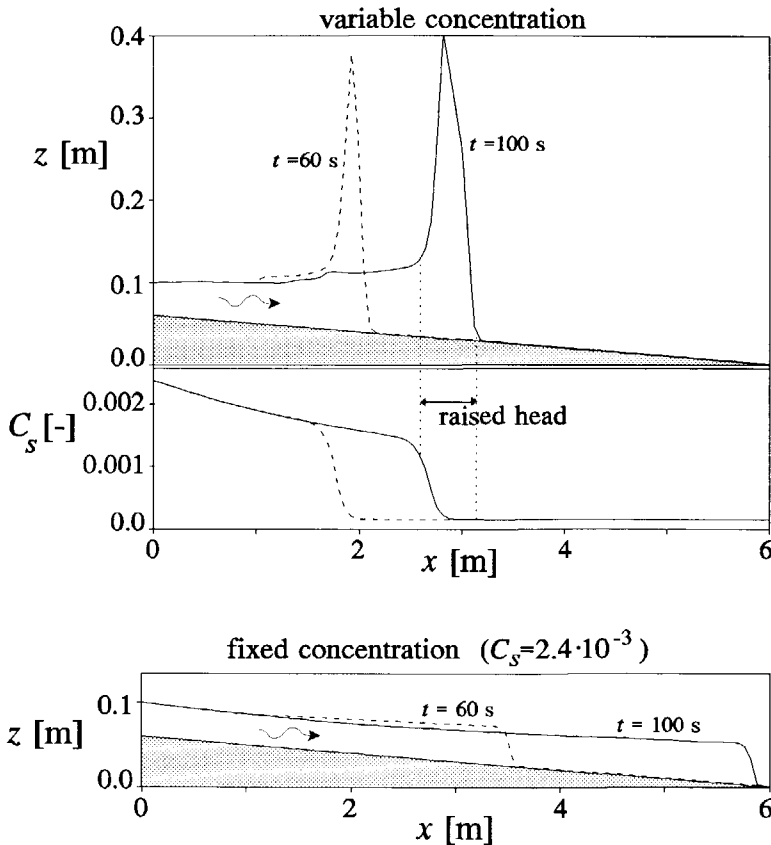


Figure 6.28 Computation of turbidity current experiment TK1306 (Altinakar et al., 1990) illustrating the large overshoot at the front if  $C_s$  is variable.

In figure 6.28 computed results are presented of a turbidity current developing on a slope in a laboratory flume (experiment TK 1306) as reported by Altinakar et al. (1990). In this figure a comparison between results computed with a fixed concentration ( $C_s[x] = C_s[0]$ ) and a variable concentration (Galappatti's equation) clearly shows how the latter is characterized by a large overshoot near the front. While the front with variable concentration is running over the small low-density layer, the concentration requires a certain length to adapt to the new situation. The system responds to the low density by a significant overshoot of the underflow depth and a decrease of front speed. This phenomenon is not to be mistaken with the increased head height observable in nature, as this is purely a computational matter. The strong gradients and rapid flow variations at the front do repudiate the use of Galappatti's model which is only valid in relatively smooth flows. Instead another approach must be applied which extends the information about density into the front without sensing the low concentration ahead of the front. For instance in the constant concentration case in figure 6.2 the front maintains its original density irrespective of the downstream conditions, and therefore its height and celerity are greatly preserved. The correct average front speed  $u_f$  measured by Altinakar et al. (1990), which was 0.047 m/s, lies exactly between the variable concentration result ( $u_f = 0.027$  m/s) and the fixed concentration result ( $u_f = 0.057$  m/s).

To solve the overshoot problem an upwind extrapolation of concentrations is used to replace Galappatti's equation locally at the front. The exact location of the front must be known, for instance by tracking it during the computation. Defining a slope parameter

$$\theta_{f,i} = \frac{a_{2,i-1} - a_{2,i+1}}{a_{2,i}} \quad (6.87)$$

the front is located in the section where this parameter exceeds a certain value  $\theta_{cf}$  (e.g.,  $\theta_{f,i} > 2$ ), indicating the large gradient associated with the shock. Note that wiggles do not affect  $\theta_{f,i}$  by considering a section of  $2 \cdot \Delta x$ . Furthermore, in any numerical approach the front is slightly smeared such that we are dealing with a front section rather than a point.

After the front section is traced the most important part of this procedure is the determination of its concentrations. Different approaches are examined and finally a choice is made for a very simple upwind zeroth-order extrapolation of the upstream concentration into the front section:

$$C_{s,i} = C_{s,i-1} \quad \text{if} \quad \theta_{f,i} > \theta_{cf} \quad (6.88)$$

where  $\theta_{cf}$  is the value of the slope parameter above which the flow is assumed discontinuous. The algorithm now computes concentrations starting from the upstream boundary until the front section is reached. From that location the

concentration is extrapolated down to the downstream boundary. Other approaches such as upwind discretization and solution of concentration terms or higher-order extrapolation methods appeared to be unsuccessful and resulted in inaccurate solutions. Also from a physical and mathematical point of view the zeroth-order extrapolation is most meaningful. In section 4.2 we already showed how the frontal region is characterized by increased turbulence opposing settlement of sediment particles. Consequently, while neglecting the effect of entrainment locally on the shock, it is justified to assume that the density in the front section equals that of the gravity current just upstream. In a mathematical context, when  $\Delta x$  and  $\Delta t$  vanish and the front section reduces to a point, this is indeed the only correct shock solution. The concentration at this point is only determined by upstream conditions since Galappatti's equation always has a positive characteristic.

In figure 6.29 the new shock-tracking algorithm is applied to recompute the previously described experiment. The computed front speed ( $u_f = 0.049$  m/s) now corresponds very well to the measured speed ( $u_f = 0.047$  m/s). Accuracy of the results is very good and the overshoot is fully eliminated.

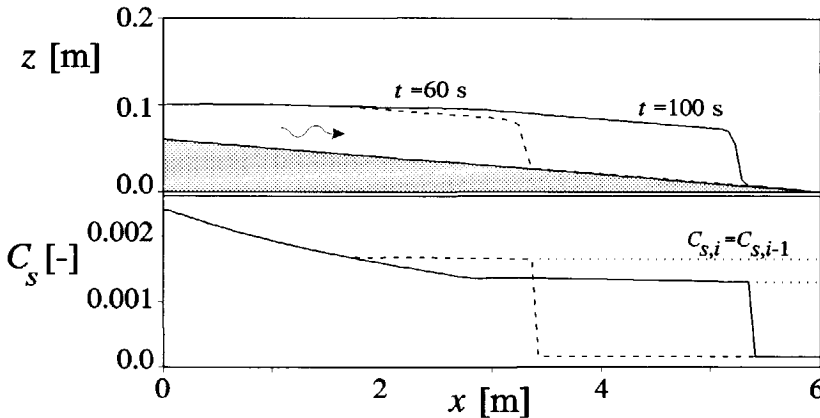


Figure 6.29 Computation with shock-tracking of turbidity current experiment TK1306 (Altinakar et al., 1990).

It is also recommendable to use the shock-tracking approach if dilution by entrainment is considered into an otherwise conservative gravity current. Here the downstream depth has a concentration equal to the inflow, which (due to adaptation as mixing occurs over a certain distance) results in overestimated concentrations in the front region. This is illustrated in figure 6.30 for the TK1306 experiment, now without sediment deposition. Clearly the front is flattened and moves too fast. Applying the shock-tracking technique to this example correct results are obtained as presented in figure 6.31.

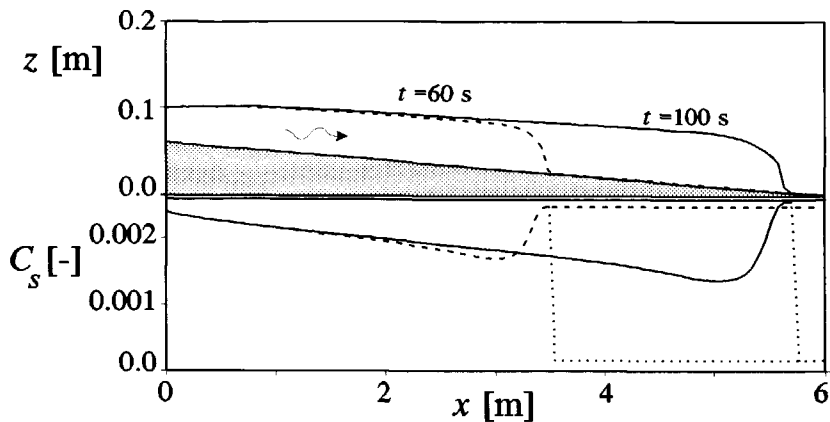


Figure 6.30 Erroneous results of a conservative density current with entrainment (based on the data for run TK1306).

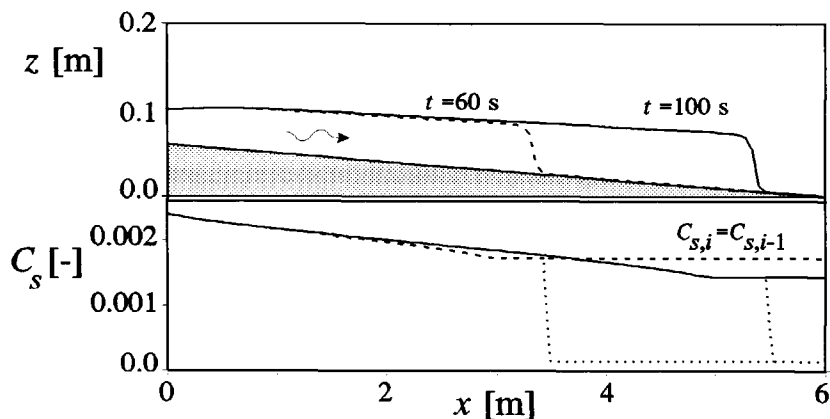


Figure 6.31 Computation using shock-tracking of a conservative density current with entrainment (based on the data for run TK1306).

This technique yields results which are practically equivalent to those computed with shock-fitting techniques. However, it is a very simple approach and sometimes it is necessary to adjust the critical slope parameter  $\theta_{cf}$  for accuracy. With respect to accuracy it must be remarked that a small decrease in the front speed is found if the positivity coefficient  $\alpha_i$  in equation 6.74, necessary to preserve the small downstream layer, is varied while using the shock-tracking approach. This is clearly not occurring when fixed-concentration and conservative entraining gravity currents are computed.

## 6.10 Conclusions

In this chapter a 1-D numerical model is presented to simulate gravity currents intruding into a reservoir. It is designed to compute the two-layer flow including its discontinuities, notably gravity-current fronts, and to achieve this in a robust and accurate way. Therefore a choice is made for an appropriate finite difference scheme, after a literature survey of various methods with shock-capturing abilities which have been developed during the last decades. From these methods MacCormack's (1969) space-centred approach is chosen for its accuracy in smooth flows, and its robustness and simplicity in dealing with discontinuous flows.

MacCormack's method is explicit and consists of a predictor and corrector step, such that it is a special form of the classical Lax-Wendroff (1960, 1964) scheme. For a good performance it is advisable to cycle between forward and backward differences which compose the two steps of MacCormack's method. The discretization is applied to the baroclinic (internal) flow and sediment equations. Also source terms are discretized explicitly. The barotropic (external) flow equations are decoupled and solved in a quasi-steady manner without significantly affecting the accuracy. This means that they are computed as a steady-flow profile at each baroclinic time step using a standard fourth-order Runge Kutta integration method. For 1-D flows the quasi-steady approach is efficient, but it is shown that in 2-DH flows it is better to solve the full unsteady barotropic flow equations with a smaller time step than baroclinic flow.

As a consequence of the second-order accuracy of MacCormack's scheme dispersion errors are generated near discontinuities, resulting in oscillations or wiggles. Since these wiggles can result in strongly distorted solutions without any physical relevance it is necessary to add artificial viscosity to the numerical method in order to damp them out or fully eliminate them. Therefore two different types of artificial viscosity are implemented in the model. The first type is the conventional artificial viscosity which is based on an explicit addition of diffusion terms to the flux terms. Unfortunately these terms contain empirical coefficients which require calibration and diminish the robustness of the model. It is shown that wiggles cannot satisfactorily be eliminated, especially in mobile-bed cases. To get round these disadvantages the second, more advanced, type of viscosity is implemented in the model. This total variation diminishing (TVD) viscosity prevents the occurrence of wiggles rather than damping them out afterwards and can therefore effectively eliminate all oscillations. Its definition is based on flux limiters which suppress automatically that part of the numerical flux which generates the oscillations. For our non-linear model a linearization and characteristic decomposition introduced by Roe (1981) is used. Experience showed that the flux-limiters must be based on ratios of flux differences rather than on ratios of variable differences (as in literature). When using the TVD viscosity method an entropy fix must be added to

enable a correct computation of rarefaction waves with a transcritical flow point. Clearly the results are superior to those computed with conventional viscosity, and more than counterbalancing the increase in computational effort.

Due to its importance for accuracy and stability of the model the type and discretization of boundary conditions (b.c.) is given special attention. The requirement of well posedness of the problem (based on in- and outgoing characteristics) is used to define the required number and possible types of physical b.c. on in- and outflow boundaries (table 6.1). The remaining numerical boundary conditions (variables not given by the physical b.c.) have to be computed explicitly from the interior flow field. To accomplish this, different alternative discretizations are studied ranging from variable extrapolation to backward differences applied to compatibility equations. Experiments revealed that when shocks pass through or reflect against the boundary the most robust approach is the introduction of additional ('ghost') points outside the computational domain. Boundary values are solved with the interior scheme in a consistent and accurate way. Additionally to conduct the shock through the boundary a Froude number check is implemented which enables an automatic choice of correct boundary conditions.

Initial conditions also have a significant affect on the computed gravity current, especially in the developing stage. From the different proposed initial states the 'zero' underflow depth is most appropriate for computing the gravity current development. Here the front runs over a small initial layer (with internally subcritical flow) which preserves its shape in undisturbed regions by means of a conditional statement, and simultaneously acts as a lower limit for flow variables to preserve their positivity.

To gain more insight in the numerical errors inherent in the chosen approach, the local truncation error as well as an extended von Neumann analysis are used. These results indicate that a distorting effect is due to source terms (e.g., friction) but it remains acceptable since these terms are usually small. By comparing exact and numerical results it is shown that damping errors increase for shorter waves, with a high dependence on the Courant number  $\sigma$  (no damping at  $\sigma=0$  and  $\sigma=1$ ). Introducing artificial viscosity to the model increases the damping, but at high values of  $\sigma$  excessive viscosity may lead to amplification of the shortest waves resulting in instability. Phase errors in convected waves (dispersion errors) become more pronounced at low Courant numbers. The associated wiggles can therefore be controlled by using high  $\sigma$  values (large  $\Delta t$ ). In computations with significant differences in characteristic speeds (e.g., in a mobile bed case) wiggles always occur when artificial viscosity is not adopted to the associated Courant numbers. Again this pleads for the use of the TVD artificial viscosity which automatically adjusts its value to the appropriate celerities.

In case of a non-conservative gravity current, e.g., with interfacial mixing and



settling of sediment particles, a correction near the front is required to compensate the adaptation effect. Due to this effect the concentration cannot instantaneously adjust to the new flow state appearing directly after passage of the front, which can result in a non-physical overshoot. This problem is repaired by using a shock-tracking approach in which the front is tracked and in which its density is replaced by values extrapolated from the current just upstream of the front. The front is detected on basis of gradients for which an additional empirical coefficient is introduced.

By applying the proposed algorithms, considering the presented limitations, the model can be used to simulate a wide range of gravity-current events. Its merits are the possibility of dealing with discontinuous underflows in reservoirs with finite depths and the robustness and simplicity of the chosen approach. By means of some examples and verifications this is illustrated in the following chapter.



# Chapter 7

## Test cases

### 7.1 Introduction

The proposed two-layer model can be considered as a blend of conventional approaches and state-of-the-art techniques. For instance the use of the proposed shock-capturing techniques and the application of Galappatti's approach (section 2.3) has not been shown yet. To test and verify the chosen approach it is essential to compare the calculations with real physical data, or with exact analytical solutions. Therefore, especially during the development of the numerical model, a large number of numerical experiments were carried out. Often these tests resulted in a revision of the code which finally led to a reasonably general research model. Some comparisons between numerical and analytical similarity solutions have been given in chapter 6. They motivated us to adopt the TVD artificial viscosity approach through which the numerical solution appeared to correspond excellently with the analytical solution (see the examples in section 6.6).

In this chapter some test cases are presented based on data-sets from laboratory and field studies reported in literature. With the help of these examples we will try to summarize the possibilities and limitations of the model as we encountered during these and various other tests. It should be emphasized that the primary difficulty in this study was the lack of appropriate and detailed data on turbidity currents in reservoirs. This forced us to introduce schematizations which may look rigorous, but certainly do not devalue the model. They merely provoke new topics for further research.

### 7.2 Laboratory experiments of turbidity currents in Minnesota

Laboratory experiments in a flume in St. Anthony Falls Hydraulic Laboratory, University of Minnesota, were carried out by Garcia (1989, 1990, 1993). The measurements of these steady turbidity currents and saline underflows with relatively low densities have been shown to be quite useful for the derivation of our model in chapter 2. Experiments were conducted in a sloping flume, as well as in the flume schematized in figure 7.1. The latter facility consists of an inclined bed

(4.6°) and a horizontal bed with a width of 0.3 m and a total length of 11.6 m. The dense fluid (either salt or sediment) was prepared in a mixing tank and released through a submerged sluice gate into the flume. During the experiment the water level was maintained constant, while at the end of the horizontal section the dense fluid dropped into a damping tank such that this downstream end acted as a submerged overfall.

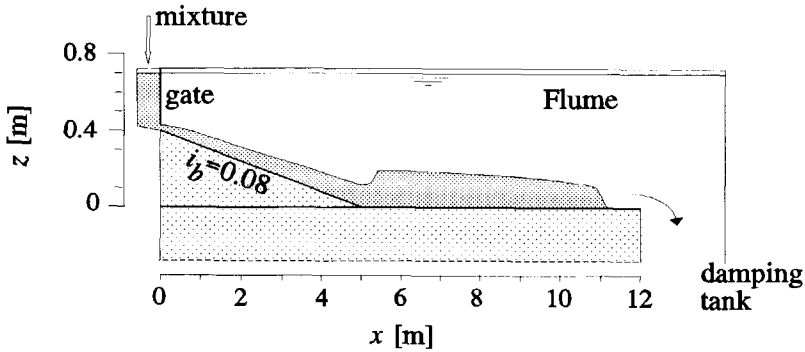


Figure 7.1 Experimental setup for Garcia's (1990) laboratory study.

For the verification of the computational model we have simulated several of Garcia's experiments. For the saline currents we found that a fair amount of friction is needed, i.e.,  $C_D=0.01$  and  $C_{Di}=0.002$  to calibrate depths and velocities. In figure 7.2 velocity profiles for experiment SAL11 at two locations are plotted. These are computed with the semi-empirical relations from section 2.4.

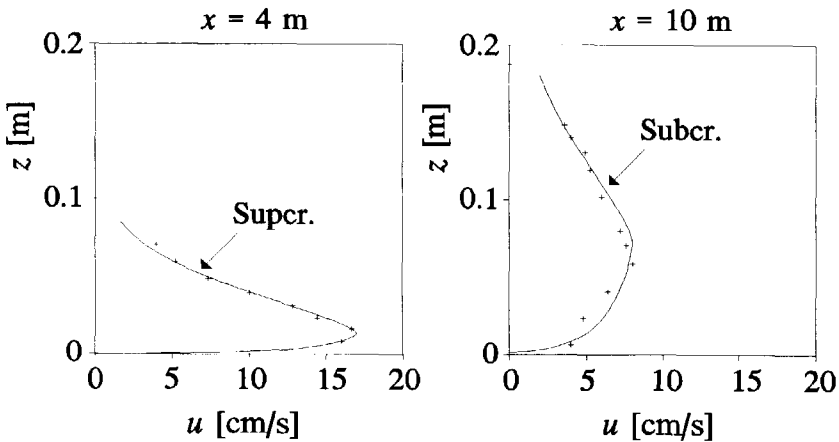


Figure 7.2 Measured (crosses) and computed (lines) velocity profiles for a saline underflow experiment SAL11, internal super- and subcritical flow.

In this experiment a saline mixture with a density  $\rho_2=1013 \text{ kg/m}^3$  is discharged

with a rate  $q_2(0)=0.0033 \text{ m}^2/\text{s}$  under the sluice with initial depth of 3 cm. In the resulting equilibrium situation (after about 10 min.) it can be shown that on the sloping floor the flow is internal supercritical, while in the horizontal floor the flow becomes internal subcritical. Fitting the relations for the vertical structure as presented in section 2.4 (only for velocity since the salt distribution is not equivalent to a sediment distribution), we found from the profiles at  $x=4 \text{ m}$  that  $a_2=8.5 \text{ cm}$ ,  $u_2=9.2 \text{ cm/s}$ , and at  $x=8 \text{ m}$  that  $a_2=18 \text{ cm}$ ,  $u_2=5.5 \text{ cm/s}$  (while Garcia, 1990, 1993, reported  $a_2=6.4 \text{ cm}$ ,  $u_2=11.8 \text{ cm/s}$  and  $a_2=15.1 \text{ cm}$ ,  $u_2=5.9 \text{ cm/s}$  respectively, obtained from the slab approximation in sub-section 2.4.5). The calculations of this experiment are conducted with  $\Delta x=0.12 \text{ m}$ ,  $\Delta t=0.6 \text{ s}$  using the minmod (TVD) limiter. Computed depths after 20 minutes (equilibrium state) are plotted in figure 7.3.

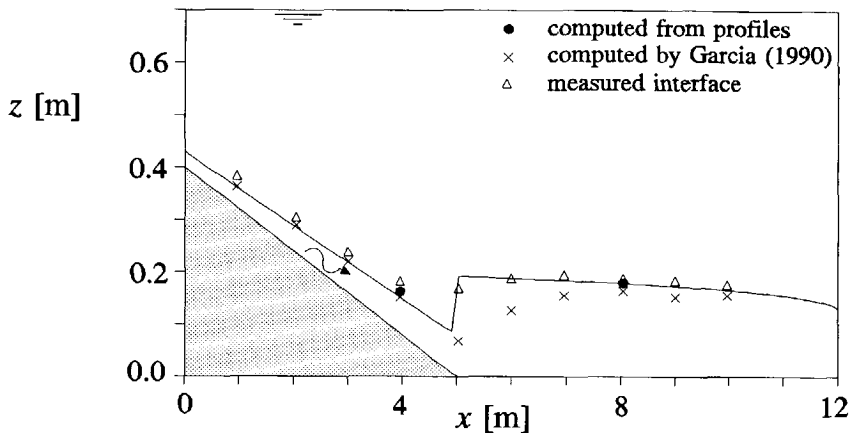


Figure 7.3 Computed and measured depths for experiment SAL11 (salt water).

In this figure measured interface values are defined as the level where the velocity becomes zero. To obtain these results the entrainment rate computed with the Parker et al. (1987) relation is reduced with 30% to obtain a reasonable agreement between measured and computed depths and velocities. On the sloping floor (internal supercritical flow) the depths and velocities correspond to those reported by Garcia (1993), e.g., at  $x=4 \text{ m}$  we computed  $a_2=6.8 \text{ cm}$  and  $u_2=11 \text{ cm/s}$  with a density of  $\rho_2 \approx 1005.6 \text{ kg/m}^3$ . This is consistent with the model equations. Near the transition to the horizontal bed an internal hydraulic jump is found. Although this jump is computed as a shock it can be seen from the figure that on the experimental scale the jump extends over a section of 2 to 3 m. Again an excellent agreement between computed and measured depths and velocities exists downstream of the jump (at  $x=8 \text{ m}$  we computed  $a_2=18 \text{ cm}$  and  $u_2=5 \text{ cm/s}$  with a density of  $\rho_2 \approx 1004.8 \text{ kg/m}^3$ ).

The computation of these saline currents confirmed that friction and entrainment

are the primary calibration parameters. For this problem the effect of interfacial friction can be superimposed on bed friction since  $u_1$  is small compared to  $u_2$  (e.g., taking  $C_D=0.012$  and  $C_{Di}=0$  does not change the result significantly). This is in agreement with physical considerations in sub-section 2.4.3 where it was shown that near the 'zero-velocity' interface turbulent shear stresses become negligible. These results also apply for the turbidity-current experiments of Garcia. Computations of these experiments showed that the flow can be fitted again on basis of friction and entrainment. However, compared to the saline underflows the computation of turbidity currents required a larger bottom friction. Various phenomena can be responsible for this deviation, for instance the presence of bed forms and bed-load transport as reported (in mobile bed conditions) by Garcia (1990) and Garcia and Parker (1993). By means of the computation of experiment DAPER2 the results are illustrated.

In this experiment DAPER2 a sediment-fluid mixture with a concentration  $C_s=1.33 \cdot 10^{-3}$  of silt particles with  $D_{50}=9 \mu\text{m}$  is discharged in the flume with a rate  $q_2(0)=0.0025 \text{ m}^2/\text{s}$  (with initial sluice depth of 3 cm). Again an equilibrium state is established (after at least 20 minutes) with an internal hydraulic jump comparable to experiment SAL11. Nevertheless, here the jump seems to extend over a longer distance. Fits of velocity and concentration profiles in sub- and supercritical sections (using the semi-empirical relations from section 2.4) are given in fig. 7.4.

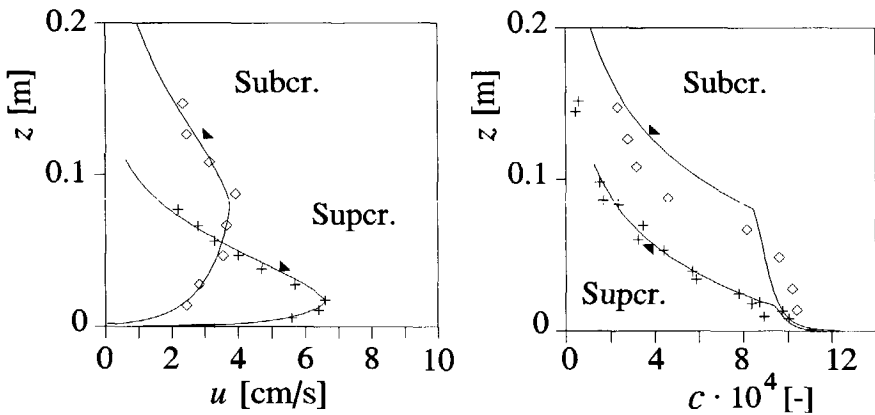


Figure 7.4 Computed (lines) and measured velocity and concentration profiles (symbols) of turbidity-current experiment DAPER2.

The calculations of this experiment are conducted with  $\Delta x=0.12 \text{ m}$ ,  $\Delta t=0.6 \text{ s}$  using the minmod (TVD) limiter. Computed depths after 20 minutes (equilibrium state) are plotted in figure 7.5. Here measured interface values correspond again to levels of zero velocity. For these computations friction coefficient were taken  $C_D=0.02$  and  $C_{Di}=0$  without reduction of the Parker et al. (1987) entrainment relation. Again, with only minor changes to the solution, part of this large bed

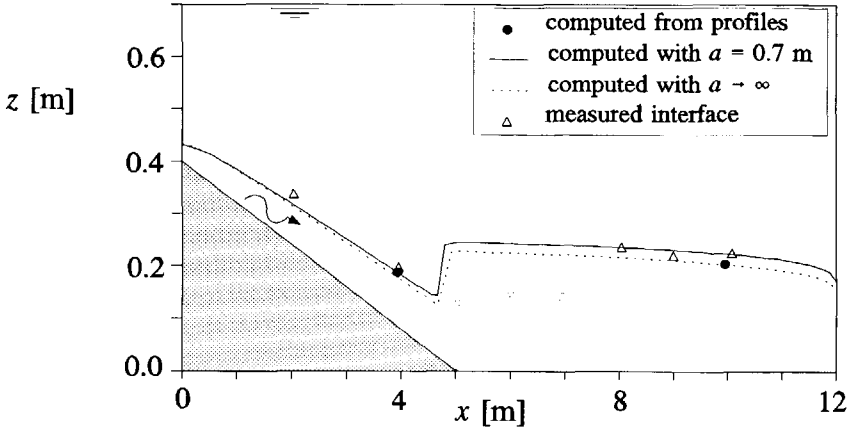


Figure 7.5 Computed and measured depths for experiment DAPER2 (turbidity).

friction can be transferred to interfacial friction (e.g.,  $C_D=0.015$ ,  $C_{Di}=0.005$ ). The proposed combination of friction and entrainment was necessary to obtain a good fit with the measured flow conditions.

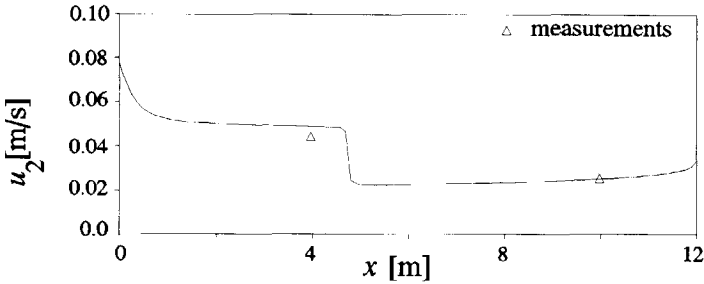


Figure 7.6 Computed and measured velocities of experiment DAPER2.

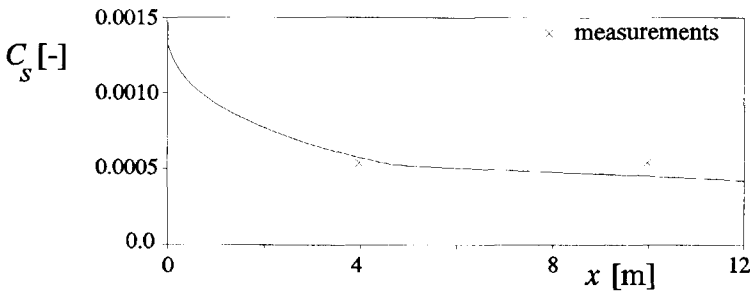


Figure 7.7 Computed and measured concentrations of experiment DAPER2.

Computed velocities and concentrations are given in figures 7.6 and 7.7. With

smaller friction coefficients (e.g., those of the SAL11 computation) the velocities in the turbidity current are highly overrated. Alternative combinations with better results are not precluded.

The decrease of concentration along the flume is primarily due to entrainment. The small sediment particles in this experiment remain in suspension, hence the current is practically conservative within the length of the flume. Deposition is insignificant as was already noticed by Garcia (1990, 1993). Furthermore some small variations in depth, velocity and concentration can be found if the underflow is computed in an infinitely deep reservoir. In general a very deep reservoir results in faster propagation speed of the front, higher concentrations, and lower depths. These effects are more noticeable during the development of the flow than in its equilibrium state.

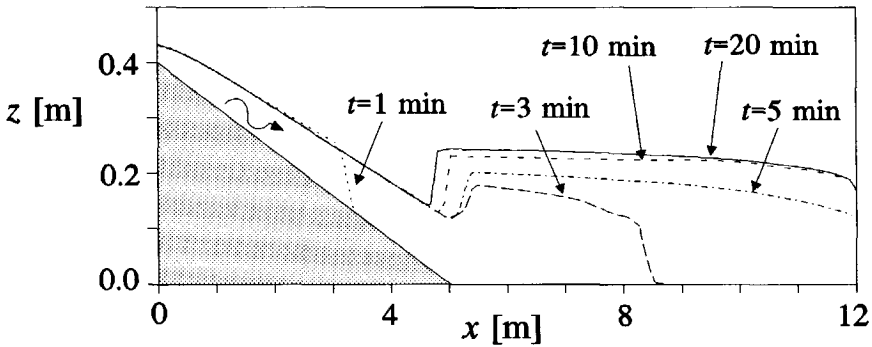


Figure 7.8 Development of the turbidity current in experiment DAPER2.

The progression of the turbidity current during the initial stage of the experiment is plotted in figure 7.7. It clearly shows how the front advances through the reservoir, and how an internal bore (moving jump) develops near the slope transition. During the first 5 minutes the current is internal supercritical over its complete length (it is critical at the downstream end). Only due to the rise of interface downstream of the jump the final state in this region will become internal subcritical. Experiments with coarser sediments (i.e.,  $30 \mu\text{m}$  and  $65 \mu\text{m}$ ) appeared to be so strongly depositional in this region that an internal subcritical state could not be reached as the current quickly disintegrated, often before reaching the downstream end (Garcia, 1993).

To validate the computed velocities and depths another turbidity current experiment NOVA7 is computed with  $D_{50} = 4 \mu\text{m}$  and inflow conditions  $C_3(0) = 7.3 \cdot 10^{-3}$ ,  $a_2(0) = 3 \text{ cm}$ ,  $q_2(0) = 0.033 \text{ m}^2/\text{s}$  using the same friction coefficient ( $C_D = 0.02$ ) and entrainment relation. The numerical computations resulted (after 20 minutes) in the following depths and velocities: at  $x = 3 \text{ m}$  (internal supercritical)  $a_2 = 6.1 \text{ cm}$  and  $u_2 = 9.9 \text{ cm/s}$ ; at  $x = 8 \text{ m}$  (internal subcritical)  $a_2 = 17.4 \text{ cm}$  and  $u_2 = 4.5 \text{ cm/s}$ .



Subsequently these values are used to compute the vertical profiles using the model of chapter 2. From the results, plotted as lines in figure 7.9, compared to measured data, can be concluded that in the supercritical region the depths are slightly underrated while the velocity is slightly overrated. In the subcritical region the agreement is striking.

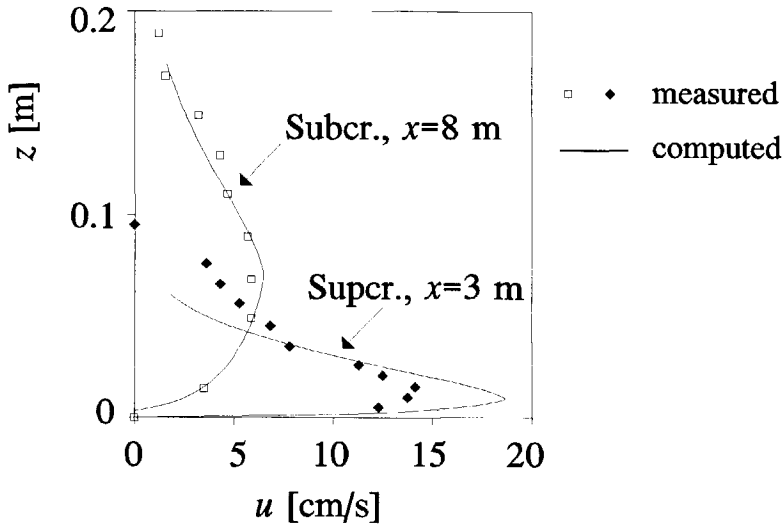


Figure 7.9 Validation of velocity profiles for experiment NOVA7.

The internal hydraulic jumps in these experiments are relatively weak (Garcia, 1993). Therefore entrainment at the discontinuity is small and the shock-relation for the non-entraining hydraulic jump is applicable. This is illustrated in section 4.4 (fig. 4.6) by comparing measured and computed depth-ratios as function of the downstream Froude number. The insignificance of entrainment in the weak jump are confirmed by the findings of Wood and Simpson (1984).

Summarizing these results it was found that experiments reported by Garcia (1990, 1993) can be modelled satisfactory if appropriate values for friction coefficients and entrainment are adopted. Also vertical profiles for sediment and concentration can be modelled accurately. All examples discussed in this section (experiment SAL11, DAPER2, and NOVA7) exhibit conservative behaviour with dilution effects primarily caused by entrainment. Therefore the turbidity current hardly deposits any sediments. Near the transition in bottom slope eventually a non-entraining internal hydraulic jump is formed where the flow changes from an internal sub- to supercritical state (initially the current is completely internal supercritical). Quite similar experiments were carried out in the fluid mechanics laboratory of Delft University. This is the topic of the following section.

### 7.3 Laboratory experiments of turbidity currents in Delft

Laboratory experiments in a flume in the laboratory of fluid mechanics of the Civil Engineering department of Delft University of Technology were carried out by Cordi and Ophem (1994) under supervision of Kranenburg and Van Tessel. Some of these fluid-mud experiments were laminar but also a number of turbulent underflows was established. From the latter experiments we have chosen turbidity-current experiment RUN5, with the lowest concentration for further examination. The experimental setup and initial conditions for this experiment are summarized in figure 7.10.

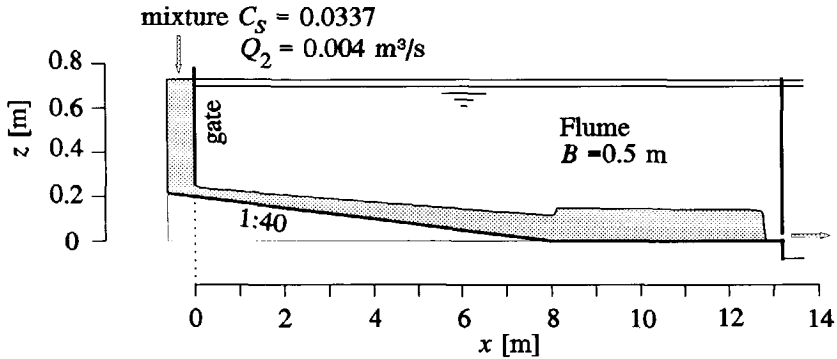


Figure 7.10 Experimental setup in Fluid Mechanics laboratory: Run 5.

Comparing this with figure 7.1 it is clear that the facility is similar to that of Garcia (1990) except for the downstream end and the milder slope. Different to Garcia's experiments are also the high concentrations released in the flume (for RUN5 about 25 times the concentration of DAPER2).

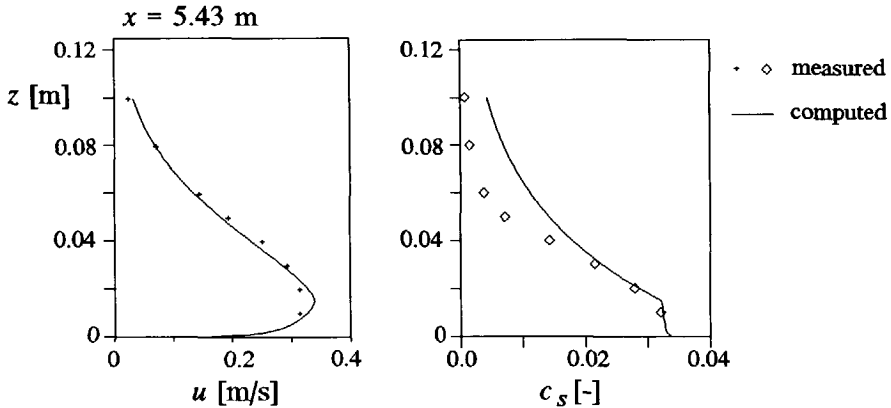


Figure 7.11 Measured and computed velocity and concentration profiles.

At two locations in the sloping region the velocity and concentration profiles are measured:  $x=1.27$  m and  $x=5.43$  m from the inflow sluice. A fit of the computational profiles (obtained from the relations in section 2.4) to those measured in  $x=5.43$  is given in figure 7.11. A reasonable fit for profiles at  $x=1.27$  m could not be found, most likely due to the adaptation of the profiles at the inflow boundary. At this point the underflow is not fully developed and equilibrium relations are not valid. Also application of Galappatti's model at this point becomes arguable since the inflow concentration profile (almost uniform) differs significantly in shape from the equilibrium profile. Note that Galappatti's adaptation length near the entrance is about 30 to 40 m which is much higher than the length of the flume.

The numerical computations were carried out with  $\Delta x=0.033$  m and  $\Delta t=0.06$  s. Friction coefficients were taken  $C_D=0.006$  and  $C_{D_i}=0$ , while entrainment is computed with the entrainment relation of Parker et al. (1987) increased with 50 %. A particle size of  $D_{50}=14 \mu\text{m}$  is used in the model. Computed and measured depth, velocities and concentrations are plotted in figures 7.12 to 7.14.

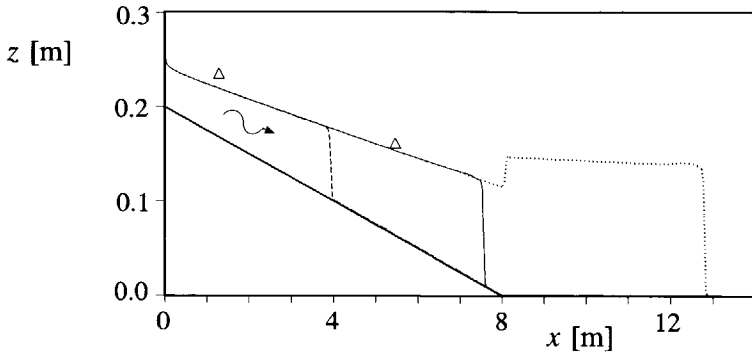


Figure 7.12 Computed underflow depth, dashed line  $t=20$  s, drawn line  $t=40$  s, dotted line  $t=72$  s, triangle: measured depth.

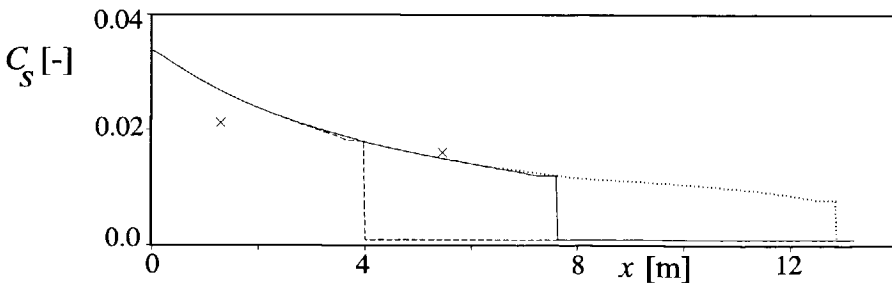


Figure 7.13 Computed concentration; legenda: see figure 7.3.

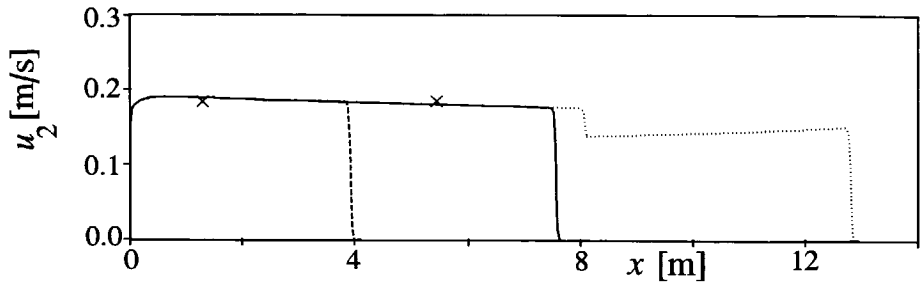


Figure 7.14 Computed velocity; legenda: see figure 7.3.

Again other combinations of friction and entrainment are not precluded (e.g., higher  $C_D$  might reduce the required amount of entrainment). Furthermore it can be shown that the current is practically conservative due to small fall velocities, and that the presented dilution effects are primarily due to entrainment. Therefore deposition is insignificant (less than 1 mm). These results are comparable to the outcome of the previous section.

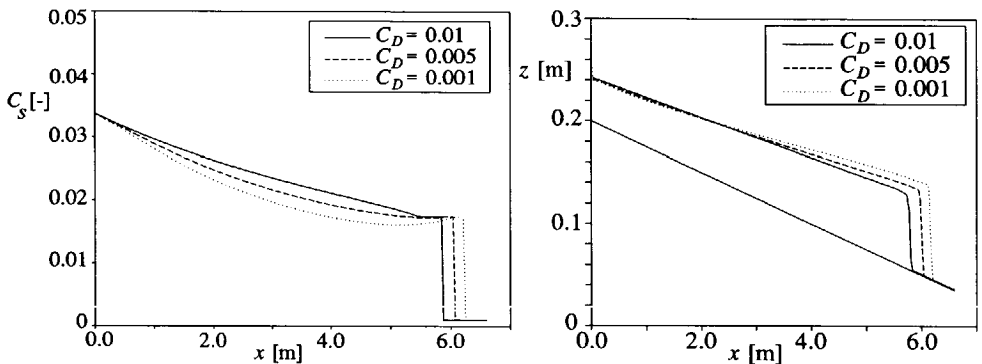


Figure 7.15 Sensitivity to bottom-friction coefficient.

By means of varying  $C_D$  and the amount of entrainment (Parker's relation multiplied with a factor  $C_w$ ) the sensitivity of the computations is illustrated in figures 7.15 and 7.16. Clearly depths and concentrations (and velocities) in the current are highly dependent on the choice of these parameters. On the other hand the sensitivity to the reservoir depth  $a$  and sediment-transport related parameters is very small.

The computed front celerity is about 0.2 m/s which is only slightly smaller than the measured front celerity of 0.24 m/s. Figures 7.15 and 7.16 indicate a dependence on the chosen combination of friction and entrainment. This celerity remains almost constant throughout the complete flume (irrespective of the change in slope). When the front reaches the downstream end it is reflected, resulting in an important

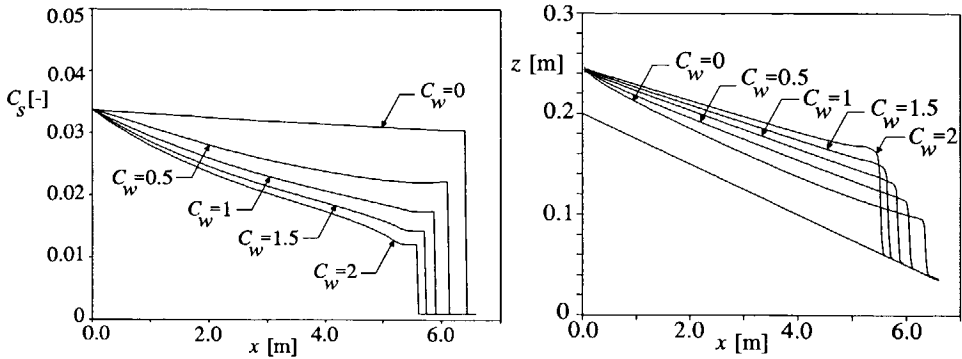


Figure 7.16 Sensitivity to interfacial mixing.

increase of underflow depth.

The computational results for this experiment showed that for these relatively high concentrations the model is less suitable. Although the calculations fit well to the data the agreement is less distinct than in the low concentration experiments of Garcia (1990) in the previous section. It was found that in another experiment RUN10 with a higher slope (1:20) the computation, calibrated for RUN5, appeared to give inaccurate values. Therefore in the following section only laboratory experiments for low-concentration currents are used to verify the front celerity.

## 7.4 Experiments of turbidity-current fronts in Lausanne

Turbidity-current and saline-current experiments in a 16.55 m long, 0.5 m wide, and 0.8 m high flume were reported by Altinakar et al. (1990). For a large number of low-concentration density currents on different bed slopes the measured gravity-current front celerities and dimensions were summarized. Using the two-layer model with  $\Delta x = 0.06$  m,  $C_D = 0.005$ ,  $C_{Di} = 0$ , and using the entrainment relation of Parker et al. (1987) several of these experiments were simulated numerically. During the experiments two sediment grain sizes were used (K-06:  $D_{50} = 32$   $\mu\text{m}$ , K-13:  $D_{50} = 14$   $\mu\text{m}$ ). Bed slopes in these computations varied between  $i_b = 0$  and  $i_b = 0.03$ , with inflows varying from  $q_2(0) = 22 \cdot 10^{-4}$   $\text{m}^2/\text{s}$  to  $72 \cdot 10^{-4}$   $\text{m}^2/\text{s}$ , and with inflow concentrations varying from  $C_s(0) = 1.1 \cdot 10^{-3}$  to  $6.5 \cdot 10^{-3}$ . An example of such a computation is given in section 6.10 for experiment TK 1306 ( $i_b = 0.01$ ,  $C_s = 2.24 \cdot 10^{-3}$ ,  $q_2 = 22 \cdot 10^{-4}$   $\text{m}^2/\text{s}$ ). It was shown that a very accurate approximation of the front celerity is possible by using a numerical shock-tracking technique.

A comparison of the calculated and measured front celerities in figure 7.17 is used

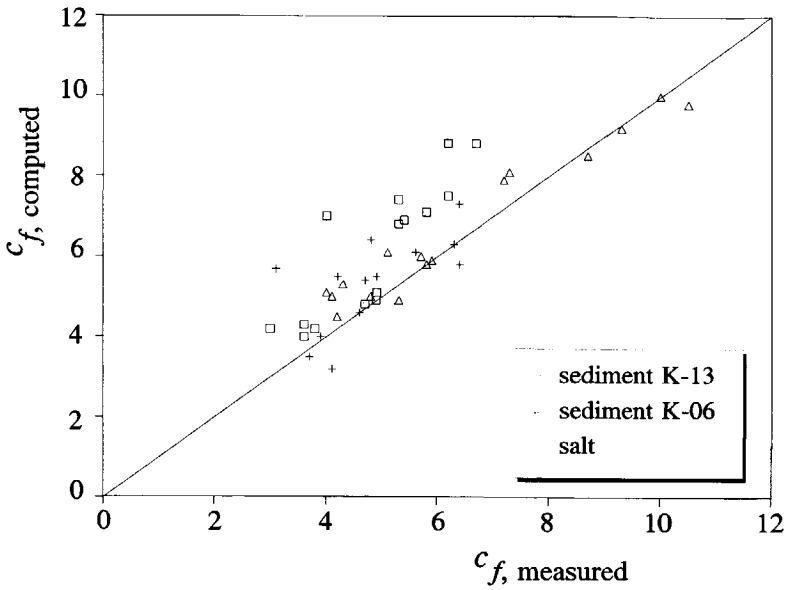


Figure 7.17 Comparison of measured and computed front celerities from the experiments of Altinakar et al. (1990).

to summarize the results. A first glance at this figure shows that a majority of the computed front celerities is too large, which agrees with earlier conclusions in chapter 5 (the mathematical approach cannot always provide sufficient energy losses). Furthermore the figure shows some scatter, particularly for the turbidity-current experiments. By using different (empirical) shock relations in combination with a numerical shock-fitting technique the computed front-celerities can be reduced. However, this cannot diminish the observed scatter as the analyses by Altinakar et al. (1990) clearly demonstrate. For instance the erratic behaviour of the front is demonstrated by the deviations in front celerities of five identical experiments EXP01 to EXP05 ( $i_b=0.0114$ ,  $q_2=26 \cdot 10^{-4} \text{ m}^2/\text{s}$ ,  $C_s=1.58 \cdot 10^{-3}$  and K-13 sediment). For each experiment a different front celerity was measured ranging from 3.0 to 3.6 cm/s (the computations yielded  $c_f=4.3$  cm/s).

Some of the calculations appeared to break down due to settling of the single-size particles, while in the experiments the turbidity currents persisted since finer fractions remained in suspension. This can be fixed by using a graded-sediment model (definition of Galappatti's equations for different fractions). For instance extensions of the sediment-mass balance for more than one fraction were given by Stacey and Bowen (1988b) and Garcia (1990). Garcia's (1990, 1994) measurements on poorly sorted turbidity currents indeed showed a decrease in average grain-size in longitudinal as well as in vertical direction, which indicates that further research to this grading effects is worthwhile.

Despite these inaccuracies and crudeness of the approach, it can still be concluded that for practical applications the front celerities of turbidity currents can be computed satisfactory with the present model. For approximating the travel distance before break-down of a poorly-sorted turbidity current it seems useful to study a further extension of the model for multiple sediment fractions. An example of such a break-down of the computed underflow is shown in the following section in a particle-driven lock-exchange experiment.

## 7.5 Laboratory experiments of lock-exchange flows

Turbidity currents generated in lock-exchange experiments in two different flumes with horizontal bottom in the University of Cambridge (UK) were reported by Bonnetaze et al. (1993). In such an experiment a gate separating two fluids of different density in a flume is suddenly removed. The design of Bonnetaze's experiments greatly coincides with the saline lock-exchange experiments of Rottman and Simpson (1983) illustrated in section 5.2 (also performed in Cambridge). To introduce Bonnetaze's experiments numerical computations of Rottman and Simpson's small-scale saline currents are illustrated in figure 7.18.

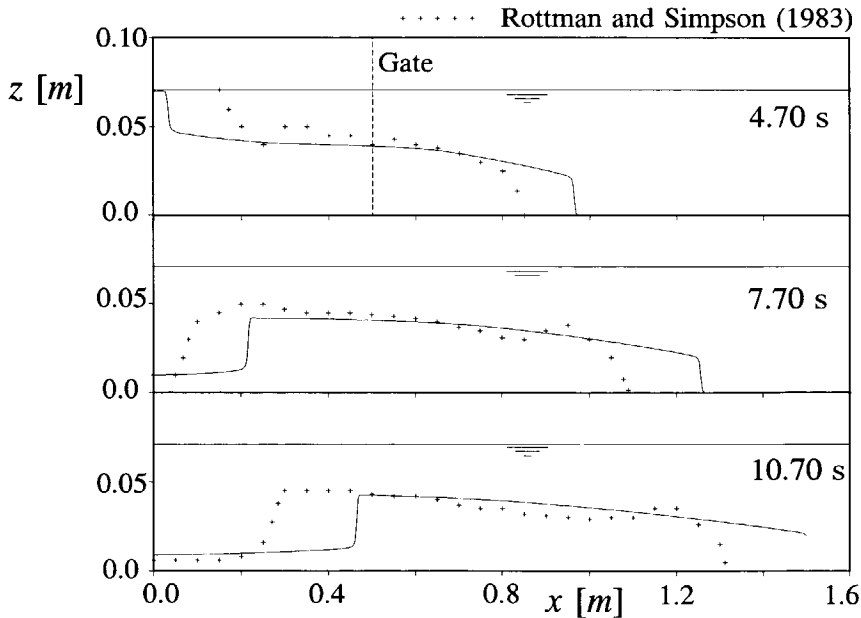


Figure 7.18 Computed and measured depths (from shadowgraphs) for a saline lock-exchange experiment of Rottman and Simpson (1983).

In this figure the measured interface levels are obtained from shadowgraphs.

Consequently they correspond to an approximate visual interface which is less accurate for the two-layer model than theoretical depths obtained from velocity profiles. Computations were carried out with  $\Delta x=3.75$  mm,  $\Delta t=0.014$  s, minmod limiter, Parker et al. (1987) entrainment,  $C_D=0.02$ , and  $\rho_2=1047.9$  kg/m<sup>3</sup> (equivalent to  $C_s=0.029$ ). It should be remarked that the density of the saline underflow is large, and that we applied a high value for  $C_D$ . Shortly after removing the gate a bottom and surface front are travelling in opposite directions, with, as expected, a somewhat overrated front celerity (which cannot be fixed by increasing entrainment and friction). If the surface front reaches the upward end of the flume it is reflected and continues as an internal bore, only leaving a small layer of dense fluid behind. In a very deep reservoir this behaviour is not seen as is illustrated for the identical numerical experiment in deep water in figure 7.19.

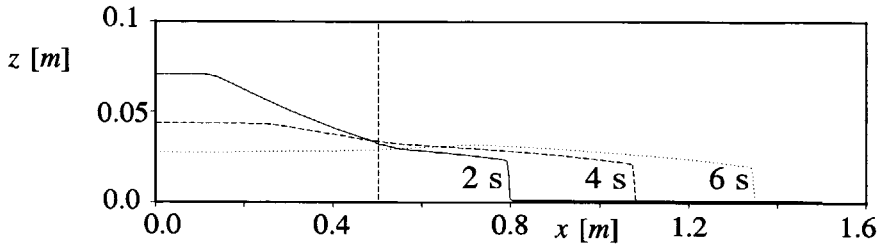


Figure 7.19 Rottman and Simpson's lock-exchange experiment computed in a very deep reservoir (with entrainment and friction).

It can be shown that in deep water the computed front celerity is larger.

Also in Bonneau's experiments with a lock-exchange flow of turbid water a similar behaviour was seen. The experiments were carried out in a small and a large flume with different grain sizes. Again numerical calculations are compared to depths obtained from shadowgraphs given in Bonneau et al. (1993) for a lock-exchange flow in the small flume with  $D_{50}=53$   $\mu\text{m}$ . In the 1.6 m long flume with a width of 0.27 m and a water depth of 0.14 m the gate is located 0.08 m from the upper end of the flume. The computations are carried out with an initial concentration of  $C_s=9.4 \cdot 10^{-3}$ ,  $\Delta x=0.002$  m,  $\Delta t=0.006$  s, and with  $C_D=0.01$  ( $C_{Di}=0$ ). Results for three time levels are plotted in figures 7.20 to 7.22.

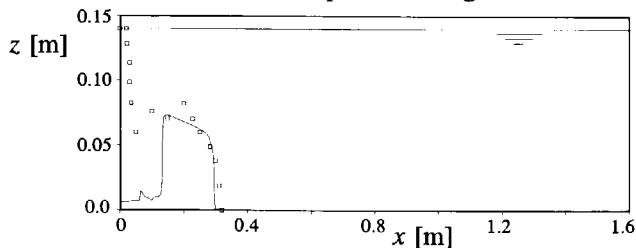


Figure 7.20 Measured and computed turbidity current 3 s after release.



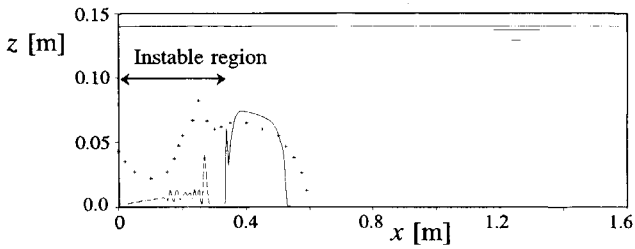


Figure 7.21 Measured and computed turbidity current 7 s after release.

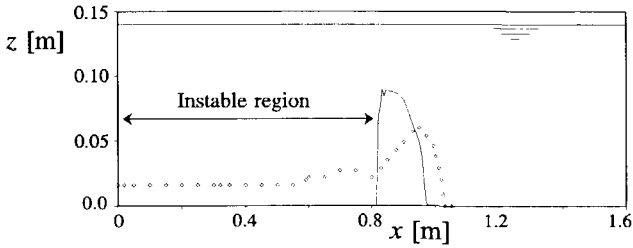


Figure 7.22 Measured and computed turbidity current 7 s after release.

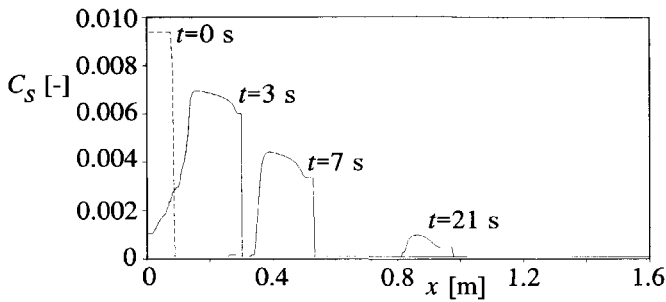


Figure 7.23 Development of the computed concentration during the experiment.

Differences in the behaviour of the turbidity current compared to a saline current are caused by settling of sediments, notably in the thin flow layer remaining after passage of the reflected internal bore. For this example the loss of buoyancy in this section due to insignificance of turbulence (i.e. of  $u_*$ ) results in instability of the two-layer model and the numerical solution. Here condition (3.12) is violated. Physically this means that the two-layer flow becomes an ordinary open-channel suspension flow with a non-equilibrium concentration profile. Since the numerical computation does not completely break down it can be shown that the stable region (near the gravity-current front) can travel a relatively long distance before losing its buoyancy. In figure 7.23 is shown how the concentration develops during the experiment. The physical break-down of the two-layer flow due to sedimentation was also reported by Garcia (1993) for experiments with  $30 \mu\text{m}$  sediment and was already mentioned in the previous section. Also in Bonnecaze's experiments the failure can be delayed by using a graded-sediment model (see section 7.3).

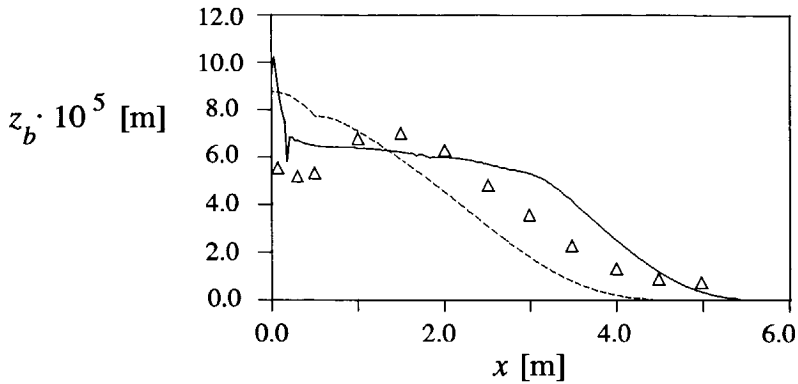


Figure 7.24 Turbidites deposited by a lock-exchange with  $23 \mu\text{m}$  sediment; drawn line: shallow water, dashed line: deep water, triangles: measurements.

Turbidites deposited by an experiment with  $23 \mu\text{m}$  sediment in the larger flume (10 m long, 0.26 m wide, and 0.3 m deep) were weighed by Bonneau et al. (1993) and compared with their numerical results. The stable results computed with our model are presented in figure 7.24. The densities of deposits given by Bonneau are translated to bed levels using a porosity of 30% (as was used in the model). The agreement between computations and measurements is very good, especially when realizing that we did not calibrate this experiment. Only at the upper boundary a large 'overshoot' is computed which develops directly in the initial stage of the experiment due to deposition in the section left of the gate. This defect is most likely enhanced due to the boundary treatment, but it is irrelevant for the turbidity current (bed-dimensions are much smaller than depth of the flow). During propagation of the underflow the bed forms a wave propagating downstream. Its speed reduces rapidly until the concentration of the underflow becomes very low (after one or two minutes). Then it ceases and results in the profile as plotted in figure 7.24. If the experiment is computed with an infinite deep ambient the shape of the profile clearly does not fit the shape of the observed bed. The results in figure 7.24 agree with the findings of Bonneau et al. (1993).

The smooth morphological computations in this section do not require sophisticated shock-capturing techniques. Therefore they cannot be used for verifying these techniques implemented in our numerical model. Instead we studied propagation of a bottom step due to bed-load transport in an open-channel flow. In the following section this is shown by using a simple adaptation of input data in the two-layer model.

## 7.6 Morphological computation of a bed front in a channel

To verify the bed-evolution predicted by the model some detailed data sets are required. However, only some limited bed measurements from turbidity currents are reported in literature. Mainly they were obtained by measuring the remaining deposits after a turbidity-current experiment (e.g., Bonnetcaze et al., 1993, Garcia, 1990, Lüthi, 1981, and Middleton and Neal, 1989), or in the field by geological survey of turbidites from former events (e.g., Edwards, 1993). An example is shown in section 7.4. None of these studies report discontinuities and propagation effects in the bed, which would be particularly heavy test cases for the model. Therefore we have chosen to use morphological data from an experiment in open-channel flow which does reveal these phenomena. It was shown in chapter 3 that propagation of bed-disturbances (celerities) is determined by the bed-load transport rate. It is primarily bed-load, not suspended load, which for instance determines the propagation rate of a delta front, or the rate of retrogressive erosion during flushing operations in a reservoir. A typical experiment which illustrates these features is reported by Brush and Wolman (1960) who carried out flume experiments with a steady flow over a forward-facing step in a sand bed. Later Bhallamudi and Chaudry (1991) tried to simulate one of the experiments (Run 1) numerically using MacCormack's scheme and Jameson's (1981) artificial viscosity with a model not quite different to ours. However, their results could only qualitatively fit the experiment, which we suppose to be caused partially by the typical (erroneous) formulation of the sediment-transport rate.

Brush and Wolman (1960) carried out their experiments in a 15.8 m long, 1.2 m wide flume in which they molded a trapezoidal channel of 21 cm width and about 3 cm deep in non-cohesive sand with  $D_{50}=0.67$  mm and  $D_{90}\approx 1$  mm. At about 10.8 m from the entrance the reach was oversteepened to create a drop of about 3 cm, with the intention to study the knick-point behaviour. With a discharge of  $5.95\cdot 10^{-4}$  m<sup>3</sup>/s in Run 1 no bed-load transport occurred in the mildly sloping reaches (slope  $\approx 0.1\cdot 10^{-2}$ ) due to the low Shields values (coarse grains and low shear stress). The most suitable transport formula for this experiment was found to be that of Meyer-Peter and Müller (1948), which accounts for initiation of motion as well.

To compute this experiment we use the analogy between a conservative underflow ( $C_s=\text{const.}$ ) in an infinitely deep reservoir and a regular open-channel flow. In fact it can be seen quite easily that by taking  $g' (=g\sigma' C_s)$  equal to  $g$ . By means of computed results the development of the bed front and the flow during the experiment is represented. For the numerical computations a spatial step  $\Delta x=0.16$  m is used, which needs a time step  $\Delta t=0.15$  s for stability (using the van Leer TVD-limiter). As (numerical) initial condition we started with a uniform depth of  $a_2=0.0305$  m and a steady inflow discharge is imposed of  $q_2(0)=0.002787$  m<sup>2</sup>/s. The computational results for  $t=2.7$  h, with  $C_D=0.0103$  and after reducing

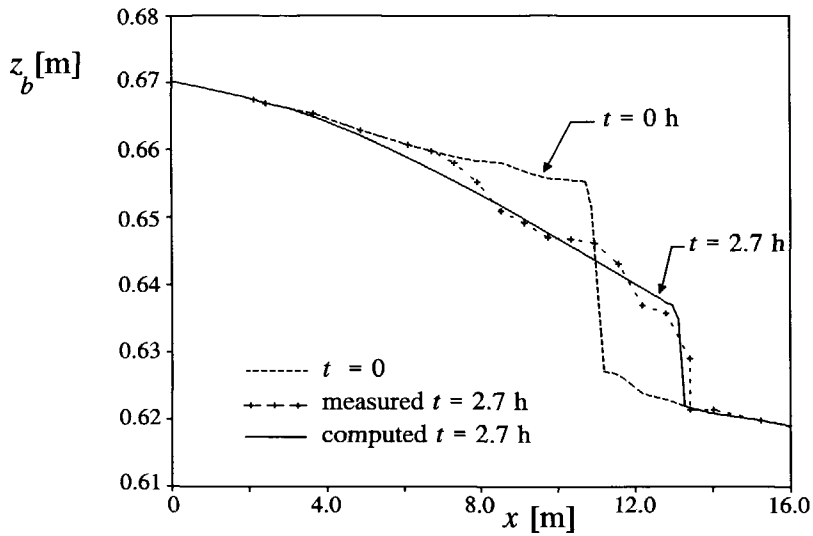


Figure 7.25 Computed and measured bed-levels for the open-channel flow experiment of Brush and Wolman (1960).

sediment transport with 30%, are compared with the observed bed levels in figure 7.25.

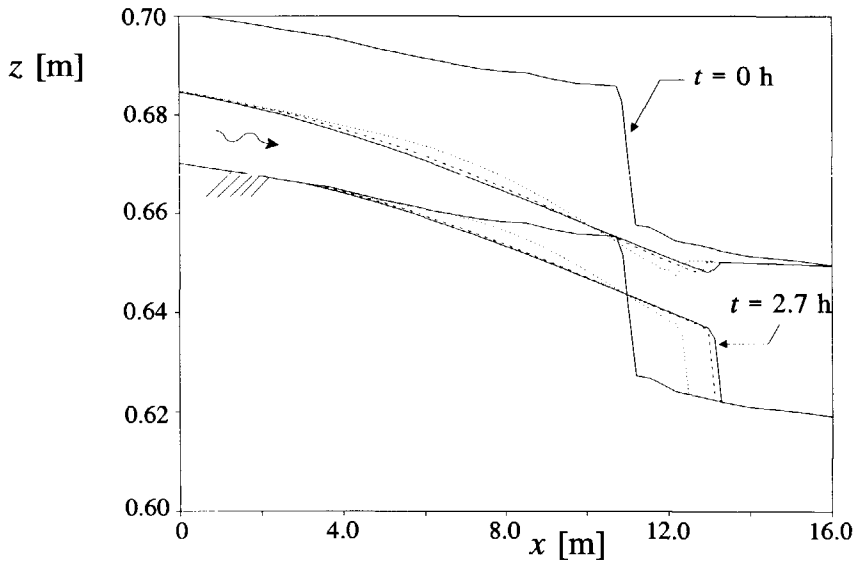


Figure 7.26 Computed flow and bed evolution for different time steps.

The results of this computation are very good, even when realizing that due to incision of the eroding parts the average width of the channel may vary. At certain

parts of the channel no sediment is transported since shear stresses drop below their critical value for initiation of motion. In figure 7.26 is shown how the computed bed develops, and how the bottom front is eventually arrested by this effect of low shear. This explains the advantage of Meyer-Peter and Müller (1948) formula.

The fully coupled computation of flow and morphology in this example with various discontinuities illustrates the power of the MacCormack scheme in combination with TVD artificial viscosity to deal with mobile bed problems. Brush and Wolman's experiment shows a large analogy with draw-down flushing operations in a reservoir with processes as retrogressive erosion and propagation of the delta front. Also the formation of the delta by back-water deposition can be computed successfully with this approach as is illustrated in figure 1.2 in chapter 1. Considering these results, it seems worthwhile to study this relatively simple numerical approach more carefully in future studies and compare them with other 1-D models.

The computations in this section and all previous sections are all verified by means of laboratory data. This is a consequence of the unavailability of detailed and accurate field data. Only data presented by Chikita et al. (e.g., 1991) are sufficiently comprehensive to be used for verification purposes. This is the subject of the following section.

## **7.7 Turbidity current in glacier-fed Peyto Lake, Alberta, Canada**

The occurrence of turbidity currents in the glacier-fed Peyto Lake has been reported by Chikita et al. (1991) during a snow-melt period. Peyto Lake is located in Alberta, Canada. It is fed by the braided inflowing Peyto Creek which has a drainage area of about 45 km<sup>2</sup> of which an area of about 13 km<sup>2</sup> is glacier-covered (Peyto Glacier). Extensive field measurements were obtained during high inflows at 9-15 July 1987 (melting water produced at the glacier surface), and in this section we intend to simulate (at least qualitatively) the observed phenomena.

To illustrate the typical geometry a bathymetric map from Chikita et al. (1991) is given in figure 7.27. On the south-side, a delta front of pebble and cobble-gravels advances into the lake with a speed of about 1.45 m/a. Near the foreset slope (sloping down at about 11°) the inflow with concentrations of mud and silt plunges below the lake surface to form a bottom current (just before point C). The plume advances northward to the central part of the lake where it meets a sub-aqueous sill. Whether it passes the sill and enters the northern sub-basin (point E) depends on the magnitude of the underflow and lake circulation.

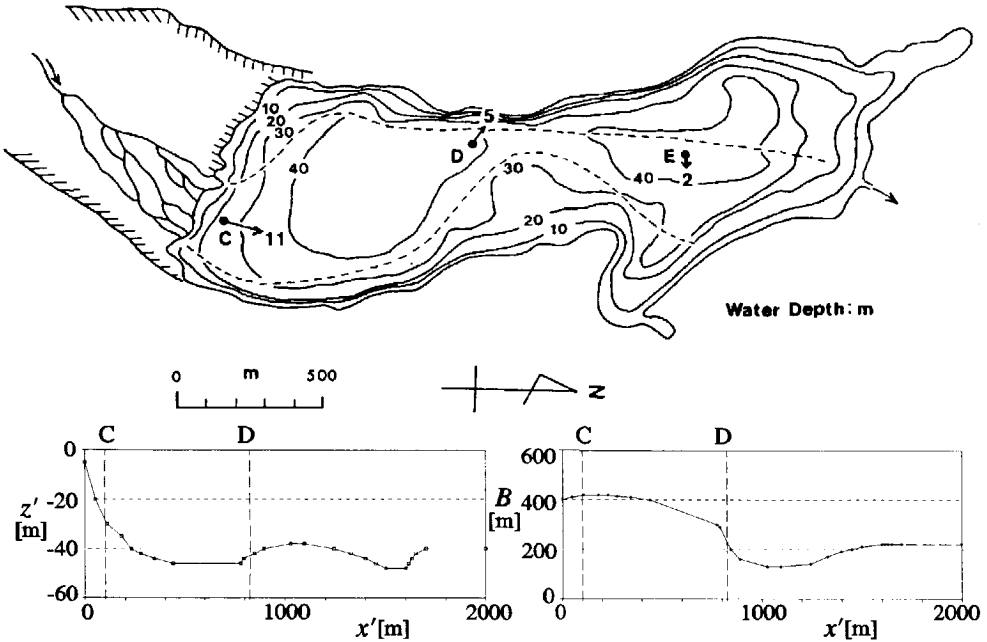


Figure 7.27 Bathymetric map of Peyto Lake (from Chikita et al., 1991) and the schematized geometry for the two-layer model.

During the high inflow at the 14th and 15th of July 1987 velocity and concentration profiles were measured and analyzed at station C, D and E. These profiles, and subsequent measurements carried out by Chikita and co-workers (in 1993, to be published later) clearly reveal the presence of turbidity currents which were able to pass the sill. Before crossing this narrow elevation they observed that the underflow builds up in front of it while reducing its velocity. At this point only reasonably strong underflows can maintain their stability to cross the sill. Chikita et al. also noticed that due to dominantly northward katabatic winds a lake-circulation is generated with a northward surface current compensated by a deep-water southward current opposing the underflow (especially when the underflow is weak). On the other hand this current provides additional energy (turbulence) for maintaining suspension which can contribute to the possibility of passing the sill.

To simulate the observed phenomena in order to validate the 1-D numerical model we have computed the turbidity event of July 14 and 15. The unsteady inflow of water and sediment at station C ( $x=0$ ,  $x'=100$  m) is used as the inflow boundary and extrapolated from the recorded inflow hydrograph of Peyto Creek and the measured profiles as shown in figure 7.28.

Furthermore the geometry is adopted from figure 7.27 (schematization to

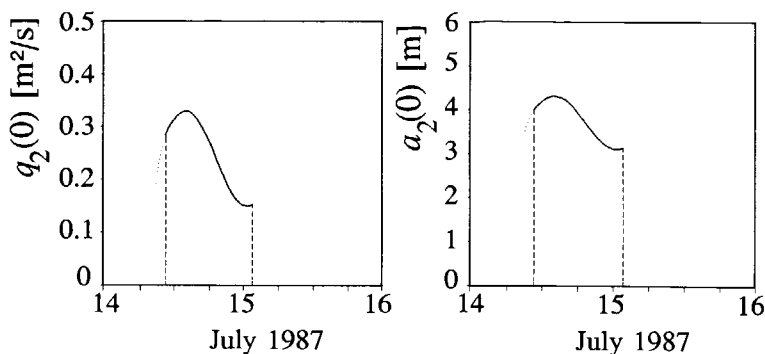


Figure 7.28 Inflow boundary condition for the underflow at point C.

rectangular cross sections) and a constant concentration of 60 mg/l is imposed at the upper boundary. Interfacial friction is neglected compared to entrainment, while the latter is obtained from the Parker et al. (1987) formulation reduced with 80% (to prevent instability). The bottom friction coefficient is taken  $C_D=0.005$ . The fall velocity of the cohesionless silt and clay particles (Chikita et al., 1991, 1992) was taken  $2.8 \cdot 10^{-5}$  m/s (Stokes law). We realize that the actual situation is simplified noticeably for the computation, for instance by the choice of a rectangular cross-section and by neglecting the effect of the wind-driven circulation currents.

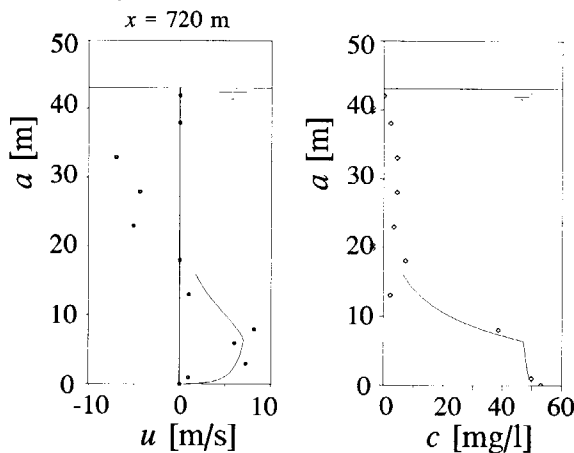


Figure 7.29 Measured and computed profiles at station D, 14 July 1987.

Quantification of the measured profiles in station D (14 July, time 17:02 to 19:12), using the model of section 2.4 is given in figure 7.29. To the measured profiles, which were corrected for the direction of the underflow velocity, corresponds a computed value of  $a_2=16$  m,  $u_2=5$  cm/s, and  $C=30.5$  mg/l (which is internal subcritical). In this plot the negative velocity above the underflow is the sum of

return flow and wind-driven circulation. A similar profile with similar depth ( $a_2 \approx 15$  m) can be plotted for station E (15 July, time 10:07-12:28), but with a lower velocity and concentration ( $u_2 = 1$  to 2 cm/s,  $C = 10$  to 15 mg/l). In this figure the velocities transversally to the underflow are not plotted, but they were found to be of the same order of magnitude as the velocities along the underflow.

The 1-D numerical computation is carried out with  $\Delta x = 5$  m,  $\Delta t = 15$  s, using the minmod flux limiter. The total discharge  $Q$  is taken very small to obtain a return flow which approaches the observed one. The resulting depth, velocities and concentrations are plotted in figures 7.30 to 7.32 relative to station C.

Note that the development of the current is not computed at E since we assumed an open end at the downstream boundary. In reality only surface outflow is possible, hence all sediments reaching E will eventually settle out. The computational results indicate that the measured profiles at station D correspond to a time-average situation at approximately three hours after the passage of the front through the inflow boundary C. After this period the velocity drops and interface rises quickly in this southern sub-basin, resulting in a subcritical flow situation due to the backward propagation jump. Furthermore it was found that the computed gravity current front at the bed moves with a quite constant speed of  $c_f \approx 6.5$  cm/s downstream as is shown in figure 7.33. Unfortunately there is no data which can support this result.

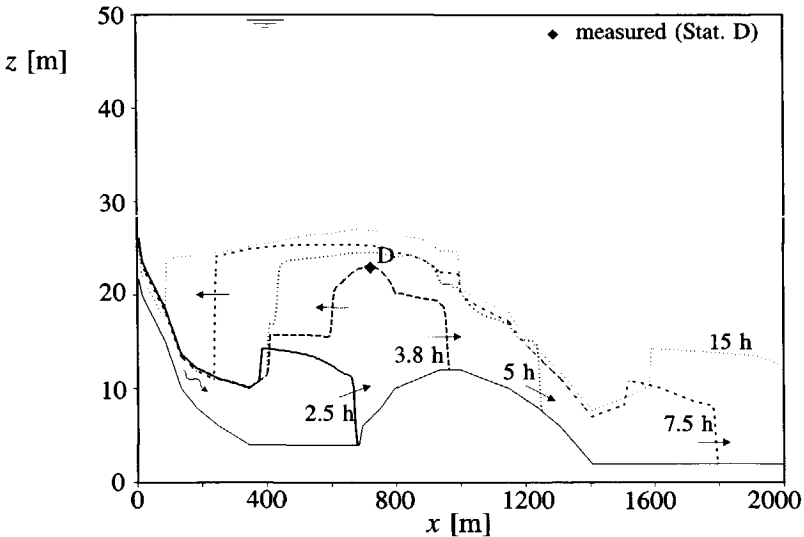


Figure 7.30 Computed development of the underflow in Peyto Lake (depth).

Due to the low settling velocity the dilution effects observable in figure 7.32 are primarily caused by entrainment. Computed bed-levels only show deposition of the order of 0.1 mm during the development of the current which is negligible. Obviously sedimentation does not occur during propagation, but occurs afterwards



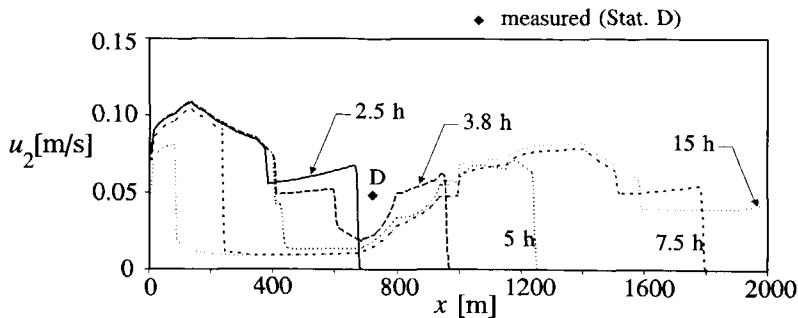


Figure 7.31 Underflow velocities for the computed turbidity current.

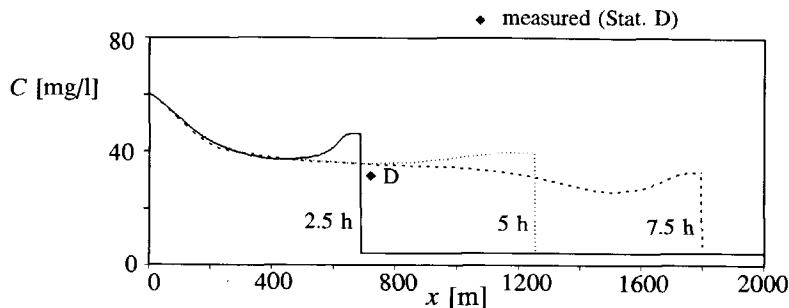


Figure 7.32 Underflow concentrations for the computed turbidity current.

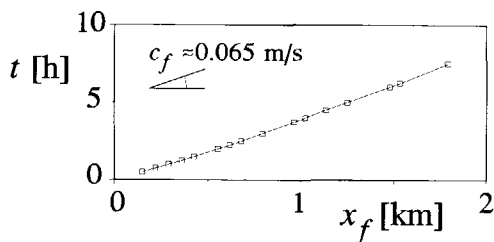


Figure 7.33 Computed propagation of the turbidity-current front.

when the current is dissolved (as it cannot be sluiced from the lake). Although the concentrations seem small during this event, still about  $200 \cdot 10^3$  kg sediment enters the lake in a period of 12 hours. Chikita (1992) shows that the total contribution of underflows to yearly sedimentation is about 61% (primarily in the period June to September). Another 32% of the total sedimentation is due to the delta propagation (which corresponds to  $30 \cdot 10^6$  kg/a). Still the life span of Peyto Lake with this sedimentation rate was estimated to be about 600 years.

Further to this computation the effects of counter-currents and increased entrainment and interfacial friction have been studied as well. A counter-current

(impose a negative  $Q$ ) only slightly decreases the front celerity and only slightly affects the underflow, primarily due to a modified entrainment rate. Also interfacial friction does not qualitatively change the results. Increasing the entrainment rate without counter-current appeared to be more forceful. By doubling the entrainment rate a noticeable dilution effect after some time at the crest of the sill resulted in a local breakdown of the two-layer model. At this point the flow locally becomes an ordinary suspension flow (still part of the underflow reaches point E).

It is likely that the computational results qualitatively represent the actual observed phenomena in the lake. New continuously recorded data during some events in Peyto Lake in 1993 by Chikita et al. confirm this conclusion. However, due to the limitations of the reported data, a complete quantitative verification is not possible. In most field studies this is the primary deficiency. Although observations prove the existence of turbidity currents in lakes and reservoirs, it is virtually infeasible to survey the complete turbidity-current development in detail. It was found that other data sets in literature (for instance from China, Fan, 1986, 1991) cannot provide a better validation than Chikita's measurements, and these computations are therefore not presented in this thesis.

## 7.8 Conclusions

The integral behaviour and performance of the 1-D computational model in the real world is studied by means of laboratory and field data reported in literature. The limitations of the model, primarily induced by schematization to one dimension and empiricism, are set against the uncertainties and inaccuracies of the observations. Some detailed data sets from laboratory flumes are used to verify the behaviour of steady intruding gravity currents and lock-exchange flows. Furthermore a flume experiment with open-channel on a sediment bottom-step are used to verify the power of the morphological computations. To conclude the validation of the model it is applied to an comprehensive data set from field measurements of an unsteady turbidity current in a glacier lake.

For the test cases it can be concluded that the overall behaviour consisting of different physical processes are satisfactory represented by the model. This is true for the two-layer numerical model as well as for the velocity and density profiles. The best quantitative results are obtained for low concentration turbidity currents (e.g.,  $C_s < 0.01$ ) or low density saline currents. Turbidity currents in reservoirs are usually of a low density type as confirmed by the presented field case and by other field observations mentioned in literature (e.g., Fan, 1991). For calibration of the model it is sufficient to tune primarily on bottom friction and the entrainment parameter for interfacial mixing. Due to small upper-layer velocities in the upper

layer it is allowed in many cases to superpose interfacial friction to bottom friction which eases the calibration. Furthermore, due to an insensitivity to the near-bed concentration  $c_n$ , it is often justified to neglect this concentration in depositing low-concentration turbidity currents.

In agreement with the conclusions in chapter 5 it is shown that the application of the new shock-capturing technique still results in a slight overestimation of front and bore celerities. Nevertheless for turbidity-current fronts, in combination with friction, deposition and entrainment in the following current, the accuracy of the computations is acceptable for practical purposes. That is when compared to the irregularity of the observed celerities. Here an important contribution in a correct prediction of the front and current is due to the finite reservoir depth, which appears to be especially important for lock-exchange flows (presence of a reflected bore). Generally the often applied deep-water model or one-layer model overpredicts the concentrations and front celerities of an intruding turbidity current, while it underrates the depths, and is therefore inferior to a two-layer approach.

During some computations we found a break down of the current due to a loss of density by particle settling. However, due to the presence of very fine sediment fractions in the flow the actual turbidity current continued over a longer distance. To fix this deficiency it is recommended to extend the sediment balance equation for multiple fractions when dealing with graded sediment. Furthermore it is worthwhile to study in more detail the excellent performance of the MacCormack scheme in combination with TVD artificial viscosity to compute the morphology of discontinuous sediment beds as shown in section 7.5. In the context of reservoir sedimentation its merits lie in the prediction of delta-front advance and erosion of deposits during draw-down flushing. Although in most of the presented test cases the amount of deposition was of negligible magnitude, it can be concluded that the morphology and development of turbidites are also well predicted by the model.

A one-dimensional computation of the unsteady turbidity current in Peyto Lake in Canada suffers from more uncertainties since the uncontrolled conditions and 3-D processes require a more radical schematization. Furthermore the data is less detailed than in a laboratory experiment. The observed behaviour of this rather heavy test case is still satisfactory represented by the model, for instance by the computed built up of dense fluid against a subaqueous sill, and the overflow of the current over the sill. Again the current is mainly sensitive to bottom friction and entrainment (for instance enhanced by wind-generated turbulence). The analysis of the present data set, as well as other field data, shows that it is not worthwhile to apply more refined approaches to compute turbidity currents in reservoirs. This conclusion justifies the use of a simple 1-D model, or alternatively a 2-DH model (for cases with rapid width changes such as in Peyto Lake), for practical applications.



## Chapter 8

### Conclusions

The performance of reservoirs designed to store river runoff is seriously threatened by sedimentation processes. As the demand for storage, and the constraints on replacement of lost storage increase, a growing effort is therefore made to maximize long-term storage volume and to minimize the trap efficiency of these reservoirs. To design techniques for capacity maintenance it is necessary to understand and to quantify the hydrodynamic and morphological processes involved. For instance, to support decisions regarding design and operation of the reservoir it is preferable and most promising to use 1-D and 2-D mathematical models. On the other hand, it is the lack and inaccuracy of available data on the flow in the reservoir, and the sediment entering the reservoir from the catchment or the river, which limits the accurate prediction of the long-term storage loss due to reservoir sedimentation.

Since it affects directly the active storage part of the reservoir it is delta formation which gains much attention in these studies. The exact distribution of these deposits is complex and irregular, and the highly empirical predictions are still uncertain. For rather narrow reservoirs the use of 1-D in which the delta is computed as a shock are known to yield promising results (e.g., Hotchkiss and Parker, 1991). By means of an example it is shown that simple numerical shock-capturing schemes of the Lax-Wendroff type can be used in combination with an appropriate artificial viscosity term. This type of viscosity, preferably the TVD type presented in chapter 6, is necessary to suppress the significant oscillation (wiggles) appearing near the bottom shock during the morphological computation. In future extensions of these ideas on delta computation, graded material and unsteady flow sequences (in combination with sound predictions of the sediment yield) must be included.

Also (reservoir-sedimentation) mitigating measures have become an important research topic. Apart from reducing the sediment inflow and the mechanical removal of deposits, methods based on hydraulic flushing and sluicing of sediments (reservoir operation strategies) have proven to be very effective and attractive ways to increase the reservoir life in many cases. Therefore design of new reservoirs should if possible accommodate large bottom sluices or other constructions which enable these sluicing and flushing operations. More research is required to methods for computing flushing operations. Important prior conditions for this research are the formulation of the formation of a flushing channel by retrogressive erosion, the unsteadiness of the flow and sorting effects of sediment particles. Theoretical

approaches stand or fall with the formulations of these erosion processes (so far no satisfactory theory exists for the formation of a channel). Overall can be concluded that investments in sedimentation mitigation measures must become an integral part of the cost-benefit analyses for the design of dams.

Turbidity currents in reservoirs can be an important transport medium for sluicing fine sediments. This type of low velocity density current has been observed in many reservoirs and can be used to sluice the fine sediments without significant water losses, since they are capable of carrying large quantities of sediments over long distances. Time and length scale of these underflows correspond roughly to the scale of the flood wave entering the reservoir. From the various sedimentation and transport processes we have chosen to consider the development of these turbidity currents in more detail. A mathematical two-layer (depth-averaged) model has been developed to study their behaviour and to predict their development. Therefore the original two-layer concept, which has proven its applicability for a wide range of stratified phenomena, is reformulated in a 2-DH form for turbidity currents. It was found that the most crucial difficulty in modelling the underflow is the delicate sediment/fluid interaction which governs its behaviour.

For the studied low concentration ( $C_s < 0.01$ ) depositing turbidity currents the interaction between flow turbulence and sediment concentration can be expressed by means of the depth-integrated form of the convection-diffusion equation proposed by Galappatti (1983). This approach based on a theoretically exact asymptotic solution of the 3-D convection-diffusion equation for the suspended sediment is very robust and suitable for turbidity-current parts where the shape of the actual concentration profile does not deviate to much from the equilibrium profile (for the local flow state). The adaptation length and time of the concentration redistribution expressed by this Galappatti's model are dependent on shape functions for equilibrium concentration and velocity profiles. They can be well expressed by the presented semi-empirical approach, that is based on empirically indicated similarity of these profiles for different flow conditions combined with the mixing-length concept and the convection-diffusion equation.

The validity and behaviour of the solutions of this two-layer model can be analyzed mathematically by means of the method of characteristics. It gives insight in the development of wave fronts in the solution, by which this hyperbolic model is characterised. In a 2-DH model the wave-like solutions originating from a point disturbance are circular or elliptic (typical for surface and interfacial waves) and star-shaped (typical for bed waves and vorticity disturbances). Differences in model behaviour are found for internal subcritical flow (low densimetric Froude numbers) and internal supercritical flow (high densimetric Froude numbers, at least larger than unity). In a critical and supercritical 2-DH two-layer flow the computation of bed morphology and baroclinic flow cannot be decoupled, contrary to a smooth internal subcritical flow. In a 1-D two-layer flow this restriction on decoupling is

only present in a near-critical situation. On the other hand, for small density differences between the layers, it is always possible to decouple morphology and barotropic-flow computation. Barotropic (external) flow in a reservoir can be computed in a quasi-steady approach.

The method of characteristics shows how the two-layer model loses its stability (its hyperbolicity, or stability of internal waves) in situations with high velocity differences between layers and low density differences. Practically this limitation can be associated to the breakdown of the turbid underflow, a phenomenon for which 2-DV or 3-D computational models are probably more appropriate. Further, the method of characteristics provides us with rules for imposing the number and type of boundary conditions. They are also shown to play an evident role in computing shocks and jumps in the solutions. These discontinuities form where characteristics intersect. For instance the formation of a leading front and internal bores and hydraulic jumps are regular phenomena for turbidity currents in the field, and must be accounted for in the computational model.

Such a turbidity-current front advancing into the reservoir is modelled as a shock-wave solution of the two-layer model in a way that also the classical steady state solutions are satisfied. This can be achieved either by adding an internal boundary condition or a resisting force locally at the discontinuity. However, from a computational point of view it is preferred to rewrite the momentum equations (originally with gradients of discharge  $q_2$  and depth  $a_2$ , the  $q,a$ -form) into a formulation with gradients of the velocity  $u_2$  and depth  $a_2$  (the  $u,a$ -form), and computing the front as an internal bore running over a very thin dense layer. The weak solutions and jump conditions of fronts and bores for the system of equations in  $u,a$ -form were found to correspond very well to the classical steady-state solutions (e.g., Benjamin, 1969) and the available data sets. The primary advantage of this property is the possibility to use shock-capturing schemes for 1-D and 2-DH numerical computation which precludes the necessity of using difficult shock-fitting techniques with moving internal boundaries to compute the gravity-current front.

The observation that the weak solutions of the equations in  $u,a$ -form satisfy the shock relations of real gravity-current fronts implies that velocity is conserved rather than momentum. When the basic equations are expressed in terms of momentum conservation (equations in  $q,a$ -form) therefore an additional dissipating force must be added locally at the front to simulate the loss of momentum and energy. This approach is followed to define a conceptual model for fronts in 2-DH developing plumes where the effect of a tangential velocity along the front is used to allow for arresting of side fronts. The present theory for 2-DH fronts is not further elaborated since we expect that the use of shock-capturing techniques in combination with  $u,a$ -equations will yield satisfactory results.

To compensate for the scarcity of appropriate and accurate data, analytical

similarity solutions can be used to verify 1-D and 2-DH numerical results and to analyze their sensitivity. These self-similar solutions can be formulated for slightly simplified intruding gravity currents into an ambient flow on a horizontal bed. In this thesis they are determined for 1-D and 2-DH lock-exchange flows (analogous to dam-break flows) and for 1-D sluicing operations. Self-similar solutions have been shown to reveal many insights in the complex physical and mathematical behaviour of the developing two-layer flow. For instance the transformation from an internal subcritical to an internal supercritical state due to the effect of a limited ambient flow depth in a 1-D approach is a result with significant mathematical and physical significance as it determines the controlling conditions. Essentially these solutions are composed of shock waves (compression shocks and expansion waves) and uniform flow sections and are therefore quite simple to construct. In a 2-DH radially developing flow a self-similar solution is derived which shows how such a plume is composed of a narrow rim behind the front, followed by a spreading highly internal supercritical region. This supercritical region is subject of intensive interfacial mixing and friction, and is therefore an important argument to switch to a more complete numerical solution for 2-DH flows.

Due to this increased interfacial-mixing intensity in spreading underflows, the self-similar (or numerical) solution shows that these jet and plume-type currents rapidly lose their driving force and transport capacity by dilution (and successive settling). Therefore the presence of a river or flushing channel in the reservoir bed, which confines the spreading of the underflow is favourable for sluicing operations. Also in narrow (run-of-the-river) reservoirs the probability that turbidity currents reach the dam is much higher. It is obvious that obstacles in the bed (such as small or large roughness elements) are also unfavourable for the propagation of the turbidity current.

To obtain a more complete solution for developing turbidity currents in a reservoir a numerical model is developed. So far the numerical approach is 1-D, but during its development an eventual future extension to 2-DH is continuously anticipated. The numerical solution method is chosen from established approaches which has proven their robustness, applicability for similar models, and capability to deal with shock waves. The simple and accurate MacCormack (1969) shock-capturing scheme was found to be the most appropriate scheme for our model (that means for its baroclinic part). It is an explicit predictor-corrector scheme of the family of Lax-Wendroff schemes, and it can easily be extended to two dimensions.

In the numerical computations the turbidity front is computed as an internal bore, but due to 2-nd order accuracy oscillations (wiggles) are formed near such shocks. To reduce and prevent these errors it is necessary to add artificial viscosity. Wiggles and physically incorrect solutions cannot be fully prevented with conventional artificial viscosity methods, and calibration is required. However, it is found that complete oscillation-free and correct solutions are computed with



artificial viscosity terms based on flux limiters (which make the scheme Total-Variation Diminishing, TVD). This advanced technique requires an increased computational effort, but prevents the need for calibrating diffusion coefficients. In a 2-DH model these TVD-techniques are less successful (due to a reduction to first-order accuracy) such that enhanced forms of the conventional artificial viscosity terms may become superior. Further, fronts computed in a non-conservative gravity current, e.g., with interfacial mixing and settling of sediment particles, need a correction in density to prevent a large overshoot. This effect is not caused by the numerical scheme but is caused by the adaptation scales for the sediment concentration. To correct this problem a shock-tracking technique is defined in which the front is tracked during the computation, and where its density is replaced in a physically correct upwind manner.

Even more important for the stability and accuracy of the numerical solution is the correct treatment of boundary- and initial conditions. Difficulties arise when shocks pass through, or reflect against the boundary. Most extrapolation techniques appeared to fail here. Instead a 'ghost'-point approach is used in which the computational grid is extended one additional point outside the boundary. A Froude-number check is added to guarantee the correct choice of number and type of boundary conditions. The number and type of imposed boundary conditions are defined from the results of characteristic analyses and characteristic wave decomposition. Also the initial condition is chosen such that realistic solutions are computed. Often this is a very small dense layer which can be overrun by the front.

Although these results imply that stability and accuracy of the solutions can be controlled greatly by means of artificial viscosity and the treatment of conditions, the Courant number ( $\sigma = c \cdot \Delta t / \Delta x$ ) and its interaction with artificial viscosity and source terms (friction and entrainment) is still dominating the numerical errors. A numerical analysis of general Lax-Wendroff type numerical methods (including MacCormack's scheme) shows that a stable solution can be found for a Courant number less than unity. However, this criterium is lowered if the amount of artificial viscosity or the effect of source terms increases. On the other hand it is shown that by decreasing the Courant number (e.g., decreasing the time step) an increase of wiggle formation occurs near shocks. If different characteristic celerities occur simultaneously in the problem (e.g., a fully coupled hydraulic and morphological computation) this effect always results in oscillations in the slowest travelling short-wave phenomena. Only with TVD artificial viscosity we were able to eliminate these errors from our Lax-Wendroff type discretization.

So far the overall behaviour of turbidity (and saline) currents are satisfactory represented for low-concentration turbidity currents (e.g.  $C_s < 0.01$ ). Primary difficulty in this study was the lack of appropriate and detailed data on turbidity currents in reservoirs. This forced us to introduce seemingly rigorous

schematizations, which, on the other hand, do not devalue the model. They merely provoke new topics for further research. Numerical computations of measured saline and turbid underflows confirmed that bed friction and entrainment are the primary calibration parameters (interfacial friction is usually negligible). Compared to saline currents a larger bed friction is needed in turbidity currents, presumably due to bed forms and bed-load transport. In a shallow reservoir the effect of ambient-flow depth also becomes more noticeable, compared to an equilibrium state. In a deep reservoir fronts move faster, concentrations are higher, and underflow depth is lower. Nevertheless, in a majority of numerical experiments the computed front celerities (internal jumps and gravity-current fronts) are slightly too large, but sufficiently accurate for engineering purposes.

Sediment gradation may prevent a quick breakdown of the underflow due to a diminishing density difference by settling of grains. Whereas the uniform-sediment model predicts a breakdown, the finest grains in the actual current may remain in suspension providing sufficient density for maintaining the stratification. A reformulation of the model for different sediment fraction for natural poorly sorted turbidity currents seems worthwhile when reviewing several test cases.

Other points of research are the effects of discrepancies in the definition of interface level when comparing various studies, and the location and characteristics of the plunge point. The definition of the interface level is for instance essential for the magnitude of interfacial friction and mixing. The plunge point, where the turbid water plunges below the clear reservoir water, is an important control to the turbid underflow. It is characterised by a complex and rapid 3-D flow variation. Empirically it is shown that at the plunge point the densimetric Froude number is near unity in a depth-averaged approach, whereas the variation around this condition is usually expressed by empirical relations. Plunge point relations are not studied here, but further research is necessary for a more complete simulation of the processes. In practice the plunge point is usually located near the foreset slope of the delta.

In the present study we were not able to derive general operation rules for sluicing turbidity currents through reservoirs. Therefore too many parameters are involved, and too many limitations exist. For design purposes the chosen approach is more useful to investigate the propagation and distribution of turbidity currents and their sensitivity to various parameters in the considered project. It can also be helpful for real-time operation decisions in existing practical situations.

## References

- Abbott, M.B. (1966) *An introduction to the method of characteristics*.  
Thames & Hudson, London, and American Elsevier, New York, 243 pp.
- Abbott, M.B. (1975) Weak solutions of the equations of open channel flow.  
In: Mahmood, K. and V. Yevjevich (eds.) *Unsteady flow in open channels*.,  
Vol.1, Water Res. Publ., Fort Collins, Colorado, USA, p.283-311.
- Abbott, M.B. (1979) *Computational hydraulics; Elements of the theory of free surface flows*.  
Pitman, London, 324 pp.
- Abbott, M.B. and D.R. Basco (1989) *Computational fluid dynamics: an introduction for engineers*.  
Longman Scientific & Technical, England.
- Abraham, G. and C.B. Vreugdenhil (1971) Discontinuities in stratified flows.  
*J. Hydr. Res.*, IAHR, Vol.9, No.2, p.293-308.
- Abraham, G., M. Karelse and G. van Os (1979) On the magnitude of interfacial shear of subcritical stratified flows in relation with interfacial stability.  
*J. Hydr. Res.*, IAHR, Vol.17, No.4, p.273-287.
- Ackers, P. and G. Thompson (1987) Reservoir sedimentation and influence of flushing.  
In: Thorne C.R., Bathurst, J.C. and Hey, R.D. (eds.) *Sediment transport in gravel-bed rivers*, Wiley, Chichester, UK, p.845-868.
- Akiyama, J. and H.G. Stefan (1985) Turbidity current with erosion and deposition.  
*J. Hydr. Engrg.*, ASCE, Vol.111, no.12, p.1473-1496.
- Akiyama, J. and H.G. Stefan (1988) Turbidity current simulation in a diverging channel.  
*Water Resources Research*, Vol. 24, No.4, p.579-587.
- Alavian, V. (1986) Behaviour of density current on an incline.  
*J. Hydr. Engrg.*, ASCE, Vol.112, No.1, p.27-42.
- Albeda, G.D., B. van Leer, and W.W. Roberts (1985) A comparative study of computational methods in cosmic gas dynamics.  
*Astron. Astrophysics*, Vol.108, p.76-84.
- Altinakar, S., W.H. Graf and E.J. Hopfinger (1990) Weakly depositing turbidity current on a small slope.  
*J. Hydr. Res.*, IAHR, Vol.28, No.1, p.55-80.
- Ashida, K. and S. Egashira (1975) Basic study on turbidity currents.  
*Trans. Jpn. Soc. Civ. Engrg.*, Hydr. Sanit. Engrg. Div., No.7, p.83-86.
- Bagnold, R.A. (1962) Auto-suspension of transported sediment; turbidity currents.  
*Proc. Royal Society of London; Series A. Mathematical and physical sciences*,  
Vol.265, p.315-319.
- Beam R.M. and R.F. Warming (1976) An implicit finite-difference algorithm for hyperbolic systems in conservation-law form.  
*J. Computational Physics*, Vol.22, No.1, p.87-110.
- Beam R.M. and R.F. Warming (1978) An implicit factored scheme for the compressible Navier-Stokes equations.  
*AIAA Journal*, Vol.16, No.4, p.393-402.
- Benjamin, T.B. (1968) Gravity currents and related phenomena.  
*J. Fluid Mech.*, Vol.31, Part 2, p.209-248.

- Bhalla, S.M. and M.H. Chaudry (1991) Numerical modelling of aggradation and degradation in alluvial channels.  
*J. Hydr. Engrg., ASCE*, Vol. 117, No.9, p.1145-1164.
- Bonnecaze, R.T., H.E. Huppert and J.R. Lister (1993) Particle-driven gravity currents.  
*J. Fluid Mech.*, Vol.250, p.339-369.
- Boris, J.P. and D.L. Book (1973) Flux-corrected transport. I. SHASTA, A fluid transport algorithm that works.  
*J. Computational Physics*, Vol.11, No.1, p.38-69.
- Britter, R.E. and P.F. Linden (1980) The motion of the front of a gravity current travelling down an incline.  
*J. Fluid Mech.*, Vol.99, Part 3, p.531-543.
- Brown, C.B. (1943) The control of reservoir silting.  
 U.S. Department of Agriculture. Miss. Publ. No.521, Aug. '43.
- Brørs, B. and K.J. Eidsvik (1989) Self-accelerated turbidity current prediction based upon the dynamic turbulence models.  
 In: Wang, S.S. (ed.) *Sediment transport modelling*, Proc. Int. Symp., New Orleans, p.190-196.
- Bruk, S. (1985) *Methods of computing sedimentation in lakes and reservoirs*.  
 Unesco, February 1985, Paris, France, 224 pp.
- Brune, G.M. (1953) Trap efficiency of reservoirs.  
*Trans. Am. Geoph. Union*, Vol.34, no.3.
- Brush, L.M. and M.G. Wolman (1960) Knickpoint behavior in noncohesive material: a laboratory study.  
*Bulletin of the geological society of America*, Vol.71, p.59-73.
- Bühler, J., S.J. Wright and Y. Kim (1991) Gravity currents advancing into a coflowing fluid.  
*J. Hydr. Res., IAHR*, Vol. 29, No.2, p.243-257.
- Chakravarthy, S.R. and S. Osher (1983) High resolution applications of the Osher upwind scheme for the Euler equations.  
 AIAA paper 83-1943, Proc. AIAA 6th Computational Fluid Dynamics Conf., Danvers, Mass., p.363-373.
- Chikita, K. (1989) A field study on turbidity currents initiated from spring runoffs.  
*Water Resources Res.*, Vol.25, p.257-271.
- Chikita, K. (1992) The role of sediment-laden underflows in lake sedimentation: Glacier-fed Peyto Lake, Canada.  
*J. Faculty of Science, Hokkaido Univ. (Sapporo, Japan), Series VII (Geophysics)*, Vol.9, No.2, p.211-224.
- Chikita, K., N. Yonemitsu and M. Yoshida (1991) Dynamic sedimentation processes in a glacier-fed lake, Peyto Lake, Alberta, Canada.  
*Japanese. J. of Limnology*, Vol.52, No.1, p.27-43.
- Chow, V.T. (1959) *Open channel hydraulics*.  
 McGraw-Hill, New York, 680 pp.
- Churchill, M.A. (1948) Discussion of "analysis and use of reservoir sedimentation data" by L.C. Gottchalk.  
 Proc. of the Federal Inter-Agency Sedimentation Conference, Washington DC., Jan.1948, p.139-140.

- Cordi, E. and V. van Ophem (1994) Comportement des boues liquides sur fond légèrement incliné.  
Appendix, M.Sc. thesis, Delft University of technology, The Netherlands.
- Courant, R., K.O. Friedrichs and H. Lewy (1928) Über die partiellen Differenzgleichungen der mathematischen Physik.  
Math. Ann., Vol.100, p.32-74.
- Courant, R., Isaacson, E. and M. Rees (1952) On the solution of nonlinear hyperbolic differential equations by finite differences.  
Comm. on Pure and Applied Mathematics, Vol. 5, No.3, p.243-255.
- Courant, R. and Hilbert, D. (1962) *Methods of mathematical physics, Vol. II: Partial differential equations*.  
Interscience publishers, New York, 830 pp.
- Daubert, A., Graffe, O. (1967) Quelques aspects des écoulements presque horizontaux a deux dimensions en plan et non permanents application aux estuaires.  
La Houille Blanche No.8, p.847-860 (in French).
- DeVantier, B.A. and Larock, B.E. (1987) Modelling sediment induced density currents in sedimentation basins.  
J. Hydr. Engrg., ASCE, Vol.112, No.1, p.80-96.
- Di Silvio, G. (1990) Modeling desiltation of reservoirs by bottom-outlet flushing.  
In: H.W. Shen (ed.) *Movable bed physical models*. Kluwer Academic Publishers, Netherlands, p.159-171.
- Duquenois, H. (1956) New methods of sediment control in reservoirs.  
Water Power, May, p.174-180.
- Edwards, D.A. (1993) Turbidity currents: dynamics, deposits and reversals.  
Lecture Notes in Earth Sciences, Vol.44, Springer Verlag, Berlin, 173 pp.
- Eidsvik, K.J. and B. Brørs (1989) Self-accelerated turbidity current prediction based upon ( $k-\epsilon$ ) turbulence.  
Continental Shelf Research, Vol. 9, No.7, p.617-627.
- Ellison, T.H. and Turner, J.S. (1959) Turbulent entrainment in stratified flows.  
J. Fluid Mech., Vol.6, Part 3, p.423-448.
- Fan, J. (1985) Methods of preserving reservoir capacity.  
In: Bruk, S. (ed.) *Methods of computing sedimentation in lakes and reservoirs*. Unesco, Paris, p.65-164.
- Fan, J. (1986) Turbid density currents in reservoirs.  
Water International, IWRA, Vol.11, No.3, p.107-116.
- Fan, J. (1991) Density currents in reservoirs.  
Workshop on Management of Reservoir Sedimentation, New Delhi, June 1991, p.3.1.1-3.1.13.
- Fan, J. and G.L. Morris (1992a) Reservoir sedimentation. I: Delta and density current deposits.  
J. Hydr. Engrg., Vol.118, No.3, p.354-369.
- Fan, J. and G.L. Morris (1992b) Reservoir sedimentation. II: Reservoir desiltation and long-term storage capacity.  
J. Hydr. Engrg., Vol.118, No.3, p.370-384.
- Fennema, R.J. and M.H. Chaudry (1986) Explicit numerical schemes for unsteady free-surface flows with shocks.  
Water Resources Res., Vol.22, No.13, p.1923-1930.

- Fennema, R.J. and M.H. Chaudry (1990) Explicit methods for 2-D transient free-surface flows.  
*J. Hydr. Engrg.*, ASCE, Vol. 116, No.8, p.1013-1034.
- Finlayson, B.A. (1992) *Numerical methods for problems with moving fronts*.  
 Ravenna Park Publ., Seattle, USA, 605 pp.
- Gabutti, B. (1983) On the two upwind finite-difference schemes for hyperbolic equations in non-conservative form.  
*Comput. Fluids*, Vol.11, No.3, p.207-230.
- Galappatti, R. (1983) A depth-integrated model for suspended sediment transport.  
*Comm. on Hydr.*, Report No. 83-7, Delft Univ. of Techn., 114 pp.
- Galappatti, R. and Vreugdenhil, C.B. (1985) A depth-integrated model for suspended sediment transport.  
*J. Hydr. Res.*, IAHR, Vol.23, No.4, p.359-377.
- Garcia, M.H. (1990) Depositing and eroding sediment-driven flows: Turbidity currents.  
 Ph.D. thesis, Project Report No. 306, University of Minnesota, St. Anthony Falls Hydr. lab., Minneapolis, 179 pp.
- Garcia, M.H. (1993) Hydraulic jumps in sediment-driven bottom currents.  
*J. Hydr. Engrg.*, ASCE, Vol.119, No.10, p.1094-1117.
- Garcia, M.H. (1994) Depositional turbidity currents laden with poorly sorted sediment.  
*J. Hydr. Engrg.*, ASCE, Vol.120, No.11, p.1240-1263
- Garcia, M., Yu, W., Parker, G. (1986) Experimental Study of Turbidity Currents.  
 In: Stefan, H.G. et al. (ed.) *Advancements in Aerodynamics, Fluid Mechanics, and Hydraulics*. Proc. Conf. ASCE, Minneap., Minnesota, p.120-127.
- Garcia, M.H. and G. Parker (1993) Experiments on the entrainment of sediment into suspension by a dense bottom current.  
*J. Geophysical Res.*, Vol.98, No.C3, p.4793-4807.
- García-Navarro, P., F. Alcrudo, and J.M. Savorín (1992) 1-D open-channel flow simulation using TVD-McCormack scheme.  
*J. Hydr. Engrg.*, ASCE, Vol. 118, No.10, p.1359-1372.
- Garvine, R.W. (1984) Radial spreading of buoyant, surface plumes in coastal waters.  
*J. Geophysical Res.*, Vol.89, No.C2, p.1989-1996.
- Glaister, P. (1988) Approximate Riemann solutions of the shallow water equations.  
*J. Hydr. Res.*, IAHR, Vol. 26, no.3, p.293-306.
- Glaister, P. (1990) Approximate Riemann solutions of the two-dimensional shallow-water equations.  
*J. Engineering Mathematics*, Vol.24, p.45-53.
- Godunov, S.K. (1959) A finite-difference scheme for the numerical computation of discontinuous solutions of the equations of fluid dynamics.  
*Mathematicheskii Sbornik*, Vol.47, No.3, p.271-290 (in Russian).
- Goodman, J.B. and R.J. LeVeque (1985) On the accuracy of stable schemes for 2D scalar conservation laws.  
*Mathematics of Computation*, Vol.45, No.171, p.15-21
- Gould, H.R. (1960) Turbidity currents.  
 USGS Prof. Pap. 295, U.S. Geological Survey, Washington D.C, p.201-207
- Graf, W.H. (1983a) The hydraulics of reservoir sedimentation.  
*Int. Water Power and Dam Construction*. Vol 35, no.4, p.45-52, april. (Also Communication no.51 du Laboratoire Hydraulique EPFL, Lausanne).

- Graf, W.H. (1984) Storage losses in reservoirs.  
Int. Water Power and Dam Construction. Vol 36, no.4, p.37-40, april. (Also Communication no.51 du Laboratoire Hydraulique EPFL, Lausanne).
- Gratton, J. and C. Vigo (1994) Self-similar gravity currents with variable inflow revisited: plane currents.  
J. Fluid Mech., Vol.258, p.77-104.
- Grundy, R.E. and J.W. Rottman (1985) The approach of self-similarity of the solutions of the shallow-water equations representing gravity-current releases.  
J. Fluid Mech., Vol. 156, p.39-53.
- Grundy, R.E. and J.W. Rottman (1986) Self-similar solutions of the shallow-water equations representing gravity currents with variable inflow.  
J. Fluid Mech., Vol. 169, p.337-351.
- Gustafsson, B. (1975) The convergence rate for difference approximations to mixed initial boundary value problems.  
Mathematics of Computation, Vol.29, p.396-406.
- Hauenstein, W. and Th. Dracos (1984) Investigation of plunging density currents generated by inflows in lakes.  
J. Hydr. Res., IAHR, Vol.22, no.3, p.157-179.
- Harten, A. (1983) High resolution schemes for hyperbolic conservation laws.  
J. Computational Physics, Vol.49, No.3, p.357-393.
- Harten, A. (1984) On a class of high resolution total-variation-stable finite-difference schemes.  
SIAM J. Numerical Analysis, Vol. 21, No.1, p.1-23.
- Harten, A. and J.M. Hyman (1983) Self-adjusting grid methods for one-dimensional hyperbolic conservation laws.  
Journal Computational Physics, Vol.50, p.235-269.
- Harten, A., Lax, P.D., and B. Van Leer (1983) On upstream differencing and Godunov-type schemes for hyperbolic conservation laws.  
SIAM Review, Vol.25, No.1, p.35-61.
- Harten, A. and S. Osher (1987) Uniformly high-order accurate nonoscillatory schemes, I.  
SIAM J. Numerical Analysis, Vol.24, No.2, p.279-309
- Hay, A.E. (1987) Turbidity currents and submarine channel formation in Rupert inlet, British Columbia; 2. The roles of continuous and surge-type flow.  
J. Geophys. Res., Vol.92, No. C3, p.2883-2900.
- Hay, A.E, R.W. Burling and J.W. Murray (1982) Remote acoustic detection of a turbidity current surge.  
Science, 217, p.833-835.
- Heezen, B.C. and M. Ewing (1952) Turbidity currents and submarine slumps and the 1929 Grand Banks earthquake.  
Am. J. Sci., 250, p.849-873.
- Hinze, J.O. (1960) On the hydrodynamics of turbidity currents.  
Geologie en Mijnbouw, 39e jaargang, p.18-25.
- Hirsch, C. (1988) *Numerical computation of internal and external flows*; Vol.1, Fundamentals of numerical discretization.  
Wiley Series in Numerical Methods in Engrg., J. Wiley & Sons, England, 515 pp.

- Hirsch, C. (1990) *Numerical computation of internal and external flows: Volume 2: Computational methods for inviscid and viscous flow.*  
Wiley Series in Numerical Methods in Engrg., J. Wiley & Sons, England, 691 pp.
- Hotchkiss, R.H. and G. Parker (1991) Shock-fitting of aggradational profiles due to backwater.  
J. Hydr. Engrg., ASCE, Vol. 117, No.9, p.1129-1144.
- Huppert, H.E. and J.E. Simpson (1980) The slumping of gravity currents.  
J. Fluid Mech., Vol.99, p.785-799.
- Hürzeler, B.E., J. Imberger, and G.N. Ivey (1996) Dynamics of turbidity current with reversing buoyancy.  
J. Hydr. Engrg., ASCE, Vol. 122, No.5, p.230-236.
- Inman, D.L., C.E. Nordstrom and R.E. Flick (1976) Currents in submarine canyons: an air-sea-land interaction.  
Ann. Rev. Fluid Mech., 8, p.275-310.
- Jameson, A., W. Schmidt, and E. Turkel (1981) Numerical solutions of the Euler equations by finite volume methods using Runge Kutta time-stepping schemes.  
AIAA Paper 81-1259, Proc. AIAA 14th Fluid and Plasma Dynamics Conf., Palo Alto, Calif. USA.
- Jiménez, O.F. and M.H. Chaudry (1988) Computation of supercritical free-surface flows.  
J. Hydr. Engrg., ASCE, Vol. 114, No.4, p.377-395.
- Johnson, T.R., C.R. Ellis, G.J. Farrell, and H.G. Stefan (1987) Negatively buoyant flow in a diverging channel. II: 3-D flow field descriptions.  
J. Hydr. Engrg., ASCE, Vol.113, no.6, p.731-742.
- Katopodes, N. and T. Strelkoff (1978) Computing two-dimensional dam-break flood waves.  
J. Hydr. Div., ASCE, Vol.104, No. HY9, p.1269-1288.
- Keunen, Ph. H. (1951) Properties of turbidity currents of high density.  
In: Turbidity currents and the transportation of coarse sediments to deep water.  
Special Publ. Soc. Economic Paleont. and Mineral., No. 2, p.14-33.
- Keunen, Ph. H. (1952) Estimated size of the Grand Banks turbidity current.  
American J. of Science, No.250, p.874-884.
- Klemp, J.B., R. Rotunno and W.C. Skamarock (1994) On the dynamics of gravity currents in a channel.  
J. Fluid Mech., Vol. 269, p.169-198.
- Knapp, R.T. (1938) Energy balance in streams carrying suspended load.  
Trans. Am. Geophys. Union, Vol.19, p.501-505.
- Kranenburg, C. (1978) Internal fronts in two-layer flow.  
J. Hydr. Div., ASCE, Vol.104, No.HY10, p.1449-1453.
- Kranenburg, C. (1993a) Gravity-current fronts advancing into horizontal ambient flow.  
J. Hydr. Engrg, ASCE, Vol.119, No.3, p.369-379.
- Kranenburg, C. (1993b) Unsteady gravity currents advancing along a horizontal surface.  
J. Hydr. Res., IAHR, Vol.31, No.1, p.49-60.
- Lambert, A.M. and F. Giovanoli (1988) Records of riverborne turbidity currents and indications of slope failures in the Rhone delta of Lake Geneva.  
Limnol. Oceanogr., 33, p.458-468.
- Launder, B.E. and D.B. Spalding (1972) *Mathematical models of turbulence.*  
Academic, Orlando, Florida, 169 pp.



- Lax, P.D. (1954) Weak solutions of non-linear hyperbolic equations and their numerical computation.  
Comm. Pure and Applied Mathematics, Vol.7, No.1, p.159-193.
- Lax, P.D. (1957) Hyperbolic systems of conservation laws II.  
Comm. Pure and Applied Mathematics, Vol.10, p.537-566.
- Lax, P.D. and B. Wendroff (1960) Systems of conservation laws.  
Comm. Pure and Applied Mathematics, Vol.13, No.2, p.217-237.
- Lax, P.D. and B. Wendroff (1964) Difference schemes for hyperbolic equations with high order of accuracy.  
Comm. Pure and Applied Mathematics, Vol.17, No.3, p.381-398.
- Leer, B. van (1973) Towards the ultimate conservative difference scheme, I. The quest of monotonicity.  
Lecture Notes in Physics, Vol.18, p.163-168, Springer Verlag, Berlin, Germany.
- Leer, B. van (1974) Towards the ultimate conservative difference scheme. II. Monotonicity and conservation combined in a second-order scheme.  
J. Computational Physics, Vol.14, No.4, p.361-370.
- Leer, B. van (1979) Towards the ultimate conservative difference scheme. V. A second-order sequel to Godunov's method.  
J. Computational Physics, Vol.32, No.1, p.101-136.
- Leer, B. van (1982) Flux vector splitting for the euler equations.  
Proc. 8th Int. Conf. on Numerical Methods in Fluid Dynamics 1982. In Krause, E. (ed.) Lecture Notes in Physics, Vol.170, Springer Verlag, p.507-512.
- Leer, B. van, J.L. Thomas, P.L. Roe, and R.W. Newsome (1987) A comparison of numerical flux formulas for the Euler and Navier Stokes equations.  
AIAA Paper 87-1104, AIAA 8th Computational Fluid Dynamics Conference, Honolulu, Hawaii, p.36-41.
- Lerat, A. (1983) Implicit methods of second-order accuracy for the Euler equations.  
AIAA Paper 83-1925, Proc. AIAA 6th Computational Fluid Dynamics Conference, Danvers, Mass., p.274-282.
- Lerat, A. and R. Peyret (1974) Noncentred schemes and shock propagation problems.  
Computers and Fluids, Vol.2, No.1, p.35-52.
- Lerat, A. and R. Peyret (1975) The problem of spurious oscillations in the numerical solution of the equations of gas dynamics.  
In: Richtmyer, R.D. (ed.) Proc. Int. Conf. on Numerical Methods in Fluid Dynamics, Univ. of Colorado, Lecture Notes in Physics, Vol. 35, Springer Verlag, p.250-255.
- LeVeque, R.J. (1990) *Numerical methods for conservation laws*.  
Lectures in Mathematics, ETH Zürich, Birkhäuser Verlag, Basel, 214 pp.
- Lüthi, S. (1981) Experiments on non-channelized turbidity currents and their deposits.  
Marine Geology, Vol.40, Letter section, p.M59-M68.
- MacCormack, R.W. (1969) The effect of viscosity in hypervelocity impact cratering.  
AIAA Paper 69-354, 7th Aerospace Sciences Meeting, Cincinnati, Ohio.
- MacCormack, R.W. (1981) A numerical method for solving the equations of compressible viscous flow.  
AIAA Paper 81-0110, AIAA 19th Aerospace Science meeting, St. Louis, Missouri.

- MacCormack, R.W. (1982) Numerical solution of the equations of compressible viscous flow.  
In: Meyer, R.E. (ed.) *Transonic, Shock, and Multidimensional flows: Advances in scientific computing*, Academic Press, p.161-179.
- MacCormack, R.W. and A.J. Paullay (1972) Computational efficiency achieved by time splitting of finite difference operators.  
AIAA Paper 72-154.
- MacCormack, R.W. and B.S. Baldwin (1975) A numerical method for solving the Navier Stokes equations with application to shock-boundary layer interactions.  
AIAA Paper 75-1, AIAA 13 th Aerospace Sci. Meeting, Pasadena, Calif, USA.
- Mahmood, K. (1987) Reservoir sedimentation: Impact, extent, and mitigation.  
Techn. Paper No.71, The World Bank, Washington D.C., USA.
- Maxworthy, T. (1983) Gravity currents with variable inflow.  
J. Fluid Mech., Vol.128, p.247-257.
- McClimans, T.A. (1978) Fronts in fjords.  
Geophys. Astrophys. Fluid Dynamics, Vol. 11, Gordon & Breach Science publ., p.23-34.
- Meyer-Peter, E. and R. Müller (1948) Formulas for bed-load transport.  
Proc. IAHR, Stockholm, Vol.2, Paper 2, p.39-64.
- Middleton, G.V. and W.J. Neal (1989) Experiments on the thickness of beds deposited by turbidity currents.  
J. Sedimentary Petrology, Vol.59, No.2, p.297-307.
- Miles, J. (1990) Richardson's number revisited. In: List, E.J. & G.H. Jirka (eds.) Proc. Int. Symp., *Stratified flows*, ASCE, Pasadena, Calif., USA, p.1-7.
- Moretti, G. (1975) On the matter of shock fitting.  
In: Richtmyer, R.D. (ed.) Proc. 4th Int. Conf. on Numerical Methods in Fluid Dynamics, Univ. of Colorado, Lecture Notes on Physics, Vol.35, Springer Verlag, p.287-292.
- Moretti, G. (1979) The  $\lambda$ -scheme.  
Computers and Fluids, Vol.7, No.3, p.191-205.
- Moretti, G. (1987) A technique for integrating two-dimensional Euler equations.  
Computers and Fluids, Vol.15, No.1, p.59-75
- Nizery, A. and J. Bonnin (1953) Observations sytematiques de courants de densité dans une retenue hydroelectrique.  
Proc. Minnesota Intern. Hydraulics Convention, Sept.1-4, 1953, Minneapolis, Minnesota, p.369-386.
- Noh, Y. and H.J.S. Fernando (1992) The motion of a buoyant cloud along an incline in the presence of boundary mixing.  
J. Fluid Mech., Vol.235, p.557-577.
- Normark, W.R. and F.H. Dickenson (1976) Man-made turbidity currents in Lake Superior.  
Sedimentology, Vol.23, p.815-831.
- Olesen, K.W. (1987) Bed topgraphy in shallow river bends.  
Communications on Hydr. and Geotechn..Engrg., Report No.87-1, Delft Univ. of Techn., Delft, 265 pp (doctoral thesis).
- Osborne, J. (ed.) (1995) Int. Water Power & Dam Construction Handbook 1995.  
Reed Business Publishing.

- Osher, S. (1981) Numerical solution of singular perturbation problems and hyperbolic systems of conservation laws.  
In: O. Axelsson et al (eds.) Proc. Conf. on analytical and numerical approaches to asymptotic problems, Nijmegen, June 1980; North-Holland Mathematics studies, No.47, Amsterdam, The Netherlands.
- Pallesen, T.R. (1983) Turbidity currents.  
Inst. Hydrodyn. Hydraul. Engrg., Techn. Univ. Denmark, Series Paper No. 32, 115 pp.
- Pantin, H.M. (1979) Interaction between velocity and effective density in turbidity flow: phase-plane analysis, with criteria for autosuspension.  
Marine Geology, Vol.31, p.59-99.
- Paolo, C., G. Parker, R. Seal, S.K. Sinha, J.B. Southard and P.R. Wilcock (1992) Downstream fining by selective deposition in a laboratory flume.  
Science, Vol. 258, p.1757-1760.
- Parker, G., Y. Fukushima and H.M. Pantin (1986) Self-accelerating turbidity currents.  
J. Fluid Mech., Vol. 171, p.145-181.
- Parker, G., Garcia, M., Fukushima, Y. and Yu, W. (1987) Experiments on turbidity currents over an erodible bed.  
J. Hydr. Res., IAHR, Vol.25, No.1, p.123-147.
- Pazwash, H. (1982) Sedimentation in reservoirs case of Sefidrud dam.  
Proc. 3rd Congress of the APD, IAHR, Bandung, Indonesia, Vol.C, Paper Cc7., p.215-223.
- Piat, J.F. and E.J. Hopfinger (1981) A boundary layer topped by a density interface.  
J. Fluid Mech., Vol.113, p.411-432.
- Plapp, J.E. and J.P. Mitchell (1960) A hydrodynamic theory of turbidity currents.  
J. Geophys. Res., Vol.65, No.3, p.983-992.
- Preissmann, A. (1961) Propagation des intumescences dans les canaux et rivières.  
Proc. 1st Congress of the French Association for Computation, AFCAL, Grenoble, France, p.433-442 (in French).
- Prior, D.B., B.D. Bornhold, W.J. Wiseman and D.R. Lowe (1987) Turbidity current activity in a British Columbia Fjord.  
Science, Vol.237, p.1330-1333.
- Richardson Y.F. and W.N Zaki (1954) Sedimentation and fluidization, Part 1.  
Trans. Inst. Chem. Engrs., Vol.32, p.35-53.
- Richtmyer, R.D. and K.W. Morton (1967) *Difference methods for initial value problems*.  
J. Wiley and Sons, New York.
- Rijn, L.C. van (1984a) Sediment transport, Part I: Bed-load transport.  
J. Hydr. Engrg., ASCE, Vol.110, No.10, p.1431-1456.
- Rijn, L.C. van (1984b) Sediment transport, Part II: Suspended-load transport.  
J. Hydr. Engrg., ASCE, Vol.110, No.11, p.1613-1641.
- Rijn, L.C. van (1984c) Sediment transport, Part III: Bed forms and alluvial roughness.  
J. Hydr. Engrg., ASCE, Vol.110, No.12, p.1733-1754
- Rijn, L.C. (1987) Mathematical modelling of morphological processes in the case of suspended sediment transport.  
Doctoral thesis, Delft University of Technology, 208pp.

- Roe, P.L. (1981a) The use of the Riemann problem in finite difference schemes.  
In: Reynolds, W.C. et al. (eds.) Proc. 7th Int. Conf. on Numerical Methods in Fluid Dynamics 1980. Lecture Notes in Physics, Vol. 141, Springer Verlag, Berlin, p.354-359.
- Roe, P.L. (1981b) Approximate Riemann solvers, parameter vectors, and difference schemes.  
J. Computational physics, Vol.43, No.2, p.357-372.
- Roe, P.L. (1985) Some contributions to the modelling of discontinuous flows.  
In: Engquist, B.E. et al. (eds.) Proc. AMS-SIAM Summer Seminar 1983: Large-Scale Computations in Fluid Mechanics. Lectures in Applied Mathematics, Vol.22, Part 2, AMS, Providence, Rhode Island, p.163-193.
- Rottman, J.W. and J.E. Simpson (1983) Gravity currents produced by instantaneous releases of a heavy fluid in a rectangular channel.  
J. Fluid Mech., Vol 135, p.95-110.
- Rottman, J.E. and J.E. Simpson (1984) The initial development of gravity currents from fixed-volume releases of heavy fluid.  
Ooms, G. & H. Tennekes (eds.) Atmospheric dispersion of heavy gases and small particles. Proc. IUTAM Symposium in Delft, The Netherlands, 1983, Springer Verlag, Berlin, p.347-359.
- Scheuerlein, H. (1987) Sedimentation of reservoirs - methods of prevention, techniques of rehabilitation.  
First Iranian Symp. on Dam Engrg., Teheran, Iran, June '87.
- Schijf, J.B. and J.C. Schönfeld (1953) Theoretical consideration on the motion of salt and fresh water.  
Proc. Minnesota Int. Hydraulics Conv., IAHR/ASCE, Minnesota, USA, p.321-333.
- Schoklitsch, A. (1935) *Stauraumverlandung und Kolkabwehr*.  
Springer Verlag, Wien, 178 pp.
- Sedov, L.I. (1993) *Similarity and dimensional methods in mechanics*.  
10th Edition. CRC Press, Boca Raton, Florida, USA, 479 pp.
- Shepard, F.P., P.A. McLoughlin, N.F. Marshall and G.G. Sullivan (1977) Current-meter recordings of low-speed turbidity currents.  
Geology, Vol.5, p.297-301.
- Sieben, A. (1994) Notes on the mathematical modelling of alluvial mountain rivers.  
Comm. on hydr. and geotechn. engrg., Report No. 94-3, Delft Univ. of Techn., The Netherlands, 134 pp.
- Sieben, A. and C.J. Sloff (1994) Analysis of a 2-DH mathematical model for mountain rivers with graded sediment.  
Proc. International Workshop on Floods and Inundations related to Large Earth Movements, Trento, Italy, p.A3.1-A3.12.
- Simpson, J.E. (1987) *Gravity currents: In the environment and the laboratory*.  
Ellis Horwood, 244 pp.
- Simpson, J.E. and R.E. Britter (1979) The dynamics of the head of a gravity current advancing over a horizontal surface.  
J. Fluid Mech., Vol.94, Part 3, p.477-496.

- Sloff, C.J. (1991) Reservoir sedimentation: a literature survey.  
Comm. on hydr. and geotechn. engrg., Report No.91-2, Delft Univ. of Technology, The Netherlands, 126 pp.
- Sloff, C.J. (1992) The method of characteristics applied to analyse 2DH hydraulic models.  
Comm. on hydr. and geotechn. engrg., Report No.92-4, Delft Univ. of Technology, The Netherlands, 62 pp.
- Sloff, C.J. (1993a) Analysis of basic equations for sediment-laden flows.  
Comm. on hydr. and geotechn. engrg., Report No.93-8, Delft Univ. of Technology, The Netherlands, 54 pp.
- Sloff, C.J. (1993b) Study on modelling the morphology of torrents on volcano slopes.  
J. Hydr. Research, IAHR, Vol.31, No.3, p.333-345.
- Sloff, C.J. (1994a) Modelling turbidity currents in reservoirs.  
Comm. on hydr. and geotechn. engrg., Report No.94-5, Delft Univ. of Technology, The Netherlands, 142 pp.
- Sloff, C.J. (1994b) Application of the method of characteristics to a 2-DH 2-layer model for sedimentation in reservoirs.  
In: M. B elorgy et al. (eds.) Sediment transport mechanisms in coastal environments and rivers. Proc. Euromech 310 conf. 1993, World Scientific Publ., Singapore, p.152-166.
- Smith, W.U., C.P. Vetter and C.B. Cumming (1964) Comprehensive survey of sedimentation in Lake Mead, 1948-1949.  
USGS Prof. Pap. 295, U.S. Geological Survey, Washington D.C.
- Stacey, M.W. and A.J. Bowen (1988a) The vertical structure of density and turbidity currents: Theory and observations.  
J. Geophysical Res., Vol.93, No.C4, p.3528-3542.
- Stacey, M.W. and A.J. Bowen (1988b) The vertical structure of turbidity currents and a necessary condition for self maintenance.  
J. Geophysical Res., Vol.93, No.C4, p.3543-3553.
- Steger, J.L. and R.F. Warming (1981) Flux vector splitting of the inviscid gas dynamic equations with application to finite-difference methods.  
J. Computational Physics, Vol.40, No.2, p.263-293.
- Stoker, J.J. (1957) *Water waves. The mathematical theory with applications.*  
Pure and Applied Math., Vol.IV, Interscience publ., New York, 567 pp.
- Strang, G. (1968) On the construction and comparison of difference schemes.  
SIAM Journal of Numerical Analysis, Vol.5, p.506-517.
- Sweby, P.K. (1984) High resolution schemes using flux limiters for hyperbolic conservation laws.  
SIAM J. Numerical Analysis, Vol.21, No.5, p.995-1011.
- Sweby, P.K. (1985) High-resolution TVD schemes using flux limiters.  
In: Engquist, B.E. et al. (eds.) Proc. AMS-SIAM Summer Seminar 1983: Large-Scale Computations in Fluid Mechanics. Lectures in Applied Mathematics, Vol.22, Part 2, AMS, Providence, Rhode Island, p.289-309.
- Tan Weiyang (1992) *Shallow water hydrodynamics: mathematical theory and numerical solution for a two-dimensional system of shallow water equations.*  
Elsevier Oceanography Series, 55, Elsevier Science Publishers, The Netherlands, 434 pp.

- Thorpe, S.A. (1971) Experiments on the stability of stratified shear flows: miscible fluids.  
*J. Fluid Mech.*, Vol.46, p.299-319.
- Tolouie, E., J.R. West and J. Billam (1993) Sedimentation and desiltation in the Sefid-Rud reservoir, Iran.  
 In: J. McManus & R.W. Duck (eds.) *Geomorphology and sedimentology of lakes and reservoirs*. J. Wiley & Sons, England, Chapt.9, p.125-138.
- Valiani, A. (1993) Numerical approach to hydraulic jump in non-prismatic channels.  
 In: Bélorgey, M. et al. (eds.) *EUROMECH 310; Sediment transport mechanisms in coastal environments and rivers*. World Scientific, Singapore, p.182-197.
- Vanoni, V.A. (1977) *Sedimentation engineering*.  
 ASCE, New York, p.587-604 and p.616-618.
- Veltrop, J.A. (1991) Water, dams and hydropower in the coming decades.  
*Int. Water Power & Dam Construction*, June 1991, p.37-44.
- Von Neumann, J. and R.D. Richtmeyer (1950) A method for the numerical calculations of hydrodynamical shocks.  
*J. Mathematical Physics*, Vol.21.
- Vreugdenhil, C.B. (1979) Two-layer shallow-water flow in two-dimensions, a numerical study.  
*J. Computational Physics*, Vol.33, p.169-184.
- Vreugdenhil, C.B. (1989) *Computational hydraulics: an introduction*.  
 Springer Verlag, Berlin, Germany, 182 pp.
- Vreugdenhil, C.B. (1994) *Numerical methods for shallow-water flow*.  
 Water Science and Technology Library, Vol.13, Kluwer Academic Publishers, Dordrecht, The Netherlands, 261 pp.
- Vriend, H.J. de (1985) Flow formulation in mathematical models of 2DH morphological changes.  
 Delft Hydraulics Lab., TOW-report R1747-5, 64 pp.
- Vriend, H.J. de (1987a) Analysis of 2DH morphological evolutions in shallow water.  
*J. Geoph. Res.*, No.92, p.3877-3893.
- Vriend, H.J. de (1987b) 2DH mathematical modelling of morphological evolutions in shallow water.  
*Coastal Engineering*, Vol.11, p.1-27
- Vries, M. de (1959) Transients in bed-load transport (basic considerations).  
 Delft Hydraulics, Report R3, Delft.
- Vries, M. de (1965) Considerations about non-steady bed-load transport in open channels.  
*Proc. IAHR, Leningrad*, Sept. 1965, p. 3.8.1 - 3.8.8.
- Vries, M. de (1993) *Use of models for river problems*.  
 Studies and reports in hydrology 51, Unesco Publishing, Paris, 85 pp.
- Wang, Z.B. (1989) Mathematical modelling of morphological processes in estuaries.  
 Communications on Hydr. and Geotechn. Engrg., Report No.89-1, Delft Univ. of Techn., Delft, 208 pp (doctoral thesis).
- Wang, Z.B. (1992) Theoretical analysis on depth-integrated modelling of suspended-sediment transport.  
*J. Hydr. Res., IAHR*, Vol.30, No.3, p.403-421.

- Wang, Z.B. and J.S. Ribberink (1986) The validity of a depth-integrated model for suspended-sediment transport.  
 J. Hydr. Res., IAHR, Vol. 24, No.1, p.53-67.
- Weirich, F.H. (1984) Turbidity currents: monitoring their occurrence and movement with a three-dimensional sensor network.  
 Science, Vol.224, p,384-387.
- Wood, I.R. and J.E. Simpson (1984) Jumps in layered miscible fluids.  
 J. Fluid Mech., Vol.140, p.329-342.
- Yang, J.Y., Hsu, C.A. and S.H. Chang (1993a) Computations of free surface flows, Part 1: One-dimensional dam-break flow.  
 J. Hydr. Res., IAHR, Vol. 31, No.1, p.19-34.
- Yang, J.Y., C.A. Hsu (1993b) Computations of free surface flows, Part 2: Two-dimensional bore diffraction.  
 J. Hydr. Res., IAHR, Vol. 31, No.3, p.403-413.
- Yee, H.C. (1987) Construction of explicit and implicit symmetric TVD schemes and their applications.  
 J. Computational Physics, Vol.68, No.1, p.151-179.
- Yee, H.C., R.F. Warming, and A. Harten (1985) Application of TVD schemes for the euler equations of gas dynamics.  
 In: Engquist, B.E. et al. (eds.) Proc. AMS-SIAM Summer Seminar 1983: Large-Scale Computations in Fluid Mechanics. Lectures in Applied Mathematics, Vol.22, Part 2, AMS, Providence, Rhode Island, p.357-377.
- Zel'dovich, Ya. B. and Yu. P. Razier (1966) *Physics of shock waves and high-temperature hydrodynamic phenomena*, Vol.I.  
 Academic Press, New York, USA, 464 pp.
- Zel'dovich, Ya. B. and Yu. P. Razier (1967) *Physics of shock waves and high-temperature hydrodynamic phenomena*, Vol.II.  
 Academic Press, New York, USA, 916 pp.
- Zhang, R. and Qian, N. (1985) Lecture notes on the training course on reservoir sedimentation.  
 IRTCES (Int. Research and Training Centre on Erosion and Sedimentation), Sed. Research Lab. of Tsinghua Univ., Beijing, China, sponsored by UNESCO and PRC.





## Main Symbols

$a$	total water depth = $a_1 + a_2$	[L]
$\tilde{a}_f$	dimensionless depth of density-current front	[-]
$a_g$	depth of a gate	[L]
$a_i$	depth of the interfacial layer	[L]
$\tilde{a}_0$	equilibrium concentration-profile function = $c_e(\eta)/C_{se}$	[-]
$\tilde{a}_k$	dimensionless shape functions for Galappatti's approach ( $k=1,2$ )	[-]
$\tilde{a}_1, \tilde{a}_2$	dimensionless upper- and lower-layer depth	[-]
$a_1, a_2$	depth of upper layer and lower layer respectively	[L]
$a_{1l}, \tilde{a}_{1l}$	depth and dimensionless depth of upper layer left of an internal jump	[L, -]
$a_{1r}, a_{2r}$	depth of upper layer and lower layer right of an internal jump	[L]
$a_{2l}$	depth of lower layer left of an internal jump	[L]
$\tilde{a}_{20}$	relative depth of dense fluid before removal of the gate	[-]
$A$	cross-sectionally area	[L <sup>2</sup> ]
$B$	channel width	[L]
$B_2$	width of underflow layer	[L]
$B_g$	width of a gate	[L]
$c_s$	local volumetric suspended-sediment concentration	[-]
$C$	Chézy roughness coefficient	[L <sup>1/2</sup> /T]
$\tilde{c}$	dimensionless front celerity	[-]
$c_a$	(near-bed) reference concentration for suspended sediment	[-]
$C_D$	bed friction coefficient	[-]
$C_{Di}$	interfacial friction coefficient	[-]
$c_e$	local equilibrium suspended-sediment concentration	[-]
$c_f$	front celerity	[L/T]
$c_m$	concentration at level of maximum velocity ( $\eta = \eta_m$ )	[-]
$c_N$	front celerity normal to a 2-DH front	[L/T]
$\hat{c}_r$	relative phase error	[-]
$c_s$	local sediment volume concentration	[-]
$C_s$	depth-averaged volumetric suspended-sediment concentration	[-]
$C_{se}$	depth-averaged equilibrium suspended-sediment concentration	[-]
$C_{st}$	depth-averaged suspended-sediment concentration left of a jump	[-]
$C_0$	maximum suspended-sediment concentration	[-]
$\tilde{d}$	amplitude factor	[-]
$D_{50}$	median particle size	[L]
$E_i$	local truncation error	[-]
$e_w$	entrainment parameter = $w_{ie}/u_2$	[-]
$F'$	local baroclinic forces resisting a front	[L <sup>3</sup> /T <sup>2</sup> ]
$f_b$	derivative of bed-load transport (in flow direction) = $ds_b/du_2$	[L]
$fr_0$	linearized friction coefficient	[T <sup>-1</sup> ]
$F_R$	local barotropic forces resisting a front	[L <sup>3</sup> /T <sup>2</sup> ]
$\tilde{F}_R$	dimensionless value of $F_R$	[-]
$Fr_1, Fr_2$	densimetric Froude number upper layer, lower layer	[-]
$g$	gravity-acceleration vector = $(g_x, g_y, g_z)$	[L/T <sup>2</sup> ]
$g_z'$	reduced gravity = $g\sigma' C_s$	[L/T <sup>2</sup> ]

$h_s$	water-surface level = $z_b + a_2 + a_1$	[L]
$i_b$	bed slope	[-]
$k$	Kranenburg's empirical energy loss coefficient	[-]
$k_1, k_1', k_2$	empirical energy-loss coefficients for a 2-DH front	[-]
$L$	wave length	[L]
$L_a'$	dimensionless adaptation length for suspended sediment	[-]
$l_m$	mixing length for momentum (turbulence length scale)	[L]
$m, m'$	coefficients	[-]
$n$	coordinate in normal direction (normal to a front)	[L]
$n_f$	power in damping function $F(Ri)$	[-]
$p'$	bed porosity = $1 - \epsilon_p$	[-]
$\bar{q}$	dimensionless reservoir flow: discharge per unit of width	[-]
$q_x, q_y$	total discharge in $x, y$ -direction per unit of width ( $q_x = q_{1x} + q_{2x}$ )	[L <sup>2</sup> /T]
$\bar{q}_{1l}, \bar{q}_{1r}$	dimensionless upper-layer discharge left and right of jump	[-]
$q_{1x}, q_{1y}$	discharge per unit width in $x, y$ -direction in upper layer	[L <sup>2</sup> /T]
$\bar{q}_{2l}, \bar{q}_{2r}$	dimensionless lower-layer discharge left and right of jump	[-]
$\bar{q}_{2s}$	dimensionless tangential lower-layer discharge	[-]
$q_{2x}, q_{2y}$	discharge per unit width in $x, y$ -direction in lower layer	[L <sup>2</sup> /T]
$Q$	total discharge in flow direction	[L <sup>3</sup> /T]
$Q_g$	discharge through a gate	[L <sup>3</sup> /T]
$Q_{R,i}$	discretized friction term	[L/T <sup>2</sup> ]
$r$	radius	[L]
$R$	amplification factor	[-]
$r_0$	radius of near-field boundary	[L]
$Re_D$	Reynolds number of the underflow	[-]
$Ri$	gradient Richardson number	[-]
$Ri_{0\Delta}$	overall Richardson number based on velocity difference $\Delta u$	[-]
$R_\alpha$	convergence radius	[-]
$s$	coordinate in tangential direction (tangential to a front)	[L]
$s_{biot}$	total bed-load transport = $\sqrt{(s_{bx}^2 + s_{by}^2)}$	{L <sup>2</sup> /T}
$s_{bx}, s_{by}$	bed-load transport in $x, y$ -direction	[L <sup>2</sup> /T]
$s_{sx}, s_{sy}$	suspended-load transport in $x, y$ -direction	[L <sup>2</sup> /T]
$S_{xz}, S_{yz}$	local turbulent shear stresses in $x$ - and $y$ -direction	[M/(LT <sup>2</sup> )]
$t$	time coordinate	[T]
$\bar{t}$	transformed dimensionless time coordinate	[-]
$T$	wave period	[T]
$T_a'$	dimensionless adaptation time for suspended sediment	[-]
$u, v, w$	local fluid velocity in $x, y, z$ -direction	[L/T]
$u_f$	flow velocity behind the front (head velocity)	[L/T]
$u_{nor1}, u_{nor2}$	flow-velocity normal to the boundary upper and lower layer	[L/T]
$u_1, v_1$	depth-averaged flow velocity upper layer in $x$ - and $y$ -direction	[L/T]
$\bar{u}_1$	dimensionless upper-layer flow velocity in $x$ -direction	[-]
$\bar{u}_{1l}, \bar{u}_{1r}$	dimensionless upper-layer velocity left and right of jump	[-]
$u_2, v_2$	depth-averaged flow velocity lower layer in $x$ - and $y$ -direction	[L/T]
$\bar{u}_2$	dimensionless lower-layer flow velocity in $x$ -direction	[-]
$\bar{u}_{2l}, \bar{u}_{2r}$	dimensionless lower-layer velocity left and right of jump	[-]
$u_{2st}$	tangential flow velocity	[L/T]

$u_{2tot}$	total flow velocity = $\sqrt{(u_2^2 + v_2^2)}$	[L/T]
$u_*$	shear velocity in direction of velocity vector	[L/T]
$u_{*x}$	shear velocity in $x$ -direction = $\tau_{bx}/(\tau_b \rho_f)^{1/2}$	[L/T]
$w_{ie}$	fluid entrainment velocity at the density interface	[L/T]
$w_{iem,i}$	discretized entrainment term	[L/T <sup>2</sup> ]
$w_e'$	normalized fluid entrainment coefficient = $w_{ie}/w_s$	[-]
$w_s$	fall velocity of sediment particles (relative to $z$ -axis)	[L/T]
$x, y, z$	spatial coordinates ( $x, y$ = horizontal, $z$ = vertical)	[L]
$\tilde{x}$	transformed dimensionless horizontal $x$ -coordinate	[-]
$Z$	suspension parameter	[-]
$Z'$	corrected suspension parameter = $Z + \varphi$	[-]
$z_a$	reference level for suspended-sediment concentration	[L]
$z_b$	bed level	[L]
$z_i$	interface level	[L]
$\alpha, \alpha_j$	coefficients	[-]
$\alpha$	unit vector = $(\alpha_x, \alpha_y)$	[-]
$\alpha_r$	dimensionless depth downstream of density-current front	[-]
$\beta$	factor in suspension parameter $Z$	[-]
$\delta^v$	discrete artificial viscosity term	[L/T]
$\Delta E_1$	bottom-turbulence generated energy loss	[ML <sup>-1</sup> T <sup>-2</sup> ]
$\Delta E_2$	energy loss associated to flow in a gravity-current head	[ML <sup>-1</sup> T <sup>-2</sup> ]
$\Delta t$	numerical time step	[T]
$\Delta u$	layer velocity difference in $x$ -direction = $u_2 - u_1$	[L/T]
$\Delta x$	numerical space step	[L]
$\varepsilon$	density difference = $\sigma' C_s$ (where $g_c' = g \cdot \varepsilon$ )	[-]
$\varepsilon_i$	gradient parameter in artificial viscosity term	[L/T]
$\varepsilon_p$	porosity of the bed material	[-]
$\varepsilon_{fml}, \varepsilon_{fmi}$	maxima of $\varepsilon_{fx}$ in lower and upper sub-layer respectively	[L <sup>2</sup> /T]
$\varepsilon_{fx}$	fluid-mixing coefficient in $x$ -direction	[L <sup>2</sup> /T]
$\varepsilon_{sx}, \varepsilon_{sy}, \varepsilon_{sz}$	sediment-mixing coefficients in $x, y, z$ -direction	[L <sup>2</sup> /T]
$\varepsilon_{sz}'$	normalized vertical-diffusion coefficient = $\varepsilon_{sz}/(w_s a_s)$	[-]
$\phi$	damping coefficient in suspension parameter $Z$	[-]
$\hat{\phi}$	dimensionless celerity = $\phi/u_2$	[-]
$\phi_j$	characteristic celerity 1-D = $dx/dt$ ( $j=1, 2, \dots$ )	[L/T]
$\Phi^+, \Phi^-$	limiter functions (flux limiters for TVD approach)	[-]
$\gamma_j, \gamma'$	coefficients	[-]
$\gamma_s$	dummy coefficient (equal to zero or unity)	[-]
$\hat{\eta}$	dimensionless elevation = $(z - z_b)/a_2$	[-]
$\hat{\eta}_a$	dimensionless reference level for suspended sediment concentration	[-]
$\hat{\eta}_m$	dimensionless level at which $u(z)$ is maximal	[-]
$\hat{\eta}_{zm}$	dimensionless level at which $Ri(z)$ is maximal	[-]
$\hat{\eta}_0$	dimensionless roughness scale: the elevation at which $u(z)=0$	[-]
$\varphi_0$	constant	[-]
$\varphi'$	factor in the suspension parameter $Z$ equal to $\beta \cdot \phi$	[-]
$\varphi$	overall correction coefficient for suspension parameter $Z$	[-]
$\kappa$	von Karman constant ( $\approx 0.4$ )	[-]
$\lambda_k$	eigenvalue ( $k=1, 2, \dots$ )	[-]

$\lambda_a$	dimensionless depth parameter = $a_1/a_2$	[-]
$\lambda_N$	numerical viscosity parameter	[-]
$\lambda_s$	bottom friction effect	[-]
$\mu_g$	discharge coefficient for a gate	[-]
$\nu$	kinematic viscosity	[L <sup>2</sup> /T]
$\nu_x, \nu_y$	artificial viscosity coefficients	[L <sup>2</sup> /T]
$\theta$	angle	[-]
$\theta_{fi}$	slope parameter (critical value $\theta_{cf}$ )	[-]
$\theta_k$	slope ratios for TVD limiters ( $k=1,2,\dots$ )	[-]
$\theta_x, \theta_y$	average bottom slope in $x$ - and $y$ -direction	[-]
$\rho$	local fluid density	[M/L <sup>3</sup> ]
$\rho_f$	density of water	[M/L <sup>3</sup> ]
$\rho_m$	density of water-sediment mixture	[M/L <sup>3</sup> ]
$\rho_s$	density of sediment particles	[M/L <sup>3</sup> ]
$\rho_2$	density of lower layer = $\rho_f(\sigma' C_s + 1)$	[M/L <sup>3</sup> ]
$\sigma$	Courant number = $\phi_{\max} \Delta t / \Delta x$	[-]
$\sigma'$	relative sediment density = $(\rho_s - \rho_f) / \rho_f$	[-]
$\tau$	normalized time coordinate	[-]
$\tau_b$	bed shear-stress vector = $\sqrt{(\tau_{xb}^2 + \tau_{yb}^2)}$	[M/(LT <sup>2</sup> )]
$\tau_{xb}, \tau_{yb}$	bed shear-stress in $x$ - and $y$ -direction	[M/(LT <sup>2</sup> )]
$\tau_{xi}, \tau_{yi}$	interfacial shear-stress in $x$ - and $y$ -direction	[M/(LT <sup>2</sup> )]
$\omega_k$	Riemann variable or characteristic variable associated to celerity $\phi_k$	[.]
$\Omega$	internal flow variable (velocity difference) = $u_2 - u_1$	[L/T]
$\xi$	normalized horizontal coordinate ( $x$ -direction)	[-]
$\xi_x, \xi_y, \xi_z$	components of vector $\bar{\xi}_k$ normal to corresponding charact. surface	[L, T, T]
$\psi$	dimensionless bed-load transport parameter = $f_b / (a_2 \{p' - \gamma_s C_s\})$	[-]
$\psi_u, \psi_v$	normalized flow-velocity profile in $x, y$ -direction (= $u(\hat{\eta})/u_2$ )	[-]
$\psi_{um}$	normalized main flow-velocity profile in $x$ -direction = $u(\hat{\eta})/u_{\max}$	[-]
$\Psi$	non-linear limiter function	[-]
$\zeta, \zeta'$	similarity parameters for 1-D underflow	[-]
$\zeta_r$	similarity parameter for 2-DH underflow	[-]
$\zeta_r^*$	similarity parameter for 1-D underflow based on layer depth	[-]
$\zeta$	normalized horizontal coordinate ( $y$ -direction)	[-]
$\zeta_m$	dimensionless matching location 1-D self-similar solution	[-]
$\zeta_f$	similarity parameter for front location	[-]
$\zeta_0$	similarity parameter for reverse flow, or for near field boundary	[-]

## Acknowledgements

This study on reservoir sedimentation was carried out by the writer at the faculty of Civil Engineering at the Delft University of Technology. It is Delft Hydraulics and its cooperation with the Delft University of Technology which enabled the initiation and realisation of the project. Both Delft Hydraulics and Delft University are gratefully acknowledged for their contribution and support to the project.

I am especially indebted to Prof. Dr. M. de Vries for guiding the project. I am thankful for his inspiring support and critical reading of the work, as well his stimulation to complete the final concept of this thesis during my employment at Delft Hydraulics.

Dr. Z.B. Wang of Delft Hydraulics is gratefully acknowledged for his useful comments and the critical reading of this thesis. Also the support and discussions of Dr. E. Mosselman, as well as Messrs. J.J. v.d Zwaard, J.R. Moll, N. Struiksma, G.J. Klaassen (all of Delft Hydraulics) and Mr. H.J. Barneveld (HKV) have contributed among others to the outcome of this study. Their contributions and critical comments are greatly appreciated.

An essential element for the completion and verification of the model was a collection of field and laboratory data. I would like to express my appreciation to Prof. M.H. Garcia, Prof. G. Parker, Dr. C. Kranenburg, Dr. K. Chikita, Mr. T. van Kessel, and Dr. H.M. Pantin and other colleagues for providing me with these essential data and other useful information.

Special thanks are also due to Mr. A. Sieben for being a loyal and inspiring room-companion during the final years of this study. Also the other PhD researchers working with Prof. de Vries during my employment at the University, and colleagues from the Hydraulics group are gratefully acknowledged, with emphasis on the pleasant cooperation and interesting conversations.

I am most grateful to Laura for accompanying and supporting me during this study. Her patience and care have shown to be indispensable incentives for attaining the presented results. Finally, for designing and drawing the cover of this thesis I would like to express my gratitude to my sister Renske.



# **Appendices**





## Appendix A

### Conceptual model for front propagation in a 2-DH 2-layer model

We consider the Boussinesq equations for 2-DH baroclinic flow (decoupled internal flow) in  $q, a$  form as presented by Sloff (1994). Similarly to the 1-D decoupled model these equations can be written in a quasi-conservative form :

$$\frac{\partial \mathbf{U}}{\partial t} + \frac{\partial \mathbf{G}}{\partial x} + \frac{\partial \mathbf{H}}{\partial y} = \mathbf{Q}_R \quad (\text{A.1})$$

Now consider a discontinuity in the flow as schematized in figure A.1 (i.e. its projection on the  $x, y$ -plane). The flow and the front motion is from left to right. Coordinate axes  $s$  and  $n$  are the axes transversal and normal to the front in the considered point respectively. The angle between the local  $s$ -axis and the  $x$ -axis is  $\theta$ . Clearly this angle, and hence the direction of the local  $s, n$ -coordinate system varies along the front.

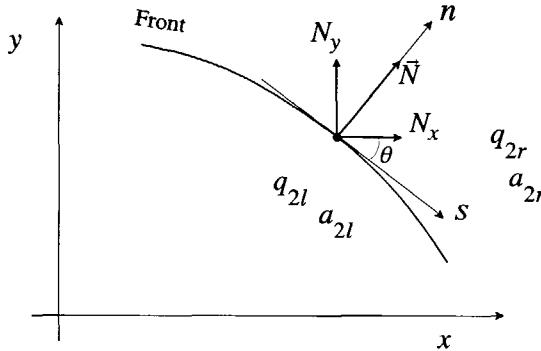


Figure A.1 Discontinuity in a 2-DH model

By analogy with the 1-D case we can derive a shock relation which has to be satisfied at the discontinuity. For the shock in fig.A.1 we obtain (e.g., Tan Weiyan, 1992):

$$N_x(\mathbf{U}_r - \mathbf{U}_l) + N_x(\mathbf{G}_r - \mathbf{G}_l) + N_y(\mathbf{H}_r - \mathbf{H}_l) = -\mathbf{F}' \quad (\text{A.2})$$

where  $N_x, N_x, N_y$  are components of a normal vector  $\vec{N}$  at that point on the discontinuity. We normalize this vector by

$$\vec{N} = (-c_N, v_x, v_y) \quad ; \quad |\mathbf{v}| = 1 \quad (\text{A.3})$$

With this normalized vector equation (A.2) is the Rankine Hugoniot condition for the discontinuity. The right-hand side is a scalar product of vector  $\mathbf{v}$  and vector  $([\mathbf{G}_r - \mathbf{G}_l], [\mathbf{H}_r - \mathbf{H}_l])$  similarly to eq.(6.5) for the 1-D case.

If  $t = \psi(x, y)$  is the equation for the discontinuity surface in the  $t, x, y$ -space then in the physical space  $(x, y)$ -space its normal vector is  $(-1, \partial\psi/\partial x, \partial\psi/\partial y)$  or

$$v_x = c_N \frac{\partial\psi}{\partial x} \quad ; \quad v_y = c_N \frac{\partial\psi}{\partial y} \quad ; \quad c_N = \left[ \sqrt{\left(\frac{\partial\psi}{\partial x}\right)^2 + \left(\frac{\partial\psi}{\partial y}\right)^2} \right]^{-1} \quad (\text{A.4})$$

The Rankine Hugoniot conditions can be reduced to an equivalent 1-D formulation after transformation to  $s, n$  coordinates. We define the following transformation of independent variables:

$$x = n \cdot \cos(\theta) + s \cdot \sin(\theta) \quad ; \quad y = n \cdot \sin(\theta) - s \cdot \cos(\theta) \quad (\text{A.5})$$

$$\frac{\partial}{\partial x} = \cos(\theta) \frac{\partial}{\partial n} + \sin(\theta) \frac{\partial}{\partial s} \quad ; \quad \frac{\partial}{\partial y} = \sin(\theta) \frac{\partial}{\partial n} - \cos(\theta) \frac{\partial}{\partial s} \quad (\text{A.6})$$

$$q_{2x} = q_{2n} \cdot \cos(\theta) + q_{2s} \cdot \sin(\theta) \quad ; \quad q_{2y} = q_{2n} \cdot \sin(\theta) - q_{2s} \cdot \cos(\theta) \quad (\text{A.7})$$

and similarly for  $q_{1x}$ ,  $q_{1y}$ , and forces in the momentum balance. The transformed system of Boussinesq equations for baroclinic flow then becomes

$$\begin{aligned} \frac{\partial q_{2s}}{\partial t} - \left(\frac{a_2}{a_1}\right) \frac{\partial q_{1s}}{\partial t} + \frac{\partial}{\partial s} \left( \frac{q_{2s}^2}{a_2} \right) - \left(\frac{a_2}{a_1}\right) \frac{\partial}{\partial s} \left( \frac{q_{1s}^2}{a_1} \right) + \frac{\partial}{\partial n} \left( \frac{q_{2s} q_{2n}}{a_2} \right) - \left(\frac{a_2}{a_1}\right) \frac{\partial}{\partial n} \left( \frac{q_{1s} q_{1n}}{a_1} \right) + \\ + \frac{1}{2} g_z \sigma' \frac{\partial C_s a_2^2}{\partial s} + g_z a_2 \sigma' C_s \frac{\partial z_b}{\partial s} = \frac{a}{a_1} \frac{\tau_{is}}{\rho_f} - \frac{\tau_{bs}}{\rho_f} + g_s a_2 \sigma' C_s \end{aligned} \quad (\text{A.8})$$

$$\begin{aligned} \frac{\partial q_{2n}}{\partial t} - \left(\frac{a_2}{a_1}\right) \frac{\partial q_{1n}}{\partial t} + \frac{\partial}{\partial s} \left( \frac{q_{2s} q_{2n}}{a_2} \right) - \left(\frac{a_2}{a_1}\right) \frac{\partial}{\partial s} \left( \frac{q_{1s} q_{1n}}{a_1} \right) + \frac{\partial}{\partial n} \left( \frac{q_{2n}^2}{a_2} \right) - \left(\frac{a_2}{a_1}\right) \frac{\partial}{\partial n} \left( \frac{q_{1n}^2}{a_1} \right) + \\ + \frac{1}{2} g_z \sigma' \frac{\partial C_s a_2^2}{\partial n} + g_z a_2 \sigma' C_s \frac{\partial z_b}{\partial n} = \frac{a}{a_1} \frac{\tau_{in}}{\rho_f} - \frac{\tau_{bn}}{\rho_f} + g_n a_2 \sigma' C_s \end{aligned} \quad (\text{A.9})$$

$$\frac{\partial a_2}{\partial t} + \frac{\partial q_{2s}}{\partial s} + \frac{\partial q_{2n}}{\partial n} = -w_{ie} \quad (\text{A.10})$$

which can be written again in the following 'conservative' form

$$\frac{\partial \mathbf{U}'}{\partial t} + \frac{\partial \mathbf{G}'}{\partial s} + \frac{\partial \mathbf{H}'}{\partial n} = -\mathbf{F}'' \quad (\text{A.11})$$

Since variables are only discontinuous in  $n$ -direction, while they are continuous in  $s$ -direction, the corresponding Rankine Hugoniot conditions follow from

$$c_N(\mathbf{U}'_l - \mathbf{U}'_r) = (\mathbf{U}'_l - \mathbf{U}'_r) - \mathbf{F}'' \quad (\text{A.12})$$

with  $c_N$  is the front celerity in  $n$ -direction (normal to the front). The continuous derivative  $\partial \mathbf{G}' / \partial x$  adds up to the forces on the right-hand side of the equation. We assume that the effect of these terms on frontal motion is small compared to the strong discontinuous terms in the equations.

From these we obtain for a front at the bottom:

$$c_N \left[ q_{2sl} - \frac{\bar{a}_2}{\bar{a}_1} (q_{1sl} - q_{1sr}) \right] = \frac{q_{2sl} q_{2nl}}{a_{2l}} - \frac{\bar{a}_2}{\bar{a}_1} \left( \frac{q_{1sl} q_{1nl}}{a_{1l}} - \frac{q_{1sr} q_{1nr}}{a_{1r}} \right) - F_s'' \quad (\text{A.13})$$

$$c_N \left[ q_{2nl} - \frac{\bar{a}_2}{\bar{a}_1} (q_{1nl} - q_{1nr}) \right] = \frac{q_{2nl}^2}{a_{2l}} - \frac{\bar{a}_2}{\bar{a}_1} \left( \frac{q_{1nl}^2}{a_{1l}} - \frac{q_{1nr}^2}{a_{1r}} \right) + \frac{1}{2} g_z r a_{2l}^2 - F_n'' \quad (\text{A.14})$$

$$c_N (a_{2l} - a_{2r}) = q_{2nl} - q_{2nr} \quad (\text{A.15})$$

Variables with a bar ( $\bar{a}_1, \bar{a}_2$ ) are the respective quantities linearly averaged over the discontinuity.

From the conditions above the variables associated to the upper layer can be eliminated using the (continuous) values of  $q_s$ ,  $q_n$  and  $a$  from the barotropic (external) flow computation. If the stream-lines of upper and lower layer flow are primarily normal to the front ( $q_{1sl} \approx q_{1sr} \approx q_{2sl} \approx q_{2sr} \approx 0$ ) then only the conditions (A.14) and (A.15) remain, which are identical to the 1-D Rankine Hugoniot conditions which were derived in section 6.4. This situation occurs near the foremost point of the advancing plume, but not necessarily at its (sometimes arrested) sides.

We assume the force  $F_n''$  is again a function of relative celerity and ambient flow

velocity. Although now the appropriate components of the flow velocity have to be chosen to express the energy loss in terms of  $(\text{velocity})^2/2g$  (equivalent to Kranenburg's approach). Therefore, as an additional equation for closure of the system, we adopt the Bernoulli equation along a streamline passing through the front as proposed by Benjamin (1968) for the 1-D front. A transformation of the  $s, n$  coordinate system to a  $s', n'$  coordinate system moving with the front is useful for this purpose. In figure A.2 an example is given of the transformation and how stream lines may pass the front.

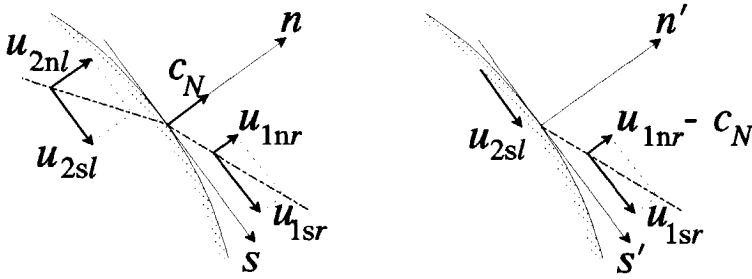


Figure A.2 Coordinate transformation and streamline (dashed line) passing through the front at a small distance above the bottom.

Along these stream lines the following Bernoulli equation is formulated:

$$\begin{aligned} \rho_f g_z a_{1r} + \frac{1}{2} \rho_f [((1 - \lambda_s) u_{1nr} - c_N)^2 + (1 - \lambda_s)^2 u_{1sr}^2] - \Delta E_1 = \\ = \rho_f g_z a_{1l} + \rho_f (1 + \sigma' C_s) g_z a_{2l} - \Delta E_2 \end{aligned} \quad (\text{A.16})$$

where  $\lambda_s$  is introduced to account for the effect of bottom shear on the velocity profile of the ambient flow. The energy loss  $\Delta E_1$  is caused by bottom generated turbulence in the ambient flow, and  $\Delta E_2$  is associated to the flow in the head of the turbidity current. In the 1-D approach we used a parametrization as proposed by Kranenburg (1978, 1993a). For a 1-D front advancing into a stagnant ambient fluid:

$$\Delta E_2 - \Delta E_1 = \frac{1}{2} \rho_f k c_N^2 \quad (\text{A.17})$$

For a 1-D front advancing into an ambient flow:

$$\Delta E_2 - \Delta E_1 = \frac{1}{2} \rho_f [k(c_N - u_{1nr})^2 + k'(c_N - u_{1nr})u_{1nr} + k''u_{1nr}^2] \quad (\text{A.18})$$

where  $k$ ,  $k'$ , and  $k''$  are energy-loss coefficients and  $u_{1nr} = q_{1nr}/a_{1nr}$ .

In a 2-DH front these parametrizations do not fully apply or need some correction.

Physical considerations indicate that processes associated to tangential velocities generate forces which counteract the net pressure force normal to the arrested front on the side of the plume (additional to gravity, friction and entrainment forces). These effects are introduced into the parametrization of the energy losses of the front by a coefficient  $k_2$ . This is shown in the following.

If  $q_{1nr} = q_{1sr} = 0$  we parametrize the energy loss in the Bernoulli equation as

$$\Delta E_2 - \Delta E_1 = 1/2 \cdot \rho_f (k_1 c_N^2 + k_2 u_{2sl}^2) \quad (\text{A.19})$$

where  $u_{2sl} = q_{2sl}/a_{2l}$ . For a 2-D front into an ambient flow we parametrize the energy loss as

$$\Delta E_2 - \Delta E_1 = 1/2 \cdot \rho_f [k_1 (c_N - u_{1nr})^2 + k_1' (c_N - u_{1nr}) u_{1nr} + k_1'' u_{1nr}^2 + k_2 u_{2sl}^2] \quad (\text{A.20})$$

where  $k_1, k_1', k_1'', k_2$  are energy-loss coefficients. Alternatively in equation (A.20)  $u_{2sl} = q_{2sl}/a_{2l}$  can be replaced by the velocity difference between the layers  $u_{2sl} - u_{1sl}$ , but this is not further elaborated here. Note that these parametrizations are similar to those in 1-D flow except for the presence of a loss term due to  $u_{2sl}$ . The results are therefore also similar to those for 1-D fronts.

For further elaboration we use the following transformations to make the relevant variables dimensionless

$$\tilde{c} = \frac{c_N}{\sqrt{g_z' a}} \quad ; \quad \tilde{q}_{1s} = \frac{q_{1sr}}{a \sqrt{g_z' a}} \quad ; \quad \tilde{q}_{1n} = \frac{q_{1nr}}{a \sqrt{g_z' a}} \quad ; \quad \tilde{q}_{2s} = \frac{q_{2sl}}{a \sqrt{g_z' a}}$$

and

$$\tilde{a}_f = \frac{a_{2l}}{a} \quad ; \quad \tilde{a}_1 = \frac{a_{1l}}{a} \quad ; \quad \tilde{F}_n'' = \frac{F_n''}{g_z' a^2}$$

where  $g_z' = g_z \cdot \sigma' \cdot C_s$ ,

Now the dimensionless front celerity can be expressed in terms of the energy loss coefficients, the dimensionless front depth, and the dimensionless flow discharges near the front. Corresponding to the 1-D approach the four Rankine Hugoniot conditions following from the momentum and mass equations for the coupled 2-DH model are combined with the Bernoulli equation (A.16) to eliminate  $q_{1sl}, q_{1nl}, q_{2nl}, a_{1l}, F_n''$  and  $F_s''$ . Then the remaining equation (in dimensionless form) expresses the front celerity. This result can be used to express the forces  $F_n''$  and  $F_s''$  acting on the front as a function of  $\tilde{q}_{2s}$ .

For the case with no ambient flow (using eq.61) we obtain (if  $C_s \ll 1$  and  $\tilde{q}_{2s}$  is small)

$$\tilde{c} \approx \sqrt{\frac{(1 - \tilde{a}_f) [(2 - \tilde{a}_f) \tilde{a}_f^3 - k_2 \tilde{q}_{2s}^2]}{\tilde{a}_f^2 [\tilde{a}_f(1 - k_1) + 1 + k_1]}} \quad (\text{A.23})$$

and

$$\tilde{F}_n'' \approx \frac{1}{4} \frac{[\tilde{a}_f^2 (1 + k_1)(1 - \tilde{a}_f)(2 - \tilde{a}_f) - 2k_2 \tilde{q}_{2s}^2]}{[\tilde{a}_f(1 - k_1) + 1 + k_1]} \quad (\text{A.24})$$

By substituting the results into equation (A.13) a similar relation for  $F_s''$  can be found. The maximum value of  $k_2$  for which  $c = 0$  is

$$k_{2,\max} = \tilde{a}_f^3 (2 - \tilde{a}_f) / \tilde{q}_{2s}^2 \quad (\text{A.25})$$

For the case with ambient flow (using eq.62) we follow Kranenburg's (1993a) derivation for the 1-D front celerity. We obtain (if  $C_s \ll 1$  and  $\tilde{q}_{2s}$  is small)

$$(\tilde{c} - \tilde{q}_{1n})^2 \left[ \frac{(1 + \tilde{a}_f)}{(1 - \tilde{a}_f)} + k_1 \right] + (\tilde{c} - \tilde{q}_{1n}) \tilde{q}_{1n} (k_1' + 2s) + \tilde{q}_{1n}^2 (k_1'' + s^2) + (\tilde{c} - \tilde{q}_{1n})^2 + \tilde{q}_{1s}^2 (1 - s)^2 + (\tilde{q}_{2s} / \tilde{a}_f)^2 k_2 - \tilde{a}_f (2 - \tilde{a}_f) = 0 \quad (\text{A.26})$$

To eliminate some of the coefficients we followed Kranenburg by stating that  $\tilde{c} - \tilde{q}$  reduces as  $\tilde{q}$  increases, and  $\tilde{c}$  must go to zero if  $\tilde{a}_f$  goes to zero. The latter case for instance corresponds to the foremost tip of an arrested salt wedge but not to the arrested sides of a plume. By approximation we obtained

$$(\tilde{c} - \tilde{q}_{1n})^2 \left[ \frac{(1 + \tilde{a}_f)}{(1 - \tilde{a}_f)} + k_1 \right] + (\tilde{c} - \tilde{q}_{1n}) \tilde{q}_{1n} (1 + k_1) + \tilde{q}_{1s}^2 + (\tilde{q}_{2s} / \tilde{a}_f)^2 k_2 - \tilde{a}_f (2 - \tilde{a}_f) = 0 \quad (\text{A.27})$$

And the force acting normal on the front becomes

$$\tilde{F}_n'' \approx \frac{1}{4} \sigma' C_s \tilde{a}_f^2 \left[ 2 - \tilde{a}_f - 2 \frac{(\tilde{c} - \tilde{q}_{1n})^2}{(1 - \tilde{a}_f)} \right] \quad (\text{A.28})$$

where  $\tilde{c}$  follows from eq.(A.27) (again a similar relation is found for  $F_s''$ ). The maximum value of  $k_2$  for which  $\tilde{c}$  remains real follows from the solution of eq.(A.27) and is a function of ambient flow and transversal discharge.

## Appendix B

### Total variation diminishing (TVD) artificial viscosity

#### B.1 Roe's linearization of the non-linear system

The scalar TVD concept can be extended to non-linear systems by using an appropriate local linearization of the Lax-Wendroff fluxes. A most popular and effective method can be obtained from Roe's (1981) approximate Riemann solver. It uses the exact solutions of a linear (constant coeff.) Riemann problem and applies this to the non-linear case. To illustrate this we start with a simple description of the solution to a linear Riemann problem by means of a wave decomposition.

##### *A linear Riemann problem*

Assume the Riemann problem for a 1-D linear homogeneous model with two dependent variables,  $\mathbf{U}=(u_1, u_2)$ , is written as

$$\frac{\partial \mathbf{U}}{\partial t} + A_0(\mathbf{U}_l, \mathbf{U}_r) \frac{\partial \mathbf{U}}{\partial x} = 0 \quad (\text{B.1})$$

with initial condition

$$\mathbf{U}(x, 0) = \begin{cases} \mathbf{U}_l & x < 0 \\ \mathbf{U}_r & x > 0 \end{cases} \quad (\text{B.2})$$

Assume that the system of two equations is hyperbolic with two constant (in time) real eigenvalues:

$$\frac{dx}{dt} = \phi_1(\mathbf{U}_l, \mathbf{U}_r) > 0 \quad ; \quad \frac{dx}{dt} = \phi_2(\mathbf{U}_l, \mathbf{U}_r) < 0 \quad (\text{B.3})$$

As they are dependent on  $\mathbf{U}_l$  and  $\mathbf{U}_r$ , they are different on both sides of the jump. In figure B.1 is shown how characteristic celerities (eigenvalues of  $A_0$ ) depart from  $t=0$  with the  $\phi_1$ -family as dotted lines and  $\phi_2$ -family as dashed lines. The initial jump split up into two shocks, which are located at the intersection of the characteristics of one of the two families starting from either side of the initial jump. Below and above the  $x, t$ -diagram impressions are given how these jumps can look like in the real world.

The classical solution to this problem can be found by means of a characteristic

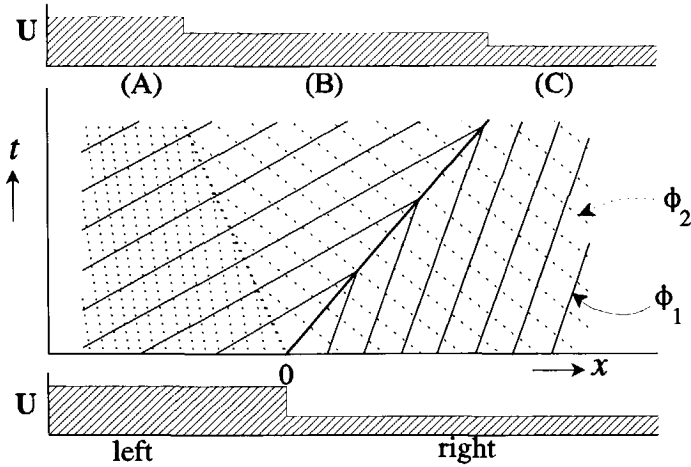


Figure B.1 Characteristic celerities  $\phi_i$  in a  $x,t$ -diagram for a linear Riemann problem with two dependent variables.

decomposition (e.g., see Le Veque, 1990). Since the system is hyperbolic its Jacobian  $A_0$  can be diagonalized by the decomposition

$$A_0 = R \Lambda_e R^{-1} \quad ; \quad \Lambda_e = \begin{pmatrix} \phi_1 & 0 \\ 0 & \phi_2 \end{pmatrix} \quad ; \quad R = (\mathbf{r}_1 \mid \mathbf{r}_2) \quad (\text{B.4})$$

Hence  $R$  is a matrix with columns formed by the right eigenvectors  $\mathbf{r}_k$  of  $A_0$  defined as

$$A_0 \mathbf{r}_k = \phi_k \mathbf{r}_k \quad , \quad k = 1, 2 \quad (\text{B.5})$$

Characteristic variables or Riemann variables can now be defined as (since  $R^{-1}$  is constant)

$$\bar{\omega} = \begin{pmatrix} \omega_1 \\ \omega_2 \end{pmatrix} = R^{-1} \mathbf{U} \quad ; \quad \mathbf{U} = R \bar{\omega} \quad (\text{B.6})$$

Elaborating the right part of (B.6) it can be seen quickly that

$$\mathbf{U}(x,t) = \sum_{k=1}^2 \omega_k(x,t) \mathbf{r}_k \quad (\text{B.7})$$

which is an eigenvector expansion of vector  $\mathbf{U}$  and represents the solution of the Riemann problem. Clearly this solution is a superposition of two single waves



advected independently, with no change of speed ( $\phi_k$ ) along the characteristics. Each wave has constant shape  $\omega_k(x,t) \cdot \mathbf{r}_k = \omega_k(x - \phi_k t, 0) \cdot \mathbf{r}_k$ , and is represented by the scalar compatibility equation

$$\frac{\partial \omega_k}{\partial t} + \phi_k \frac{\partial \omega_k}{\partial x} = 0 \quad (\text{B.8})$$

Looking at figure B.1 the solution of the problem in each point of the three regions (A), (B) and (C) is defined by the departure point of the characteristics at  $t=0$ . For instance in region (B)  $\phi_1$  characteristics carry information from the left state, while  $\phi_2$  characteristics carry information from the right state. Due to equation (B.7) the final solution is a superposition of these states.

This observation can be summarized by writing the solution as

$$\mathbf{U}(x,t) = \begin{cases} \mathbf{U}_l + \sum_{x - \phi_k t < 0} (\omega_{k,r} - \omega_{k,l}) \mathbf{r}_k \\ \mathbf{U}_r - \sum_{x - \phi_k t < 0} (\omega_{k,r} - \omega_{k,l}) \mathbf{r}_k \end{cases} \quad (\text{B.9})$$

which satisfy the Rankine Hugoniot conditions (e.g., Le Veque, 1990). The derivation above has shown that this solution evolves from the decomposition of the initial jump, i.e., linear wave decomposition, which can also be written in a more general form as

$$\mathbf{U}_l - \mathbf{U}_r = \sum_{k=1}^2 (\omega_{k,r} - \omega_{k,l}) \mathbf{r}_k \quad (\text{B.10})$$

Note that this solution only consists of discontinuities. Rarefaction waves cannot be computed or approximated, using this approach without some entropy correction.

### *Linearizing the discrete Jacobian matrix*

To get round the time consuming iteration method involved with solving non-linear Riemann problems, Roe (1981) proposed an ingenious linearization technique based on the solution of the linear Riemann problem as presented above. Since this method has proven its good performance in discontinuous flows it has become quite popular. For defining TVD methods its merits lie in the wave-decomposition of the flux-differences. Using this decomposition the system reduces to a set of decoupled scalar equations, on which the scalar TVD method can be applied. Hence flux limiters act on each simple-wave component.

Consider the linearised form of a general non-linear system of  $m$  (homogeneous)

equations with  $m$  dependent variables (forming state vector  $\mathbf{U}$ ):

$$\frac{\partial \hat{\mathbf{U}}}{\partial t} + \hat{A}(\mathbf{U}_l, \mathbf{U}_r) \frac{\partial \hat{\mathbf{U}}}{\partial x} = 0 \quad (\text{B.11})$$

The solution of this system can now be found from the previously described linear Riemann problem by using the following decomposition on the computational mesh

$$\mathbf{U}_{i+1} - \mathbf{U}_i = \Delta_x \mathbf{U} = \sum_{k=1}^m (\omega_{k,i+1} - \omega_{k,i}) \hat{\mathbf{r}}_k = \sum_{k=1}^m (\Delta_x \omega_k) \hat{\mathbf{r}}_k \quad (\text{B.12})$$

It represents the decomposition of a single discontinuity on mesh cell  $i+1/2$ , where  $\hat{\mathbf{r}}_k$  is the right eigenvector of  $\hat{A}$  associated to its eigenvalue  $\hat{\phi}_k$ . Also a similar eigenvector decomposition of flux-differences can be defined.

The most important part of the theory is the linearization applied to the Jacobian matrix  $A$ . Roe presented three conditions which has to be satisfied by  $\hat{A}$ :

- cond.1)**  $\hat{A}(\mathbf{U}_{i+1}, \mathbf{U}_i)(\mathbf{U}_{i+1} - \mathbf{U}_i) = \mathbf{f}(\mathbf{U}_{i+1}) - \mathbf{f}(\mathbf{U}_i)$  to ensure that the problem is conservative and it satisfies the Rankine Hugoniot relations.
- cond.2)**  $\hat{A}(\mathbf{U}_{i+1}, \mathbf{U}_i)$  is diagonalizable with real eigenvalues to ensure hyperbolicity.
- cond.3)** If  $\mathbf{U}_{i+1} = \mathbf{U}_i = \mathbf{U}$  then  $\hat{A}(\mathbf{U}, \mathbf{U}) = A(\mathbf{U}) = \partial \mathbf{f} / \partial x$  to ensure good behaviour on smooth solutions.

Matrix  $\hat{A}$  was derived for 1-D shallow-water equations for instance by Glaister (1988). Different to our approach the general type of shallow-water equations is of the  $q, a$ -form (i.e.,  $\partial q / \partial t + 2 \cdot \{q/a\} \cdot \partial q / \partial x + \dots$ ) representing conservation of momentum and mass. The model presented here is of the  $u, a$ -form (i.e.,  $\partial u / \partial t + u \cdot \partial u / \partial x + \dots$ ) representing conservation of velocity and mass, which results in a different Jacobian  $A$ . In  $q, a$ -form the convective flux in the momentum equation yields a division  $q/a$  in the Jacobian matrix, while in  $u, a$ -form this flux only yields a linear term  $u$ . To satisfy condition (cond.1) given above, this division  $q/a$  originating from the convective flux can only be linearized using a square-root averaging. Also the Euler equations in gas dynamics require the square-root averaging to fractions of dependent variables.

The construction of the linearized Jacobian matrix under the three presented conditions can be elaborated for the constant concentration fixed bed, and for the full mobile bed baroclinic model. The basic equations for this model are presented in section 6.4.

Taking the vector of dependent variables as

$$\mathbf{U} = (\Omega, a_2, C_s, z_b)^T \quad ; \quad \Omega = u_2 - u_1 \quad (\text{B.13})$$

it is convenient to rewrite the sediment-mass equation (6.20) in an explicit formulation

by eliminating time derivatives of  $C_s$  and  $a_2$ :

$$\begin{aligned} (1 - \epsilon_p) \frac{\partial z_b}{\partial t} + q_2 (1 - L'_a/T'_a) \frac{\partial C_s}{\partial x} + \frac{\partial s_b}{\partial x} &= \\ &= - \left( \frac{s_b}{B_2} \right) \frac{\partial B_2}{\partial x} + w_{ie} C_s - \left( \frac{w_s}{T'_a} \right) (C_{se} - C_s) \end{aligned} \quad (\text{B.14})$$

Although this equation is not in conservative form, the Rankine Hugoniot conditions and characteristics of the system are still unchanged. With respect to discontinuities the right-hand side of this equation is of minor importance, and other non-conservative terms can be linearly averaged over the shock (e.g., section 4.3, shock rel.). The bed-load transport rate per unit of width  $s_b$  is considered to be a function of  $u_2$  and its gradient can therefore be formulated as

$$\frac{\partial s_b(u_2)}{\partial x} = f_b(u_2) \frac{\partial u_2}{\partial x} = f_b(\Omega, a_2) \frac{\partial}{\partial x} [\Omega (1 - a_2/a) + Q/(B_2 a)]$$

The baroclinic part of the 1-D model now consists of four equations; equation of motion, continuity, suspended-sediment and sediment mass. The flux vector and Jacobian of this system become respectively, after bringing gradient of  $B_2$  to the right side (to the the source term):

$$\mathbf{f}(\mathbf{U}) = \begin{pmatrix} \frac{1}{2} (u_2^2 - u_1^2) + g \sigma' C_s a_2 - \frac{1}{2} g \sigma' C_s \bar{a}_2 + g \sigma' \bar{C}_s z_b \\ \frac{u_2 a_2}{\left( \frac{L'_a u_2}{T'_a} \right) C_s} \\ \left[ s_b + \frac{q_2 (1 - L'_a/T'_a) C_s}{(1 - \epsilon_p)^{-1}} \right] \end{pmatrix} \quad (\text{B.16})$$

$$A(\mathbf{U}) = \begin{pmatrix} u_2 - \frac{\Omega a_2}{a} & -\frac{\Omega^2}{a} + g \sigma' C_s & \frac{1}{2} g \sigma' a_2 & g \sigma' C_s \\ a_2 \left( 1 - \frac{a_2}{a} \right) & u_2 - \frac{\Omega a_2}{a} & 0 & 0 \\ 0 & 0 & L'_a u_2 / T'_a & 0 \\ f_b \left( \frac{1 - a_2/a}{1 - \epsilon_p} \right) & -\frac{f_b \Omega}{a(1 - \epsilon_p)} & a_2 u_2 \left( \frac{1 - L'_a/T'_a}{1 - \epsilon_p} \right) & 0 \end{pmatrix} \quad (\text{B.17})$$

Here overbars represent arithmetic averages, e.g.,  $\bar{a}_2 = 1/2 \cdot (a_{2,i+1} + a_{2,i})$ .

To elaborate the right-hand side of the condition (cond.1):  $\hat{A}(\mathbf{U}_{i+1}, \mathbf{U}_i)(\mathbf{U}_{i+1} - \mathbf{U}_i) = \mathbf{f}(\mathbf{U}_{i+1}) - \mathbf{f}(\mathbf{U}_i)$ , the following identity for quadratic functions is applied:

$$\Delta_x(ab) = \bar{a}(\Delta_x b) + \bar{b}(\Delta_x a) \quad (\text{B.18})$$

where overbars denote arithmetic averages again. Since the flux vector eq.(B.15) only contains linear and quadratic terms eq.(B.17) shows that flux-vector difference can be expanded directly in terms of differences of  $\mathbf{U}$  times these averages. Elaboration of condition (cond.1) in this way yields the following Jacobian  $\hat{A}$ :

$$\hat{A} = \begin{pmatrix} \bar{u}_2 - \frac{\bar{\Omega}\bar{a}_2}{a} & -\frac{\bar{\Omega}^2}{a} + g\sigma'\bar{C}_s & \frac{1}{2}g\sigma'\bar{a}_2 & g\sigma'\bar{C}_s \\ \bar{a}_2\left(1 - \frac{\bar{a}_2}{a}\right) & \bar{u}_2 - \frac{\bar{\Omega}\bar{a}_2}{a} & 0 & 0 \\ 0 & 0 & \overline{L'_a u_2 / T'_a} & 0 \\ \bar{f}_b\left(\frac{1 - \bar{a}_2/a}{1 - \epsilon_p}\right) & -\frac{\bar{f}_b\bar{\Omega}}{a(1 - \epsilon_p)} & \bar{a}_2\bar{u}_2\left(\frac{1 - L'_a/T'_a}{1 - \epsilon_p}\right) & 0 \end{pmatrix} \quad (\text{B.19})$$

which corresponds exactly to the original Jacobian, except that all values with overbars are averaged. This results remains unchanged for multi-dimensional flows.

Eigenvectors and eigenvalues for this matrix are identical to the original non-linear system, hence the new system automatically satisfies conditions (cond.2) and (cond.3). For the numerical model the first three eigenvalues (or characteristic celerities) follow from the following characteristic polynomial

$$\hat{\phi}^3 - 2\Gamma\hat{\phi}^2 - \hat{\phi}\left[g\sigma'\bar{C}_s\frac{\bar{a}_1}{a}\left(\frac{\bar{f}_b}{1 - \epsilon_p} + \bar{a}_2\right) - \Gamma^2 - \frac{\bar{a}_1\bar{a}_2\bar{\Omega}^2}{a^2}\right] + g\sigma'\bar{C}_s\left[\frac{\bar{f}_b\bar{a}_1\bar{u}_2}{a(1 - \epsilon_p)}\right] = 0 \quad (\text{B.20})$$

which can be solved analytically for  $\hat{\phi}_k$ ,  $k=1,3$ . Here parameter  $\Gamma$  is defined as

$$\Gamma = \bar{u}_2 - \frac{\bar{\Omega}\bar{a}_2}{a} \quad (\text{B.21})$$

A fourth characteristic originating from Galappatti's equation can be written as

$$\hat{\phi}_4 = \overline{L'_a u_2 / T'_a} \quad (\text{B.22})$$

The right eigenvectors follow from  $\hat{A}\hat{\mathbf{r}} = \hat{\phi}\hat{\mathbf{r}}$  and can be written (with subscript  $k$

referring to eigenvalue  $\hat{\phi}_k$ ):

$$\hat{\mathbf{r}}_{k=1,3} = \begin{pmatrix} \left[ \frac{-\Gamma + \hat{\phi}_k}{\bar{a}_1 \bar{a}_2 / a} \right] \\ 1 \\ 0 \\ \left[ \frac{(\hat{\phi}_k - \Gamma)^2 - \Lambda_1 \bar{a}_1 \bar{a}_2 / a}{g \sigma' \bar{C}_s \bar{a}_1 \bar{a}_2 / a} \right] \end{pmatrix} ; \quad \hat{\mathbf{r}}_4 = \begin{pmatrix} \frac{1}{2} \left[ \frac{\Upsilon_1}{\Upsilon_{\text{all}}} \right] \\ \frac{1}{2} \left[ \frac{\Upsilon_2}{\Upsilon_{\text{all}}} \right] \\ 1 \\ \frac{1}{2} \left[ \frac{\Upsilon_3}{\Upsilon_{\text{all}}} \right] \end{pmatrix} \quad (\text{B.23})$$

where

$$\Lambda_1 = -\frac{\bar{\Omega}^2}{a} + g \sigma' \bar{C}_s ; \quad \Lambda_2 = \frac{\bar{a}_2 \bar{u}_2}{(1 - \epsilon_p) (1 - L'_a / T_a)} \quad (\text{B.24})$$

$$\Upsilon_{\text{all}} = a \left[ (\hat{\phi}_4 - \Gamma)^2 \hat{\phi}_4 a - \bar{a}_1 \left\{ \frac{g \sigma' \bar{C}_s \bar{f}_b}{1 - \epsilon_p} (\hat{\phi}_4 - \Gamma) + \Lambda_1 \bar{a}_2 \hat{\phi}_4 \right\} \right] \quad (\text{B.25})$$

$$\Upsilon_1 = g \sigma' (\hat{\phi}_4 - \Gamma) a \left[ a (2 \bar{C}_s \Lambda_2 + \bar{a}_2 \hat{\phi}_4) - 2 \frac{\bar{C}_s \bar{u}_2 \bar{\Omega} \bar{f}_b}{1 - \epsilon_p} \right] \quad (\text{B.26})$$

$$\Upsilon_2 = g \sigma' \bar{a}_2 \bar{a}_1 \left[ a (2 \bar{C}_s \Lambda_2 + \bar{a}_2 \hat{\phi}_4) - 2 \frac{\bar{C}_s \bar{u}_2 \bar{\Omega} \bar{f}_b}{1 - \epsilon_p} \right] \quad (\text{B.27})$$

$$\Upsilon_3 = 2 \left( a \Lambda_2 - \frac{\bar{u}_2 \bar{\Omega} \bar{f}_b}{1 - \epsilon_p} \right) \left[ a (\hat{\phi}_4 - \Gamma)^2 - \bar{a}_1 \bar{a}_2 \Lambda_1 \right] + g \sigma' a \bar{a}_1 \bar{a}_2 \bar{f}_b \left( \frac{\hat{\phi}_4 - \Gamma}{1 - \epsilon_p} \right) \quad (\text{B.28})$$

In equation (B.4) is shown how a matrix  $R$  can be formed with the right eigenvectors as columns. If this matrix is inverted it can be used to define the difference of the characteristic variables as function of the difference in components of vector  $\mathbf{U}$ :

$$(\Delta_x \bar{\omega}) = R^{-1} (\Delta_x \mathbf{U}) \quad (\text{B.29})$$

Matrix  $R^{-1}$  is written as

$$\begin{pmatrix} \frac{\gamma_{11}}{(\hat{\phi}_1 - \hat{\phi}_2)(\hat{\phi}_1 - \hat{\phi}_3)} & \frac{\gamma_{21}}{(\hat{\phi}_1 - \hat{\phi}_2)(\hat{\phi}_1 - \hat{\phi}_3)} & \frac{\gamma_{31}}{(\hat{\phi}_1 - \hat{\phi}_2)(\hat{\phi}_1 - \hat{\phi}_3)} & \frac{\gamma_4}{(\hat{\phi}_1 - \hat{\phi}_2)(\hat{\phi}_1 - \hat{\phi}_3)} \\ \frac{-\gamma_{12}}{(\hat{\phi}_1 - \hat{\phi}_2)(\hat{\phi}_2 - \hat{\phi}_3)} & \frac{-\gamma_{22}}{(\hat{\phi}_1 - \hat{\phi}_2)(\hat{\phi}_2 - \hat{\phi}_3)} & \frac{-\gamma_{32}}{(\hat{\phi}_1 - \hat{\phi}_2)(\hat{\phi}_2 - \hat{\phi}_3)} & \frac{-\gamma_4}{(\hat{\phi}_1 - \hat{\phi}_2)(\hat{\phi}_2 - \hat{\phi}_3)} \\ \frac{\gamma_{13}}{(\hat{\phi}_1 - \hat{\phi}_3)(\hat{\phi}_2 - \hat{\phi}_3)} & \frac{\gamma_{23}}{(\hat{\phi}_1 - \hat{\phi}_3)(\hat{\phi}_2 - \hat{\phi}_3)} & \frac{\gamma_{33}}{(\hat{\phi}_1 - \hat{\phi}_3)(\hat{\phi}_2 - \hat{\phi}_3)} & \frac{\gamma_4}{(\hat{\phi}_1 - \hat{\phi}_3)(\hat{\phi}_2 - \hat{\phi}_3)} \\ 0 & 0 & 1 & 0 \end{pmatrix} \quad (\text{B.30})$$

where

$$\begin{aligned} \gamma_{1j} &= \frac{\bar{a}_1 \bar{a}_2}{a} (\beta_{il} - \beta_{i2}) \\ \gamma_{2j} &= \frac{\bar{a}_1 \bar{a}_2}{a} \Lambda_1 + \beta_{il} \beta_{i2} \\ \gamma_{3j} &= \frac{-1}{2\Upsilon_{\text{all}}} \left[ \frac{\bar{a}_1 \bar{a}_2}{a} (\Lambda_1 \Upsilon_2 + g \sigma' \bar{C}_s \Upsilon_3 + \Upsilon_1 \{\beta_{il} + \beta_{i2}\}) + \beta_{il} \beta_{i2} \Upsilon_2 \right] \\ \gamma_4 &= g \sigma' \bar{C}_s \bar{a}_1 \bar{a}_2 / a \end{aligned} \quad (\text{B.31})$$

in which

$$\beta_{il} = \Gamma - \hat{\phi}_{il} \quad ; \quad j=1 \begin{cases} i1=2 \\ i2=3 \end{cases} \quad ; \quad j=2 \begin{cases} i1=1 \\ i2=3 \end{cases} \quad ; \quad j=3 \begin{cases} i1=1 \\ i2=2 \end{cases} \quad (\text{B.32})$$

The splitting process is concluded if these results are substituted in equation (B.11). TVD artificial viscosity terms can now be formulated using these results to decompose flux differences in a similar way. Clearly this theory requires a large computational effort, but that can be significantly reduced for fixed bed computations with constant concentration. Then the number of equations, as well the number of eigenvalues and eigenvectors reduces to two. The linearisation of the Jacobian as presented above still holds. The eigenvalues can now be written explicitly as

$$\hat{\phi}_{1,2} = \bar{u}_2 - \frac{\bar{\Omega} \bar{a}_2}{a} \pm \hat{c} \quad ; \quad \hat{c} = \sqrt{\frac{\bar{a}_2 \bar{a}_1}{a^2} (g \sigma' C_s a - \bar{\Omega}^2)} \quad (\text{B.33})$$

with associated right eigenvectors

$$\hat{\mathbf{r}}_{1,2} = \left( \pm \frac{\hat{c}a}{a_2\bar{a}_1}, 1 \right)^T \quad (\text{B.34})$$

and differences of characteristic variables

$$(\Delta_x \omega_{1,2}) = \pm \frac{1}{2} \left[ \frac{\bar{a}_2 \bar{a}_1}{a} \right] \frac{(\Delta_x \Omega)}{\hat{c}} + \frac{1}{2} (\Delta_x a_2) \quad (\text{B.35})$$

## B.2 Flux limiters

The application of the TVD method to define an artificial viscosity term for the MacCormack scheme is treated in section 6.6. It is shown that the second-order correction term of the Lax-Wendroff flux (MacCormack's flux for the linearized system) can be limited by multiplying it with a limiter function. Near discontinuities with large flux differences the limiter must approach, in a non-linear way, to zero to reduce the scheme to first order, while in smooth regions the limiter must go to unity to obtain second-order accuracy.

Several appropriate limiters are reported in literature (e.g., see Sweby, 1984, Le Veque, 1990, Hirsch, 1990). The limiters are dependent on associated upwind ratios  $\theta$  of characteristic variables or fluxes, and satisfy the conditions (section 6.6)

$$0 \leq \frac{\Phi(\theta)}{\theta} \leq 2 \quad \text{and} \quad \Phi(\theta) \leq 2 \quad (\text{B.36})$$

with

$$\theta_{i+1/2}^{k,1} = \frac{(\Delta_x \omega_k)_{i+1/2-j}}{(\Delta_x \omega_k)_{i+1/2}} ; \quad \theta_{i+1/2}^{k,2} = \frac{\left[ |\hat{\phi}_k| \left( 1 - \frac{\Delta t}{\Delta x} |\hat{\phi}_k| \right) (\Delta_x \omega_k) \right]_{j+1/2-j}}{\gamma' + \left[ |\hat{\phi}_k| \left( 1 - \frac{\Delta t}{\Delta x} |\hat{\phi}_k| \right) (\Delta_x \omega_k) \right]_{i+1/2}} \quad (\text{B.37})$$

where  $j = \text{sign}(\hat{\phi}_k)$  to assure that  $\theta$  is the ratio of slopes in upwind direction;  $\gamma'$  is a small number (e.g.,  $1 \cdot 10^{-8}$ ) to prevent division by zero. An additional condition to obtain second-order accuracy is that the function  $\Phi$  must pass through the point  $\Phi(1)=1$  since in smooth parts, where  $\Phi$  should go to unity, values of  $\theta$  are close to one. Furthermore it must lie between  $\Phi(\theta)=\theta$  and  $\Phi(\theta)=1$  (Sweby, 1984). This is illustrated in figure B.2.

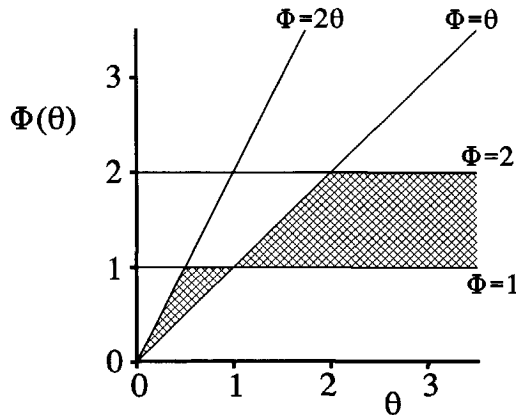


Figure B.2 Second-order TVD region (shaded).

Limiter functions which satisfy equation (B.36) but lie below the shaded region in figure B.2 give to smoothening, while those which lie above this region give to much compression (turning a sine-wave into a square wave in time).

The upper boundary of this region is expressed by the 'superbee' limiter of Roe (1985):

$$\Phi(\theta) = \max[0, \min(1, 2\theta), \min(\theta, 2)] \quad (\text{B.38})$$

The lower boundary of this region is expressed by the 'minmod' function:

$$\Phi(\theta) = \max[0, \min(1, \theta)] \quad (\text{B.39})$$

All other limiters are located within these two bounds. Well known is van Leer's (1974) limiter which is a continuous function of  $\theta$ :

$$\Phi(\theta) = \frac{\theta + |\theta|}{1 + \theta} \quad (\text{B.40})$$

A general family of limiters can be defined as (Sweby, 1984)

$$\Phi(\theta) = \max[0, \min(\alpha\theta, 1), \min(\theta, \alpha)] \quad 1 \leq \alpha \leq 2 \quad (\text{B.41})$$

which also contains the boundaries of the TVD region. Smoother than van Leer's limiter is that of van Albeda et al. (1982):

$$\Phi(\theta) = \frac{\theta^2 + \theta}{1 + \theta^2} \quad (\text{B.42})$$



Alternatively a monotonized centred limiter can be used:

$$\Phi(\theta) = \min[|\alpha|, 2, 2|\theta|] \cdot \text{sign}(1, \alpha) \quad ; \quad \alpha = \frac{1}{2}(1 + \theta) \quad (\text{B.43})$$

For application of these limiters to the Lax-Wendroff flux Hirsch (1990) showed that they must satisfy a symmetry property

$$\frac{\Phi(\theta)}{\theta} = \Phi\left(\frac{1}{\theta}\right) \quad (\text{B.44})$$

which can be shown to hold for all the presented limiters above.

More details on these limiters can be obtained from the mentioned references. The list of limiter functions given above is implemented in the numerical model.

### B.3 Entropy fix

A disadvantage of using the solution to the linear Riemann problem, in order to define the numerical fluxes, is the impossibility to compute rarefaction waves. The difficulties occur only when the expansion contains a transcritical point, i.e., a change from subcritical to supercritical flow. Details on this problem are for instance well described by Hirsch (1990) and Le Veque (1990). The most popular solution to this deficiency is an entropy fix introduced by Harten and Hyman (1983). Effectively it introduces a local expansion fan in the approximate Riemann solution when it is required. Therefore it is necessary to modify the modulus of eigenvalue  $\phi_k$  in the computation of the viscosity term (algorithm 6.2) and the slope ratio  $\theta^k$  (eq. B.37). Following Harten and Hyman this is realized by

$$|\hat{\phi}_{k,i+1/2}| = \begin{cases} |\hat{\phi}_{k,i+1/2}| & \text{if } |\hat{\phi}_{k,i+1/2}| \geq \epsilon_r \\ \epsilon_r & \text{if } |\hat{\phi}_{k,i+1/2}| < \epsilon_r \end{cases} \quad (\text{B.45})$$

where

$$\epsilon_r = \max\left[ 0, \left( \hat{\phi}_{k,i+1/2} - \phi_{k,i} \right), \left( \phi_{k,i+1} - \hat{\phi}_{k,i+1/2} \right) \right] \quad (\text{B.46})$$

When there is no transcritical point the formulation above yields the original moduli, otherwise the formulation yields an entropy fix to Roe's approximate Riemann solution.



## Curriculum vitae

- 20-4-1966      Cornelis Johannes Sloff, geboren te Heerjansdam.
- 1978 - 1984      Atheneum (VWO), Walburg College, Zwijndrecht.
- 1984 - 1990      Ingenieursopleiding Civiele Techniek, Technische Universiteit Delft.
- 1989              Stage aan de ITS Universiteit in Surabaya, Indonesië, als onderdeel van het afstudeeronderzoek naar de morfologie van vulkaanrivieren.
- 1990              Ingenieursexamen Civiele Techniek, Vakgroep Waterbouwkunde, afstudeerhoogleraar: prof.dr.ir. M. de Vries.
- 1990 - 1995      Assistent in opleiding, Vakgroep Waterbouwkunde, Faculteit Civiele Techniek, Technische Universiteit Delft. Promotieonderzoek in samenwerking met het Waterloopkundig Laboratorium naar sedimentatie in stuwmeren, onder leiding van prof.dr.ir. M. de Vries. Tevens assistentie bij het begeleiden, opleiden en tentamineren van doctoraal studenten in het vak rivierwaterbouwkunde aan de Technische Universiteit.
- 1992              Deelname aan de 'Second Summer School on Stability of River and Coastal Forms', Sapporo, Japan.
- 1995 - heden      Projectingenieur Waterloopkundig Laboratorium. Met name betrokken bij de morfologische en hydraulische studies van rivieren.

